



HAL
open science

Smart control of nonlinear effects in guided optics : Numerical and experimental studies towards novel imaging applications

Lynn Sader

► **To cite this version:**

Lynn Sader. Smart control of nonlinear effects in guided optics : Numerical and experimental studies towards novel imaging applications. Optics / Photonics. Université de Limoges, 2023. English. NNT : 2023LIMO0057 . tel-04691723

HAL Id: tel-04691723

<https://theses.hal.science/tel-04691723v1>

Submitted on 9 Sep 2024

HAL is a multi-disciplinary open access archive for the deposit and dissemination of scientific research documents, whether they are published or not. The documents may come from teaching and research institutions in France or abroad, or from public or private research centers.

L'archive ouverte pluridisciplinaire **HAL**, est destinée au dépôt et à la diffusion de documents scientifiques de niveau recherche, publiés ou non, émanant des établissements d'enseignement et de recherche français ou étrangers, des laboratoires publics ou privés.

University of Limoges
ED 653 - Sciences et Ingénierie (SI)
XLIM Research Institute of Limoges

A thesis submitted to University of Limoges
in partial fulfillment of the requirements of the degree of
Doctor in information science and engineering
Photonics

Presented and defended by
Lynn SADER

On November 24, 2023

**Smart Control of Nonlinear Effects in Guided Optics: Numerical and
Experimental Studies towards Novel Imaging Applications**

Thesis supervisor: Benjamin Wetzel, Vincent Kermène

JURY:

President of jury

Mrs. Agnès Desfarges-Berthelemot, Professeur des Universités, Institut XLIM,
Université de Limoges

Reporters

Mr. Arnaud Mussot, Professeur des Universités, Laboratoire PhLAM, Université de
Lille

Mr. Thibaut Sylvestre, Directeur de Recherche CNRS, Institut FEMTO-ST, Université
de Franche-Comté

Examiners

Mr. Michael Kues, Professor, Institute of Photonics, Leibniz University Hannover

Guests

Mr. Vincent Kermène, Directeur de Recherche CNRS, Institut XLIM, Université de
Limoges

M. Benjamin Wetzel, Chargé de Recherche CNRS, Institut XLIM, Université de
Limoges



Dedication

To my family and friends

“If you feel you are in a black hole, don’t give up. There’s a way out.” -
Stephen Hawking

Acknowledgements

As my doctoral journey ends, I am humbled to express my sincere gratitude to those whose invaluable support and contributions helped me get where I am today.

First, I extend my sincere gratitude to the members of the jury, Mr. Arnaud Mussot and Mr. Thibaut Sylvestre, for their invaluable time and effort in evaluating my work, and to Mrs. Agnès Desfarges-Berthelemot and Mr. Michael Kues, for their insightful comments on my manuscript. A special thanks goes to my supervisors, Vincent Kermene and Benjamin Wetzel, whose guidance and support were essential in completing my thesis and delivering a successful defense. I am particularly grateful to Benjamin for his help all along these three years, providing leadership, direction, and encouragement. With his role as a mentor and supervisor I was able to succeed in this job and accomplish important research work.

I would like to acknowledge the collaborative effort with my teammates. Van Thuy Hoang, Alexis Bougaud, Bruno Chavez, Manal Arbati, and Yassin Boussafa, each played a unique and crucial role in making my journey enjoyable and educational. Yassin, my office mate, deserves a special mention for his understanding of my habits and for all the fun we had in organizing events together. Gratitude extends to Michael Kues's team for their hospitality during my two-week stay in their lab, leading to successful experiments and published results. Working with Michael, Surajit Bose, and Raktim Haldar was both productive and pleasurable.

I am also deeply appreciative of the University of Limoges and XLIM Institute, and the Region Nouvelle Aquitaine and the European Research Council (ERC) for their financial support. Special thanks to Nathalie Buisson and Françoise Merigaud for their indispensable assistance during missions and to all the personnel at XLIM with whom I had the privilege to work with.

My heartfelt thanks go to my family—my parents, my brothers Chady and Elie— my support team. They have consistently lifted my spirits and boosted my morale during moments of exhaustion and despair. To Toni, who gracefully tolerated my occasional moods of stress during those tough workdays and never gave up on me, no matter what. To my best friends Ghewa Barakat and Celia Hasrouni, and to Sara Modni and Alexis Dufour, who shared a similar journey, your encouragement and friendship meant the world.

I am grateful for the colleagues who became ones of the most important people in my life, Sahar Wehbi and Sidi-Ely Ahmedou, two exceptional individuals. A special mention goes to Cristian Jimenez, who has the kindest heart. It was a pleasure to be your friend and I thank you for all the times you helped me, I couldn't do it without you. I extend my thanks to Colman Buckley, my first office mate, for introducing me to everyone. Gratitude also to my colleagues Raphael Jauberteau, Yann Leventoux, Yago Arosa, Geoffroy Granger, Romain Dauliat, Amine Benazza, Flavien Beffara, Joelle Youssef, Clara Abbouab, Melek Jedidi, Lamine Ferhat, Idris Tiliouine, Issoufou Zamkoy, Yasmine Asselah, Clément Goicoechea, Rosu Baby, Ali Al Dhaybi, Jim Ignacchiti, Heloise Orihuel, Nour Tabcheh, Ali Dia, Youssef Rammal, and the funniest duo Maxime Jonard and Benjamin Gobé.

To everyone mentioned and those not named, your contributions have made this journey memorable and rewarding. Thank you all for being an integral part of my academic and personal growth.

Rights

This creation is available under a Creative Commons contract:
« **Attribution-Non Commercial-No Derivatives 4.0 International** »
online at <https://creativecommons.org/licenses/by-nc-nd/4.0/>



Table of Contents

General Introduction.....	17
Chapter I. Nonlinear phenomena in optical fibers	22
I.1. Fiber and guided optics overview	22
I.1.1. Principle and guiding properties.....	24
I.1.2. Fabrication	26
I.1.3. Other specialty fibers and optical waveguide.....	27
I.2. Pulse propagation in guided optics.....	30
I.2.1. Linear propagation	31
I.2.1.1. Dispersion.....	32
I.2.1.2. Attenuation and losses	35
I.2.2. Nonlinear propagation.....	36
I.2.2.1. Kerr effect.....	38
I.2.2.2. Raman effect	39
I.3. Modeling of nonlinear pulse propagation.....	41
I.3.1. The nonlinear Schrödinger equation	41
I.3.2. The generalized nonlinear Schrödinger equation	42
I.3.3. Numerical propagation framework: The split-step Fourier method	43
I.4. Overview of different pulse propagation regimes	43
I.4.1. Dispersion regimes	44
I.4.2. On the balance between nonlinearity and dispersion – The soliton order	45
I.5. Examples of nonlinear phenomena in a self-focusing NLSE regime	47
I.5.1. Optical solitons.....	47
I.5.1.1. Fundamental solitons	47
I.5.1.2. Higher-order solitons	48
I.5.1.3. Soliton fission and self-frequency shift:	49
I.5.2. Modulation instability (MI)	51
I.5.2.1. Induced MI regime.....	53
I.5.2.2. Spontaneous MI regime	54
I.5.2.3. Other frameworks for the description of MI	55
I.6. Supercontinuum (SC) generation	58
I.6.1.1. Concept of spectral coherence.....	59
I.6.1.2. SC generation in the normal dispersion regime	60
I.6.1.3. SC generation in the anomalous dispersion regime.....	61
Chapter II. Ultrafast pulse control and characterization	63
II.1. Time-frequency duality in the Fourier transform.....	63
II.2. On the control of optical wavepacket properties.....	66
II.2.1. Spectral control of optical pulse properties	67
II.2.2. Temporal control of optical pulse properties	71
II.3. Machine learning control.....	74
II.3.1. Introduction to machine learning	74
II.3.2. Evolutionary algorithms.....	78
II.4. Characterization techniques	81
II.4.1. Complete pulse properties characterization.....	81
II.4.2. Real-time temporal characterization techniques	87
Chapter III. Ultrasensitive DFT-based characterization technique	92

III.1. The dispersive Fourier transform technique: Overview & applications	92
III.2. Frequency-to-time mapping in quantum science	96
III.3. Ultra-sensitive DFT: Case study of MI in nonlinear fiber optics	99
III.3.1. Comparison of DFT characterization techniques and statistical analysis	103
III.3.2. Analysis and control of cascaded FWM processes in noise-driven MI	109
Chapter IV. Smart control of modulation instability	117
IV.1. Influential factors in MI spectral broadening	118
IV.2. Numerical study: Modulation instability control via optical seeding	120
IV.2.1. Coherent optical seeding	122
IV.2.2. Quasi-coherent optical seeding	124
IV.3. Experimental demonstration: Optimization of noise-driven MI dynamics	126
IV.3.1. Experimental setup	127
IV.3.2. Experimental results: First MI sideband optimization	128
IV.3.3. Complementary studies: MI optimization extended to the second sideband	133
IV.3.4. Complementary studies: MI control in a high noise level regime	133
IV.3.5. Complementary studies: On the coherence of optical seeds in experiments	134
IV.4. Discussion on the MI optimization results	136
IV.4.1. Comparison of optimization algorithms	136
IV.4.2. Insight into the underlying MI conversion processes	136
Conclusion	142
Appendices	145
Bibliography	160

List of Figures

Figure I.1 Illustration of the different layers of an optical fiber and the total reflection of light (orange) between the core and the cladding.....	25
Figure I.2 A single-mode highly nonlinear fiber with 5.6 μm core diameter observed with a microscope.....	26
Figure I.3 Fabrication process: (a) Preform preparation of a Ge-doped silica fiber using the MCVD technique. (b) Fiber drawing by heating and stretching of the preform in fiber tower, creating a thin optical fiber and coating with a thin layer of resin.	27
Figure I.4. Illustrative examples of specialty optical fibers: (a) PM fiber; (b) Multicore fiber; (c) Solid-core PCF; (d) Hollow-core PCF; (e) Tapered fiber.....	28
Figure I.5 Photonic on-chip processor with integrated waveguide circuit seen on a computer keyboard to illustrate its size, and under microscope with a guided red laser to better see its design.....	30
Figure I.6 Representation of the dispersion of a homemade highly-nonlinear fiber (HNLF), both designed and fabricated at XLIM. The GVD parameter β_2 is represented in red and follows an opposite direction to the dispersion D . The ZDW is marked by an arrow at 1525 nm, where β_2 changes sign.	34
Figure I.7 Illustration of the intrinsic losses in the fiber: Rayleigh scattering (red arrows) where the light is scattered due to impurities in the fiber, and the absorption losses (in yellow), where a part of the light is absorbed by the fiber's material.	35
Figure I.8 Representation of the evolution of a hyperbolic secant optical pulse with a temporal width of 100 ps experiencing SPM at different nonlinear phase shifts, considering only Kerr effect in an SMF with $\beta_2 = 21.8 \text{ ps}^2 \cdot \text{km}^{-1}$ and $\gamma = 3 \text{ W}^{-1} \cdot \text{km}^{-1}$. In red, we show the normalized input pulse with $\Delta\phi_{SPM} = 0$, and in black we can see the output spectrum when increasing the nonlinear phase shift to $\Delta\phi_{SPM} = \pi, 1.5\pi$, and 2.5π	39
Figure I.9 Principle of the Raman effect and the energy transfer from E_0 to create the Stokes components (in green) with an lower energy $E_0 - \Delta E$ and anti-Stokes components (in red) with a higher energy $E_0 + \Delta E$, on both sides of the pump.....	40
Figure I.10 Normalized Raman gain as a function of the frequency. Generated with data from [53].	40
Figure I.11 Temporal evolution of the intensity profiles (top) and temporal phases (bottom) of a hyperbolic secant pulse with $T_0 = 1 \text{ ps}$ and $P_0 = 0.1 \text{ W}$, traveling within a 150 m - SMF with $\gamma = 3 \text{ W}^{-1} \cdot \text{km}^{-1}$ and $ \beta_2 = 21.8 \text{ ps}^2 \cdot \text{km}^{-1}$, considering only GVD dispersive effects, either in a normal dispersion regime (left) or in an anomalous dispersion regime (right).....	45
Figure I.12 Temporal (bottom left) and spectral (bottom right) evolution of a fundamental soliton with a peak power $P_0 = 22.58 \text{ W}$, $T_0 = 1 \text{ ps}$, propagating along a SMF with $L = 1 \text{ km}$. The normalized temporal and spectral intensity profiles are shown in the top panel indicating the superposition between the input (red) and output (dashed black).	48
Figure I.13 Temporal and spectral evolution (top) of a second-order soliton and (bottom) of a third-order soliton with a temporal width $T_0 = 1 \text{ ps}$ and a peak power of $P_0 = 90.32 \text{ W}$ and $P_0 = 203.22 \text{ W}$, respectively.	49

Figure I.14 Soliton fission in the temporal and spectral domains for the same soliton illustrated in Figure I.13 ($N = 3$), using the GNLSE, and a fiber length $L = 200 m$.	50
Figure I.15 Soliton self-frequency shift process of the fundamental soliton represented in Figure I.12, using the GNLSE and a fiber length of $L = 1 km$.	50
Figure I.16 Modulation instability gain in the frequency domain, calculated for the HNLF fiber used in our studies with $\beta_2 = -1.78 ps^2.km - 1$; $\gamma = 8.4 W - 1.km - 1$ with $P_0 = 30 W$. The frequency cutoff ω_c (in blue) and the maximum gain frequency ω_{max} (in red) are also presented.	53
Figure I.17 Induced modulation instability process occurring due to the addition of a weak modulation on a CW pump as described in (Eq. I.58). The temporal intensities are illustrated after propagation in the HNLF in the top panels at different distances ($z = 0, z = 10 m, z = 15 m$) normalized with respect to the CW input power $P_0 = 20 W$, and the spectral intensities are shown in the bottom panels. The 2 THz modulation here has a magnitude equal to 1% of the CW signal.	54
Figure I.18 Spontaneous modulation instability process occurring due to the MI amplification of a white noise of 3 photons per spectral mode $n_{noise} = 3$ [62] during the propagation of a CW pump in the HNLF fiber. The temporal intensities are illustrated after propagation in the HNLF in the top panels at different distances ($z = 0, z = 20 m, z = 25 m$) normalized with respect to the CW input power $P_0 = 30 W$, and the spectral intensities are shown in the bottom panels.	55
Figure I.19 Numerical simulation of the SBF: (a) Akhmediev breather; (b) Peregrine soliton; (c) Kuznetsov-Ma soliton. Reproduced from [78].	57
Figure I.20 Formation of randomly localized pulses during spontaneous MI (noise-driven) evolution of a CW signal of a 5 W peak power, within an 8 km-SMF in the temporal domain. The x-axis represents the time, and the y-axis represents the distance.	58
Figure I.21 Photography of a visible supercontinuum generated via nonlinear fiber propagation. We observe a progressive shift of pulse color towards the white as new frequencies are generated during propagation, which is dispersed at the fiber output to form a rainbow spectrum. Credits: B. Wetzal.	59
Figure I.22 Example of coherent supercontinuum generated in the anomalous dispersion from a 100 fs input pulse with $P_0 = 3 kW$ propagating in our HNLF with $\beta_2 = -1.78 ps^2.km - 1$, $\beta_3 = 0.07 ps^3.km - 1$, $\gamma = 0.008 W - 1.km - 1$, and represented for a length $L = 2 m$.	61
Figure II.1 Representation in the temporal domain (top panel) and the spectral domain (bottom panel) of a (a) continuous wave; (b) continuous wave with a 2 THz modulation added to the initial pulse with a magnitude equal to 1% of the CW signal; (c) a 250 fs Gaussian pulse.	65
Figure II.2 Comparison between an input Gaussian pulse (in red) with the corresponding output spectra after traveling in the HNLF with different input peak powers decreasing from $P_0 = 2.5 W$ to $P_0 = 2 W$ and $P_0 = 1.5 W$.	68
Figure II.3 (a) Finisar Waveshaper 4000A model with four output ports. (b) Schematic illustrating the principle of operation of a Waveshaper: An input signal is reflected by a cylindrical mirror to a conventional grating, where its spectral components are dispersed. These components then pass through an LCoS optical processor, allowing for precise manipulation of the spectrum. Afterward, they are sent back to the conventional grating to get	

recombined and exit through the output port, resulting in a modified output signal with controlled spectral characteristics. – Reproduced from [118]	69
Figure II.4 (a) Input signal generated from a femtosecond laser (C-fiber) with an average power $P_{avg} = 60 \text{ mW}$. (b) Spectral filtering obtained using the Waveshaper to apply a Gaussian filter, centered at 1560 nm with a spectral bandwidth $\sim 0.1 \text{ nm}$	70
Figure II.5 Schematic diagram of the IPPP chip constituted of various Mach-Zehnder interferometers with two electrodes on each to control, by tuning the phase difference $\Delta\phi$, the splitting of optical pulses into different paths and the output train of pulses. Adapted from [43].	72
Figure II.6 Temporal (top) and spectral (bottom) output profiles of a 100 fs laser pulse (with $P_0 = \text{kW}$) after propagating within the IPPP with different splitting ratios. Reproduced from [44].	73
Figure II.7 Diagrams of machine learning types. Supervised learning: classifying labeled data; Unsupervised learning: Discovering patterns in unlabeled data; Reinforcement learning: Learning actions to maximize rewards.	75
Figure II.8 Representation of a feed-forward neural network architecture, with $x_i + n$ the input data $w_j, i + n$ are the weights associated with the connections between neurons in different layers, $y_j = \sum_i = 1N(x_iw_i + b_i)$ is the weighted sum of inputs with the bias term b_j and $act()$ is the activation function, with $i, j \in \mathbb{N}, n \in \mathbb{Z} +$	76
Figure II.9 Schematic representation of a genetic algorithm reproductive cycle.	78
Figure II.10 Schematic representation of PSO evolution within the parameter space.	80
Figure II.11 Setup of an ultrashort pulse measurement via intensity autocorrelation/FROG: The initial pulse $E(t)$ is split and recombined in a SHG crystal with a delayed pulse replica $Et - \tau$. The SHG signal can be measured either by a photodiode (to find the autocorrelation trace), or by a spectrometer (for a complete characterization of the pulse and the measurement of the FROG spectrogram).	82
Figure II.12 Experimental FROG trace of a laser pulse centered at 1550 nm with an average input power $P_{avg} = 40 \text{ mW}$. The experimental trace is represented along the reconstructed FROG trace and the corresponding retrieved intensity and phase (in both time and frequency domains).	84
Figure II.13 ‘Home-made’ FROG, set in our laboratory, constituted from a collimator to focus a 1550 nm laser pulse into a beam splitter, where it is divided into two optical paths: The first beam (in green) passes through a reflectometer and arrives into a D-mirror where it reflects towards an elliptical mirror. The second beam (in orange) is reflected by 4 different mirrors before arriving at the elliptical mirror. Both beams are focused into the BBO and their SHG signal is measured with a spectrometer.	86
Figure II.14 Principle of (a) the time-lens technique and (b) the DFT technique.	88
Figure II.15 (Top) Principle of DFT: A broadband optical signal is temporally stretched after linear propagation in a highly dispersive fiber. The various spectral components of the optical signal are directly mapped in the temporal domain. (Bottom) Real-time spectra acquired from PD measurements by readily analyzing shot-to-shot fluctuations from successive traces. ...	89

Figure II.16 Stochastic simulations of a 30 ps Gaussian pulse with $P_0 = 2.5$ W propagating in 485 m of HNLF ($\beta_2 = -1.78$ ps².km⁻¹, $\beta_3 = 0.07$ ps³.km⁻¹, $\gamma = 8.4$ W⁻¹.km⁻¹). The figure shows the four fluctuating MI output spectra simulated with the same parameters apart from a different initial noise seed. These spectra can be measured using real-time detection with the DFT technique. The average spectrum of 1000 realizations is shown in red, as a smooth artificial spectrum, preventing us from accessing to the incoherent shot-to-shot fluctuations of the noise-driven nonlinear dynamics.....90

Figure III.1 (a) Average OSA spectrum and Pearson's correlation map extracted from a DFT measurement using a DCF with a dispersion $DDFT = 478$ ps/nm, of 500 fluctuating spectra in a spontaneous MI regime. (b) Corresponding numerical results using GNLSSE simulations with 2000 random Monte Carlo realizations with different noise seeds. (c) Same numerical results as (b) but adding an incoherent weak seed (-35 dB) to the pump before nonlinear propagation (seed with a frequency detuning of 800 GHz and a relative spectral phase $\phi = 0$).....93

Figure III.2 Example of DFT schemes and mitigation techniques for achieving enhanced spectral resolutions (a) Schematic of the DFT of a pulse train broadened after propagation in an HNLF. (b) Enhancement of the equivalent spectral resolution of DFT measurements by tuning the amount of dispersion. This can lead to a temporal overlap between successive time-stretched waveforms. (c) Pulse picking can be employed on the initial pulse train, to mitigate pulse temporal overlap and enable extremely high resolution. This comes at the expense of reducing temporal intensity of the DFT stretched waveform.95

Figure III.3 (a) Experimental setup for SPDC spectral properties characterization in the temporal domain using the DFT technique and multiple single-photon detection (D1-D4): A 10 μ W laser pulse centered at 778.8 nm with 50 MHz repetition rate, enters a PPLN waveguide. After down-conversion, the SPDC spectrum is time-stretched and converted in the temporal domain using the DFT technique via a DCF with a dispersion of $DDFT = 960$ ps/nm. Using a Waveshaper, the SPDC spectrum was then filtered within an 800 GHz bandwidth window (400 GHz for the signal, and 400 GHz for the idler regarding the degeneracy wavelength 1557.6 nm). Each 400 GHz- spectrum is then divided by a 50:50 splitter and respectively sent into two single photon detectors (D1-D2, and D3-D4).98

Figure III.4 Principle of DFT detection via two single photon detectors (SPD-DFT): The intra-pulse and inter-pulse dynamics are differentiated by blue and red arrows, respectively. The corresponding joint and independent probabilities between the detected photo-events in the spectral domain (λ_1 and λ_2), represented with 2D maps allow for the reconstruction of mutual information correlation maps. 100

Figure III.5 Experimental setup showing the comparison between standard DFT with fast photodiode (PD) and our novel approach using ultra-sensitive single photon detectors (SPDs) for the spectral characterization of incoherent MI dynamics. 101

Figure III.6 Pulse spectrum broadening through noise-driven MI in both (a) spectral and (b) temporal domains. Top panels: Results of Monte-Carlo simulations with 2000 different noise seeds (i.e. vacuum noise with one photon with random phase per spectral bin) showing spectral and temporal fluctuations for 10 realizations (grey traces), and one randomly selected realization (black trace), compared to averaged spectra (red) representative of an OSA measurement. Bottom panels: Corresponding spectral and temporal pulse evolutions of a randomly selected realization (i.e. black traces on the top panel)..... 102

Figure III.7 Output MI spectrum detected by various detection methods: (a) OSA spectrum with the first MI sidebands highlighted in grey, (b) 500 fluctuating spectra (light dotted lines) obtained from PD-DFT detection and the resulting average spectrum (thick solid blue line), achieved by filtering the first MI sidebands (grey-shaded), (c) Comparison between the average SPD-DFT (dashed red), the average PD-DFT (solid blue) and an OSA (dotted grey) measurement of the 1st sidebands MI output spectrum. The figure underscores a good agreement between these methods within a limited dynamic range above the detection noise floor. 103

Figure III.8 Correlation analysis of the first MI sidebands. (a) Pearson’s correlation map of the MI sidebands obtained from PD-DFT analysis. (b) Mutual information map of the MI sidebands obtained from SPD-DFT analysis (when considering intra-pulse events). (c) Mutual information map of the MI sidebands from SPD-DFT analysis (when considering inter-pulse events). . 104

Figure III.9 Second-order correlation map g_2 derived from both (a) PD-DFT and (b) SPD-DFT measurements, along with (c) the relative error comparison. 105

Figure III.10 Evolution of mutual information spectral maps within the MI sidebands with different input pump power adjusted by attenuating the input pump signal using the Waveshaper from -4 to -1.5 dB. The transition from a single sideband to more intricate correlation patterns reflects the emergence of nonlinear processes and cascaded FWM. ... 106

Figure III.11 Comparison of Pearson's correlation for MI spectrum measurements with different PD-DFT detection schemes: Top panels: Average spectra of 500 traces collected via PD-DFT detection using two different DCFs with a dispersive factor of respectively 403 ps/nm (solid red) and 565 ps/nm (dashed black). In (a) and (b), we represent the average spectra as well as Pearson’s correlation maps of the DFT measurements with both DCFs, obtained from the MI spectrum with pump filtering, using a 5 GHz PD and a 45 GHz PD, respectively. In (c) and (d), we represent the average spectra and the zoomed-in correlation maps of the DFT measurements with both DCFs, obtained for filtering the 1st MI sidebands only, using a 5 GHz PD and a 45 GHz PD, respectively. 108

Figure III.12 (a) First and second MI sidebands located at the long wavelength edge of the spectrum, (b) symmetrical second MI sidebands, (c) and symmetrical third MI sidebands, are represented by their spectral mutual information correlation maps, derived from experimental SPD-DFT measurements (selectively filtered and transmitted to each SPD). The corresponding OSA spectra for each sidebands’ combination are captured for two different input power levels before HNLf propagation and represented in the top panel: 0 dB attenuation are solid red lines, -2 dB attenuation are dashed black lines, while the sideband locations are highlighted in grey. 110

Figure III.13 Comparison of the averaged OSA spectra (top panels) and correlation maps (bottom panels) of the complete MI spectrum over a spectral range between 1532 nm and 1568 nm, using distinct approaches: (a) PD-DFT measurements after pump filtering based on 500 experimental measurements. (b) SPD-DFT measurements via spectral signal equalization. (c) GNLS simulations with 2000 numerical realizations. The green shadings in the average spectra highlight the signal's dynamic range after processing, respectively indicating 16 dB, 6 dB, and 38 dB, for each case. 111

Figure III.14 (a) Output MI spectra with controlled seeding: MI spectra resulting from spontaneous MI (in black dashes) and the introduction of two coherent input seeds at frequency detuning of 400 GHz and 800 GHz (green arrows). These input seeds have distinct

spectral phase differences: $\Delta\phi = 0$ (blue) and $\Delta\phi = \pi$ (red). (b) Spectral mutual information maps with seeded MI: Correlation maps obtained from SPD-DFT measurements with two weak coherent seeds added to the pump for three different selected spectral regions. Inverting the phases of the seeds can modify the sign (and shape) of the mutual information map highlighted in the white-circled areas within the maps..... 113

Figure III.15 Mutual information correlation maps of the first symmetrical MI sidebands acquired through SPD detection for different measurement integration times: 3, 15, and 30 minutes..... 115

Figure IV.1 Numerical simulations showing the average spectra (top panels) and Pearson's correlation maps (bottom panels) of a 30 ps laser pulse centered a 1550.65 nm propagating into 385 m of HLNF, whose parameters are $\beta_2 = -2.15 \text{ ps}^2 \cdot \text{km}^{-1}$; $\beta_3 = 0.07 \text{ ps}^3 \cdot \text{km}^{-1}$; and $\gamma = 3.5 \text{ W}^{-1} \cdot \text{km}^{-1}$. The figure illustrates the evolution of the MI process with various input peak powers with (a) 10 mW, (b) 13 mW, and (c) 14 mW..... 118

Figure IV.2 Visual representation in both the temporal (top panels) and spectral (bottom panels) domains of (a) a Gaussian 30 ps laser pump centered at 1550.6 nm, (b) the pump signal with an added weak modulation at 1555 nm (in red) with 10 dB attenuation ($a_1 = 10\%$) and a phase $\phi_1 = 0$, (c) the signal with an additional modulation (in blue) centered at 1560 nm, with $a_2 = 10\%$ and $\phi_2 = 0$, (d) Total signal achieved by adjusting the phase $\phi_2 = \pi$ 119

Figure IV.3 Illustration of the experimental setups and numerical scenarios studied in this chapter within the framework of MI control. (a) Noise-driven MI regime (spontaneous MI) achieved by amplifying a filtered 30 ps pump with an EDFA and applying a bandpass filter (BPF) to limit the impact of ASE noise before propagation in a HNLf. (b) MI regime with coherent optical seeding, using a single output of a Waveshaper to filter additional weak signals combined with the pump. (c) Quasi-coherent optical seeded MI regime, using two distinct Waveshaper outputs: one for the pump which will be amplified, and the other for the generation of the seeds. The three signals are in this case combined before nonlinear propagation but experience partial propagation along different optical paths. 121

Figure IV.4 Average spectra (top panels) and Pearson's correlation maps (bottom panels) obtained after HNLf propagation and resulting from a coherent seed added to the pump with 22 dB attenuation and adjustable parameters by (a) detuning the seed by $\Delta\nu_1 = 200 \text{ GHz}$, (b) varying its phase from 0 to $\phi_2 = \pi$, (c) increasing the frequency detuning to $\Delta\nu_1 = 400 \text{ GHz}$ with $\phi_1 = 0$ 122

Figure IV.5 Influence of dual seed parameters on the MI output spectrum (top panels) and the correlation maps (bottom panels) obtained from 200 simulations with random initial noise seeds. The figure explores the effects of varying the frequency and phase of coherent seeds ν_1, ϕ_1 and ν_2, ϕ_2 , with a 22 dB attenuation, on the resulting MI dynamics: (a) for a frequency detuning $\Delta\nu_2 = 2\Delta\nu_1$ with $\phi_1 = \pi/2$ and $\phi_2 = 0$; (b) by varying the phase to $\phi_2 = \pi/2$; (c) by shifting the frequency of the second seed by $\Delta\nu_2 = 3\Delta\nu_1$, with $\phi_1 = \pi/2$ and $\phi_2 = \pi/2$ 123

Figure IV.6 Average spectra (top panel) and correlation maps (bottom panel) obtained from 1500 simulations with random initial seeds, demonstrating the effect of a quasi-coherent single seeds added to the pump when considering $g = 0.3$. The results are primarily driven by noise, with slight variations based on the weak seed parameters: (a) 35 dB attenuation and a

frequency detuning of $\Delta\nu_1= 600$ GHz, (b) 35 dB attenuation and a frequency detuning of $\Delta\nu_1= 800$ GHz, and (c) lower attenuation at 29 dB with a frequency detuning of $\Delta\nu_1= 800$ GHz. 124

Figure IV.7 Average spectra (top panel) and correlation maps (bottom panel) obtained from 500 simulations with random initial seeds, demonstrating the effect of a weak quasi-coherent single seed with 29 dB attenuation added to the pump when considering a frequency detuning $\Delta\nu_1= 800$ GHz. The results are shown for 3 different decoherence parameters (a) for $g = 0.1$, (b) $g = 0.3$ and (c) $g = 0.6$ 125

Figure IV.8 Illustration of the effect of introducing two weak quasi-coherent seeds to copropagate with the pump. Both the average spectrum (top panels) and the correlations (bottom panels) obtained from 500 simulations with random initial noise, are represented for 32 dB attenuated input seeds with frequency detunings $\Delta\nu_2 = 2\Delta\nu_1$, and a decoherence degree $g = 0.3$. The results are shown for three different cases: (a) $\Delta\nu_1= 400$ GHz with $\phi_1 = 0$ and $\phi_2 = \pi/2$, (b) a shift in the frequency by $\Delta\nu_1= 600$ GHz, and (c) a variation of the phase using ($\Delta\nu_1= 600$ GHz, $\phi_1= 0$), and ($\Delta\nu_2= 1200$ GHz, $\phi_2 = \pi$). 126

Figure IV.9 An 80 fs laser pulse centered at 1560 nm is reshaped using a programmable spectral filter (Waveshaper) into a picosecond pump and two seeds with adjustable spectral detuning and phase. The signals are then amplified using an EDFA and filtered between 1559.42 nm and 1564.63 nm to reduce the ASE. After propagation in a HNLFF, we can either visualize the output with an OSA or perform a real-time detection using the DFT technique. A genetic algorithm is used to optimize the correlation between two specific wavelengths in the output spectrum by iteratively adjusting the input seed parameters. 127

Figure IV.10 Representation of the experimental principles for MI optimization and varying parameters: (a) In the frequency domain, we select two targets ν_a and ν_b , positioned at higher frequencies than the pump. With the GA, we iteratively optimize the correlation between these two target wavelengths by adding coherent dual seeds ((ν_1, ϕ_1) and (ν_2, ϕ_2)) on the other side of the pump where the seed will experience MI gain. The seeds are intentionally weak, approximately matching the level of the ASE noise. (b) Spectral representation of the target wavelength on a seeded but fluctuating MI output spectrum. Note that here only the average spectrum is represented for clarity. (c) Representation of the location of both the targets and the seeds in the spectrum. In the case presented here, the seeds have variable central wavelengths that are tunable over only the first MI sideband located across the pump (compared to the target wavelengths). 128

Figure IV.11 GA optimization of the correlation between two frequency targets ν_a and ν_b , when (a-c) $\Delta\nu_b = 2\Delta\nu_a$ and (d-f) $\Delta\nu_b = 1.5\Delta\nu_a$. For both cases, we present the GA evolution of the best and average values obtained in each generation when (a,d) maximizing the correlation and (b,e) minimizing the correlation. (c,f) Comparison of the distribution of the GA results with the ones obtained from Monte-Carlo measurements for iteratively generating random seed parameters. 130

Figure IV.12 GA-optimized spectrum (a) and correlation maps (b,c) with the seed parameters (λ_1, ϕ_1) and (λ_2, ϕ_2) obtained for a maximal correlation between two frequency targets ν_a and ν_b with $\Delta\nu_a= 0.225$ THz and $\Delta\nu_b= 0.45$ THz. The targets wavelengths are shown with white circles on the correlation maps indicating a positive correlation. (d-f) The same results for a minimal correlation between ν_a and ν_b . In the output spectra of (a) and (d), the frequency targets ν_a and ν_b are shown with purple arrows and the optimized seed parameters (and

spectral locations) are shown, for each case, with blue and red dots. In the correlation maps (b) and (e), the seed locations are shown with green circles. 131

Figure IV.13 GA-optimized spectrum (a) and correlation maps (b,c) with the seed parameters (λ_1, ϕ_1) and (λ_2, ϕ_2) obtained for a maximal correlation between two frequency targets ν_a and ν_b with $\Delta\nu_a = 0.3$ THz and $\Delta\nu_b = 0.45$ THz. The targets wavelengths are shown with white circles on the correlation maps indicating a positive correlation. (d-f) The same results for a minimal correlation between ν_a and ν_b . In the output spectra of (a) and (d), the frequency targets ν_a and ν_b are shown with purple arrows and the optimized seed parameters (and spectral locations) are shown, for each case, with blue and red dots. In the correlation maps (b) and (e), the seed locations are shown with green circles. 132

Figure IV.14 (a) GA evolution of the correlation between $\Delta\nu_a = -0.9$ THz and $\Delta\nu_b = 0.9$ THz along 30 generations with 50 individuals each. (b) MI average spectrum and the correlation map obtained after nonlinear propagation with the best seeds' parameters. 133

Figure IV.15 (a) GA evolution of the correlation between $\Delta\nu_a = -0.225$ THz and $\Delta\nu_b = -0.45$ THz obtained from the new setup configuration for noisy MI optimization. (b) MI average spectrum and the correlation map obtained after nonlinear propagation with the best seeds' parameters. 134

Figure IV.16 Comparison of the average spectra (top panel) and correlation maps (bottom panel) of a quasi-coherent single seed added to the pump with 35 dB attenuation and a frequency detuning of $\Delta\nu_1 = 800$ GHz, and $\phi_1 = 0.25\pi$, obtained (a) numerically from 500 GNLSE simulations with random initial seeds and considering $g = 0.3$, and (b) from 500 fluctuating spectra measurements collected experimentally using the DFT technique. 135

Figure IV.17 Comparison of optimization algorithms: GA (in green) and PSO (in yellow), for (a) maximal correlation or (b) a minimal correlation between the frequency targets with a detuning of $\Delta\nu_a = -0.45$ THz and $\Delta\nu_b = 0.45$ THz. 136

Figure IV.18 Evolution of (a) the frequency detuning ratio $\Delta\nu_r$ between ν_1 and ν_2 , and (b) the phase difference between ϕ_1 and ϕ_2 , during GA correlation maximization between $\Delta\nu_a = 0.225$ THz; $\Delta\nu_b = 0.45$ THz. (c) A 3D representation of both the frequency detuning ratio and the phase difference as a function of the GA generation. 137

Figure IV.19 Evolution of (a) the frequency detuning ratio between ν_1 and ν_2 , and (b) the phase difference between ϕ_1 and ϕ_2 , during GA correlation maximization between $\Delta\nu_a = 0.3$ THz; $\Delta\nu_b = 0.45$ THz. (c) A 3D representation of both the frequency detuning ratio and the phase difference as a function of the GA generation. 138

Figure IV.20 Illustration of the FWM processes potentially occurring during MI evolution and resulting from the interaction between the pump and the optimal coherent seeds (ν_1, ν_2) , obtained for a maximal correlation between (a) $\Delta\nu_a = 0.225$ THz; $\Delta\nu_b = 0.45$ THz, and (b) $\Delta\nu_a = 0.3$ THz; $\Delta\nu_b = 0.45$ THz. Parameters: For (a), the optimized seeds have a detuning $\Delta\nu_1 = -0.36$ THz and $\Delta\nu_2 = -0.32$ THz. For (b), the optimized seed detuning's are respectively $\Delta\nu_1 = -0.12$ THz and $\Delta\nu_2 = -0.35$ THz. 139

List of Tables

Table III.1 Specifications of PDs, oscilloscopes, and total spectral resolution for different detection setups.	107
Table IV.1 Quantitative analysis of the experimental results obtained for seeded MI optimization. The table indicates the optimal seeds parameters and correlation coefficients obtained after GA optimization, when either maximizing or minimizing the correlation coefficient $\rho(\lambda_1, \lambda_2)$ between the five different pairs of target wavelengths. Note that the phases are here given in units of π	129

General Introduction

“... and there was light.”

As the evolution of the universe has unfolded throughout the ages, one entity has consistently held a place of paramount significance - *light*. From the very inception of time, light has spread its luminescent thread through the formation of our universe, an enduring symbol of both mystery and illumination. It is a phenomenon that never fades, for even in the darkest corners of space, traces of light persist, as an eternal element of this world. Through ingenuity and curiosity, humans learned to harness and manipulate this force, discovering new enlightenment areas. It is a story of invention, exploration, and scientific revelation. Starting from the ancient civilizations of Egypt and Mesopotamia, where humans first wondered at the principles of reflection and refraction, to the Greeks, particularly Euclid, who laid the earliest foundations of geometrical optics in the 3rd century BCE. Jumping forward to the 11th century, to the Arab scholars with Alhazen, who explored the principles of vision, light, and the formation of images in his work “Book of Optics”, setting the stage for the next scientific revolution in optics. In the 17th century, the genius, Sir Isaac Newton with his groundbreaking experiments with prisms demonstrating the dispersion of white light into colors, revealed the true nature of light's composite character. The 19th century witnessed important discoveries in optics, including Augustin-Jean Fresnel's wave theory of light, which elegantly explained phenomena like diffraction and interference, and James Clerk Maxwell's famous equations, unifying electricity and magnetism and identifying light as an *electromagnetic wave*.

The journey continued, marked by intriguing inventions and demonstrations in the field of optics over the years, until a revolutionary chapter began in 1960 - *the invention of lasers*. It was Dr. Theodore Maiman's pioneering work that led to the birth of the laser [1], a breakthrough technology that set the stage for advancements in the world of optics. Following this discovery, both new experimental explorations and reevaluation of prior studies saw an exponential acceleration in the years that followed [2]. In 1961, Peter Franken and his team showed the first experimental nonlinear effect using a ruby laser demonstrating the phenomenon of second-harmonic generation [3]. In the remaining years of the 1960s, the revelation that under certain conditions, when intense light interacts with a nonlinear medium, new frequencies can be produced, led to various other nonlinear optical phenomena, including four-wave mixing, frequency broadening, and phase modulation, unlocking an immense potential of nonlinear optics in shaping the future of technology and communication. This was mostly recognized in 1966 with Charles Kao and George Hockham's work on optical communication [4] who paved the way toward the development of optical fibers, leading to modern telecommunications networks. As the exploration of nonlinear effects in optical media gained momentum, new horizons opened up. Notably, in 1970, the work of Robert Alfano and Sidney Shapiro [5] leading to *supercontinuum generation*, involved exploiting the nonlinear properties of glass to broaden the spectral range of initially monochromatic light. Six years after, Lin and Stolen [6] were able to demonstrate such phenomena in optical fibers. The supercontinuum generation process, achieved by focusing high-intensity laser pulses into nonlinear media, demonstrated the remarkable ability to create broadband optical sources spanning a vast range of wavelengths, from ultraviolet to infrared. Supercontinuum generation, alongside spectral broadening and frequency conversion processes in guided optics [7], are examples of complex nonlinear optical phenomena that have formed the foundation of demanding fields spanning

advanced light source development, telecommunications, metrology, spectroscopy, and microscopy - to only name a few.

Researchers soon realized that the *control and optimization* of these processes have become essential to tailor nonlinear interactions and achieve the desired output properties, paving the way towards the enhancement and adaptability of photonic sources for various applications. Over the last few years, science went globally through a major change with the rise of artificial intelligence (AI). AI and machine learning quickly spread to many areas of optical science, such as telecommunication, sensing, imaging, and even ultrafast optics [8]. In many ways, this rise of AI completely transformed how scientists approached complex problems and made the most of nonlinear optical effects. Machine learning thus became popular due to its ability to find patterns, predict behaviors, and process big data. In nonlinear optics, it became an important part of experiments and numerical simulations, helping scientists understand and control complex effects and develop advanced technological solutions such as smart photonic sources.

The research work presented in this manuscript directly fits in this research area, and aims to contribute to the study and development of novel approaches for generating and characterizing broadband light with tailored multidimensional properties. To this end, the approach currently explored within my research team aims at leveraging machine learning techniques to optimize ultrashort pulses and their properties during complex nonlinear propagation within single-mode fibers, integrated optical waveguides, or even multimode optical fibers. Overall, the research efforts surrounding my thesis are presented in Figure. 1, illustrating the different scientific and technologic building blocks being currently addressed.

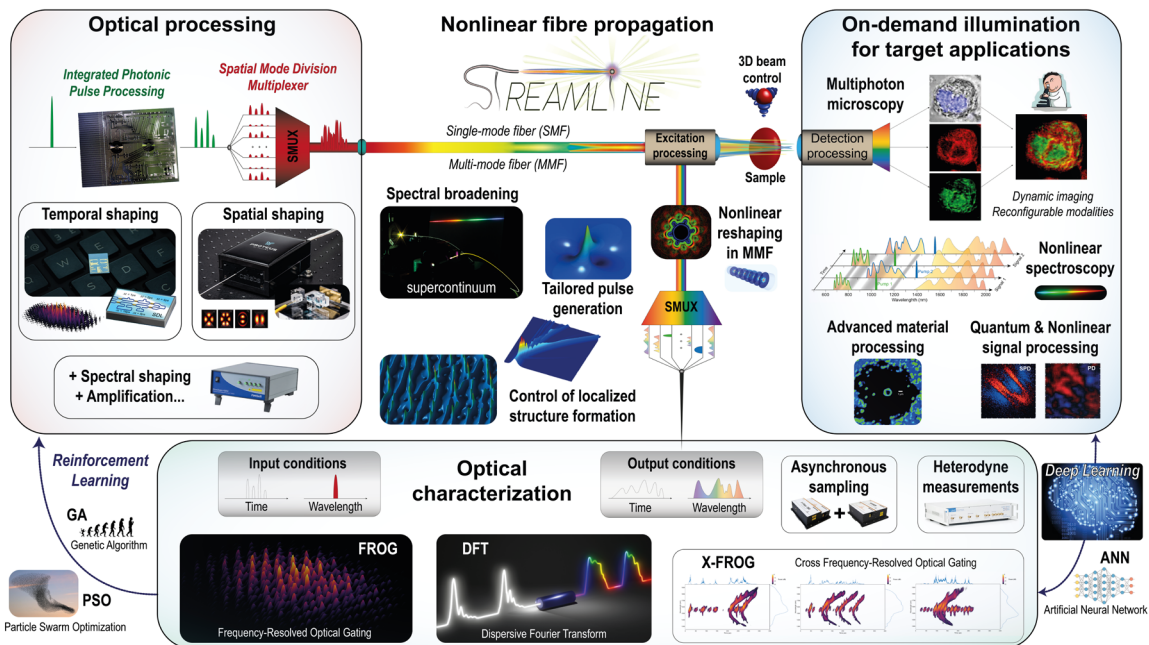


Figure. 1 Overview of the current research directions of the project team for the development of smart photonic sources, along with its different technological and scientific building blocks. The approach taken includes advanced and multidimensional optical processing of ultrashort pulses, the study of nonlinear propagation dynamics, and the development of suitable optical monitoring tools for multidimensional characterization. The targeted applications of these “smart sources” are also summarized on the right panel.

This thesis took place at the XLIM Research Institute at the University of Limoges, within a collaborative regional project SCIR from Nouvelle-Aquitaine (AAP-2020), focusing on the optimization and control of coherence dynamics and instabilities in the infrared region. However, my work is also encompassed in a broader ERC Starting Grant project called STREAMLINE and funded by the European Research Council. STREAMLINE (*Smart PhoTonic sources harnessing Advanced Multidimensional Light Optimization towards machine-learning-Enhanced imaging*), is a multidisciplinary research project aiming at advancing the control of optical wavepackets and their nonlinear evolution dynamics through machine learning techniques. It seeks to develop smart optical sources with reduced complexity, advanced functionalities, and on-demand reconfigurability. These smart sources aim at being implemented into various applications such as metrology and microscopy, but more specifically towards novel multimodal imaging architecture, with the target of driving a paradigm shift in computational imaging.

Globally, our research focuses on the multidimensional control over the spectral, temporal, and spatial properties of ultrafast pulses, providing an extremely large parameter space and numerous degrees of freedom to explore rich nonlinear propagation dynamics. While the spatial dimension (and multimode propagation dynamics) remains outside the scope of this thesis, my research was oriented towards complementary tasks related to the spectral and temporal control of optical waveforms, the study of their propagation dynamics and, finally, their characterization.

In the spectral domain, optical processing is studied and performed using a programmable Fourier filter known as a Waveshaper. In the temporal domain, pulse processing is achieved with an integrated waveguide system constituting an integrated photonic pulse processor (IPPP). The latter works by splitting an ultrashort pulse into multiple replicas with adjustable power, temporal separation, and optical patterns that can be optimized to e.g. favor specific spectral enhancements during nonlinear propagation. Leveraging machine learning techniques (such as genetic algorithms (GA) and particle swarm optimization (PSO)), allows optimizing these parameters and achieve a desired pulse shaping for particular applications.

Understanding the propagation of light in waveguides, especially the various nonlinear processes that can occur during nonlinear fiber propagation, is essential to successfully control these propagation dynamics and implementing the necessary characterization tools is of paramount importance in this case. To assess such a large and finely-tunable parameter space, one indeed needs to rely on advanced optical monitoring methods such as Frequency-Resolved Optical Gating (FROG) or high-resolution real-time characterization techniques. With such approaches, we can measure and identify the properties of the different signals studied in our system as well as the stability of broadened output spectra obtained after nonlinear propagation in optical fibers.

Importantly, the beginning of my thesis coincided with the initial stages of the laboratory setup. I therefore strongly contributed to the lab's establishment by initiating the assembly of experimental setups. Among others, this included creating a homemade FROG aiming to measure, over a large span ($> \text{ns}$), the multiplexed train of pulses ($< \text{ps}$) generated within the IPPP chip, to finely tune their temporal properties. Similarly, as the central objective of this work revolves around intelligent control, I devoted a large portion of this thesis to the creation

of computer-based interfaces, designed to facilitate the operation of all the instruments acquired and used in our experimental setups.

Furthermore, as scientific environment and circumstances evolved—such as the launch of a new project, the onset of the COVID-19 pandemic, and the arrival of new Ph.D. students—my research direction shifted toward the development of innovative techniques focused on shaping, optimizing and characterizing relevant spectral properties in incoherent nonlinear fiber optics. In this context I set up a real-time *Dispersive Fourier-transform* (DFT) characterization technique within the lab, allowing for the detection of shot-to-shot fluctuating dynamics in broadband output spectra after highly nonlinear fiber propagation.

Overall, my thesis thus mainly focuses on the smart control of incoherent nonlinear effects in single-mode optical fibers, achieved by optimizing the spectral properties of ultrafast pulses. In this framework, this manuscript is organized in four main chapters summarizing the core of my thesis work, while complementary experimental and numerical work is also provided in the Appendices section for completeness.

In **Chapter I**, I provide an overview of the main phenomena observed in guided nonlinear optics, with a specific focus on noise-driven and incoherent nonlinear dynamics that will occupy an important part in this thesis.

Chapter II focuses on optical pulse processing and characterization techniques commonly used in the literature and specifically implemented in our experimental work. After an introduction on the time-frequency duality in ultrafast optical processing, I discuss in three parts: (i) the control of ultrafast pulses using both spectral and temporal shaping strategies; (ii) the optical techniques employed for characterizing these signals, and (iii) the different approaches used for the optimization of these properties and nonlinear dynamics via machine learning strategies. In this chapter, we also introduce and devote a particular attention to real-time characterization techniques, especially the dispersive Fourier-transform method, that will be further discussed and studied in the next chapter.

The wide-ranging applications of this DFT technique across various domains are detailed in **Chapter III**. Here, we introduce and study in details a novel DFT approach. This work, done in collaboration with the Institute of Photonics at Leibniz University of Hannover in Germany, combines quantum-based technology measurements and the study of incoherent nonlinear dynamics. We report in this case the enhancement of the detection quality using such real-time characterization techniques. To achieve this, I conducted a two-week experimental campaign in Hanover, resulting in the development and validation of a new DFT-based approach, with higher performances in terms of sensitivity and resolution. These results demonstrate the applicability of our DFT scheme for the characterization of optical quantum states, the measurement of noise-driven fiber propagation dynamics, and further opens up exciting possibilities for improved imaging and detection capabilities. This, among others, allows to bridge our studies with imaging applications that stand to benefit from the project's advancements, but also provide an important framework for optimizing nonlinear instabilities as discussed in the next chapter.

In **Chapter IV**, we focus on the concept of “smart control” of nonlinear effects studied in this thesis. First, we perform a numerical study of the behavior of a nonlinear phenomenon known as modulation instability (MI), by exploring its dynamical response to different optical seeding scenarios and various initial conditions in the presence of noise. We also report experimental

demonstrations of our ability to optimize this noise-drive MI process via evolutionary algorithm and DFT measurements, thus allowing us to find the optimal parameters of optical seeds to imprint on the initial pulse depending on the targetted properties.

The innovations carried out and the results obtained through this thesis paves the way towards complementary development of smart photonics sources. We discuss this point in the **Conclusion** of this manuscript and develop briefly the perspectives of this work and their related applications.

Finally, in the **Appendices** section, we report on the complementary work carried out during this thesis. In particular, Appendix 1. discusses numerical studies related to the optimization of supercontinuum for multiphoton microscopy. This optimization is obtained numerically by leveraging suitable optical pulse pattern formation with an integrated photonic pulse processor system available in the lab. Similarly, Appendix 2. illustrates the work made for the in-house development of a special FROG system allowing for the experimental characterization of such pulse patterns with a good resolution and a large temporal span.

Chapter I. Nonlinear phenomena in optical fibers

In this chapter, I provide an overview of the key nonlinear phenomena occurring in optical waveguides, specifically optical fibers. Optical fibers are an important tool in light and information transmission. Understanding their various properties and their associated linear and nonlinear effects is essential for enabling efficient light manipulation for targeted applications. We start with an overview of fibers and guided optics in **Section I.1**. First, we underline the principles of fiber optics and the guiding properties that allow effective light propagation. Additionally, we succinctly introduce the fabrication techniques employed in creating these waveguides, and briefly touch upon the most common types of waveguides used in guided optics. In **Section I.2**, we focus on the principles of pulse propagation in optical fibers by elaborating on both linear and nonlinear underlying mechanisms and by describing the wave propagation equation in fiber optics. We also explore the different key linear phenomena that can occur during propagation such as dispersion, and, which influences the form of the pulse and its power attenuation along the fiber (**Section I.2.1**). In the realm of nonlinear propagation (**Section I.2.2**), we investigate the Kerr effect, by describing the process of phase modulation and its impact on the pulse propagation, as well as the Raman effect occurring from the light interacting with the fiber material. **Section I.3** examines the methods employed to solve the intricate equations governing these nonlinear phenomena. We discuss the Nonlinear Schrödinger Equation and its generalized form used for modeling and understanding pulse propagation in optical fibers, but also the split-step technique used to numerically easily solve these equations. Expanding upon this foundation, **Section I.4** explores different propagation regimes that can typically occur during propagation depending on the underlying nonlinear effects, and the parameters of both the pulse and the guiding material. We discuss the interplay between the dispersion and nonlinear effects and their link to the formation of optical solitons. Additionally, we examine the dispersion regimes, which play a pivotal role in shaping the dynamics of pulse propagation. To provide practical insights, **Section I.5** presents examples of various propagation regimes. We begin by providing an overview of the different types of optical solitons encountered in fiber optics including fundamental solitons and higher-order solitons and breathers. Moreover, we briefly introduce the modulation instability (MI) process which will be the main studied nonlinear phenomenon in this thesis. We further explore the principles of four-wave mixing and associated propagation dynamics encountered when adding a weak modulation to the system, or from noise amplification. Lastly, in **Section I.6** we discuss the generation of supercontinuum, by examining their different formation mechanisms and associated properties depending on the input pulse characteristics and the different dispersion regimes. This chapter aims at enhancing our understanding of the various dynamics occurring in optical fibers, paving the way for the core focus of the thesis: the characterization, control and optimization of selected effects and phenomena arising during nonlinear propagation.

I.1. Fiber and guided optics overview

An optical fiber typically consists of a cylindrical dielectric waveguide that has the property of guiding light over long distances. Commonly, it consists of a thin filament waveguide that confines an electromagnetic wave between two different layers — the core and the cladding — with different refractive indices n_{core} and $n_{cladding}$. While early work on guided optics [9] was investigated by Colladon and Babinet, and Tyndall in 1870 showing how light can travel in a stream of water opening the possibility of light transmission in glass rods, the first

significant advancement in the development of optical fibers in 1966 can be attributed to George Hockham and Charles Kao, who was awarded the Nobel Prize in Physics in 2009 for his work on achieving long-distance optical communication using these low-loss optical fibers [4]. It involved purifying Silica glass fibers to significantly reduce light scattering, enabling them to guide the light over long distances with minimal output loss. This breakthrough laid the foundation for the development of practical optical fibers and their adoption as a high-speed and efficient telecommunication channel. Fiber optics quickly gained attention from various fields, specifically, the low-loss transmission of light signals through fiber optics led to a revolution in the telecommunications industry. Their capability to enable high-speed data transmission and facilitate the growth of the internet networks, allowed for the transmission of vast amounts of information across continents, contributing to the development of global communication systems [10].

Apart from telecommunication, fiber optics found diverse applications in numerous fields of optics and beyond. For example, fiber optics are extensively used in sensing applications [11], [12] to measure physical quantities such as temperature, strain [13], pressure, and chemical composition. Optical fiber sensors offer high sensitivity, immunity to electromagnetic interference, and the ability to remotely monitor conditions in challenging environments. With this development, fiber optics led to a revolution in medical imaging techniques. Flexible fiber optic bundles are nowadays used in endoscopy [14], to visualize and diagnose internal organs, as well as in the development of new high-precision and high-resolution internal imaging techniques [11]. Most importantly, fiber optics brought tremendous advances in laser technology with the creation of fiber lasers [15]. Before the development of fiber optics, lasers primarily used bulk materials as the gain medium for light transmission. For example, T. Maiman is known for developing the first laser using a ruby crystal. Subsequently, other crystal lasers emerged, such as the Nd:YAG and Ti:Sa lasers. In addition, lasers like the He-Ne and CO₂ lasers, based on gases, can be used in various applications. However, these lasers often offer limitations in terms of size, robustness, flexibility, and efficiency. With the introduction of optical fibers, the gain medium and the laser cavity can be integrated into flexible and compact fiber cables, enabling efficient, stable and versatile laser operation [2]. Fiber lasers use the unique properties of optical fibers to confine and guide laser light within the fiber core. This confinement allows for efficient light amplification and generation of high-power laser beams with excellent spatial beam properties. In addition, different dopants or specialty-tailored fibers have been developed to provide a versatile platform for various laser configurations and designs, including emission wavelength, repetition rate, pulse duration..., enabling precise control and targeting of laser energy. Fiber lasers have been extensively used in both scientific research and industrial applications. Moreover, with the ability to generate ultrashort and high-power laser pulses within fibers, the fundamental study of nonlinear phenomena in fiber optics has become a research field in its own right. Starting from the mitigation of transmission impairments in telecommunication (i.e. using higher power laser to limit the number of amplifiers along the transmission line), nonlinear fiber optics have been an active research field for almost half a century, driving fundamental knowledge and associated technological advances in many related fields spanning instrumentation, sensing, and metrology (e.g. frequency- comb-based measurements – Nobel Prize in Physics 2005 [16]).

I.1.1. Principle and guiding properties

As mentioned before, an optical fiber must be composed of at least two layers with different refractive indices in order to guide light effectively. Generally, it is comprised of three main layers: the core, the cladding, and the coating:

The core of the fiber is most commonly made of pure silica, providing an excellent transparency from ~800 to 2000 nm [10], and thus making them the weapon of choice in most telecommunication applications (e.g. in the C-band around 1.5 μm).

However, it is worth noting that there are various types of fibers with cores made from different materials. Doped silica (such as germanium dioxide (GeO_2)) can increase the refractive index of the core and is often used in telecommunication fibers. Polymers can also be used depending on the intended application and desired optical properties, such as polymethyl-methacrylate (PMMA) plastic optical fibers, and polycarbonate fibers [17].

So-called “active fibers” acquire distinctive optical properties by the addition of selective dopants (e.g. Erbium, Ytterbium) within the fiber core (and eventually the fiber cladding). These dopants provide optical gain, resulting in the amplification of the optical signal within particular spectral regions. Such active fibers have been instrumental to fiber laser development and form the backbone of widespread telecom components such as Erbium-doped fiber amplifier (EDFA) [18]. Other types of glasses with extended transparency above 2 μm (e.g. chalcogenide, or heavy metal fluoride glasses (ZBLAN fibers), etc.) have also been used for the operation of optical fibers in the mid IR window [19], [20].

Regarding the geometrical arrangement of optical fiber, the core’s diameter generally varies between 10 μm and 85 μm , depending on the type of the fiber [21] and guiding properties required for a targeted application.

The optical cladding, surrounding the core, is also typically made of glass material, and is designed to have a lower refractive index. Lastly, the plastic coating serves to protect the optical fiber and facilitate its handling, it acts as an insulator against external factors such as rain, storms, and humidity.

Guidance in an optical fiber can be explained when the differences in the refractive indices between the core and the cladding enable the common phenomenon known as total internal reflection [9]. This means that light incident in the core with the correct angle is endlessly reflecting at the fiber’s core-cladding interface (see Figure I.1).

In order for total internal reflection to occur, two crucial conditions must be met. Firstly, the refractive index of the core must exceed that of the cladding ($n_{core} > n_{cladding}$). Secondly, total internal reflection is achieved when the incident angle (Φ) formed between the incident beam and the normal to the core-cladding interface is greater than a critical angle (Φ_c) defined by the Snell-Descartes law ($\sin(\Phi_c) = \frac{n_{cladding}}{n_{core}}$).

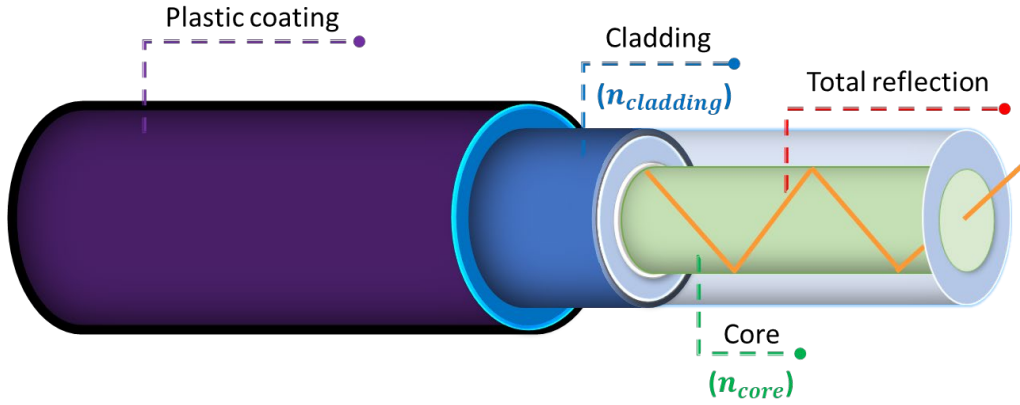


Figure I.1 Illustration of the different layers of an optical fiber and the total reflection of light (orange) between the core and the cladding.

An electromagnetic wave traveling within an optical fiber can be defined by its propagation vector \vec{k}_0 . The magnitude of the propagation vector, represented as $|\vec{k}_0|$, is inversely proportional to the wavelength of the wave λ_0 , with $k_0 = \frac{2\pi}{\lambda_0}$ [22]. The direction of the propagation vector indicates the direction in which the wave is traveling. When the wave enters the fiber, it can propagate along multiple paths or modes within the core, depending on the core diameter, the wavelength operating range, and the fiber's material.

These modes correspond to different spatial distributions of the electric and magnetic fields associated with the light wave, and each one of them is associated with a unique constant of propagation: $\beta_0 = k_0 n_{eff} = \frac{2\pi}{\lambda_0} n_{eff}$, where n_{eff} is the refractive index of the guided modes.

For a mode to be guided, it should then satisfy the condition:

$$k_0 n_{cladding} < k_0 n_{eff} < k_0 n_{core} \quad (\text{Eq. I.1})$$

In this case, to describe the mode's propagation characteristics [23], one can compute the normalized frequency (V), following the relation:

$$V = \frac{2\pi}{\lambda_0} a NA \quad (\text{Eq. I.2})$$

where a is the core radius, and NA the numerical aperture defined as:

$$NA = \sqrt{n_{core}^2 - n_{cladding}^2} \quad (\text{Eq. I.3})$$

Based on the value of V , different light propagation regimes can occur in an optical fiber. The two main regimes are mode number dependent. As a consequence, they are named in accordance with their guiding capabilities as single-mode fibers (SMF) and multimode fibers (MMF).

Typically, when $V < 2.405$, the fiber supports only the so-called fundamental mode so that, at the operating wavelength λ_0 , only one mode is allowed to propagate. In this thesis, we mainly work with a central wavelength around 1550 nm. In such a regime, light propagation does not experience significant modal dispersion nor walk-off and typically allows for long-distance signal transmission with high bandwidth.

On the other hand, when V is larger than the cutoff value for single-mode operation ($V > 2.405$), the fiber can support multiple modes to propagate simultaneously. However, due to the different propagation paths taken by the modes (when considering a geometrical optics description), multimode fibers suffer from modal dispersion, leading to temporal walk-off and significant signal distortion.

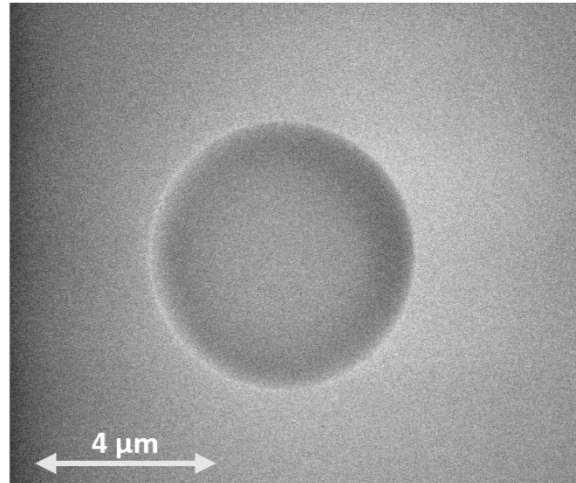


Figure I.2 A single-mode highly nonlinear fiber with 5.6 μm core diameter observed with a microscope.

It is important to note that the regimes previously mentioned are strictly associated to fibers exhibiting a step-index profile. However, as previously hinted there are numerous variations in fiber types, allowing guided propagation with properties depending on the fiber design, material, and characteristics of the fiber. Among others, graded-index (GRIN) profiles which can be obtained by the specific diffusion of dopants in the fiber core to offer a reduced core size and enhanced nonlinearity (via large index contrasts between the core and the cladding) to obtain a so-called highly nonlinear fiber (HNLF). Conversely, large mode area (LMA) fibers allow for single mode operation with large core size, thus allowing the delivery of higher power optical signals without significant nonlinear distortions (via extremely weak index contrasts).

In the following work, detailed in Chapter III and Chapter IV, we mainly focus on standard single-mode optical fibers, including both step-index telecom fibers (i.e. SMF 28) and HNLF fibers operating in the telecom band around 1550 nm (see Figure I.2). For completeness, we also provide a succinct overview in section I.1.3 of the most common fibers and waveguides for which the reported study may be readily transposed.

I.1.2. Fabrication

The fabrication process of fiber optics (see Figure I.3) begins with the manufacture of a glass preform, which is a large cylindrical structure that contains both the core and cladding glass materials and serves as the precursor of the fiber. As we mentioned before, high-purity fused silica (SiO_2) is commonly the most used material for its ease of shaping, isotropic nature, and resistance to thermal and mechanical shocks. Dopants such as Germanium (Ge) and Titanium (Ti) can be added to create a slight refractive index difference between the core and cladding. The preform is typically made by processes such as modified chemical vapor deposition (MCVD) or vapor axial deposition (VAD) [24], [25]. These techniques involve depositing multiple layers of materials with specific refractive index profiles onto the inner surface of a glass tube.

Once the glass preform is synthesized, it undergoes cleaning and inspection to remove impurities and defects. Then, the preform is heated in a fiber drawing tower, until it softens and collapses under its own weight. The softened preform is then carefully stretched, and the fiber is continuously drawn from the preform at a controlled speed, resulting in a long, thin strand of glass. To protect the delicate fiber and provide mechanical strength, a protective coating is applied to the drawn fiber. Subsequently, a curing process is implemented to harden the coating, enhancing its mechanical strength.

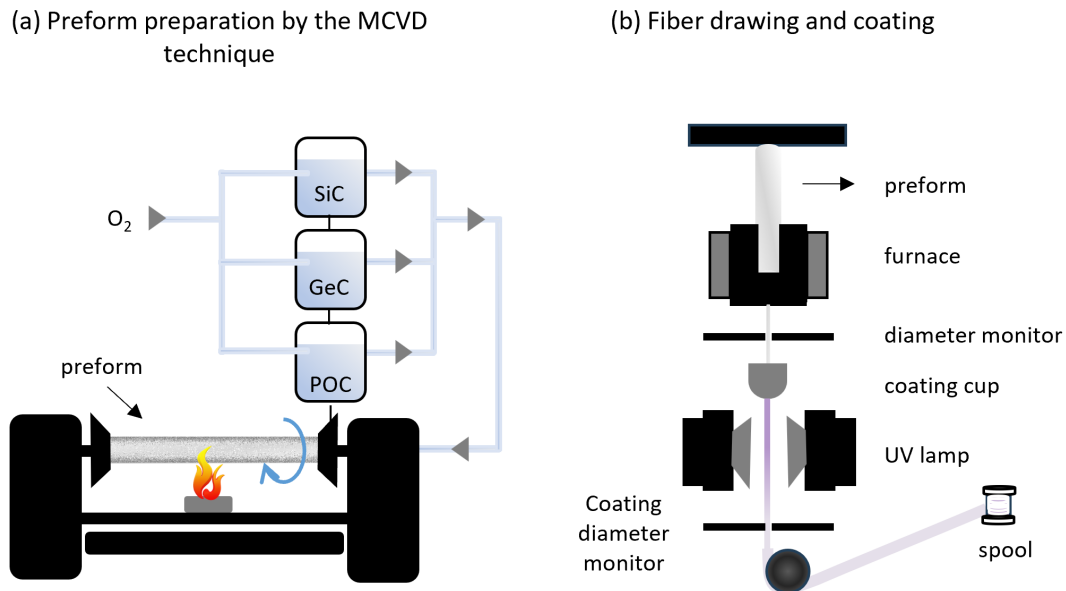


Figure 1.3 Fabrication process: (a) Preform preparation of a Ge-doped silica fiber using the MCVD technique. (b) Fiber drawing by heating and stretching of the preform in fiber tower, creating a thin optical fiber and coating with a thin layer of resin.

Finally, a fiber testing is applied where various tests and inspections are conducted to ensure the quality and performance of the fiber. Optical and mechanical tests are performed to measure parameters such as optical loss, attenuation, bandwidth, and physical properties. These tests ensure that the fiber meets the required specifications. After successfully completing the testing phase, the fiber is spooled onto large reels or spools to facilitate its handling, storage, and transportation. This process should be carried out in a controlled environment to minimize the introduction of contaminants or excessive mechanical stresses on the fiber, and appropriate tension on the fiber should be ensured. Clean rooms or controlled manufacturing areas help maintain the desired cleanliness and temperature conditions during the spooling process.

While the basic steps of fabrication remain similar for different types of fibers, there may be some variations and additional steps depending on the specific requirements of the fibers, as we will see in the following section.

1.1.3. Other specialty fibers and optical waveguide

As mentioned before, optical fibers are structures with the main role of guiding light. In fact, these can be classified within a more general class of optical waveguides. We refer to optical

waveguides as every structure that consists of at least two layers with different refractive indices and possessing the ability to confine the spatial region in which light can propagate.

We provide below a quick overview of the most common optical waveguides used for the study and control of nonlinear effect, also illustrated in Figure I.4.

However, it is worth noting that other type of optical waveguides spanning plasmonic waveguides (based on evanescent coupling), spatial filaments/plasma waveguides [21], as well as liquid-based suspensions and biological waveguides (e.g. RBC) [26], also exists but fall out of the scope of the current study.

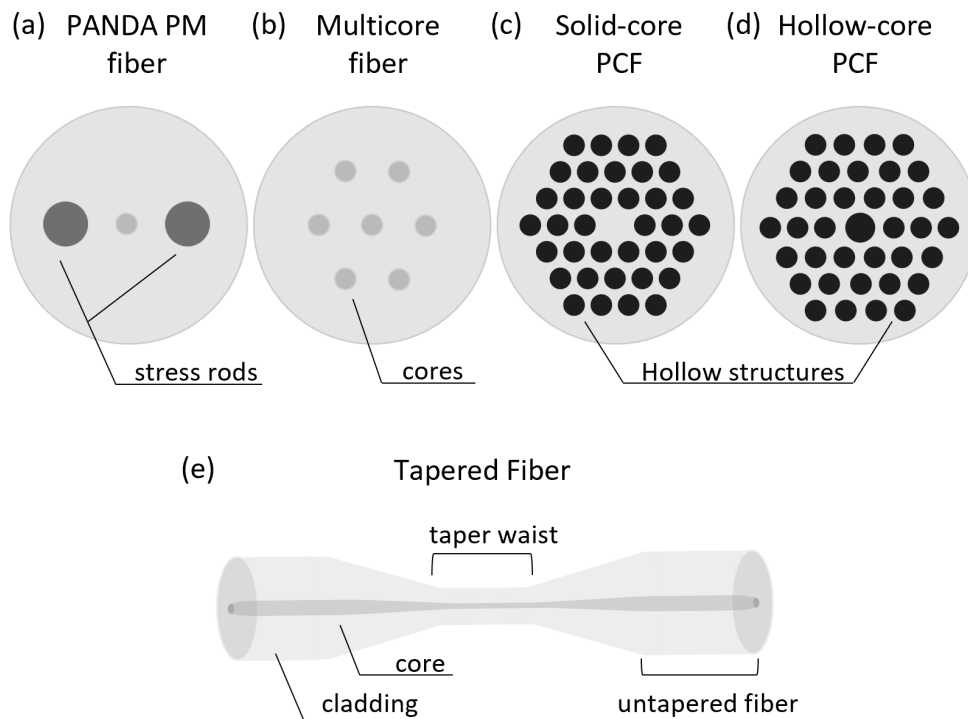


Figure I.4. Illustrative examples of specialty optical fibers: (a) PM fiber; (b) Multicore fiber; (c) Solid-core PCF; (d) Hollow-core PCF; (e) Tapered fiber.

Specialty optical fibers:

Apart from the standard fibers, one can find specialty optical fibers, tailored to possess unique optical properties and characteristics. For instance, polarization maintaining (PM) fibers are special types of fibers designed to maintain the polarization state of light as it travels through them. They enable for the two orthogonal polarized modes to travel at different velocities by introducing anisotropy within the core of the fiber, by using an elliptical core, or through the application of controlled uniaxial stress such as showed in Figure I.4.a, for the PANDA fiber [27].

One can also find optical fibers featuring multiple individual cores within a single fiber structure. They are known as multicore fibers (Figure I.4.b). In such fibers, each core acts as a separate waveguide and carry its independent optical signal. As in this case, the phase changes in each beam, caused by external factors, are quite similar, making it easier to recombine the beams, where the relative phase values will have the most significant impact [28], [29].

In addition, there are some specialized types of fiber, such as photonic crystal fibers (PCF) that are composed of a periodic transverse arrangement of holes running along the length of the fiber.

PCF can have various refractive index profiles depending on the specific arrangement of periodic holes (see Figure I.4.c-d). For example, some PCFs have a solid core surrounded by microstructured holes with specific arrangement and a lower average refractive index [30], [31]. Such design allows for a precise control over the fiber's dispersion properties. These fibers offer a broadband guiding, making them highly versatile for applications like supercontinuum generation and nonlinear optics. On the other hand, hollow core PCFs (HC-PCF) have a central hollow region or with an index lower than the cladding. The presence of the hollow core creates a photonic band gap (PBG) or a region where certain wavelength of light cannot propagate. This unique property allows HC-PCFs to confine light within the hollow core, making them suitable for various applications [32]. One of the key advantages of HC-PCFs is their potential for filling the hollow regions with different gases or liquids, which can significantly modify the behavior of light passing through. This tunability makes them valuable in applications where precise control over light-matter interactions or the propagation dynamics of light are required [33], [34], [35].

Additionally, there are other specialized types of waveguides like nanowire waveguides, enabling strong light confinement and allowing to guide and manipulate light at a nanoscale, or high-index glasses-based waveguides (Hydex) with tunable optical properties which are highly used in photonics integrated circuits, and have been demonstrated to present various capabilities and application for nonlinear optics in CMOS-compatible platforms [36] (see below). One can also mention tapered fibers (Figure I.4.e). These fibers are created by heating and pulling to reduce their diameter along a certain length, enabling mode matching and efficient light coupling, thus reducing losses, and enhancing for example, the nonlinear effects and sensing performances [37].

Integrated waveguides:

Integrated waveguides are a fundamental component of modern photonics and nonlinear optics and are an essential component in photonic integrated circuits (PIC) devices. These waveguides are fabricated using materials like silicon (Si), indium phosphide (InP), or germanium arsenide (GeAs), etc., enabling to effectively control light within sub-micron-scale structure due to their high transparency and refractive indices. The choice of substrate material in waveguides fabrication plays a critical role in either enabling advantages or imposing constraints on the technology. For example, for optical fibers communication applications, commercialized InP-based integrated waveguides are highly used [38]. One key advantage of integrated waveguides, is also their ability to leverage crystalline structures like silicon, introducing nonlinear properties (featuring both second and third-order nonlinear responses). Additionally, these waveguides can harness the potential of heterogeneous structures and hybrid materials, permitting tailored designs for various applications. In this context, silicon nitride (SiN), silicon oxynitride (SiON), and silica (SiO₂) waveguides have gained popularity [39]. Silica-on-silicon integrated optics, using silicon wafers allows for the creation of diverse components, such as couplers, filters, and modulators into one single device, achieved in a scalable manner, allowing for the development of compact and highly efficient photonic circuits [40], [41]. Silica glass also plays a role in waveguide fabrication due to its extremely low-loss and its compatibility with standard semiconductor fabrication techniques, specifically with the introduction of high index doped-silica (Hydex) in optical photonic

integrated circuits [42], [43], [44]. In Figure 1.5, we present the Hydrex photonic integrated circuit – on chip – that we will work with during this thesis and will be further explained in Chapter II and Appendix 1. Our PIC implementation plays the role of an integrated pulse splitter, by means of Mach-Zehnder interferometers. The Hydrex glass platform of the chip is distinguished by low linear losses (< 0.06 dB/cm), negligible nonlinear (two-photon) absorption and high nonlinearity.

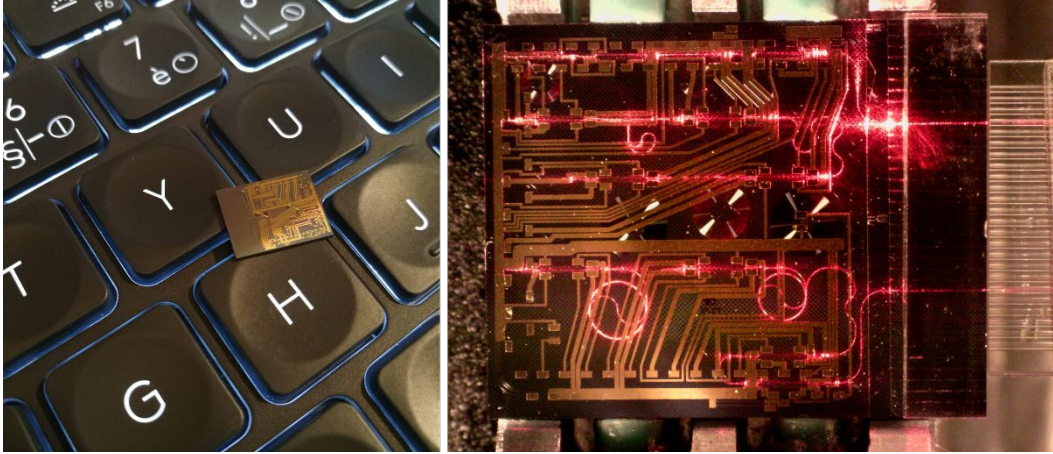


Figure 1.5 Photonic on-chip processor with integrated waveguide circuit seen on a computer keyboard to illustrate its size, and under microscope with a guided red laser to better see its design.

To understand the guided propagation of light within waveguides (and specifically, in fiber optics), we provide below a succinct review of key effects and related linear and nonlinear phenomena.

1.2. Pulse propagation in guided optics

Using a general approach, an electromagnetic wave can be described by Maxwell's equations [24] as:

$$\nabla \cdot \vec{D} = \rho \quad (\text{Eq. 1.4})$$

$$\nabla \cdot \vec{B} = 0 \quad (\text{Eq. 1.5})$$

$$\nabla \times \vec{E} = -\frac{\partial \vec{B}}{\partial t} \quad (\text{Eq. 1.6})$$

$$\nabla \times \vec{H} = \vec{J} + \frac{\partial \vec{D}}{\partial t} \quad (\text{Eq. 1.7})$$

Where, \vec{E} and \vec{H} are the electric and magnetic fields, respectively.

\vec{D} and \vec{B} are the corresponding electric and magnetic flux densities, respectively.

\vec{J} is the electric current density vector, and ρ is the electric charge density.

To understand the behavior of an optical pulse while propagating in a medium, we need to consider the interaction between the pulse and the medium's properties. In the case of optical fibers, the medium's response to an incident optical pulse propagating along a direction is

described by the polarization and magnetization responses \vec{P} and \vec{M} , respectively. These two can be defined through the relations:

$$\vec{D} = \epsilon_0 \vec{E} + \vec{P} \quad (\text{Eq. I.8})$$

$$\vec{B} = \mu_0 \vec{H} + \vec{M} \quad (\text{Eq. I.9})$$

With ϵ_0 and μ_0 the vacuum permittivity and permeability, respectively.

However, as optical fibers are nonmagnetic media, the magnetization M can be considered negligible ($M = 0$). In addition, as fiber optics are dielectric media, there are no free charges, which implies that $\vec{j} = 0$, and $\rho = 0$, which makes $\nabla \cdot \vec{D} = 0$ and thus, $\nabla \cdot E = 0$.

From the equations above, one can derive the wave equation considering the speed of light c as $\mu_0 \epsilon_0 = \frac{1}{c^2}$:

$$\nabla \times \nabla \times \vec{E} = -\mu_0 \epsilon_0 \frac{\partial^2 \vec{E}}{\partial t^2} - \mu_0 \frac{\partial^2 \vec{P}}{\partial t^2} = -\frac{1}{c^2} \frac{\partial^2 \vec{E}}{\partial t^2} - \mu_0 \frac{\partial^2 \vec{P}}{\partial t^2} \quad (\text{Eq. I.10})$$

The polarization response is central to the wave equation, and generally, can be represented as a Taylor expansion of the electric susceptibility χ which divides a linear response P_L from a nonlinear response P_{NL} depending on the incident electric field $\vec{E}(\vec{r}, t)$ as defined by [45]:

$$\begin{aligned} \vec{P}(\vec{r}, t) &= \epsilon_0 \sum_{j=1}^{\infty} \chi^{(j)} \vec{E}(\vec{r}, t)^j \\ &= \epsilon_0 \chi^{(1)} \vec{E}(\vec{r}, t) + (\epsilon_0 \chi^{(2)} \vec{E}(\vec{r}, t)^2 + \epsilon_0 \chi^{(3)} \vec{E}(\vec{r}, t)^3 + \dots) \\ &= \vec{P}_L(\vec{r}, t) + \vec{P}_{NL}(\vec{r}, t) \end{aligned} \quad (\text{Eq. I.11})$$

The polarization $\vec{P}_L(\vec{r}, t)$ is associated with the first-order electric susceptibility $\chi^{(1)}$ and describes a linear propagation in an optical fiber.

In our work, we consider the nonlinear polarization $\vec{P}_{NL}(\vec{r}, t)$ including the terms up until the third order, which is sufficient for the optical powers at play. However, for centrosymmetric materials like silica, which is commonly used in optical fibers, the second-order susceptibility $\chi^{(2)}$ is typically negligible.

Therefore, the nonlinear response arises mainly from the third-order susceptibility $\chi^{(3)}$, which leads to nonlinear phenomena such as the Kerr effect (self-phase modulation), four-wave mixing, and third harmonic generation, which will be further discussed.

1.2.1. Linear propagation

In this section, we first consider the linear contribution only, and thus assume that the nonlinear response is null, i.e. $\vec{P}_{NL}(\vec{r}, t) = 0$, in (Eq. I.11). Therefore, the wave equation (Eq. I.10) becomes:

$$\nabla \times \nabla \times \vec{E}(\vec{r}, t) = -\frac{1}{c^2} \frac{\partial^2 \vec{E}(\vec{r}, t)}{\partial t^2} - \mu_0 \epsilon_0 \chi^{(1)} \frac{\partial^2 \vec{E}(\vec{r}, t)}{\partial t^2} \quad (\text{Eq. I.12})$$

To further simplify the wave propagation equation, we can consider $\nabla \times \nabla \times E = \nabla(\nabla \cdot E) - \nabla^2 E$, and as in fiber optics $\nabla \cdot E = 0$, we obtain:

$$\nabla \times \nabla \times E = -\nabla^2 E \quad (\text{Eq. I.13})$$

and the (Eq. I.12) becomes:

$$\nabla^2 \vec{E}(\vec{r}, t) = \frac{1}{c^2} \frac{\partial^2 \vec{E}(\vec{r}, t)}{\partial t^2} + \frac{1}{c^2} \chi^{(1)} \frac{\partial^2 \vec{E}(\vec{r}, t)}{\partial t^2} = (1 + \chi^{(1)}) \frac{1}{c^2} \frac{\partial^2 \vec{E}(\vec{r}, t)}{\partial t^2} \quad (\text{Eq. I.14})$$

By considering $\vec{E}(\vec{r}, \omega) = \int_{-\infty}^{+\infty} \vec{E}(\vec{r}, t) e^{i\omega t} dt$ and $\tilde{\chi}^{(1)}(\omega)$ the Fourier transform of the temporal electric field $\vec{E}(\vec{r}, t)$ and the first-order susceptibility $\chi^{(1)}$ (see section 0 for more details), and the dielectric constant $\varepsilon(\omega) = 1 + \chi^{(1)}(\omega)$, we can then write the wave equation in the frequency domain as:

$$\nabla^2 \vec{E}(\vec{r}, \omega) - \varepsilon(\omega) \frac{\omega^2}{c^2} \vec{E}(\vec{r}, \omega) = 0 \quad (\text{Eq. I.15})$$

Expressing the susceptibility $\tilde{\chi}^{(1)}(\omega)$ and the dielectric constant $\varepsilon(\omega)$ as complex numbers with their real and imaginary parts as: $\chi^{(1)} = \text{Re}\{\tilde{\chi}^{(1)}(\omega)\} + i \text{Im}\{\tilde{\chi}^{(1)}(\omega)\}$

and considering that $\varepsilon_L(\omega) = \left(\frac{n+i\alpha c}{2\omega}\right)^2$ allows us to separate and quantify two aspects of the material's response that we will discuss in the following section; the refractive index n of the fiber, and the linear losses α through the two following relations:

$$n_L(\omega) = 1 + \frac{1}{2} \text{Re}\{\tilde{\chi}^{(1)}(\omega)\} \quad (\text{Eq. I.16})$$

$$\alpha_L(\omega) = \frac{\omega}{nc} \text{Im}\{\tilde{\chi}^{(1)}(\omega)\} \quad (\text{Eq. I.17})$$

I.2.1.1. Dispersion

When a pulse propagates through an optical fiber, the different wavelengths composing the pulse will travel at slightly different speeds in the waveguide, leading to a pulse distortion generating a temporal broadening of the optical pulse. This process is called *Chromatic Dispersion*. This variation in velocity can depend on the mode of propagation considered and causes a change in both the temporal profile and the spectral phase of the optical wave.

There are two main types of chromatic dispersion: material dispersion and waveguide dispersion.

1- Material Dispersion:

The refractive index $n = c/v$ is the ratio between the speed of light in vacuum (c) and in the propagation medium (v). It measures how much the speed of light changes when it passes through a particular material. In fiber optics, the refractive index can change due to the interaction between light and the materials used in the fiber and it can depend on various factors such as the material's composition, but also on the wavelength of light. This wavelength-dependent variation is known as material dispersion.

In fiber optics, the variation of the refractive index n in function of the wavelength, or the optical frequency of the electromagnetic wave ($\omega = \frac{2\pi c}{\lambda}$), can be described using the Sellmeier equation [23], [24], [46]:

$$n^2(\omega) = 1 + \sum_{j=1}^m \frac{B_j \omega_j^2}{\omega_j^2 - \omega^2} \quad (\text{Eq. I.18})$$

where ω_j and B_j are the resonance frequencies, and the coefficient of the j the resonance, respectively, which can be experimentally determined [47] and have been computed in fused silica for $m = 3$ [48]. This approximation remains valid when considering wavelengths far away for a resonance B_j , as typical of fiber optics in the telecom wavelength around 1550 nm (i.e. the case studied in this work).

To characterize material dispersion, we consider the Taylor series expansion [24] of the constant of propagation $\beta(\omega) = \frac{\omega}{c}n$ around a central frequency ω_0 :

$$\beta(\omega) = \beta_0 + \beta_1(\omega - \omega_0) + \frac{1}{2}\beta_2(\omega - \omega_0)^2 + \frac{1}{6}\beta_3(\omega - \omega_0)^3 + \dots \quad (\text{Eq. I.19})$$

In this case,

- $\beta_0 = \beta(\omega_0)$ represents the *constant of propagation* at ω_0 .
- $\beta_1 = \frac{\partial\beta_0(\omega)}{\partial\omega} = \frac{1}{c}\left(n + \omega \frac{\partial n}{\partial\omega}\right)$, with $n_g = n + \omega \frac{\partial n}{\partial\omega}$ denominated as the *group index* and equal to $n_g = \frac{c}{v_g}$ and with v_g defined as the *group velocity*. Reformulating, one can typically obtain $\beta_1 = \frac{n_g}{c} = \frac{1}{v_g}$.
- $\beta_2 = \frac{\partial^2\beta_0(\omega)}{\partial\omega^2} = \frac{1}{c}\left(2\frac{\partial n}{\partial\omega} + \omega \frac{\partial^2 n}{\partial\omega^2}\right) = \frac{1}{c}\frac{\partial n_g}{\partial\omega} = \frac{1}{\partial v_g/\partial\omega}$ represents the *group-velocity dispersion* parameter (GVD), also sometimes called *second-order dispersion*. The GVD is responsible for the dispersion of v_g and thus leads to a “symmetric” pulse distortion (i.e. temporal spreading).
- $\beta_3 = \frac{\partial^3\beta_0(\omega)}{\partial\omega^3} = \frac{1}{c}\left(3\frac{\partial^2 n}{\partial\omega^2} + \omega \frac{\partial^3 n}{\partial\omega^3}\right)$, represents the *third-order dispersion* (TOD), which becomes relevant when dealing with ultrashort pulses. In this case, TOD (and higher-order dispersion terms) may have a significant impact on the pulse propagating and such odd dispersion term inherently yields “asymmetric” pulse distortion.

In optical fibers, a particular relevant variable is the *zero-dispersion wavelength* (ZDW). This wavelength, denoted as λ_{ZDW} (see Figure I.6), corresponds to the point where the GVD value vanishes to become zero. It determines the wavelength where β_2 changes sign and where one moves from one dispersive region to another (i.e. anomalous/normal dispersion). When dealing with wavelengths close to the ZDW of a fiber, it also becomes necessary to consider TOD and higher-order dispersion terms in the Taylor expansion of (Eq. I.19).

By convention, it is usual to express the GVD using the dispersion parameter D which quantifies the dispersion of the material and is expressed as:

$$D = -\frac{\lambda_0^2}{2\pi c} \beta_2 \quad (\text{Eq. I.20})$$

2- Waveguide dispersion:

The material of the fiber is not the only factor affecting the dispersion, as the waveguide structure itself further contributes to the overall dispersion: The refractive index profile, the core size, and the geometry of the fiber can indeed also affect the chromatic dispersion. This type of dispersion arises from the differences in the propagation constant experienced by the different frequency-dependent wave vector of a given spatial mode within the fiber.

The total dispersion of the fiber can be expressed as: $D_{total} = D_{material} + D_{waveguide}$

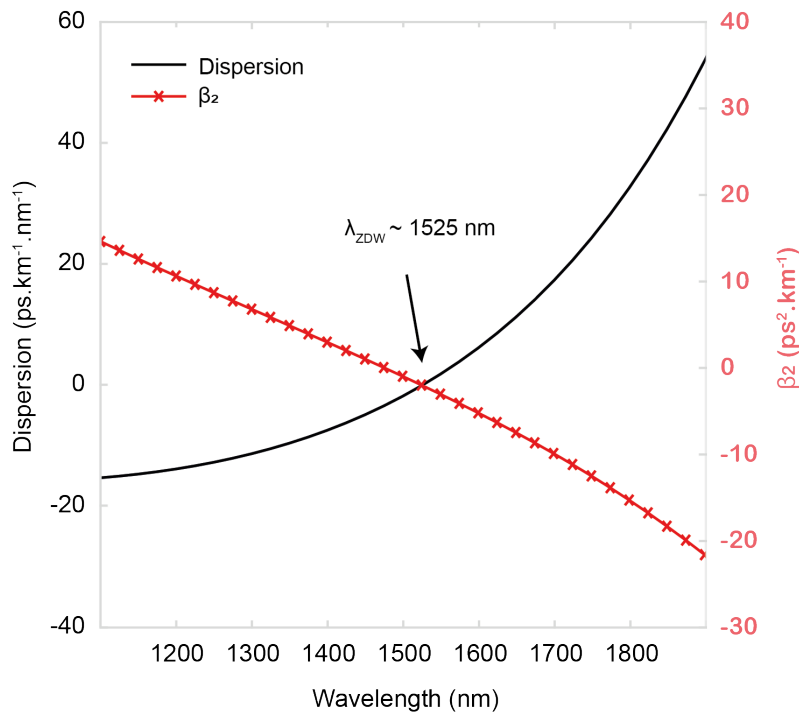


Figure I.6 Representation of the dispersion of a homemade highly-nonlinear fiber (HNLF), both designed and fabricated at XLIM. The GVD parameter β_2 is represented in red and follows an opposite direction to the dispersion D . The ZDW is marked by an arrow at 1525 nm , where β_2 changes sign.

For certain fiber designs, the waveguide dispersion can be predominant over the material dispersion itself, leading to a significant shift in the zero-dispersion wavelength. This shift, owing to different values and strength of these two dispersive contributions, allows precisely controlling and manipulating the dispersion properties of the fibers by engineering different types of fibers for specific applications.

As illustrated in Figure I.4, there is nowadays a large variety of fibers available, including dispersion-shifted fibers (with a ZDW around $1.5 \mu\text{m}$) and photonic crystal fibers (with finely-tuned dispersion properties) within the most commonly encountered types taking advantage of adjusted waveguides.

Later on, during our studies (see Chapter III and Chapter IV), we will work with a single-mode, highly nonlinear Germanium-doped silica fiber with a core diameter of $5.6 \mu\text{m}$ exhibiting a parabolic gradient-index profile. In Figure I.6, we show the overall dispersion curve of this fiber

in the near infrared region. For completeness, we also calculate the corresponding β_2 and observe that it starts with positive values for shorter wavelengths (i.e. normal dispersion), and becomes negative for longer wavelengths (i.e. anomalous dispersion) at approximately 1525 nm , which corresponds to the zero-dispersion wavelength of this fiber.

I.2.1.2. Attenuation and losses

Attenuation and losses in fiber optics refer to the decrease in signal strength as light propagates through an optical fiber. The attenuation α represents the decrease between the input optical power P_{in} and the output power P_{out} , assuming the losses are uniformly distributed all along the fiber of length L through the relation:

$$\alpha = \frac{-10}{L} \log_{10} \left(\frac{P_{in}}{P_{out}} \right) \quad (\text{Eq. I.21})$$

The attenuation α is here defined in a logarithmic scale and expressed in dB/km.

One of the most likely occurrences that can lead to increased losses in optical fibers is the minor bends in the fiber's geometry, whether introduced during manufacturing or due to external factors. Bending can cause light to hit the core-cladding interface at angles below the critical angle. This results in light escaping into the cladding material, leading to losses. Bend sensitivity is typically expressed as the attenuation, in dB/km, and given for a specific bend radius and wavelength.

Another important source of losses can be readily attributed by raw material absorption. Materials used in fiber optics (specifically silica), can absorb specific wavelengths of light, which can lead to notable energy loss. Silica-based fibers exhibit significant absorption in the ultraviolet (UV) and infrared (IR) regions. Additionally, impurities in the fiber (e.g. water and OH^- absorption peak around $1.4\ \mu\text{m}$) or dopants added to modify the refractive index can contribute to absorption losses. Overall, absorption losses in fiber optics occur due to the selective absorption of light by the materials used in the fiber, including both intrinsic absorption of silica and absorption caused by impurities or intentional doping. Minimizing these losses thus requires the use of high-purity materials and careful control of the fabrication process.

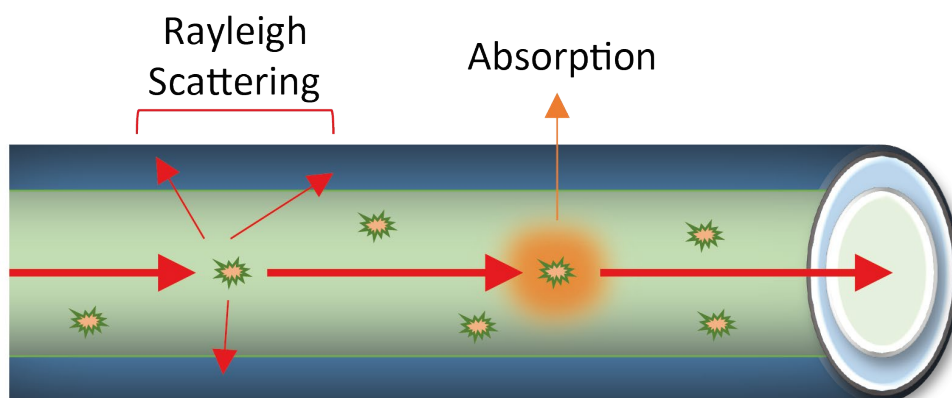


Figure I.7 Illustration of the intrinsic losses in the fiber: Rayleigh scattering (red arrows) where the light is scattered due to impurities in the fiber, and the absorption losses (in yellow), where a part of the light is absorbed by the fiber's material.

Another factor contributing to the attenuation of light is the Rayleigh scattering process. It occurs when light interacts with microscopic variations in the refractive index of the fiber core, which are much smaller than the wavelength of the incident light, leading to scattering light in various directions. This scattering process results in the loss of optical power as the light propagates through the fiber. When light propagates within the fiber, it interacts with the electron cloud of the molecules in the core, causing polarization. This leads to the absorption of some fraction of the energy by the molecules. The absorbed energy is then re-emitted in the form of scattered light, which is emitted in all directions, resulting in a random distribution of photons (see Figure 1.7). The amount of scattering depends on the size and concentration of microscopic refractive index variations in the fiber core.

This scattering process thus induces losses during fiber propagation, as some of the scattered light can escape from the core-cladding interface, reducing the overall intensity of the transmitted light: some of the re-emitted light may have angles larger than the critical angle, leading to its loss from the core. To mitigate Rayleigh scattering, optical fiber designs target highly homogeneous refractive indices in the core, minimizing the microscopic index variations and reducing the scattering, thereby minimizing losses. It is worth mentioning that, as the extent of the Rayleigh scattering depends on the wavelength of the incident light, shorter wavelengths experience stronger scattering because the scattering centers that divert the light (i.e. scattering particles or refractive index variations) become relatively larger compared to the wavelength.

In recent years, there has been significant progress in reducing losses and attenuations in optical fibers, driven by advancements in fiber designs and fabrication technologies. These developments have paved the way for enhanced performance and increased efficiency in various optical communication and sensing applications. Here we can cite for example, refined and ultra low-loss telecom fibers deployed worldwide for long-haul communications, or PCFs which have revolutionized the field of fiber optics by their unique microstructured designs, allowing for tight confinement and guidance of light. Noteworthy, while PCFs or other analogous specialty fibers may exhibit higher losses compared to traditional fibers, their design enables greatly enhanced nonlinear effects, such as increased nonlinearity and broader transparency bandwidths. In addition, the development of integrated photonic waveguides, often referred to as photonic chips or integrated optics, provided excellent control over light propagation, enabling efficient and relatively low-loss guiding of optical signals at the chip level.

1.2.2. Nonlinear propagation

In this section, we consider the case where the light intensity is strong enough so that nonlinear effects cannot be neglected anymore in the polarization of the electric field of (Eq. 1.11). In this framework, rewriting the wave propagation equation without a linear case approximation yields:

$$\nabla \times \nabla \times \vec{E}(\vec{r}, t) = -\frac{1}{c^2} \frac{\partial^2 \vec{E}(\vec{r}, t)}{\partial t^2} - \mu_0 \epsilon_0 \chi^{(1)} \vec{E}(\vec{r}, t) - \mu_0 \epsilon_0 \chi^{(3)} \vec{E}(\vec{r}, t)^3 \quad (\text{Eq. 1.22})$$

As we are working with single-mode fibers, the wave equation of second order can be reduced to a first-order equation by considering the *slowly varying envelop approximation* (SVEA) [24] of an electric field propagating along the longitudinal z-axis of the SMF with a linear polarization along the x-axis. In this case, the SVEA allows for redefining the field as:

$$E(\vec{r}, t) = \frac{1}{2} \vec{x} [F(x, y)A(z, t)e^{i(\omega_0 t - \beta_0 z)}] \quad (\text{Eq. I.23})$$

Here β_0 is the constant of propagation, ω_0 the central frequency, and $F(x, y)$ represents the transverse spatial distribution of the electric field, which is related to the mode profile in the waveguide. The slowly varying envelope function $A(z, t)$ captures the temporal and longitudinal variations of the field envelope, and the term $e^{i(\omega_0 t - \beta_0 z)}$ represents the phase of the electric field. The slowly varying envelope approximation is obtained by assuming that the spatial variation of the electric field $F(x, y)$ is much slower compared to the rapidly oscillating temporal variation of the electric field $A(z, t)$. During this approximation, we can also consider the simplification used in (Eq. I.13) because the term $\nabla(\nabla \cdot E)$ is much smaller than $-\nabla^2 E$.

With this separation, we can thus write:

$$\begin{aligned} \vec{P}(\vec{r}, t) &= \frac{1}{2} \vec{x} [F(x, y)P(z, t)e^{i(\omega_0 t - \beta_0 z)}] = \vec{P}_L(\vec{r}, t) + \vec{P}_{NL}(\vec{r}, t) \\ &= \varepsilon_0 \chi^{(1)} A(z, t) + \frac{3}{4} \varepsilon_0 \chi^{(3)} |A(z, t)|^2 A(z, t) \end{aligned}$$

and we then obtain:

$$\vec{P}(\vec{r}, t) = \left(\varepsilon_0 \chi^{(1)} + \frac{3}{4} \varepsilon_0 \chi^{(3)} |A(z, t)|^2 \right) A(z, t) \quad (\text{Eq. I.24})$$

where $|A(z, t)|^2$ represents the squared magnitude of the envelope function which is proportional to the instantaneous power of the optical field. Here, we observe that the nonlinear polarization P_{NL} captures the interplay between the power and the envelope of the optical field within a nonlinear interaction with the medium.

In an analogous way as in section I.2.1, we can find in this case the nonlinear dielectric constant:

$$\varepsilon_{NL} = \frac{3}{4} \chi^{(3)} |A(z, t)|^2 \quad (\text{Eq. I.25})$$

and identify the total permittivity as [45]:

$$\varepsilon = \varepsilon_L + \varepsilon_{NL} = 1 + \chi^{(1)} + \frac{3}{4} \chi^{(3)} |A(z, t)|^2 \quad (\text{Eq. I.26})$$

By considering again the complexity of ε and χ , we can find the nonlinear refractive index n_{NL} noted as n_2 and the nonlinear losses α_{NL} as:

$$n_2 = n_{NL} = \frac{3}{8n_L} \text{Re}\{\chi^{(3)}\} \quad (\text{Eq. I.27})$$

$$\alpha_{NL} = \frac{3\omega_0}{4n_L c} \text{Im}\{\chi^{(3)}\} \quad (\text{Eq. I.28})$$

and the total refractive index and losses as:

$$n_{tot} = n_L + n_2 |A|^2 \quad (\text{Eq. I.29})$$

$$\alpha_{tot} = \alpha_L + \alpha_{NL}|A|^2 \quad (\text{Eq. I.30})$$

As we can see from (Eq. I.29), n_{tot} is dependent on the intensity of the incident light $|A|^2$, and proportional to n_2 . In silica-based fibers, the nonlinear absorption coefficient α_{NL} is relatively small and can be neglected. Researchers often seek out materials with high refractive indices, such as chalcogenides, particularly due to their high values of n_2 within the telecommunication wavelength and their ability to offer excellent optical confinement, making them well-suited for nonlinear optical applications. Additionally, these materials generally possess a remarkably high nonlinear figure of merit, which determines the feasibility of achieving nonlinear optical effects based on a material's linear and nonlinear properties, including its refractive index and absorption characteristics. However, it is important to note that high-index materials, while powerful for nonlinear effects, can sometimes have limitations and may suffer from significant nonlinear losses. On the other hand, certain high-index glasses, like silicon oxynitride, have negligible nonlinear absorption, leading to very low figure of merit.

In the following sections, we will describe the key nonlinear effects occurring in optical fibers pertinent to our current studies. It is worth noting that Brillouin scattering will not be the focus of our discussion, as we typically work with short laser pulses, (rather than CW lasers), operating at power levels significantly below the Brillouin threshold. However it is important to acknowledge that Brillouin scattering in optical fibers, based on the inelastic scattering of light and characterized by the interaction between the optical and acoustic fields, is an intriguing field of research in its own right [49] and has recently been observed in integrated photonics systems [50], including our integrated photonic chip [51].

1.2.2.1. Kerr effect

The variation of the nonlinear refractive index n_2 with the light intensity $I = |A|^2$ is a well-known nonlinear process in fiber optics called *Kerr effect*.

This effect occurs almost instantaneously, due to the quasi-instantaneous redistribution of the electronic dipole charges during light-matter interaction. This gives rise to a large variety of nonlinear phenomena, whose most commonly encountered in fiber optics is probably *self-phase modulation* (SPM).

In the context of SPM, the optical pulse experiences a progressive change of its spectral shape due to the intensity dependence of the temporal phase created via Kerr effect. As the intensity of the pulse increases, certain regions experience a higher nonlinear refractive index compared to regions with lower intensity. This leads to a phase shift, which is the difference between different parts of the propagating pulse (see Figure I.8).

Mathematically, it can be expressed as:

$$\Delta\Phi_{SPM} = n_2 k_0 I L \quad (\text{Eq. I.31})$$

where $\Delta\Phi_{SPM}$ represents the phase shift, and L is the fiber length. It determines the extent of phase modulation induced by the intensity of the optical field. Importantly, when considering fiber propagation, it is convenient to address the nonlinearity as a function of the instantaneous power P in the mode rather than the transverse distribution of the light in the fiber. One can then readily define the parameter γ as *the nonlinear coefficient*:

$$\gamma = \gamma(\lambda_0) = n_2 \frac{2\pi}{\lambda_0 A_{eff}} \quad (\text{Eq. 1.32})$$

which represents the strength of the nonlinear optical response in the waveguide. In this case, the nonlinear coefficient γ does not only depend on the frequency and the nonlinear refractive index but also on the effective mode area A_{eff} which can be defined as:

$$A_{eff}(\lambda) = \frac{\left(\iint_{-\infty}^{+\infty} |\tilde{F}(x, y, \omega)|^2 dx dy \right)^2}{\iint_{-\infty}^{+\infty} |\tilde{F}(x, y, \omega)|^4 dx dy} \quad (\text{Eq. 1.33})$$

Following this change of variable, the phase shift induced by SPM can be then given by a simpler formula:

$$\Delta\Phi_{SPM} = \gamma P_0 L \quad (\text{Eq. 1.34})$$

where P_0 corresponds to the instantaneous optical power in the fiber mode, and the expression is conveniently used to define the magnitude of the nonlinear effects during propagation.

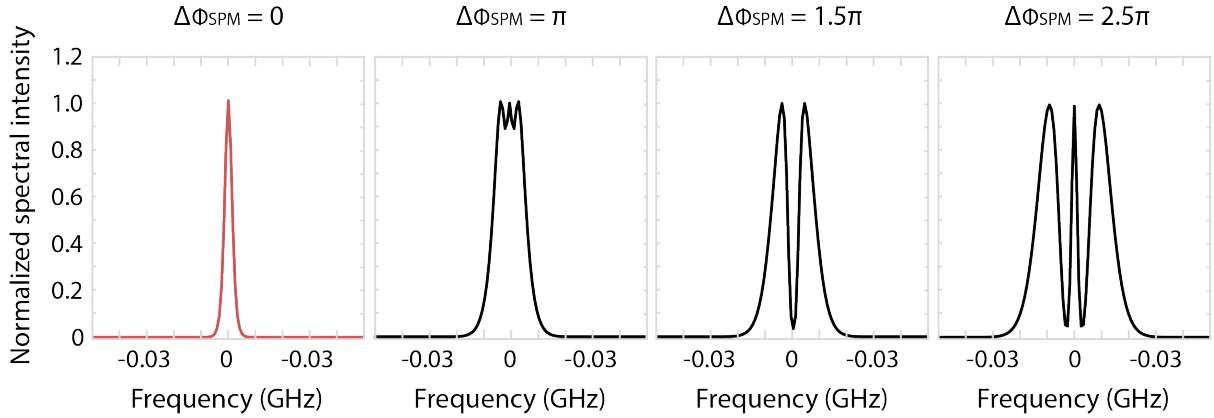


Figure 1.8 Representation of the evolution of a hyperbolic secant optical pulse with a temporal width of 100 ps experiencing SPM at different nonlinear phase shifts, considering only Kerr effect in an SMF with $\beta_2 = 21.8 \text{ ps}^2 \cdot \text{km}^{-1}$ and $\gamma = 3 \text{ W}^{-1} \cdot \text{km}^{-1}$. In red, we show the normalized input pulse with $\Delta\phi_{SPM} = 0$, and in black we can see the output spectrum when increasing the nonlinear phase shift to $\Delta\phi_{SPM} = \pi, 1.5\pi$, and 2.5π .

When the incident field consists of two different wavelengths (and/or different polarizations), experiencing SPM and interacting altogether, a new nonlinear phenomenon emerges from it, known as *cross-phase modulation* (XPM) [24]. XPM leads to a mutual influence between the components, causing a change in their phase relationship. This interaction can result in a more complex distortion of the signal's spectrum, causing an asymmetric broadening or narrowing of the individual components.

1.2.2.2. Raman effect

Another key nonlinear process that can occur during nonlinear propagation in optical fibers is *Raman scattering* which involves the inelastic scattering of photons by the vibrational modes of the molecules in the fiber material.

This interaction with the nuclei is in this case non-instantaneous (in contrast with the Kerr effect acting on the electrons of the material) and results in an inelastic exchange of energy. This interaction can lead to two outcomes: Stokes scattering, where the photon loses energy and emerges at a lower frequency, or anti-Stokes scattering, where the photon gains energy and emerges at a higher frequency (see Figure I.9).

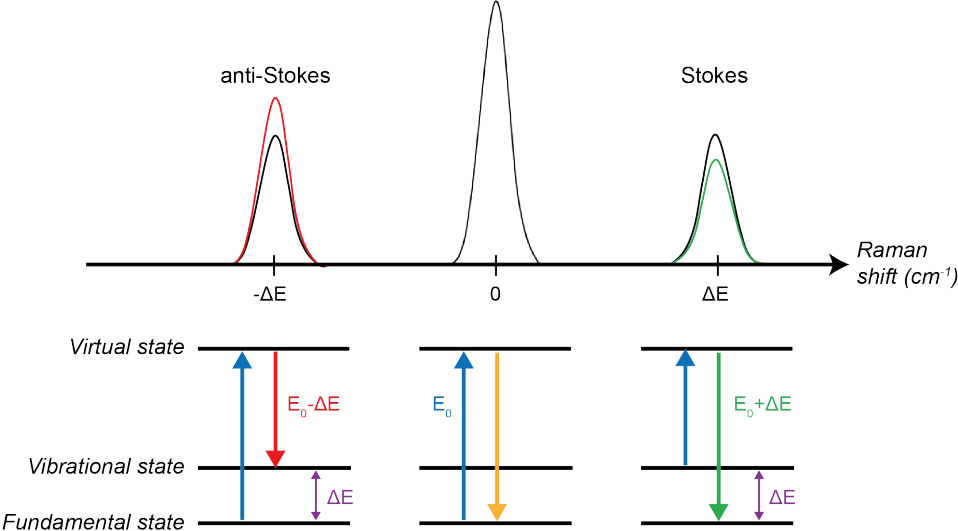


Figure I.9 Principle of the Raman effect and the energy transfer from E_0 to create the Stokes components (in green) with a lower energy $E_0 - \Delta E$ and anti-Stokes components (in red) with a higher energy $E_0 + \Delta E$, on both sides of the pump.

An important aspect of the Raman effect in nonlinear optics is *Stimulated Raman scattering* (SRS), which is a specific type of Raman scattering that involves a pumping photon being down-converted to a lower frequency, generating a Stokes wave.

The optical fibers we are using are made of silica which has broad vibrational spectra, whose peak gain occur at a frequency detuning of ~ 13.5 THz. It is important to note that the Raman gain can be calculated using analytical methods [24], [52] however, in our numerical work, we rely on the experimental measurements issued from [53], whose normalized gain profile is shown in Figure I.10.

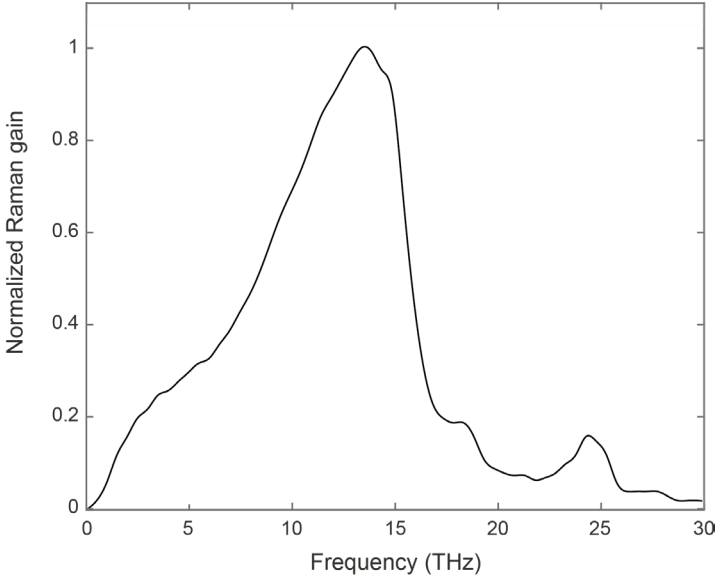


Figure I.10 Normalized Raman gain as a function of the frequency. Generated with data from [53].

SRS mechanism can be stimulated by external optical pumping fields and constitute the operation principle of Raman amplifier. However, when an optical pulse is sufficiently short, its spectrum can be broad enough to offer a non-negligible overlap with the Raman gain spectrum shown in Figure I.10, which can directly drive SRS.

Along with Raman spontaneous emission, this phenomenon can lead to a variety of nonlinear effects as the optical pulse interacts with the fiber medium. Among others, spectral broadening can be obtained from Raman cascaded amplification. Similarly, ultrashort pulses known as solitons can also experience a Raman-induced frequency shift towards longer wavelengths, which constitute a key mechanism for the generation of a broadband *supercontinuum* (SC) – see further details about these phenomena in section I.6.

Overall, it is important to note that the *complete nonlinear response* $R(t)$ of the material comprises two components: the instantaneous electronic response (associated with the Kerr effect) and the delayed Raman contributions, yielding:

$$R(t) = (1 - f_R)\delta t + f_R h_R(t) \quad (\text{Eq. I.35})$$

Here, f_R denotes the fractional Raman contribution, which corresponds to the ratio of delayed Raman effect within the complete nonlinear response. In this case, δt is the instantaneous electronic response of the material while h_R corresponds to the vibration of the material molecules by the optical field as illustrated in Figure I.10).

In silica, the Raman fraction is usually considered as $f_R = 0.18$ making Kerr effect (i.e. $1-f_R = 82\%$) predominant and about 5-fold stronger than Raman in optical fiber.

I.3. Modeling of nonlinear pulse propagation

As previously mentioned in section I.2.2, during nonlinear light propagation in optical fibers, the complex interplay between the electromagnetic fields and the polarization responses of the fiber medium leads to a wide range of intriguing phenomena.

In order to analyze and model this propagation, various mathematical frameworks and numerical techniques have been developed over the years. In this section, we discuss two prominent models employed for resolving nonlinear wave propagation in optical fibers: the *nonlinear Schrödinger equation* (NLSE), which provides a powerful analytical framework for describing the evolution of the electric field in a nonlinear medium, and the *generalized nonlinear Schrödinger equation* (GNLSE) which constitutes an extension of the NLSE incorporating additional higher-order effects for more accurate numerical simulations. Finally, we discuss the numerical method used to solve both of these differential equations, the Fourier split-step algorithm, which combines discrete Fourier transform techniques with stepwise integration and thus allows for efficient and accurate simulations, facilitating the exploration of diverse nonlinear phenomena.

Our focus here is primarily on scalar monomodal fiber propagation, where we consider the evolution of the linearly polarized optical waveform into a single-mode waveguide. While vectorial approaches [54] are also possible and valuable in some contexts, they are not considered in our current discussion, as they fall outside the scope of our studies.

I.3.1. The nonlinear Schrödinger equation

Starting from the approximations previously described in the section I.2.2, where an isotropic slowly varying envelope is assumed, we can now derive the linearly polarized electric field

(Eq. I.23) and the polarization (Eq. I.24) and substitute their values into the wave equation (Eq. I.22). Considering only the instantaneous Kerr effect as the nonlinear term and the group velocity dispersion during propagation, we obtain what is commonly known as the “standard” nonlinear Schrödinger equation in the form of:

$$\frac{\partial A(z, t)}{\partial z} - \beta_1 \frac{\partial A(z, t)}{\partial t} + i \frac{\beta_2}{2} \frac{\partial^2 A(z, t)}{\partial t^2} = i\gamma |A(z, t)|^2 A(z, t) \quad (\text{Eq. I.36})$$

Here, the Kerr effect is included via the nonlinear parameter γ and the dispersion parameters are the results of Taylor’s expansion of the dispersion curve already developed in section I.2.1.1. Importantly, the NLSE can be further simplified by considering the temporal evolution of the field A in a reference frame moving at the group velocity of the waveform: $T = t - \frac{z}{v_g}$.

In this comoving frame, which can be expressed through the constant of propagation $\beta_1 = 1/v_g$, (Eq. I.37) becomes a simplified version of the NLSE, widely used in nonlinear fiber optics:

$$i \frac{\partial A(z, T)}{\partial z} - \frac{\beta_2}{2} \frac{\partial^2 A(z, T)}{\partial T^2} + \gamma |A(z, T)|^2 A(z, T) = 0 \quad (\text{Eq. I.37})$$

In this case, the pulse evolution is typically associated with two key parameters γ and β_2 , respectively accounting for strength of nonlinear and dispersive effects in the fiber (see section I.4 for further details).

I.3.2. The generalized nonlinear Schrödinger equation

In our work, we are interested in the nonlinear evolution and spectral broadening of ultrashort pulses during their propagation in optical fibers. The complex interplay of a variety of linear and nonlinear phenomena during pulse propagation requires a refined description of the evolution dynamics beyond the standard NLSE in order to ensure the most accurate prediction of the pulse evolution and associated nonlinear broadening.

It is then important to consider attenuation, higher-order dispersive effects as well as both instantaneous (Kerr) and non-instantaneous (Raman) nonlinear effects to expand the NLSE into the generalized nonlinear Schrödinger equation for a better representation of pulse dynamics. The GNLSE equation can be described as:

$$\frac{\partial A}{\partial z} + \frac{\alpha}{2} A - \sum_{n=2}^{\infty} \frac{i^{n+1}}{n!} \beta_n \frac{\partial^n A}{\partial T^n} = i\gamma \left(1 + \frac{i}{\omega_0} \frac{\partial}{\partial T} \right) \left(A(z, t) \int_{-\infty}^{\infty} R(T') |A(z, T - T')|^2 dT' \right) \quad (\text{Eq. I.38})$$

The equation can be analyzed by first looking at the left-hand side. The linear propagation is described under the different derivation of the constant of propagation $\beta_n = \frac{\partial^n \beta}{\partial \omega^n}$, typically up to the third-order (or beyond, depending on pulse bandwidth and the required accuracy on the dispersion model), as well as the linear losses α .

On the right-hand side of the equation, we can identify the nonlinear effects associated with the nonlinear coefficient $\gamma(\omega_0) = \frac{\omega_0 n_2}{c A_{eff}}$.

To account for the dispersion of the nonlinearity γ , the GNLSE also includes a corrective “optical shock term” that can take a simplified form as $1/\omega_0$. Altogether, this corrected nonlinear coefficient acts on the total nonlinear response of the GNLSE, which not only include the

instantaneous Kerr effect, but also the delayed Raman contribution (Eq. I.39) in function of the time T' as:

$$\int_{-\infty}^{\infty} R(T') |A(z, T - T')|^2 dT' = (1 - f_R) |A(z, T)|^2 + f_R \int_{-\infty}^{+\infty} h_R(T') |A(z, T - T')|^2 dT' \quad (\text{Eq. I.39})$$

I.3.3. Numerical propagation framework: The split-step Fourier method

Although a pure one-dimensional NLSE (Eq. I.36) is integrable, the nonlinear propagation of optical pulses usually a numerical approach, especially when considering accurate modeling with the GNLSE. In our work, we use the split-step Fourier method. This technique takes into account that the GNLSE can be written as a combination of linear and nonlinear terms noted as \hat{D} and \hat{N} , respectively, such as $\frac{\partial A}{\partial z} = (\hat{D} + \hat{N})A$. It considers that while the pulse is propagating along a distance z of the fiber, the two effects can act independently between two points for a sufficiently small distance h . Successively, we consider firstly only the nonlinear effects ($\hat{D} = 0$), and then the dispersive effects alone ($\hat{N} = 0$).

In our case, we adopt a symmetric split-step Fourier procedure for integrating (Eq. I.38), which enhances the accuracy of the numerical model without significantly increasing computational time. This approach involves introducing the dispersion operator at every half-step ($h/2$) and solving it using the Runge-Kutta method [55], [56].

To correctly model the propagation using the split-step method, we must determine the parameters that define the spectro-temporal window. These parameters include the temporal span (T_{span}), the spectral span (F_{span}), and the number of point n_{pts} . It is also important to note that these parameters are inversely related, thus, finding the right balance between them is essential. We must consider also a sufficiently large number of integration steps n_{steps} along z , which will define our step size $h = L/n_{steps}$, where L is the fiber length. In our numerical studies, we dedicate particular attention to optimize these parameters in order to achieve a temporal and spectral resolution, and ensure an accurate capture of the complete signal, while taking into consideration the computation time.

I.4. Overview of different pulse propagation regimes

To study the propagation of an optical pulse in the fiber, we must consider the evolution of both the temporal and spectral properties of the pulse. In the temporal domain, an optical pulse can be described as a slowly varying envelope A with a corresponding phase ϕ .

To define an optical pulse with a known envelope shape, three main properties should be considered:

- The *peak power* P_0 , measured in Watt.
- The *pulse duration* T_0 , measured at $\frac{P_0}{e}$ and proportional to the *full width at half maximum (FWHM)* duration of the pulse, T_{FWHM} .
- The *chirp parameter* C which describes the phase modulation of the pulses.

The chirp refers to the temporal dependence of the instantaneous frequency deviation from the carrier frequency $\delta\omega = -\frac{\partial\phi}{\partial T}$. It represents the frequency drift of the optical pulse over time. This chirp $\delta\omega$ can be caused by effects such as dispersion, nonlinear interactions, or intentional

shaping of the pulse, and it affects the pulse's temporal shape, duration, and spectral content [24].

While the chirp can take complex forms depending on the exact dynamics at play, it is conveniently represented via a parameter C describing the slope of a linear chirp typically observed when a pulse experience pure group velocity dispersion. In this case, a chirped pulse can be either positively ($C > 0$) or negatively ($C < 0$) chirped, which means that the higher/lower frequency components of the pulse arrive earlier than the lower/higher frequency components, respectively.

There exist different types of pulse envelopes, however, in our studies, we will mainly focus on *Gaussian pulses* and *hyperbolic secant pulses*.

If $C = 0$, these two types of envelopes can be defined respectively by:

$$A_{Gauss} = \sqrt{P_0} \left(-\frac{T^2}{2T_0^2} \right), \text{ with } T_0 = \frac{T_{FWHM}}{2\sqrt{2}} \quad (\text{Eq. I.40})$$

$$A_{Sech} = \sqrt{P_0} \operatorname{sech} \left(\frac{T}{T_0} \right), \text{ with } T_0 = \frac{T_{FWHM}}{2\ln(1+\sqrt{2})} \quad (\text{Eq. I.41})$$

In this case, the pulse has a null temporal phase and is said to be *transform limited*, experiencing the lower *time bandwidth product possible* (TBP). It can be calculated by:

$$TBP = T_{FWHM} \times \nu_{FWHM} \quad (\text{Eq. I.42})$$

with ν_{FWHM} the corresponding spectral full width at half maximum. For Gaussian pulses, the TBP is around 0.44, and for hyperbolic secant pulses $TBP \sim 0.315$.

If $C \neq 0$, linear chirp term will be introduced, and we obtain:

$$A_{Gauss} = \sqrt{P_0} \left(-\frac{T^2}{2T_0^2} \right) \times e^{-\frac{iCT^2}{2T_0^2}} \quad (\text{Eq. I.43})$$

$$A_{Sech} = \sqrt{P_0} \operatorname{sech} \left(\frac{T}{T_0} \right) \times e^{-\frac{iCT^2}{2T_0^2}} \quad (\text{Eq. I.44})$$

While complex dynamics are at play during nonlinear fiber propagation, these pulse parameters, along with the prior knowledge of the fiber properties, allows anticipating the predominant phenomena for selected initial conditions. Below, we provide an overview of such effects and their conditions of occurrence.

1.4.1. Dispersion regimes

As mentioned in section 1.2.1.1, the group velocity dispersion, or GVD, corresponding to frequency dependence of the group velocity, resulting in different propagation speeds for different frequency components. In a pure dispersive regime, this leads to temporal modifications in the pulse shape, affecting both its width and the decrease of the initial peak power as it propagates along the fiber. In this case, we can distinguish two regimes of dispersion:

- Normal dispersion ($\beta_2 > 0$): In this regime, the dispersion parameter D is negative, and the higher frequency components of the light propagate slower than the lower frequency components.
- Anomalous dispersion ($\beta_2 < 0$): In the opposite way, here the dispersion parameter D is positive, and the lower frequency components of the light propagate slower than the higher frequency components.

Figure I.11 shows the temporal evolution, of both the pulse intensity and phase, between the normal and anomalous regimes:

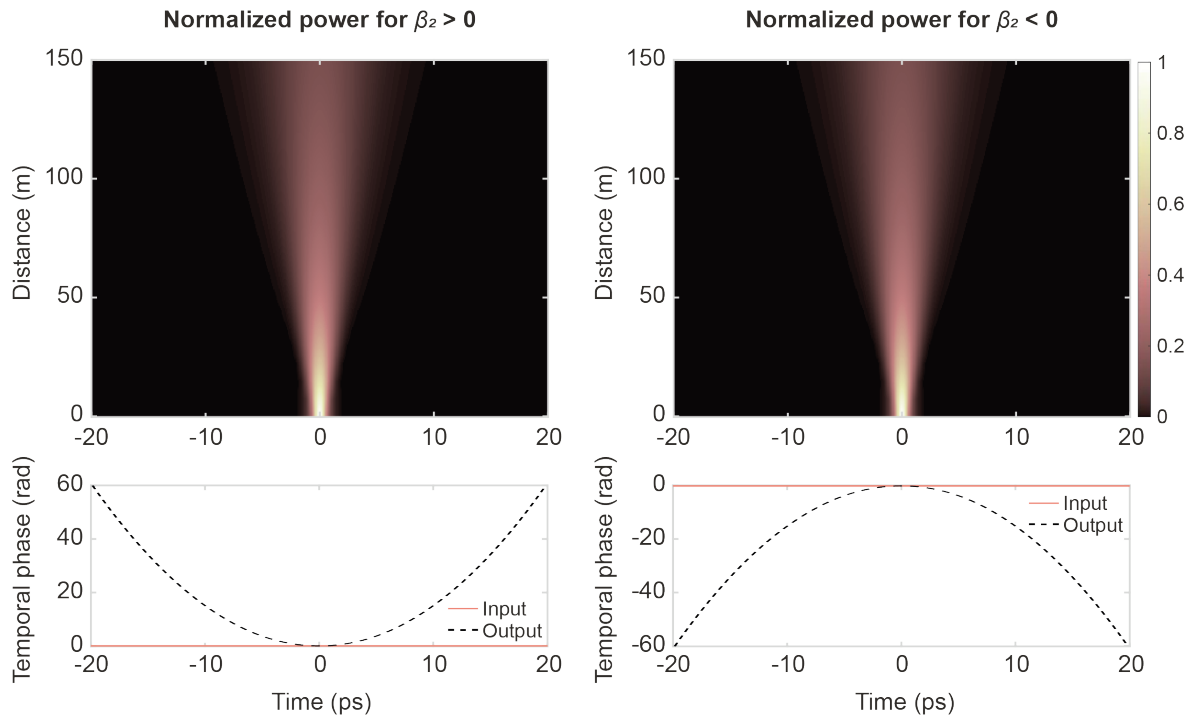


Figure I.11 Temporal evolution of the intensity profiles (top) and temporal phases (bottom) of a hyperbolic secant pulse with $T_0 = 1 \text{ ps}$ and $P_0 = 0.1 \text{ W}$, traveling within a 150 m - SMF with $\gamma = 3 \text{ W}^{-1} \cdot \text{km}^{-1}$ and $|\beta_2| = 21.8 \text{ ps}^2 \cdot \text{km}^{-1}$, considering only GVD dispersive effects, either in a normal dispersion regime (left) or in an anomalous dispersion regime (right).

As we can see, in both cases, the pulse broadens temporally and thus experiences a decrease of peak power, yet the intensity envelope is equally distorted regardless of the sign of β_2 . However, the sign of the quadratic phase accumulated via GVD (and the corresponding linear chirp parameter C) is directly related to the sign of β_2 .

Importantly, the impact of the GVD on the pulses depends on the sign of β_2 , and as a consequence, the interplay with nonlinear effects can exhibit very distinct behaviors during propagation.

I.4.2. On the balance between nonlinearity and dispersion – The soliton order

During nonlinear propagation, both nonlinear effects (due to SPM, and described by the nonlinear parameter γ) and chromatic dispersion (mainly GVD, represented by β_2), play a role in modifying the temporal and spectral shape of an optical pulse. Depending on the properties of the pulse (P_0 and T_0), either the nonlinear effects or the dispersive effects will dominate during the propagation.

For simplicity in assessing the magnitude of these effects, it is convenient to neglect the higher-order dispersion terms, attenuation and Raman scattering effects, so that to start with the standard NLSE (Eq. I.37). It is important to clarify that this simplified model does not fully describe the real case propagation scenarios such as the setup presented in the next chapters.

For instance, in our case, the initial pulse wavelength ($\lambda_0 \sim 1550 \text{ nm}$) is very close to the ZDW of the optical fiber considered ($\lambda_{ZDW} \sim 1525 \text{ nm}$ - see Figure I.6), and we thus have to take in consideration the dispersion introduced by β_3 , as well as the fiber loss, etc. However, using this simplified model allows reducing the NLSE in an adimensional form.

For convenience, and to study the different propagation regimes, it is important to introduce two terms describing the magnitude of linear and nonlinear effects in the NLSE:

$$\text{The dispersive length: } L_D = \frac{T_0^2}{|\beta_2|} \quad (\text{Eq. I.45})$$

$$\text{The nonlinear length: } L_{NL} = \frac{1}{\gamma_0 P_0} \quad (\text{Eq. I.46})$$

Starting from (Eq. I.37), and replacing $A(z, t)$ with $\sqrt{P_0} \psi(z, t)$, where $\psi(z, t)$ corresponds to a dimensionless pulse envelope, and considering the dispersion and nonlinear coefficients in function of L_D and L_{NL} , respectively, as $\beta_2 = \frac{T_0^2}{L_D}$ and $\gamma_0 = \frac{1}{L_{NL} P_0}$, we can rewrite the NLSE as:

$$\sqrt{P_0} L_D \frac{\partial \psi}{\partial z} + \frac{i \beta_2 L_D}{2 T_0^2} \sqrt{P_0} \frac{\partial^2 \psi}{\partial (T^2/T_0^2)} - i \gamma L_D P_0 \sqrt{P_0} |\psi|^2 \psi = 0 \quad (\text{Eq. I.47})$$

$$\frac{\partial \psi}{\partial (z/L_D)} + \frac{i \beta_2}{2 |\beta_2|} \frac{\partial^2 \psi}{\partial (T^2/T_0^2)} - i \frac{L_D}{L_{NL}} |\psi|^2 \psi = 0 \quad (\text{Eq. I.48})$$

By normalizing the distance $\zeta = z/L_D$, the time $\tau = T/T_0$, and introducing $N = \sqrt{\frac{L_D}{L_{NL}}}$, the NLSE then reduces to:

$$\frac{\partial \psi}{\partial \zeta} + i \frac{\text{sign}(\beta_2)}{2} \frac{\partial^2 \psi}{\partial \tau^2} - i N^2 |\psi|^2 \psi = 0 \quad (\text{Eq. I.49})$$

Under some circumstances, the GVD and nonlinear effects can interact and give rise to different phenomena, depending on the sign of β_2 .

In the normal dispersion regime, where $\beta_2 > 0$, these nonlinear and dispersive effects have the same sign in (Eq. I.49) and can act together in a so-called *self-defocusing NLSE regime*. These effects can be used, among others, for pulse compression, optical wave breaking, shock formation or the formation of so-called dark solitons [57].

In the anomalous dispersion regime, where $\beta_2 < 0$, these nonlinear and dispersive effects exhibit different signs in (Eq. I.49) can therefore act in an adverse manner and/or balance themselves in this a so-called *self-focusing NLSE regime*. These phenomena can include modulation instability (see section I.5.2) or the formation of bright solitons as discussed below.

In particular, linear and dispersive effects can exactly balance each other in (Eq. I.49) when $N = 1$. In this case, a hyperbolic secant pulse, given in (Eq. I.41), will form a *soliton pulse* [58],

where the shape of the pulse remains unchanged in frequency and time domains over long distances (see section I.5.1). For this reason, N is usually defined as a *soliton number*, where:

$$N^2 = \frac{L_D}{L_{NL}} = \frac{\gamma_0 P_0 T_0^2}{|\beta_2|} \quad (\text{Eq. I.50})$$

This variable typically provides the number of solitons that can be ejected from a single pulse, but also yields a metric to assess the interplay between linear and nonlinear effects along an optical fiber of length L .

For this specific case where a *fundamental soliton* is generated when $N = 1$, we indeed have a perfect balance between these effects so that $L_D = L_{NL}$.

More generally these effects can have different roles in the propagation dynamics, and we can usually distinguish two regimes:

- $N \ll 1$, in this case, we have $L_D \ll L_{NL}$ and the nonlinear effects will be negligible compared to the dispersion. The pulse will mainly be distorted due to the GVD effect by experiencing a temporal broadening (see section I.4.1) when the propagation length L is equal or superior to L_D .
- $N \gg 1$, in this case, we have $L_{NL} \ll L_D$, and the dispersive effects will be negligible compared to the nonlinearity. The pulse will predominantly experience SPM (see section I.2.2.1), where the pulse nonlinear phase leads to spectral broadening when the propagation length L is equal or superior to L_{NL} .

When the nonlinear and dispersive effects are such that $L \ll L_D$ and $L \ll L_{NL}$, both effects can be ignored, and the pulse will eventually lose optical power and progressively vanish through attenuation (when considering a non-conservative NLSE).

Conversely, if $L < L_D$ and $L < L_{NL}$, both the nonlinear and dispersive effects need to be considered and can lead to a variety of nonlinear phenomena in fiber optics.

I.5. Examples of nonlinear phenomena in a self-focusing NLSE regime

In the anomalous dispersion regime (i.e. self-focusing NLSE), which will be the focus of this manuscript, modulation instability and the formation of optical solitons are of particular interest for our studies and we provide below a succinct overview of these phenomena and their principles.

I.5.1. Optical solitons

I.5.1.1. Fundamental solitons

As briefly mentioned in section I.4.2, solitons (here implicitly referring to bright solitons) are a special type of nonlinear waves occurring in the anomalous dispersion regime. They exhibit a remarkable ability to propagate without any temporal or spectral deformation, maintaining their shape over long propagation distance [59]. Their resilience to temporal distortion due to dispersion or spectral reshaping via SPM arises from the delicate balance between these effects:

When $\beta_2 < 0$, the self-focusing nonlinearity counteracts the dispersion-induced spreading, resulting in a stable pulse which phase-induced chirp remains constant during propagation. The first-order soliton, also known as the *fundamental soliton*, corresponds to a hyperbolic

secant pulse (Eq. I.41) whose pulse power and duration satisfies the condition $N = 1$ (so that $L_D = L_{NL}$). At the fiber propagation onset ($\zeta = \zeta_0 = 0$), this yields the following initial conditions on the pulse envelope:

$$A(0, \tau) = \text{sech}(\tau) \quad (\text{Eq. I.51})$$

In Figure I.12, we can see the propagation of the fundamental soliton in both frequency and time domains along the length of a SMF with $\beta_2 = -21.8 \text{ ps}^2 \cdot \text{km}^{-1}$, $\beta_3 = 0.012 \text{ ps}^3 \cdot \text{km}^{-1}$, and $\gamma = 3 \text{ W}^{-1} \cdot \text{km}^{-1}$

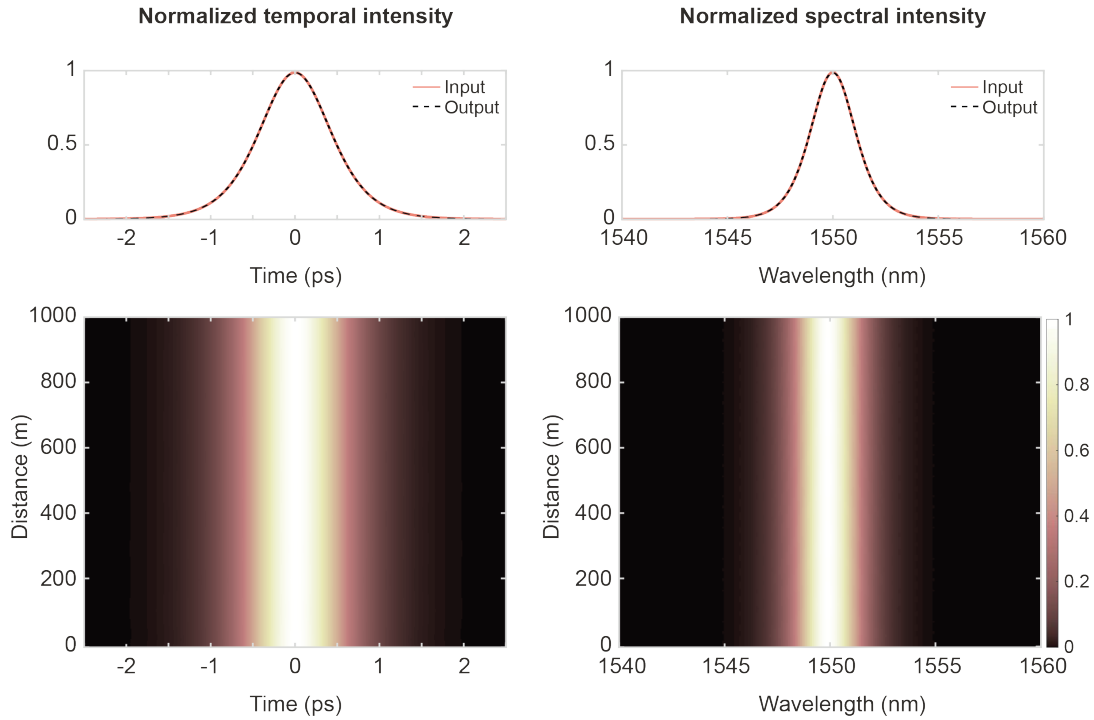


Figure I.12 Temporal (bottom left) and spectral (bottom right) evolution of a fundamental soliton with a peak power $P_0 = 22.58 \text{ W}$, $T_0 = 1 \text{ ps}$, propagating along a SMF with $L = 1 \text{ km}$. The normalized temporal and spectral intensity profiles are shown in the top panel indicating the superposition between the input (red) and output (dashed black).

I.5.1.2. Higher-order solitons

When the soliton number is larger so that $N > 1$, we talk about high-order solitons. These complex pulse structures also exhibit a long-range propagation without strong deformation but rather evolve periodically in the temporal and spectral domains. In this case, the initial conditions for the generation of such higher-order solitons becomes:

$$A(0, \tau) = N \text{sech}(\tau) \quad (\text{Eq. I.52})$$

where N is an integer and correspond to the order of the soliton.

As can be seen in (Eq. I.50), the soliton number is dependent on the peak power P_0 , which means that for the same pulse duration T_0 , we can obtain higher soliton orders by merely increasing the input power. The dynamics of these solitons are associated with a variation of the phase term of the pulse depending on ζ , leading to a periodic behavior generated from the interplay between GVD and nonlinear effects. In normalized units, this interplay exhibits a period equal to $\zeta_0 = \frac{\pi}{2}$, which yields, in real units:

$$z_0 = \zeta_0 L_D = \frac{\pi T_0^2}{2 |\beta_2|} \quad (\text{Eq. I.53})$$

This periodic behavior is clearly illustrated in Figure I.13, where we show the spectro-temporal evolution of a second-order soliton ($N = 2$) and a third order-soliton ($N = 3$) in function of the distance using a 100 m - SMF.

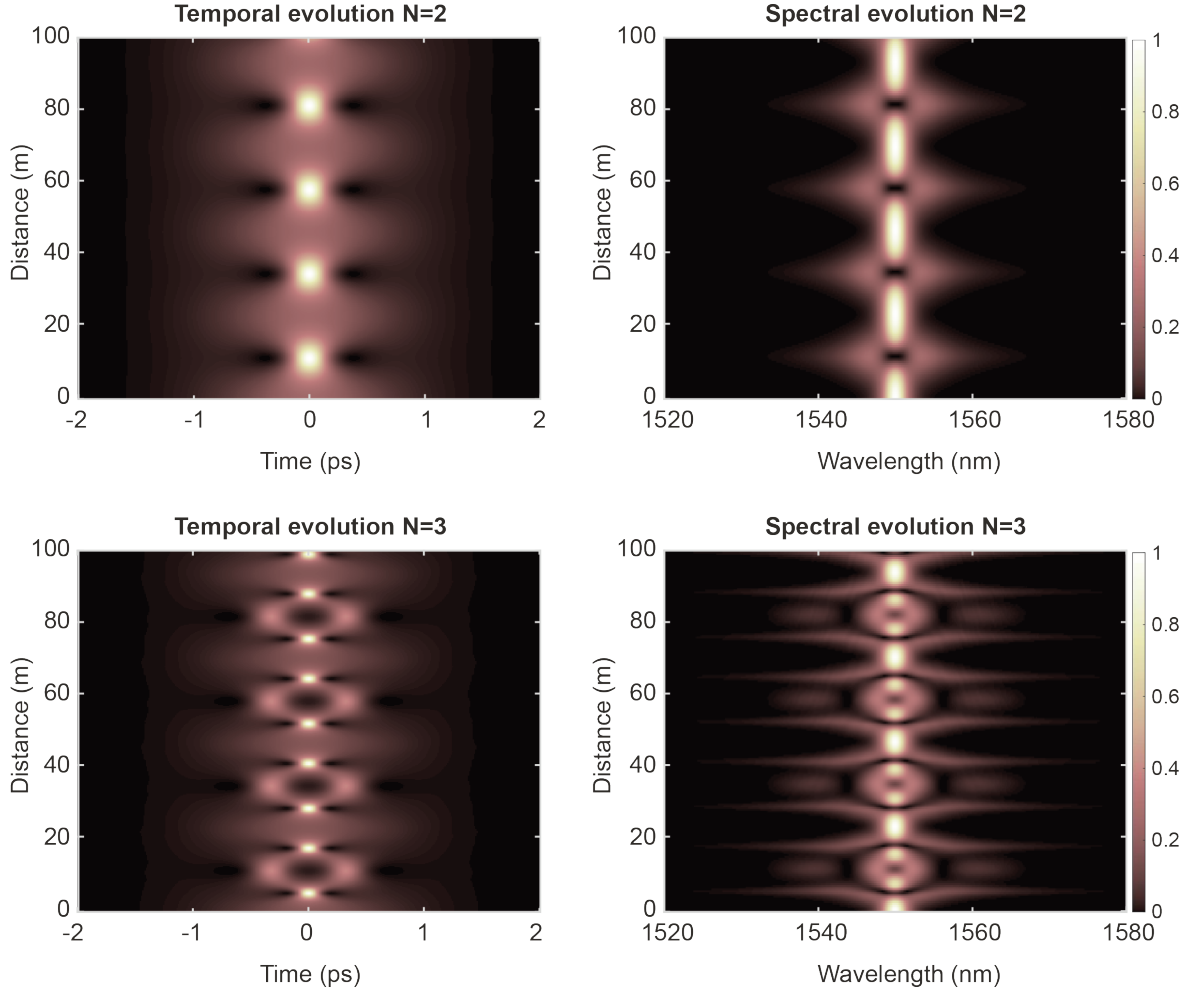


Figure I.13 Temporal and spectral evolution (top) of a second-order soliton and (bottom) of a third-order soliton with a temporal width $T_0 = 1$ ps and a peak power of $P_0 = 90.32$ W and $P_0 = 203.22$ W, respectively.

I.5.1.3. Soliton fission and self-frequency shift:

So far, we have considered soliton dynamics in an ideal NLSE framework. However, for realistic experimental conditions, one needs to consider a full GNLSE framework including higher-order dispersion terms and Raman scattering effect.

These terms are known to “break” the symmetry of the NLSE and destroy the ideal periodic evolution of higher order solitons (see Figure I.14). In this case, when a high-order soliton is temporally compressed (so that the pulse is the broadest spectrally and more subject to higher order dispersion and Raman effects), it breaks into several fundamental solitons during a process called *soliton fission* [60], [61]. The location of the breaking is directly related to the periodicity of higher-order solitons given in (Eq. I.54) and identified by the *fission length*:

$$L_{fiss} \sim \frac{L_D}{N} \quad (\text{Eq. I.54})$$

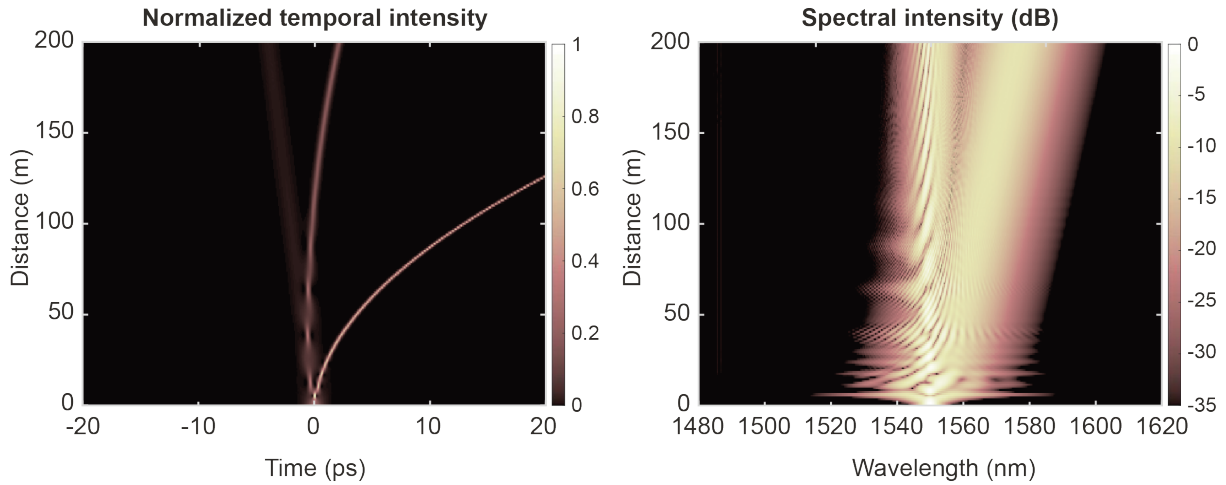


Figure I.14 Soliton fission in the temporal and spectral domains for the same soliton illustrated in Figure I.13 ($N = 3$), using the GNLSE, and a fiber length $L = 200 \text{ m}$.

In this case, once ejected from the initial pulse, the fundamental solitons experience a spectral shift to higher wavelengths (see Figure I.15).

This latter phenomenon is known as *soliton self-frequency shift* (SSFS) and arise when the spectral bandwidth of a soliton is sufficiently large to spectrally overlap (at least partially) with its own Raman gain region (see section I.2.2.2).

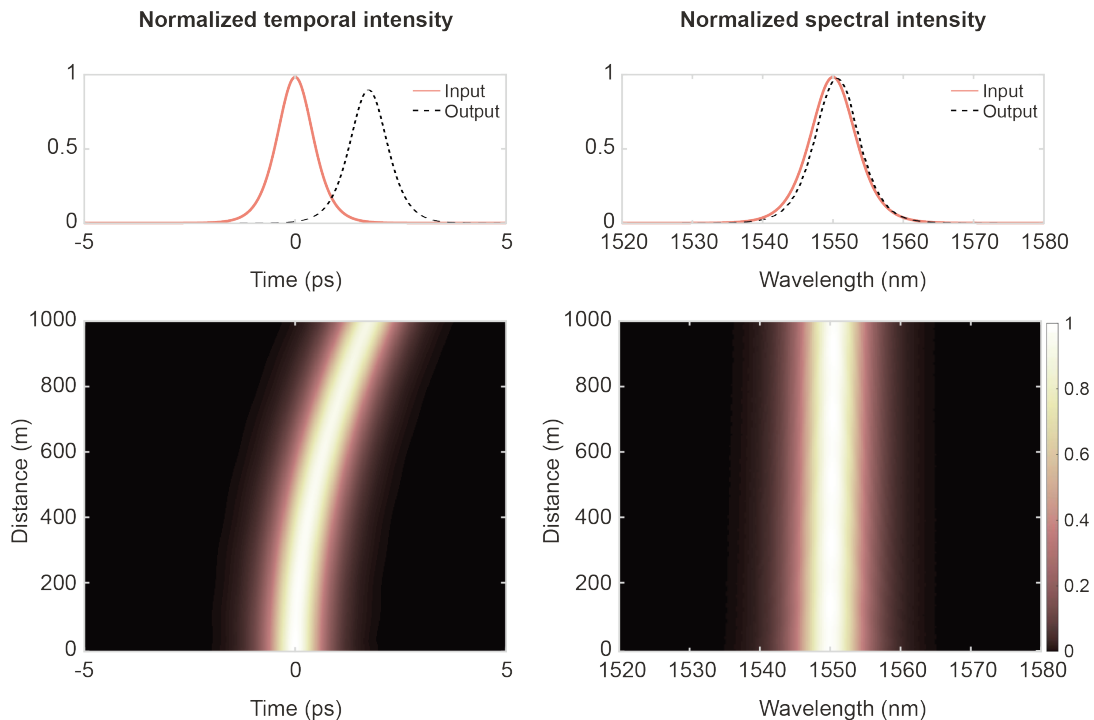


Figure I.15 Soliton self-frequency shift process of the fundamental soliton represented in Figure I.12, using the GNLSE and a fiber length of $L = 1 \text{ km}$.

In this case, the soliton can sustain “self” stimulated Raman scattering leading to a progressive energy transfer to the lower wavelengths side of the spectrum (i.e. Stokes scattering) without destroying the soliton (that remains relatively robust to these perturbations). This length-

dependent spectral shift is visible in Figure I.15, and associated with a progressive temporal delay gained by the red-shifted soliton as it propagates within the fiber at a lower speed (i.e. anomalous dispersion regime).

Analytically, when considering fundamental solitons with different power-duration relations to fulfill the condition $N = 1$, the spectral shift acquired as a function of distance for different soliton can be approximated by [62]:

$$\frac{dv}{dz} \propto \frac{|\beta_2|}{T_0^4} \quad (\text{Eq. I.55})$$

Importantly, the different nonlinear and dispersive effects responsible for pulse broadening, in addition to soliton fission and SSFS, can collectively contribute to the generation of an exceptionally broad spectrum known as a supercontinuum, and further discussed in section I.6. In addition, it is worth noting that the formation of solitons not only can be obtained from the process described above but can also arise from both coherent and noise-driven processes yielding the temporal compression of a pulse or the formation of highly-localized structures (that may ultimately lead to soliton fission). A typical nonlinear process well-known in fiber optics to trigger this type of dynamics is the phenomenon of *modulation instability* (MI), which will constitute a key element of this manuscript and that we introduce succinctly below.

I.5.2. Modulation instability (MI)

To understand modulation instability, we first have to introduce the *four-wave mixing process* (FWM). When two waves with different frequencies ω_1 and ω_2 , interact in a Kerr nonlinear medium, the intensity-dependent refractive index modulation leads to a periodic variation of this index. This modulation, combined with the dispersive effects of the material, can result in an energy transfer process between these frequencies, into the energy of two new waves at ω_3 and ω_4 . According to the conservation of energy, the total energy of the system before and after the interaction remains constant following the conditions:

$$\omega_1 + \omega_2 = \omega_3 + \omega_4 \quad (\text{Eq. I.56})$$

This condition describes a so-called *non-degenerate FWM* [45]. In fact, FWM is a crucial concept of nonlinear optics that not only depends on the frequencies but also the *phase matching* condition (associated with momentum conservation). This process refers to the condition where the relative phases of the interacting beams involved align in such a way that constructive interference occurs and the FWM remains efficient over longer distances. When the phase matching condition is satisfied, we get the following:

$$\phi_1 + \phi_2 = \phi_3 + \phi_4 \quad (\text{Eq. I.57})$$

Similar to this, *degenerate FWM* can also occur. In this case, the first two propagating waves have the same frequency and are considered as the pump wave ($\omega_1 = \omega_2 = \omega_p$). The pump interacts twice in the FWM process and creates two new frequencies on both sides of the pump (ω_{pos} and ω_{neg}), introducing the involvement of only three distinct frequencies following the condition.

$$2\omega_p = \omega_{pos} + \omega_{neg} \quad (\text{Eq. I.58})$$

This phenomenon is also denominated *three-wave* mixing (TWM) in the literature [63], [64]. However, it should not be confused for a second-order nonlinear process only involving three waves and typically occurring in $\chi^{(2)}$ nonlinear crystals.

In this framework, modulation instability can be described as a degenerate FWM occurring in the anomalous dispersion regime ($\beta_2 < 0$) of a fiber. Simply put, the conversion of the pump generates two symmetrical sidebands that will grow exponentially during propagation in the fiber.

To gain insight in the underlying physics of MI, one can start by considering a small perturbation with an amplitude a_{mod} on an initial signal $A(z, t) = \sqrt{P_0}e^{i\phi(z,t)}$ and get a total signal $A(z, t) = (\sqrt{P_0} + a_{mod}(z, t))e^{i\phi(z,t)}$. By replacing with the NLSE equation we obtain:

$$i \frac{\partial}{\partial z} a_{mod}(z, t) - \frac{\beta_2}{2} \frac{\partial^2}{\partial t^2} a_{mod}(z, t) + \gamma P_0 (a_{mod}(z, t) + a_{mod}^*(z, t)) = 0 \quad (\text{Eq. I.59})$$

In the frequency domain by introducing the wave number k and the frequency of the perturbation ω_{mod} , Eq I.59 can be resolved giving the dispersion relation [24]:

$$k^2 = \frac{\omega_{mod}^2 \beta_2^2}{4} \left(\omega_{mod}^2 + \frac{4\gamma P_0}{\beta_2} \right) \quad (\text{Eq. I.60})$$

Which means that:

$$k = \frac{|\beta_2 \omega_{mod}|}{2} \sqrt{\omega_{mod}^2 + \text{sign}(\beta_2) \frac{4\gamma P_0}{|\beta_2|}} \quad (\text{Eq. I.61})$$

As we can see the Eq I.61 depends on the sign of β_2 . In the case of normal regime ($\beta_2 > 0$), k is real and the signal travelling through the fiber is stable against all perturbations and maintains its shape. On the other hand, when $\beta_2 < 0$, we encounter the anomalous dispersion regime, and the wave number becomes imaginary for $|\omega_{mod}| < \frac{4\gamma P_0}{\beta_2}$ leading an unstable solution describing the modulation instability phenomenon and the perturbation can grow exponentially, leading to an unstable solution, which describes the modulation instability phenomenon where the perturbations grow exponentially during propagation.

Typically, MI can be explained by considering the TWM truncation of a continuous wave $A_0(z, t)$, interacting with a modulating wave (with a frequency ω_{mod}). In this case, the initial field can be defined as:

$$A(z, T) = A_0(z, T) + A_1(z, T)e^{-i\omega_{mod}T} + A_2(z, T)e^{+i\omega_{mod}T} \quad (\text{Eq. I.62})$$

This approximation is explained with the assumption that the modulation is very weak regarding the pump, so this latter can be considered as undepleted. In this case, one can find the gain of the MI resolving the degenerate FWM equations with $|A_1|, |A_2| \ll |A_0|$ (see section I.5.2.3).

However, for a simple description of modulation instability, three main parameters should be introduced as illustrated in Figure I.16:

- The frequency cutoff $\omega_c = \sqrt{\frac{4\gamma_0 P_0}{|\beta_2|}}$, refers to a critical frequency detuning below which modulation instability can occur, or in other words, it sets a threshold for the onset of MI, depending on the parameters of the fiber and the input power of the pump.
- The MI gain $G_{MI}(\omega_{mod}) = |\beta_2 \omega_{mod}| \sqrt{\omega_c^2 - \omega_{mod}^2}$. When the modulation frequency $\omega_{mod} < \omega_c$, it experiences exponential growth as it propagates through the medium. The MI gain is a measure of how much the modulation's amplitude increases as it travels within the fiber and is given in km^{-1} .
- The maximum gain frequency $\omega_{max} = \frac{\omega_c}{\sqrt{2}}$, is the modulation frequency at which the highest gain of the instability is observed.

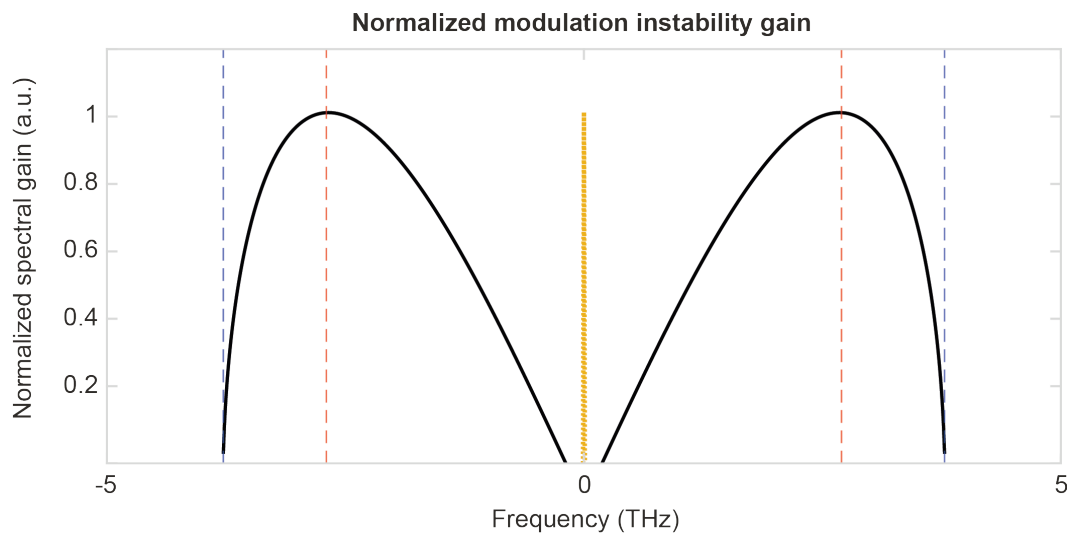


Figure I.16 Modulation instability gain in the frequency domain, calculated for the HNLF fiber used in our studies with $\beta_2 = -1.78 ps^2.km^{-1}$; $\gamma = 8.4 W^{-1}.km^{-1}$ with $P_0 = 30 W$. The frequency cutoff ω_c (in blue) and the maximum gain frequency ω_{max} (in red) are also presented.

I.5.2.1. Induced MI regime

In a regime of modulation instability, when adding a weak modulation into the pump (with a modulation frequency localized within the gain region of the MI), the modulation sidebands grow exponentially during the first stage of propagation to eventually lead to spectral broadening due to modulation instability [65].

This process is called *induced MI* regime and is illustrated in Figure I.17. Starting with a weak modulation on a continuous wave (CW), we see how the weak discrete sidebands (symmetric around the pump) start to grow in the spectral domain along with the modulation of the CW in the temporal domain [66]. With enough power and sufficient propagation, the newly-created frequencies will, in turn, act like a pump within additional FWM conversion, thus generating a *cascaded MI* process [67]. As seen in Figure I.17, cascaded MI leads to the formation of a periodic train of highly localized pulses.

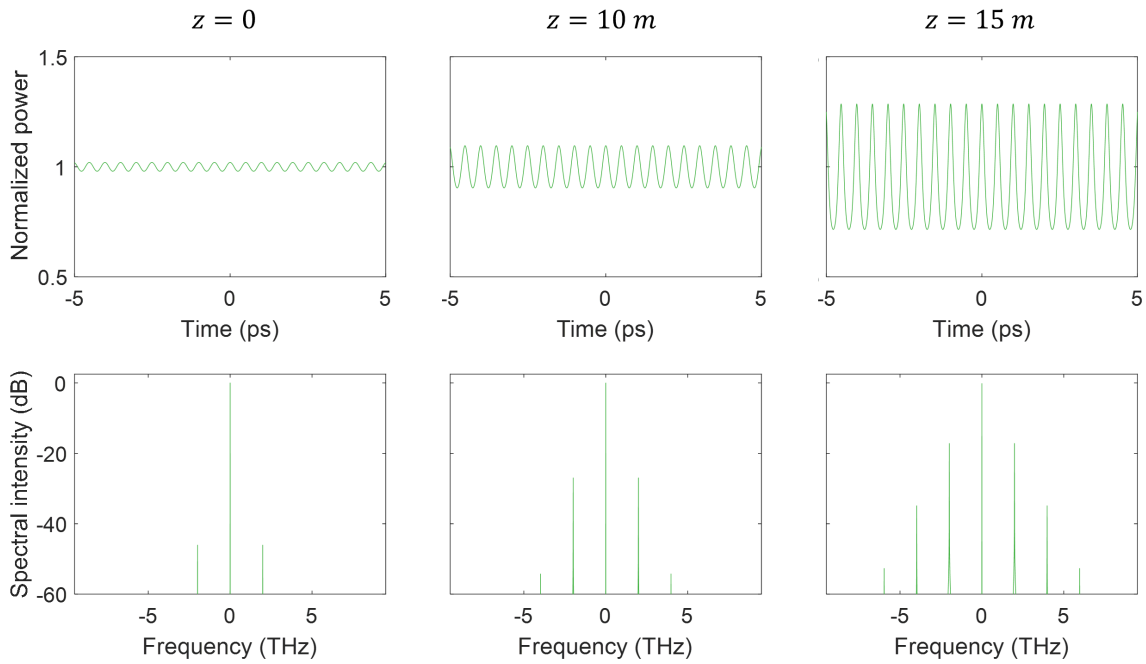


Figure I.17 Induced modulation instability process occurring due to the addition of a weak modulation on a CW pump as described in (Eq. I.58). The temporal intensities are illustrated after propagation in the HNLF in the top panels at different distances ($z = 0, z = 10 \text{ m}, z = 15 \text{ m}$) normalized with respect to the CW input power $P_0 = 20 \text{ W}$, and the spectral intensities are shown in the bottom panels. The 2 THz modulation here has a magnitude equal to 1% of the CW signal.

I.5.2.2. Spontaneous MI regime

Another important aspect of modulation instability is related to what is usually called *spontaneous MI*. Even without any external modulation, when a CW pump is slightly noisy, the frequency components of the noise already existing in the system (or even the vacuum noise) that overlap with the MI gain bandwidth can be amplified as they propagate through the fiber [68]. In this case, the amplification of the noise occurs spontaneously over the whole MI gain region, rather than being driven by a specific modulation, and leads to the formation of broadband MI sidebands.

This noise-driven process is illustrated in Figure I.18, where we observe the formation of broadband MI sidebands in the spectrum, accompanied by weak random modulation of the CW signal in the temporal domain. Similar to the induced MI regime, when the noisy spontaneous MI sidebands become strong enough, a MI cascading process can occur, leading to the formation of localized structures in the time domain.

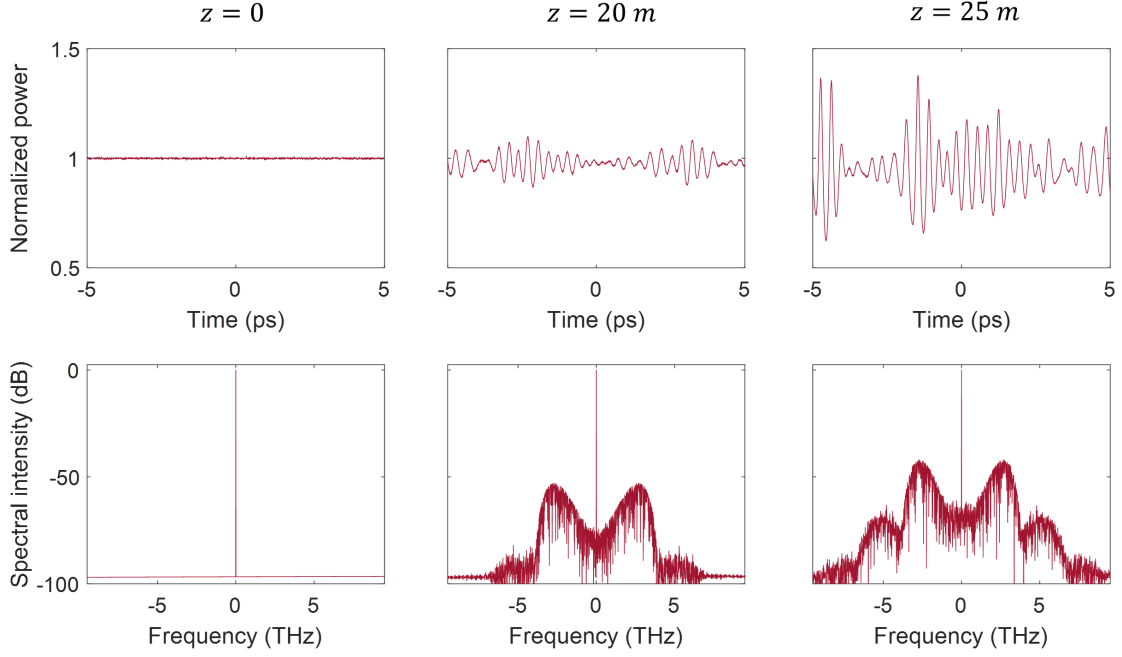


Figure I.18 Spontaneous modulation instability process occurring due to the MI amplification of a white noise of 3 photons per spectral mode $n_{noise} = 3$ [62] during the propagation of a CW pump in the HNLf fiber. The temporal intensities are illustrated after propagation in the HNLf in the top panels at different distances ($z = 0, z = 20 \text{ m}, z = 25 \text{ m}$) normalized with respect to the CW input power $P_0 = 30 \text{ W}$, and the spectral intensities are shown in the bottom panels.

I.5.2.3. Other frameworks for the description of MI

Modulation instability extends its influence across various scientific domains, from optics to hydrodynamics and plasma physics. It showcases the universal applicability of common physical principles in understanding complex phenomena. In hydrodynamics, the Benjamin-Feir instability is well-known mechanism that can explain the formation of rogue waves on deep water [69]. Such waves are characterized by their immense size and steepness; they appear instantly and disappear just as quickly. Modulation instability has also been demonstrated in plasma physics with the formation of Langmuir waves [70]. In such process, as in optics and hydrodynamics, the NLSE remains a fundamental tool for modeling the phenomenon of modulation instability.

For example, in the case of degenerate four-wave mixing, we can use the NLSE to resolve the propagation of a signal $A(z, T)$ with three fields and describe analytically the MI and degenerate FWM process obtained between a pump and generated sidebands.

$$A(z, T) = A_0(z)e^{ik_0z} + A_1(z)e^{ik_1z}e^{-i\omega_{mod}T} + A_2(z)e^{ik_2z}e^{+i\omega_{mod}T} \quad (\text{Eq. I.63})$$

With $k_0, k_1,$ and k_2 the corresponding propagation constants of the three complex fields A_0, A_1 and $A_2,$ respectively. By substituting (Eq. I.63) in the NLSE given in (Eq. I.37), we obtain the following set of equations [24], [71]:

$$\begin{cases} -i \frac{dA_0}{dz} = \gamma(|A_0|^2 + 2|A_1|^2 + 2|A_2|^2)A_0 + 2\gamma A_1 A_2 A_0^* e^{i\Delta kz} \\ -i \frac{dA_1}{dz} - \frac{1}{2} \omega_{mod}^2 \beta_2 A_1 = \gamma(|A_1|^2 + 2|A_2|^2 + 2|A_0|^2)A_1 + \gamma A_2^* A_0^2 e^{-i\Delta kz} \\ -i \frac{dA_2}{dz} - \frac{1}{2} \omega_{mod}^2 \beta_2 A_2 = \gamma(|A_2|^2 + 2|A_1|^2 + 2|A_0|^2)A_2 + \gamma A_1^* A_0^2 e^{-i\Delta kz} \end{cases} \quad (\text{Eq. I.64})$$

Where $\Delta k = k_1 + k_2 - 2k_0$.

By considering $A_i = b_i(z)e^{i\phi_i(z)}$, with $i = \{0,1,2\}$, we can obtain a general solution:

$$\begin{cases} \frac{d\phi_0}{dz} = \gamma(\phi_0^2 + 2\phi_1^2 + 2\phi_2^2) + \gamma\phi_1\phi_2\cos\phi \\ \frac{d\phi_1}{dz} - \frac{1}{2} \omega_{mod}^2 \beta_2 = \gamma(\phi_1^2 + 2\phi_2^2 + 2\phi_0^2) + \gamma\phi_2\phi_0^2\cos\phi \\ \frac{d\phi_2}{dz} - \frac{1}{2} \omega_{mod}^2 \beta_2 = \gamma(\phi_2^2 + 2\phi_1^2 + 2\phi_0^2) + \gamma\phi_1\phi_0^2\cos\phi \\ b_0 \frac{d\phi_0}{dz} = -2\gamma b_1 b_2 b_0^2 \sin\phi \\ \frac{db_1}{dz} = \gamma b_2 b_0^2 \sin\phi \\ \frac{db_2}{dz} = \gamma b_1 b_0^2 \sin\phi \end{cases} \quad (\text{Eq. I.65})$$

where $\phi = \Delta kz + \phi_1 + \phi_2 + 2\phi_0$, is the phase mismatch between the initial signal and the sidebands generated by the added modulation. These equations allow us to study the energy exchange between the pump and the generated sidebands and achieve a phase matching depending on the initial phase.

In the case of MI, we can also consider using these equations the approximation of the truncated TWM model (with the undepleted pump). In this case, the maximum growth rate of the sideband occurs when the nonlinear phase-matching condition is met. Such approximation, provide a simplified framework describing an ideal FWM model and it has been demonstrated and manipulated experimentally [72]. When pump depletion effects become non-negligible, the frequency detuning required for phase matching shifts towards lower values. When the pump depletes, its independence with the wave-vector matching increases. Consequently, what was initially a phase-matched interaction gradually becomes mismatched as power is transferred to the sidebands. This effect is particularly relevant in the strong-interaction regime [63], [73]. TWF truncation was also studied by considering different analytical approaches based on Floquet theory and compared with the NLSE [74] to study the behavior of a complex nonlinear system involving MI and Fermi-Pasta-Ulam (FPU) recurrence [75].

In addition, a powerful analytical framework based on Akhmediev breather theory [76] have been developed over the years to describe MI evolution in a realistic context beyond the ideal FWM approximation. The theory, introduced over 30 years ago, consider all the MI sidebands (without truncation) and describe a class of *soliton on a finite background* (SFB) providing perfect analytic solutions to the self-focusing NLSE in a regime associated with modulation instability [68], [77].

In this case, three different types of SFBs with different behavior can be identified (i.e. Akhmediev breathers, Peregrine solitons, and Kuznetsov-Ma breathers) and their first experimental observations where reported over the last years in fiber optics [78].

To describe these three dynamics, we can introduce two main parameters related to the gain properties of the previously explained MI:

$$a = \frac{1}{2} \left(1 - \frac{\omega_{mod}^2}{\omega_c^2} \right) \quad (\text{Eq. I.66})$$

$$b = \sqrt{8a(1-2a)} \quad (\text{Eq. I.67})$$

By using the simplified NLSE (Eq. I.37), a general solution to analytically describe these SFB can be introduced [78] as:

$$\psi(\zeta, \tau) = \left[1 + \frac{2(1-2a) \cosh(b\zeta) + ib \sinh(b\zeta)}{\sqrt{2a} \cos(\omega\tau) - \cosh(b, \zeta)} \right] e^{i\zeta} \quad (\text{Eq. I.68})$$

Depending on the value of the parameter a , different exact solutions can be obtained, and further illustrated in Figure I.19:

- **Akhmediev breathers:** This type arises when the parameter a falls within the range of $0 < a < 0.5$ (i.e. the MI gain region). It initiates with a continuous wave with a weak modulation that progressively amplifies during propagation to form a highly spatially localized but periodic temporal structure. Upon further propagation, the pulse train return to its initial state thus illustrating the FPU recurrence phenomenon associated with MI.
- **Peregrine soliton:** This prediction describes a limit case of the Akhmediev breathers. When $a \rightarrow 0.5$, the solution evolves by taking energy from the background to generate form a peak with an intensity nine times higher than the background. In this scenario, the Peregrine soliton exhibit both temporal and spatial localization simultaneously.
- **Kuznetsov-Ma breathers:** When $a > 0.5$, the breathers evolve periodically along the fiber, and possess a localization in time (i.e. the opposite of Akhmediev breathers). This case corresponds to a modulation falling outside the MI gain region, and a limit case when the spatial period tends to infinity is equivalent to the fundamental soliton described above in section I.5.1.1.

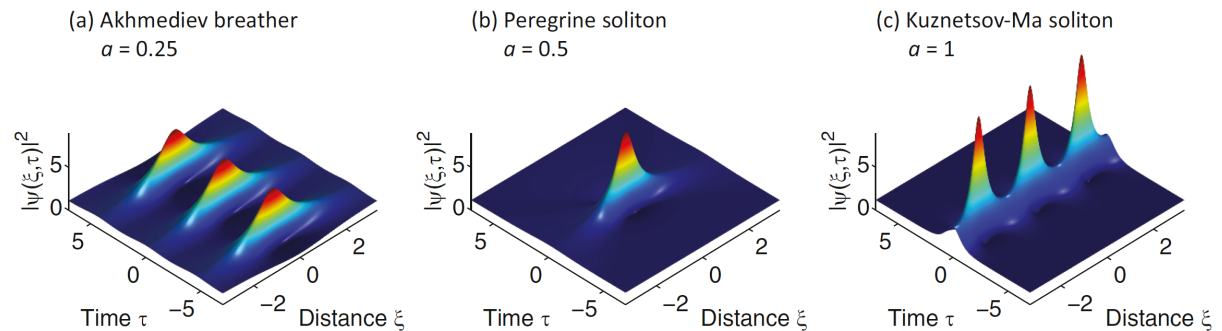


Figure I.19 Numerical simulation of the SBF: (a) Akhmediev breather; (b) Peregrine soliton; (c) Kuznetsov-Ma soliton. Reproduced from [78].

Although these SFB correspond to ideal solutions of the NLSE in the presence of a weak modulation (i.e. induced MI regime), this powerful analytical framework can also be used in a noise-driven MI regime. In particular, the propagation of CW or long pulses (i.e. quasi-CW

regime) is known to yield the formation and breathing of randomly localized pulses, as illustrated in Figure I.20:

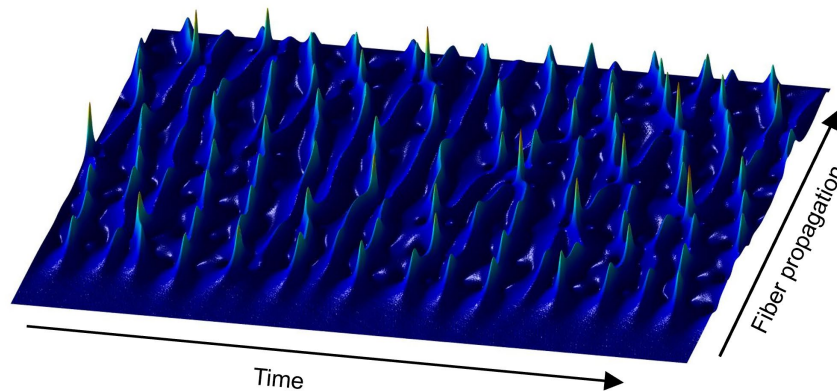


Figure I.20 Formation of randomly localized pulses during spontaneous MI (noise-driven) evolution of a CW signal of a 5 W peak power, within an 8 km-SMF in the temporal domain. The x-axis represents the time, and the y-axis represents the distance.

The formation of such localized structures can also be analyzed as the spontaneous appearance of breathers and their collision [77], [79] and the appearance of extreme events formation, also termed *optical rogue waves* [80], [81].

Indeed, as they form randomly and temporally compress through propagation, these structures can break to form solitons and subsequently drive spectral broadening as discussed in section I.5.1.3.

In case of extreme spectral broadening, we usually refer to the process of supercontinuum formation, which is briefly discussed in the next section.

Interestingly, the stochastic appearance of these pulses during propagation and associated spectral broadening dynamics sensitive to initial noise conditions have been a field that received a considerable attention over the recent years [76], [82].

An in-depth analytic study of MI and associated dynamics falls outside the scope of the work reported in this manuscript. However, in this thesis, we will here use modulation instability as an experimental testbed for advanced characterization techniques of elusive spectral fluctuations in Chapter III as well as the control and optimization of MI fluctuating properties reported in Chapter IV.

I.6. Supercontinuum (SC) generation

As briefly mentioned above, we usually refer to *supercontinuum generation* (SCG) for describing the generation of an extremely broadband spectrum from nonlinear effects.

Since the early observation of SCG in bulk media and liquids [5], [83], [84], supercontinuum in optical fibers was reported in 1976 by Lin & Stolen [6]. In fiber optics, this typically occurs when injecting an optical pulse with a sufficiently high pump power into the fiber where the dispersion and nonlinear effects create new frequencies to generate the supercontinuum, as illustrated in Figure I.21.

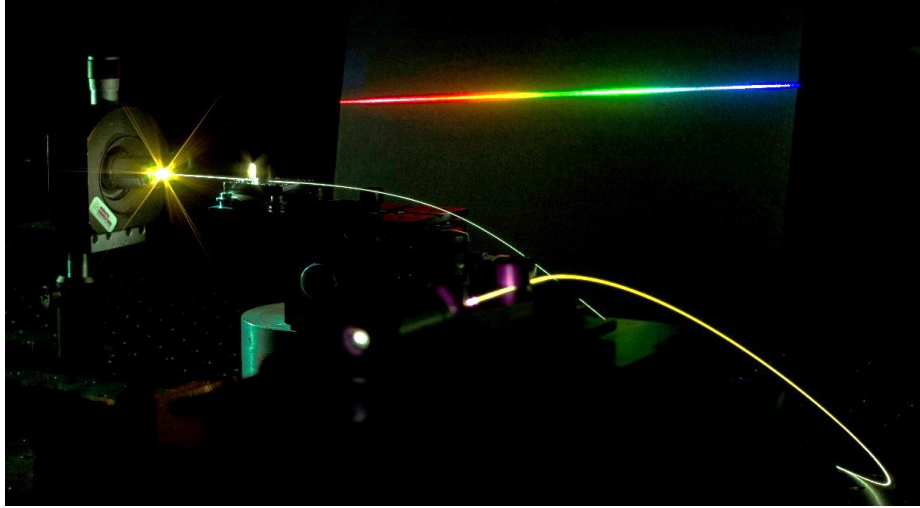


Figure I.21 Photography of a visible supercontinuum generated via nonlinear fiber propagation. We observe a progressive shift of pulse color towards the white as new frequencies are generated during propagation, which is dispersed at the fiber output to form a rainbow spectrum. Credits: B. Wetzel.

However, SCG is a complex phenomenon, as it involves the interplay of complex nonlinear and dispersive phenomena. In fact, SCG is influenced by various factors, including the properties of the input pulse, the fiber structure, and the pumping conditions [62]. Over the years, researchers have explored different regimes of supercontinuum generation, ranging from ultrashort pulses [85], [86] to continuous wave sources [87], [88], and have investigated the effects of nonlinearity and dispersion in both normal and anomalous regimes. Clearly, the choice of the pumping wavelength (and associated pulse properties) plays a crucial role in determining both the temporal and spectral characteristics of the supercontinuum. Here, we provide a quick overview of the key aspects to consider for SC generation.

I.6.1.1. Concept of spectral coherence

The SC can exhibit noisy characteristics due to various phenomena such as stimulated Raman scattering and modulation instability. These effects introduce stochastic noise into the SC generation process that can be further amplified during nonlinear propagation.

These noise effects can usually be modeled within the GNLSE framework by performing Monte-Carlo simulations and adding a random input noise seed that will slightly change the form of the SC in each simulation. This allows us to investigate how fluctuations in the input pulse and during propagation influence the intensity and phase stability of the output SC.

To study the stability of the SC, one can introduce the concept of coherence that can be readily measured via a metric termed *first order coherence* (or mutual coherence) [62], [89]. This metric can be used to measure the pulse-to-pulse intensity and phase stability in the SC. From numerical simulations, it can be obtained from different Monte-Carlo supercontinuum output spectra, respectively generated from different input noise conditions.

The equation for coherence $g^{(1)}(\lambda, t_1 - t_2)$ between two different fields is given by:

$$|g^{(1)}(\lambda, t_1 - t_2)| = \frac{\langle E_1^*(\lambda, t_1)E_2(\lambda, t_2) \rangle}{\sqrt{\langle |E_1(\lambda, t_1)|^2 \rangle \langle |E_2(\lambda, t_2)|^2 \rangle}} \quad (\text{Eq. I.69})$$

The angular brackets denote an ensemble average taken over a large number of simulations considering different combinations of supercontinuum with complex electric fields E_1 and E_2 .

When measuring the spectral coherence, one typically considers $g^{(1)}(\lambda, 0)$ at zero delay so that:

$$|g^{(1)}(\lambda, 0)| = \frac{\langle E_1^*(\lambda, 0)E_2(\lambda, 0) \rangle}{\sqrt{\langle |E_1(\lambda, 0)|^2 \rangle \langle |E_2(\lambda, 0)|^2 \rangle}} \quad (\text{Eq. I.70})$$

In addition, averaging over the whole spectrum wavelengths can be performed to obtain a representative measure of the SC coherence and ensuring that the statistical variations are representative of the overall behavior of the supercontinuum generation process. In this case, when $g^{(1)} = 1$ we have a perfect coherence, and when $g^{(1)} = 0$, the spectrum is entirely incoherent.

I.6.1.2. SC generation in the normal dispersion regime

Supercontinuum generated in a normal dispersion regime, also called ANDi (*All-Normal Dispersion*) supercontinuum, typically lead to highly coherent SC but however features limited bandwidth (for a given power budget). It is important to note that the assumption that normal SC is inherently coherent is not entirely true and is subject to specific constraints on the input pulse parameters. The generation of normal SC involves the interaction of various nonlinear phenomena besides SPM. Particular care must be taken with the stimulated Raman scattering and four-wave mixing, due to their contributions to the incoherence of the SC [62].

Optical wave breaking (OWB) occurs in the normal dispersion regime where the pulse is mainly distorted due to GVD. Additionally, due to SPM, the power dependence of the pulse's phase, induces a non-monotonic instantaneous frequency, resulting in an oscillation during spectral broadening. In the distorted pulse resulting from these two phenomena, the instantaneous frequency maxima are at the pulse center, while the corresponding pulse tails possess lower instantaneous frequency-induced chirp. Due to the different propagating speeds at both tails, the pulse progressively overlaps with two components with different instantaneous frequencies in the temporal domain which is what is commonly defined as optical wave breaking [90].

To understand the generation of SC in the normal dispersion regime, we define the wave-breaking length L_{WB} [90] which helps us understand the role of OWB in the formation of coherent SC and the length L_C at which the coherence of the pulses exceeds 0.9:

$$L_{WB} = 1.1 \frac{L_D}{N} \quad (\text{Eq. I.71})$$

$$L_C = L_R^*/L_{WB} \quad (\text{Eq. I.72})$$

where L_R^* is the characteristic length at which the parametric Raman gain becomes significant and induces a loss of coherence in the generated SC.

Based on the values of N and the temporal duration of the pulse (FWHM), spanning from the femtosecond regime to longer pulses or even continuous waves (CW), one can characterize the generation of normal dispersion SC into three main regimes [91]:

- 1- $T_{FWHM} < 1 \text{ ps}$ ($N < 400$): In this regime, the SC is primarily generated by SPM and OWB. Here, L_{WB} is very small due to the short pulse width, resulting in high coherence. On the other hand, L_C is very large, and the SC exhibits good coherence but a relatively narrow bandwidth.

- 2- $1 \text{ ps} < T_{FWHM} < 1.5 \text{ ps}$ ($400 < N < 600$): In this regime, L_C decreases rapidly and intersects with L_{WB} . The intersection point corresponds to the maximum achievable coherent bandwidth in the SC, highlighting the significant role of the fiber length in designing the SC.
- 3- $T_{FWHM} > 1.5 \text{ ps}$ ($N > 600$): In this regime, the overall coherent bandwidth and the length at which coherence occurs decrease due to the presence of incoherent OWB. This occurs for long and CW pulses, where L_C becomes larger than L_{WB} .

I.6.1.3. SC generation in the anomalous dispersion regime

To obtain an optimal bandwidth, supercontinuum generation in the anomalous dispersion regime has been extensively studied over the years, particularly for ultrashort pulses (femtosecond regime) which can also provide good SC coherence properties. This regime is commonly achieved by operating at wavelengths close to or above the ZDW, as illustrated in Figure I.22.

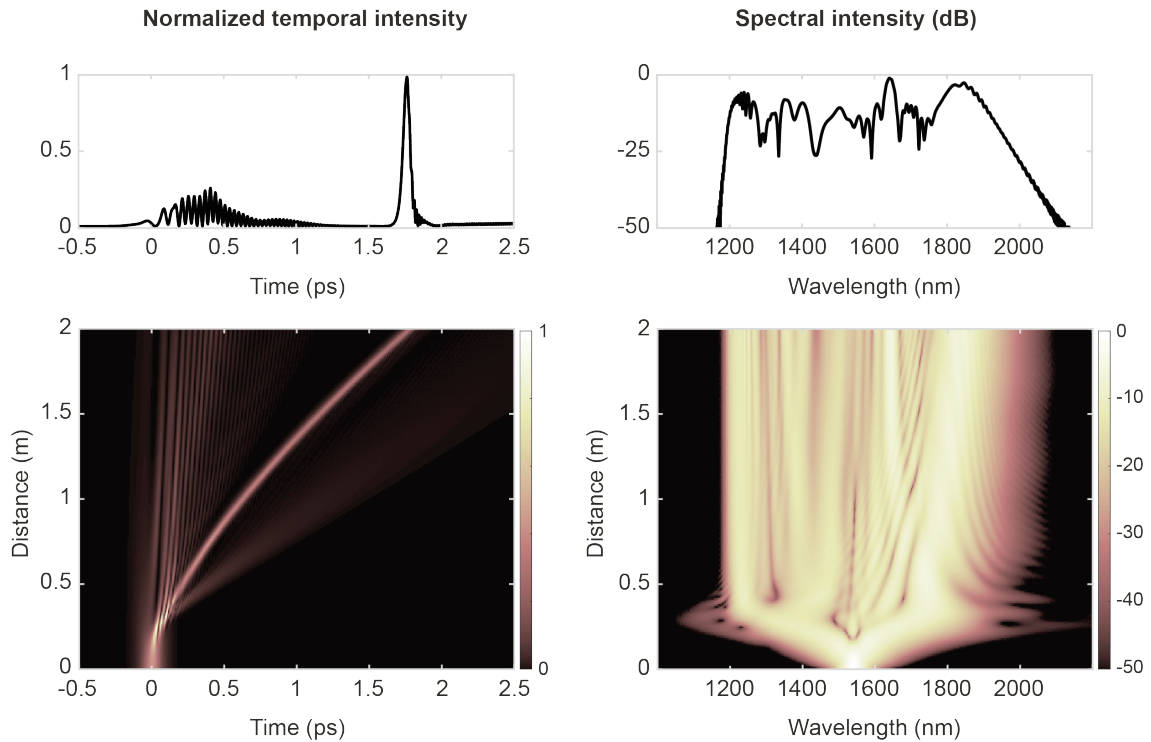


Figure I.22 Example of coherent supercontinuum generated in the anomalous dispersion from a 100 fs input pulse with $P_0 = 3 \text{ kW}$ propagating in our HNLf with $\beta_2 = -1.78 \text{ ps}^2 \cdot \text{km}^{-1}$, $\beta_3 = 0.07 \text{ ps}^3 \cdot \text{km}^{-1}$, $\gamma = 0.008 \text{ W}^{-1} \cdot \text{km}^{-1}$, and represented for a length $L = 2 \text{ m}$.

Firstly, to achieve the highest bandwidth SC, it is necessary to inject a short pulse close to the ZDW, so that the first phenomenon typically occurring is SPM. After initial spectral broadening, the pump propagating in the presence of perturbations (such as Raman effects and higher-order dispersion) breaks apart, thus generating a soliton-fission process. In addition, when pumping close to the zero-dispersion wavelength, the soliton can transfer some of its energy resonantly to spectral components known as *dispersive waves* (DWs), located in the normal dispersion regime of the fiber [62]. Dispersive waves are here associated with the stabilization of the fundamental solitons that are ejected during the fission process.

As the initial pulse breaks into multiple solitons, the energy distribution among them creates a spectral imbalance leading to the emission of DWs contributing to the overall spectral

broadening of the supercontinuum. In this regime, we can ensure a high degree of coherence when the pulse spectra broadens quickly enough to overlap with the modulation instability gain spectrum before significant noise amplification occurs, which corresponds to a case where $N < 16$. By limiting the soliton order ($N < 10$) deterministic soliton fission dominates the dynamics, leading to a controlled spectral evolution that can maintain coherence [62].

When considering longer pulses (so that $N > 16$), SC generation is strongly affected by modulation instability. In this case, as explained in section 1.5.2.2, the initial noise in the system will get amplified and generate spontaneous MI sidebands that drive the onset phase of SC spectral broadening. Contrary to the case of femtosecond pulses, where the pulse fission and dispersive waves occur in a predictable manner dictated by the GNLSE equations and the specific parameters of the system, here, the fission process is influenced by stochastic factors associated with the initial noise in the system. This introduces randomness and variability into the outcome of the pulse fission. Even for identical input pulses, different realizations considering different initial noise seeds can lead to variations in the resulting dynamics and output spectrum. The presence of noise leads to a variety of possible outcomes, resulting in a range of spectral features and intensity distributions in the supercontinuum. In this context, we talk about an incoherent (or quasi-coherent) SC.

In this context, it is important to note that the stochastic spectral fluctuations obtained due to the existing noise in the system might not be easily observed in experiments using e.g. optical spectral analyzers with limited resolution and long integration times. To suitably analyze these fluctuations, we discuss in Chapter II and Chapter III, different approaches to detect shot-to-shot fluctuations and perform real-time measurements of broadened output spectra after nonlinear propagation.

In this chapter, we saw that spectral broadening and supercontinuum generation are highly influenced by the initial conditions of both the input pulse and the fiber properties, leading to different propagation regimes and nonlinear dynamics discussed above. Therefore, a thorough understanding and control of these initial properties are crucial in manipulating the nonlinear propagation dynamics efficiently.

By studying and comprehending the interplay between initial conditions and noise-induced fluctuations, we can effectively harness and optimize nonlinear processes for various applications. These findings thus highlight the significance of precise control and thorough characterization in the generation and applications of supercontinuum sources.

Chapter II. Ultrafast pulse control and characterization

Being able to study and manipulate the characteristics of an optical pulse, or even ultrashort laser pulses, is at the core of our studies. It allows generating and tailoring different nonlinear dynamics in fiber optics and therefore manipulate the resulting output waveform. In this chapter, we explore the behavior of optical pulses in both the time and frequency domains within the framework of the Fourier transform, particularly the principle of frequency-time duality which we briefly introduce in **Section II.1**.

To control the pulse properties, we must understand their critical role in the nonlinear spectral broadening dynamics. Different techniques and approaches can be used to adjust the pulse's width, shape, and phase. In **Section II.2** we introduce the strong dependence of the spectral and temporal parameters of an input laser pulse on the spectral broadening after nonlinear propagation in optical fiber. We discuss different tools commonly used to mold the input pulse properties in both domains, and specifically focus on the instruments we will be using in this thesis for our experimental studies.

To obtain finely tuned broadband spectra and adaptable nonlinear dynamics for optimal results, we dive into the realm of machine learning. Optimization algorithms and machine learning strategies complement the pulse control methods to predict the propagation behavior based on the chosen initial parameters and employ "smart" and optimized strategies to automatically select the correct pulse properties for a given objective. **Section II.3**, provides an overview of machine learning, encompassing learning methods, algorithms, applications, and their growing significance in ultrafast optics. Evolutionary algorithms, especially genetic algorithms, take a central stage in these discussions and are explained in further detail as they constitute the predominant algorithms used in our studies.

However, to control these properties, we must first be able to accurately measure the pulses or the optical waveforms of interest. This procedure may not always be easy, especially for ultrafast pulses. Efficient characterization techniques then become indispensable in the pursuit of generating and monitoring pulses with tailored properties. In **Section II.4.**, different methods for optical waveform measurements are introduced and detailed, such as autocorrelation and the Frequency-Resolved Optical Gating (FROG) technique. The latter can for instance provide a complete characterization of the pulse by retrieving both the intensity and phase profiles of the optical signal. In addition, for real-time detection, we introduce the dispersive Fourier-transform (DFT) technique which is of paramount importance for the characterization of fluctuating optical waveforms. Here, we describe its principle and ability to reveal hidden spectral features and patterns in incoherent signals, thus proving critical in e.g. noise analysis and supercontinuum generation stability monitoring.

II.1. Time-frequency duality in the Fourier transform

To study the properties of a pulse and gain insight into its behavior within a nonlinear medium, the Fourier transform is a fundamental tool, essential to understand and model optical fiber propagation (see section I.3.3). This concept revolves around comprehending the interplay between a pulse's characteristics in the time and frequency domains, recognizing their dual nature and their intrinsic link. As succinctly described in Chapter I, any modification in one domain can drastically influence the pulse's properties in the other domain (and thus impact its evolution dynamics).

The *Fourier transform* (FT) [92] is a mathematical tool that allows us to analyze a function or a signal in both the time and frequency domains. It maps the signal from the time domain to the frequency domain, providing a representation of the signal in terms of its frequency components, and revealing valuable information about its spectral content [93]. In this case, the Fourier transform of a signal in the time domain is denoted as F , and defined as:

$$FT(f) = F(\omega) = \int_{-\infty}^{+\infty} f(t)e^{-i\omega t} dt \quad (\text{Eq. II.1})$$

Where $f(t)$ represents the signal as a function of time t , and ω is the frequency variable (here displayed as a pulsation where $\omega = 2\pi\nu$).

Conversely, we call *inverse Fourier transform*, the relation that allows us to go from the frequency domain back to the time domain. The inverse Fourier transform of a signal $F(\omega)$ in the frequency domain, denoted as $f(t)$, is given by:

$$FT^{-1}(F) = f(t) = \frac{1}{2\pi} \int_{-\infty}^{+\infty} F(\omega)e^{i\omega t} d\omega \quad (\text{Eq. II.2})$$

This equation demonstrates how the inverse Fourier transform reconstructs the original signal in the time domain from its frequency components.

The symmetry between the time and frequency domains in the Fourier transform gives rise to a concept known as time-frequency duality. Mathematically, this duality property can be expressed as the following:

$$\begin{aligned} f(t) &\leftrightarrow F(\omega) \\ F(t) &\leftrightarrow 2\pi f(-\omega) \end{aligned}$$

Here, as $f(t)$ represents the temporal signal, $F(\omega)$ represents its Fourier transform in the frequency domain. If we form a new function of time that has the functional form of the transform $F(t)$, it will have a Fourier transform $f(\omega)$ that has the functional form of the original time function (function of frequency). The factor of 2π and the negative sign in the duality relationship arise from the mathematical properties of the Fourier transform. This duality is of great significance in signal analysis and processing, allowing us to gain insights into the spectral characteristics of the pulse by examining its time domain representation (and vice-versa).

Ultrafast optical pulses are examples of signals that can be exploited to illustrate the concept of time-frequency duality [94], [95]. Similar to diffractive optics, in the spatial domain, where the far-field (Fraunhofer) diffraction pattern corresponds to the Fourier transform of the near-field, this time-frequency duality can also be leveraged for advanced pulse processing and monitoring in ultrafast photonics.

During my thesis, I essentially worked with ultrafast pulsed lasers, characterized by their extremely short duration ranging from a few picoseconds down to a few tens of femtoseconds.

In this case, the Fourier transform provides a powerful tool for analyzing and understanding these pulses properties, allowing to obtain valuable information about their spectral content and temporal profile with the best possible measurement techniques.

This time-frequency duality allows us to observe modifications in the pulse's profile in both domains and enable to retrieve, study and modify its properties that can be otherwise difficult (e.g. limited resolution of detectors in the time or frequency domain, retrieval of the pulse phase based on dual intensity observables, etc.).

For example, manipulating the pulse's spectrum using techniques like spectral filtering, or modulations have a direct impact on the pulse temporal profile: In Figure II.1, we recall and represent different examples of how an optical pulse can be manipulated in both temporal and spectral domains. When working with a continuous wave (CW) signal, we obtain a *Dirac* in the spectral domain (see Figure II.1.a) centered at a desired frequency. If this initial signal is then affected by an external temporal modulation, it will generate new frequencies in the spectral domain such as the symmetric sidelobes shown in Figure II.1.b. The complex spectrum obtained this way can then be reshaped in amplitude and phase by spectral filtering as displayed in Figure II.1.c.

This can be used to reshape the spectrum and obtain different spectral profiles (e.g. Lorentzian, Gaussian spectrum) but also to induce changes in the pulse's shape (e.g. Gaussian or Sech pulses) or duration (i.e. decrease the pulse temporal width). While trivial, this property is particularly important in our work and will be used frequently in the next chapters as it allows controlling the initial pulse parameters before nonlinear propagation in optical fibers.

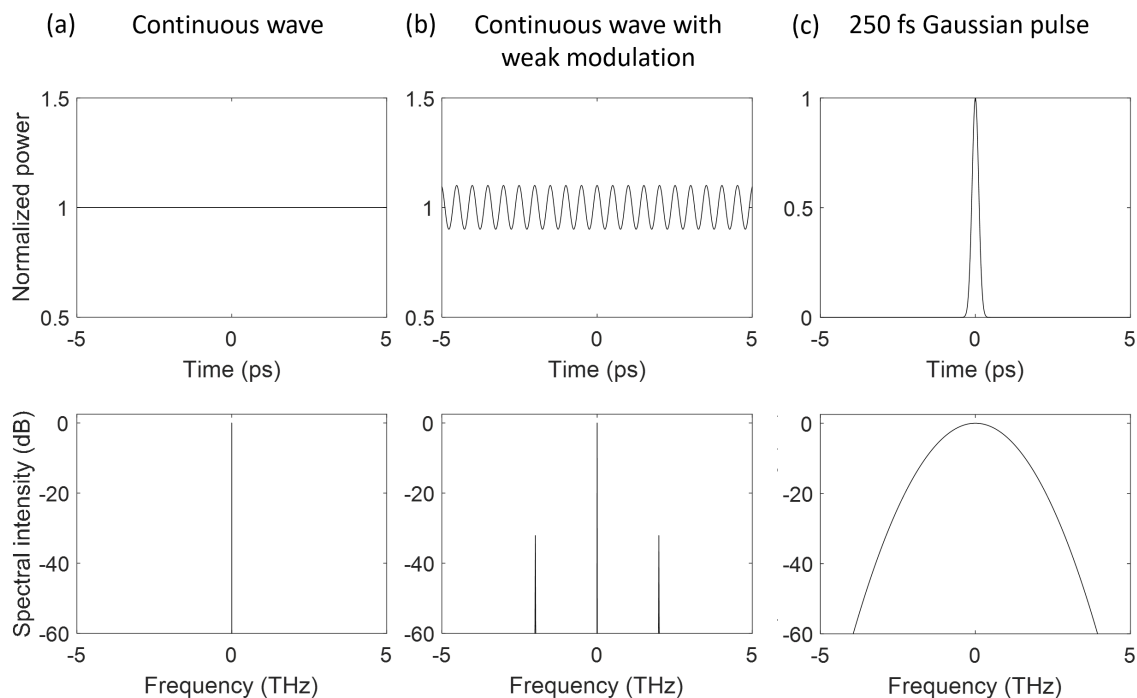


Figure II.1 Representation in the temporal domain (top panel) and the spectral domain (bottom panel) of a (a) continuous wave; (b) continuous wave with a 2 THz modulation added to the initial pulse with a magnitude equal to 1% of the CW signal; (c) a 250 fs Gaussian pulse.

It is important to note that the phase of a pulse plays an important role in its behavior in both the temporal and spectral domains. When we consider different spectral phases applied to the same pulse, we may find modifications in its temporal waveform. When the phase is constant across the pulse's spectrum, the pulse experiences no change, maintaining its original characteristics and a stable intensity profile. However, when the phase is of first order (linear

spectral phase), it introduces a time-dependent phase shift across different frequencies. While in this case, the temporal and spectral widths of the pulse remain the same, we observe a translation of the pulse along the time axis (i.e. a temporal delay). When the spectral phase is quadratic the pulse is “chirped” and also yields to a quadratic temporal phase. As already mentioned in section I.4, the chirp can be either positive (leading edge with shorter wavelength) or negative (leading edge with longer wavelengths). The pulse will then experience a temporal broadening. Of course, other higher-order phase variations exist, such as the cubic phase, related to the third-order dispersion of the pulse (TOD). This type of phase causes variations in the pulse's intensity over time and leads to temporal distortions, resulting in oscillations or asymmetry in the pulse shape.

Understanding the impact of the phase on the overall pulse properties is crucial in this research work. Being able to alter and adjust both the intensity and phase on the input pulse provides an additional degree of control to customize nonlinear fiber propagation dynamics, and thus tailor the output waveform characteristics [96], [97].

In consideration of the above, we can deduce that while time-frequency duality provides a powerful tool for monitoring and understanding optical signal properties, it is important to take into account the technical constraints and compromises associated with controlling or characterizing the pulse properties in either the spectral or the temporal domain.

For example, in the time domain, optical detectors and modulators often have finite bandwidths, which limit their ability to capture and manipulate ultrafast optical pulses. This limited speed in the time domain can lead to challenges in accurately characterizing or shaping pulses with extremely short durations. On the other hand, the limited spectral resolution of signal processing and characterization tools in the Fourier domain (i.e. frequency) make it difficult to monitor or modify long pulses with very narrow optical bandwidth. Thus, an inherent trade-off often arises, where the precision of time localization is balanced against the extent of frequency resolution, making it necessary to choose between the direct and indirect domains for optimal pulse processing and monitoring.

II.2. On the control of optical wavepacket properties

Supercontinuum generation and nonlinear spectral broadening dynamics are strongly dependent on the input parameters of the laser pulse, the fiber material, and the fiber structure. To adjust the properties of the output waveform, it is thus necessary to manipulate these initial system parameters. However, it appears clearly unpractical to change the fiber and/or modify the entire setup every time that the output spectrum/signal need to be tuned. Instead, we can manipulate the input pulse properties to achieve the desired spectral and temporal properties of the output optical signal.

In this manuscript, we only consider single-mode fiber propagation and employ several techniques to adjust the spectro-temporal properties of the input pulse in order to regulate the various nonlinear processes and dynamics responsible for spectral broadening. However, to access even more degrees of freedom, one can also consider the spatial dimension by working with multimode optical fibers that allow manipulating and controlling complex multidimensional nonlinear dynamics [98], [99], [100], [101]. In MMFs, each spatial mode has distinct nonlinear and dispersive properties, and all modes are optically coupled, allowing for intricate various intermodal nonlinear interactions. This property can pave the way to fine-tuning the characteristics of the output beam and adjusting interdependent parameters for optimal beam shaping for target applications. This particular topic falls outside of the scope of this

manuscript. However, such an approach is currently being studied within our project team with the goal of generating complex pulses and adjust their temporal, spectral, and spatial characteristics (see Figure. 1 in the Introduction). In such a case, the methods detailed below and developed within this thesis are expected to be readily transposed to a MMF framework.

Here, we work only in a single spatial mode context by exploring the frequency and time domains, directly related to each other through the Fourier transform. However, even in this case, the focus should take in consideration what we want to study, and which properties of the pulse and/or spectrum we would like to modify. Below, we provide an explanation of the importance of pulse shaping and the different techniques that can be applied in both spectral and temporal domains.

II.2.1. Spectral control of optical pulse properties

Being able to control the spectral properties of an ultrafast laser pulse allows us to manipulate light's compositions and enhance functionalities and performances. Whether it is bandwidth control, frequency centering, or spectral shaping, mastering these parameters opens the door to innovation in numerous technological domains. For example, by tailoring the spectral properties, higher data transmission rates, and improved signal-to-noise ratio could be achieved for fiber optic telecommunication applications, accurate identification and analysis of various materials and compounds can be found in spectroscopy, and even in laser-based manufacturing processes, tailored spectral profiles drive advances in precise and adjustable machining [93], [102], [103]. Spectral shaping is thus one of the most used methods to exert control over a broadband output spectrum generated after nonlinear propagation [104]. However, controlling the spectral properties of an input laser pulse before nonlinear propagation in an optical fiber allows for tailoring a wide variety of nonlinear processes, changing the dynamics of the propagation, and enabling the generation of distinct output waveforms with different spectral properties. This is due to the intricate interplay between the dispersion, nonlinearity, and attenuation that exists within the fiber. For instance, in the case of modulation instability, the peak power of the input pulse has a direct effect on the gain spectrum of the MI following the relation $\omega_c = \sqrt{\frac{4\gamma_0 P_0}{|\beta_2|}}$, where ω_c is the cut-off frequency of the MI gain spectrum [24] – see Chapter I.

From this equation, increasing the peak power of the initial pulse leads to a spectral broadening of the MI gain region, but also a shift of the location of maximal MI gain (and thus an overall change of the MI sidebands growth). In this case, the creation of significant sidebands can occur to yield the formation of a highly unstable spectrum – see Chapter I. One of the simplest ways to adjust the power of a pulse without affecting its other properties is to use an optical attenuator that introduces optical loss into the signal path, thus reducing the pulse's power level. Alternatively, one can boost the pulse's power by passing it through an amplifier. However, the latter may induce nonlinear and dispersive pulse distortion and further subject the pulse to *amplified spontaneous emission* (ASE) [24], [105], [18]. Such a broadband ASE noise is generated by the amplifier, and can significantly influence the nonlinear propagation dynamics, especially at high amplification powers.

To illustrate this property, we represent in Figure II.2 the spectrum of a 30 ps Gaussian laser pulse centered at 1550.65 nm (in red). When launched with a peak power of 2.5 W into 485 m of HNLF (with $\beta_2 = 1.78 \text{ ps}^2 \cdot \text{km}^{-1}$ and $\gamma_0 = 8.4 \text{ W}^{-1} \cdot \text{km}^{-1}$), we can see how the nonlinearity and dispersion drive a MI process within the fiber, leading to a broadened output spectrum

with cascaded sidebands formation on both sides of the pump (in blue). When decreasing the input peak power to 2 W and 1.5 W, the MI gain decreases resulting in a less significant spectral broadening. Furthermore, as we saw in (Eq. I.43) and (Eq. I.44), we also consider different laser pulse profiles. Gaussian pulses are commonly used for theoretical modeling (as generated from active mode-locking and electro-optic modulators – see below). However, if one for instance uses a hyperbolic secant pulse with the same bandwidth and power as the Gaussian pulse, a slightly broader MI spectrum will be obtained.

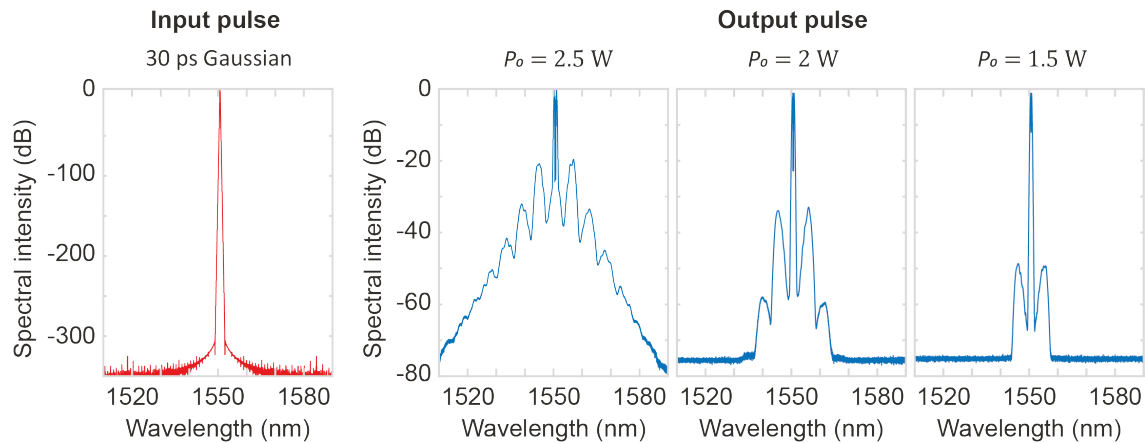


Figure II.2 Comparison between an input Gaussian pulse (in red) with the corresponding output spectra after traveling in the HNLF with different input peak powers decreasing from $P_0 = 2.5$ W to $P_0 = 2$ W and $P_0 = 1.5$ W.

There already exist numerous approaches for modifying the properties of laser pulses, each with their own advantages and limitations. In the spectral domain, these methods modify the frequency components and are typically pre-set and do not involve extensive tunability once the pulse parameters are defined.

Such a technique involves the use of a fiber Bragg grating (FBG). This method can be accomplished by sending the pulse into an optical fiber constructed in a periodic structure that allows specific wavelengths to be reflected and transmit all the others. These FBG filters can be used to reshape the pulse spectrum and tune the spectral properties of the pulse. A shift in the FBG central wavelength can be obtained by selecting the desired periodicity of the gratings.

In addition, it can be set up to obtain a desired laser pulse shape and width by pulse stretching or/and compression using a chirped fiber Bragg grating, or can be combined with other techniques to modulate the spectral phase and the chirp of the pulse [106], [107], [108], [109].

Similar to FBG, we can also add interferometer filters in this section. Such optical filters exploit several types of interference effects, such as Fabry-Perot interferometers, Mach-Zehnder interferometers, and Sagnac interferometers [110], [111], [112]. These filters work by creating an interference pattern of reflections between two reflected surfaces, a waveguide with two parallel arms, and a single-lopped fiber optic structure, respectively.

The interference pattern can be used to selectively attenuate particular wavelengths, thereby filtering the spectrum of the input laser pulse and thus adjusting the pulse temporal shape, depending on the function of the interference filter such as bandpass filters, notch filters, or high-pass or low-pass filters. However, these filtering approaches present a very limited tunability (e.g. Fabry-Perot filters can be slightly tilted to adjust the resonance wavelength) and can hardly be stacked without significant attenuation, thus hindering their scalability.

In a similar framework, liquid crystal (LC) optical filters have been used over the years for various applications and integrated into a wide range of photonic components. These filters can function as light transmission modulators, allowing specific wavelengths to pass through while blocking others [113], [114]. They typically consist of a stack of liquid crystals sandwiched between two polarizers. By applying a different voltage to the LC cells, we can tune the transmitted wavelength by changing their orientation and alter the transmission of the light passing through the filter at different wavelengths, allowing the filter to transmit the selected wavelength and blocking the others. However, these filters can suffer from high transmission loss due to the series of polarizers. Other approach includes, optical stretchers and compressors based on dispersion gratings to adjust the chirp of the pulse [115] as well as 4-F systems paired with a spatial light modulator (SLM) placed in the Fourier plane to selectively filter and/or modify the phase of selected spectral components [93].

While there are various techniques to adjust the properties of a pulse (and only a limited part is described above), each method has its limitations, hindering the tunable adjustment of multiple properties simultaneously. For instance, incorporating more than one device may be necessary to adjust the frequency, power, and phase of the pulse at the same time, leading to a more complex setup and potential signal losses. Furthermore, adjusting any of these properties requires constant modifications and replacement of the components, resulting in a time-consuming and impractical approach.

In order to gain access to a higher spectral bandwidth, improved resolution, but also the capability to modulate the phase of light, a convenient approach relies on using liquid crystal on silicon (LCoS) devices. LCoS technology combines the reflective properties of a silicon chip with the light modulation capabilities of liquid crystals [116], [117], where in this case the liquid crystals layers are between a glass substrate and a highly reflective silicon backplane.

In our experimental setups, we implemented and used a programmable Fourier spectral filter made by *Finisar* and commonly known as a *Waveshaper* (WS) (Model 4000A – both version C and C+L available in the lab). This spectral shaping device is based on LCoS technology, and its operation principle is illustrated in Figure II.3.

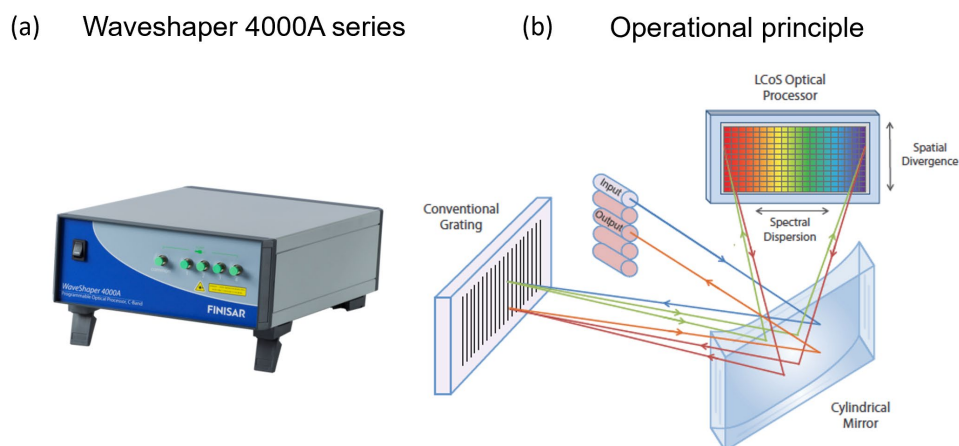


Figure II.3 (a) Finisar Waveshaper 4000A model with four output ports. (b) Schematic illustrating the principle of operation of a Waveshaper: An input signal is reflected by a cylindrical mirror to a conventional grating, where its spectral components are dispersed. These components then pass through an LCoS optical processor, allowing for precise manipulation of the spectrum. Afterward, they are sent back to the conventional grating to get recombined and exit through the output port, resulting in a modified output signal with controlled spectral characteristics. – Reproduced from [118]

When an input signal is fed into the Waveshaper device, it first passes through a grating that disperses it into its spectral components. These components then hit the LCoS processor made up of a matrix of reflective liquid crystal elements. By applying specific voltages to each of these elements, the processor can add individual phase shifts to the reflected signals, which allows for the steering of the signal components. Because the wavelengths are separated on the LCoS chip, each wavelength can be controlled independently without significantly affecting the others. We initially used this device because it can replace all the filters cited above.

One of the unique features of Waveshaper is that it is highly configurable and can be rapidly reprogrammed (\sim Hz refresh rate), allowing for fast signal adjustment, with a wide range of options, for customizing the spectral shape of the output signal by modifying the spectral filter shape, the attenuation, the dispersion, and phase of the input pulse at each wavelength [96], [77], [65].

Specifically, in our experiments, we essentially use the Waveshaper Model 4000A (in the C version) that possesses 4 reconfigurable output ports and a spectral coverage of 5 THz in the C-band, from 1527.4 to 1567.5 nm. Each LCoS pixel exhibit a 12.5 GHz linewidth and the system is optimized to provide arbitrary spectral shaping with an attenuation range between 0 and 35 dB (with a resolution of 0.01 dB) and 2π phase (with a resolution 0.01 rad).

This device therefore provides a complex and powerful tool to alter the signal with minimal insertion losses (< 3 dB) and make it possible to e.g. shape multiple peaks at once, seed multiple ports simultaneously or suppress unwanted spectral components. An example of such signal spectral shaping is shown in Figure II.4 and illustrate the versatility of the pulse preparation as long as several constraints are respected. For instance, the maximal average input power has to remain below 27 dBm, and while a spectral mask can be set with a 1 GHz resolution, one has to ensure that no significant phase wrapping, or abrupt phase jump is implemented for an optimal quality of the Waveshaper signal processing.

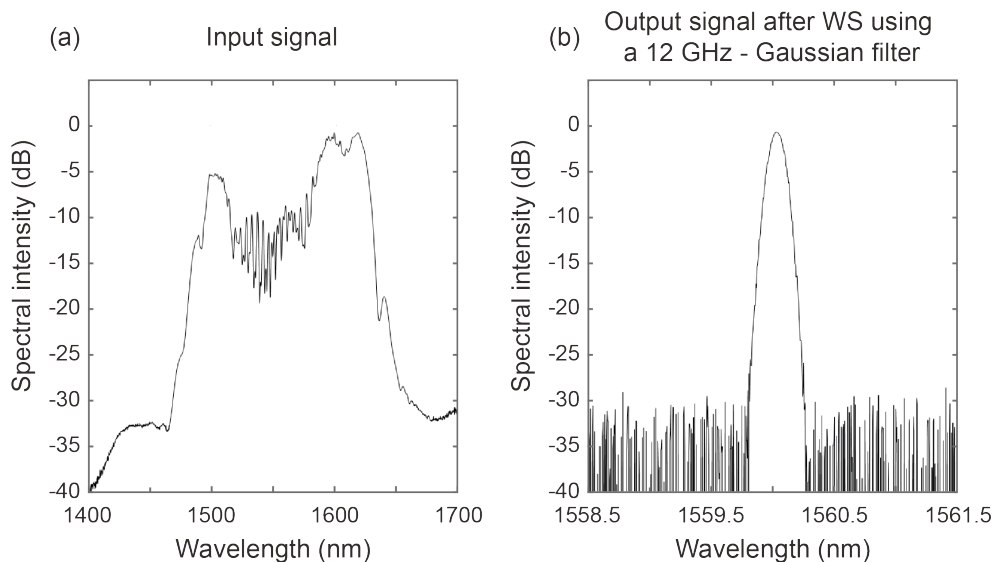


Figure II.4 (a) Input signal generated from a femtosecond laser (C-fiber) with an average power $P_{avg} = 60$ mW. (b) Spectral filtering obtained using the Waveshaper to apply a Gaussian filter, centered at 1560 nm with a spectral bandwidth ~ 0.1 nm.

Within the framework of my PhD studies, I interfaced, developed, and validated a MATLAB code allowing the upload of arbitrary spectral masks for the experimental study conducted in Chapter III and Chapter IV.

II.2.2. Temporal control of optical pulse properties

To access finer adjustments and achieve further tuning of pulse propagation dynamics, one can also implement control of the pulse properties in the temporal domain.

In the time domain, one can directly generate optical pulses and/or manipulate their temporal characteristics in an active way, through modulation of the pulse's temporal shape, phase duration, and timing.

For instance, laser pulse shaping can be achieved by using acousto-optic pulse shapers [119]. This includes the use of an acousto-optic modulator (AOM), a device that excites a sound wave obtained from a strong oscillating electrical signal creating a variation of the material's refractive index. Additionally, acousto-optic tunable filters can be implemented to change the polarization mode and, overall, gain control on the amplitude and phase of our pulse [120], [121], [122]. Nevertheless, AOM systems are usually relatively slow (typically with bandwidth in the tens of MHz range and below few GHz at best).

For faster modulation, one can usually rely on electro-optics modulators (EOMs). These devices can typically induce active phase modulation that enables the control of various related properties of light, such as intensity or polarization, using an electrical control signal [123], [124], [125], [126]. They typically employ Pockels cells and operate based on the principle of the linear electro-optic effect, commonly known as the Pockels effect. By applying an electric field to the Pockels cells, the refractive index of the crystal is modified, leading to alterations in the transmitted light's properties (typically the optical phase by inducing a modulation on the optical path length). The extent of these changes is directly proportional to the strength of the applied electric field and the electro-optic coefficient of the nonlinear crystal used (e.g. LiNbO₃ crystals are widely used at telecom wavelengths in either a Z-cut or X-cut configuration). For intensity modulation, EOMs are typically based on an interferometric scheme, where the phase modulation yields a phase dependent interference pattern between the arms of the interferometer to indirectly encode an amplitude modulation of the input signal. The most common implementation of such intensity EOM is based on a Mach Zehnder configuration, relying on two balanced interferometer arms and a 50% output coupler, with insertion loss in the order of ~ 4 dBs. These are widespread and formed the backbone of the telecom infrastructure, while other more complex interferometric schemes are nowadays implemented to accommodate advanced and faster telecom modulation formats [127], [128], [129].

When dealing with broadband pulses, AOMs face a particular challenge related to chromatic dispersion, where different wavelengths of light are deflected at slightly different angles by the AOM. Although it is theoretically possible to compensate for this dispersion, it is challenging to do so without introducing additional distortions. While AOMs are commonly used for modulation up to the MHz range, EOMs are known for their ability to modulate laser pulses over a broad range of frequencies, including the GHz range, and can be designed specifically for high-speed modulation applications up to ~ 50 GHz.

As mentioned above, the temporal properties of a pulse can be controlled by employing active phase and intensity modulation provided by EOMs. Those active modulations are however limited by the bandwidth of these electronic systems that usually remain below 100 GHz, and

thus corresponds to rise/fall time of 10 ps in the best cases. In this case, the processing of ultrashort pulses (sub-ps regime) cannot be properly implemented with such system. To mitigate this issue, we rely on the used Mach-Zehnder interferometers systems integrated in a photonic chip. In this case, the interferometers rely on the same physical mechanisms as the intensity EOM described above but are here arranged in a cascaded and unbalanced configuration that allows for a static processing of the signal (thus allowing both ultrashort-pulse processing and advanced signal tunability).

In our studies, we specifically focus on controlling a pulse's properties by splitting it into multiple different replicas with adjustable power and relative delay. For this purpose, we use the integrated photonic pulse processor (IPPP) mentioned in section I.1.3, consisting of several Mach-Zehnder interferometers (MZIs) and optical waveguides with $\gamma = 3.5 W^{-1}.km^{-1}$, $\beta_2 = -2.15 ps^2.km^{-1}$, and $\beta_3 = 0.0693 ps^3.km^{-1}$, operating as integrated delay lines (see Figure I.5 and Figure II.5) [43], [130]. The waveguides are arranged in a cascaded configuration, where the time delay on each one of them increases gradually according to the relation $\Delta_M = 2\Delta_{M-1}$, where M represents the number of the delay lines.

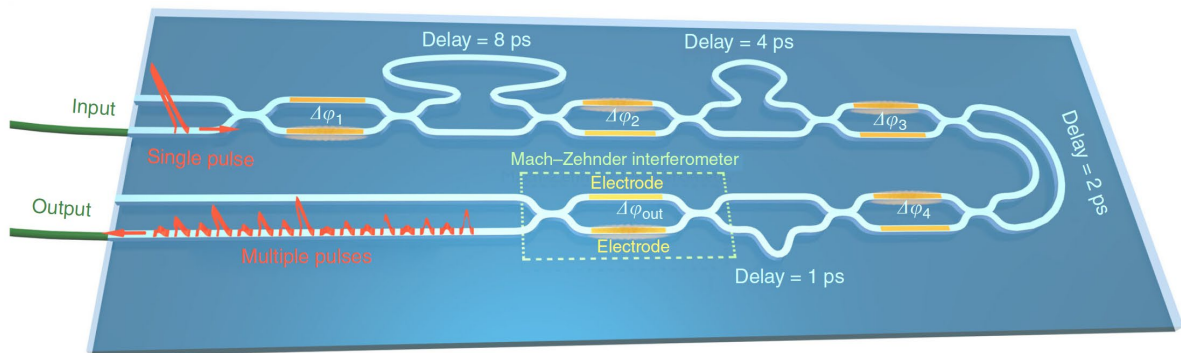


Figure II.5 Schematic diagram of the IPPP chip constituted of various Mach-Zehnder interferometers with two electrodes on each to control, by tuning the phase difference $\Delta\phi$, the splitting of optical pulses into different paths and the output train of pulses. Adapted from [43].

The schematic of the IPPP is represented in Figure II.5. The MZIs have electrodes on each arm that can be controlled via thermal effects to adjust the splitting ratio of the pulse entering the IPPP chip. When sending an input laser pulse into the chip and applying a different voltage on each arm of the MZIs, we induce a phase difference $\Delta\phi_N$, with N being the MZI index, which determines the optical path followed by the pulse into either of the two following arms. By adjusting the splitting ratio between this unbalanced waveguide structure, the power of each generated pulse can be modified, and the total train of delayed pulses will be recombined through the last interferometer to generate a pattern of temporally interleaved pulses as illustrated in Figure II.6.

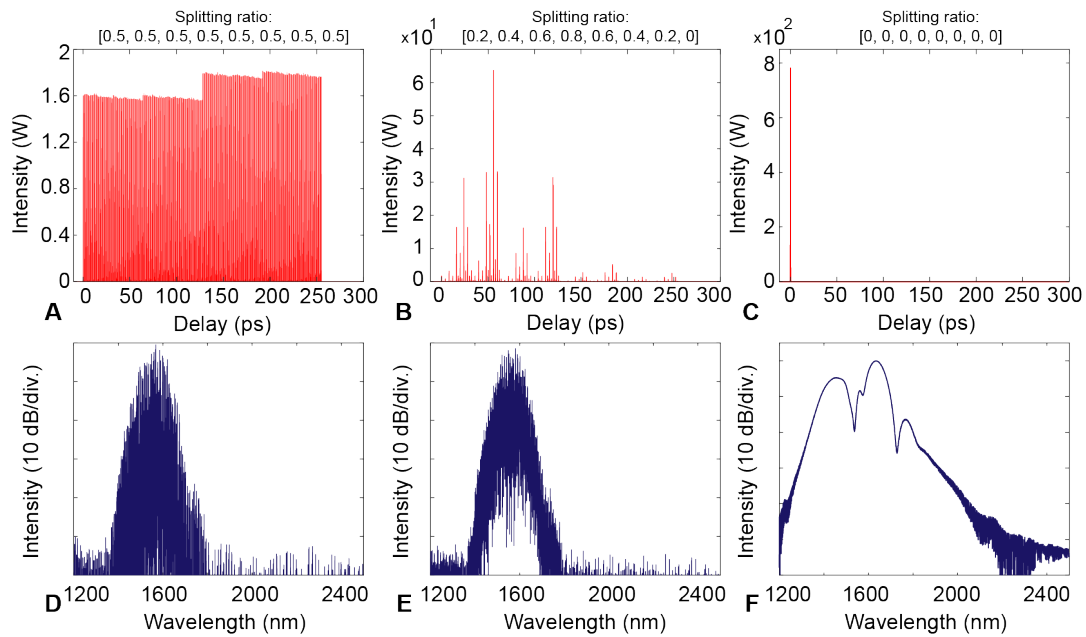


Figure II.6 Temporal (top) and spectral (bottom) output profiles of a 100 fs laser pulse (with $P_0 = \text{kW}$) after propagating within the IPPP with different splitting ratios. Reproduced from [44].

In the previously implemented IPPP architectures, the pulse separation(s) could be arbitrarily tuned with a temporal delay between them up to 256 pulse replicas ranging from 1 ps to 255 ps. In related studies [43], [130], this system was experimentally demonstrated as a suitable way to tailor a train of ultrashort pulses (< 200 fs) through each one of the MZIs and control the properties of this pattern before nonlinear propagation in an optical fiber. In particular, this approach was used to shape and customize the spectral contents of coherent supercontinuum.

Similarly, in a linear regime and using longer picosecond pulses (i.e. with a duration potentially longer than the temporal separation provided by the IPPP), this system was leveraged to achieve autonomous and arbitrary pulse shaping via coherent pulse synthesis (i.e. optimized temporal superposition and interference).

In the context of this thesis, I have contributed to the numerical studies on the implementation of this IPPP system for the generation of supercontinuum with spectro-temporal properties specifically tailored for multiphoton microscopy [44].

Within the team, we have also experimentally implemented and deployed a new set of IPPP architectures with longer unit delay, so that the overall pulse pattern can span over more than 4 ns. For this, I also provided a significant contribution by assembling an optical FROG setup (see section II.4.1) allowing to characterize these optical signals with a large temporal span (> 4 ns) and an excellent resolution (< 1 fs).

Importantly, this IPPP shaping has been numerically and experimentally studied during my doctoral work but not directly included in the core of this manuscript. We kindly refer the reader to the Appendix 1 where we provide more details on the work done in this area.

However, it is worth noting that combining spectral waveshaping and IPPP temporal shaping is expected to effectively provide access a wide range of parameters that could be further leveraged for controlling nonlinear propagation in optical fibers (see also the Conclusion section). However, as we employ all these tools, the propagation dynamics become challenging to understand and regulate. To overcome these limitations, my thesis work also aims at studying and implementing a “smart control” of nonlinear effects using machine

learning strategies [122], [124], [130], that could be transferred to other domains of wavepacket control currently being investigated in the lab (e.g. spatial control and beam shaping in multimode fibers).

II.3. Machine learning control

As we mentioned before, various methods can be applied to control the spectral and temporal properties of laser pulses for generating the desired output spectra. However, these pulse control methods and numerical modeling have limitations in predicting the propagation behavior depending on the chosen parameters. For this reason, we aim at implementing optimization algorithms to these methods, and therefore control and/or predict the desired output signal properties. In recent years, machine learning strategies have increasingly been used in different fields and applications such as ultrafast photonics to smartly enhance and optimize the desired dynamics or optical functionalities. For instance, in our case, we can use machine learning to automatically select the best initial parameters to study targeted nonlinear dynamics during fiber propagation and control the properties of spectral broadening.

II.3.1. Introduction to machine learning

Machine learning is a branch of artificial intelligence. This concept is associated in creating intelligent machines that can learn from data inputs and automatically improve their performances without being programmed explicitly. Machine learning lies at the interference between algorithms and statistics; We use computational tools and techniques to execute and implement efficiently these algorithms, while the statistical methods provide the theoretical concepts and principles to understand and analyze the probability, inference, and variability present in data [131]. In other words, the goal of machine learning is to train models on a set of data, experiences, or patterns, where the results are already known. Then, the model can be used to predict the value or category of something new, where one does not know the answer yet.

Machine learning can be classified into three main types: Supervised learning, unsupervised learning, and reinforcement learning (see Figure II.7).

- **Supervised learning:** For this type of learning, we must supervise machine learning by providing labeled training data. It requires training the model with input-output label examples until it learns to map the input features to output labels on its own. With direct feedback, the system tends to remember the results and use them in the next operation.
- **Unsupervised learning:** In this case, the algorithm learns from unlabeled data. It focuses on searching for patterns, relationships, and hidden structures within the data until it identifies similarities and differences among the different input or classify them into different groups based on their properties.
- **Reinforcement learning:** It differentiates from supervised and unsupervised learning by using training data that only indicates whether an action is correct or not, without explicitly stating the correct output. Reinforcement learning problems are characterized by closed-loop dynamics, the absence of direct instructions, and the influence of actions on subsequent rewards. It involves an “agent” exploring its environment, learning from experiences, and improving performance based on rewards and punishments through a feedback-based process.

Given its ability to improve performances and solve problems, machine learning has experienced rapid growth and become nowadays a powerful tool in numerous fields. Specifically, in the fields of optics and photonics [132], [133], machine learning enabled advances in optical characterization and microscopy [44], [134], imaging [135], [136], optical communication [137], [138], signal processing and optical performance monitoring [139], sensing and metrology applications [140], [141], optimal design and optical device optimization [142], or in nanophotonic for designing new devices [143], [144] .

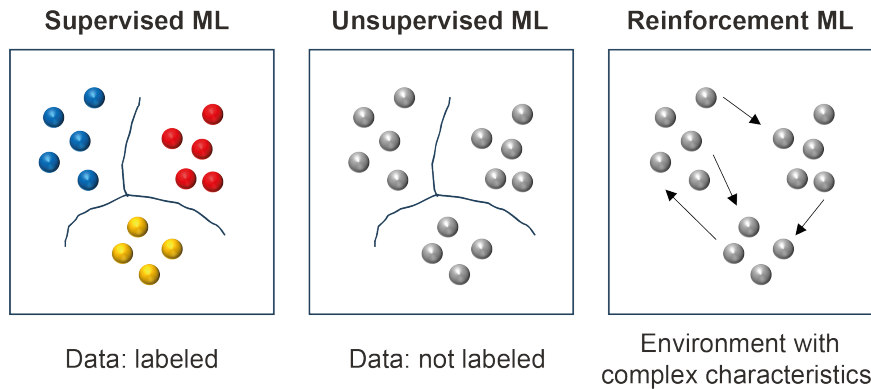


Figure II.7 Diagrams of machine learning types. Supervised learning: classifying labeled data; Unsupervised learning: Discovering patterns in unlabeled data; Reinforcement learning: Learning actions to maximize rewards.

In the domain of ultrafast nonlinear optics, numerous machine learning approaches, specifically customized to address the unique challenges and requirements of this field, have been subject to rigorous scrutiny, showcasing remarkable success [145]. Various machine learning approaches, specifically implemented to address the challenges and advancements of this field have been studied and proved successful.

A typical and widespread example consists in feed-forward neural networks (FFNN). This model is illustrated in Figure II.8, where the learning starts with input data to get an output, passing by hidden layers that can perform nonlinear operations. In each layer, individual neurons employ activation functions, which depend on weighted summations derived from the outputs of neurons in the preceding layer. These activation functions undergo adjustments during the learning process, contributing to the network's adaptability and effectiveness. In our field of studies, this network can be employed for analyzing and classifying experimental data, such as pulse shapes or broadened spectra [146]. This can also be used to learn the differential propagation dynamics of the GNLSE, by understanding how the intensity and phase of an electric field change during propagation at elementary points of the fiber [147], [148], [149], and thus finally replace the GNLSE numerical integration. This knowledge enables the neural network to predict how the light behaves over a long propagation distance based on its initial conditions and help the study of nonlinear dynamics and light evolution in optical fibers without having to perform time-consuming calculations. In addition, they also allow to compute and analyze the spectral and temporal intensity properties in the broadened output spectrum and find, for example, the correlation between various direct and indirect components in the Fourier space [150].

One can also implement, for different applications, convolutional neural networks (CNNs), which are structured to automatically learn and extract hierarchical patterns and features from the input data through multiple interconnected layers, including convolutional layers, pooling layers, and fully connected layers. They can be used to process and analyze spatially resolved

data, such as images or videos of laser beam profiles or spatially varying pulse characteristics. For example, by training deep CNNs on extensive datasets, one can efficiently predict the phase of ultrashort pulses from dispersion scan traces eliminating the need for time-consuming conventional methods [151]; or use programmable phase-change metasurfaces with waveguides, to create multimode photonic CNNs allowing programmability and reconfigurability in advanced photonic systems [152]. Furthermore, CNNs have been employed to extract characteristic features and analyze soliton dynamics, providing valuable insights into the behavior of these optical phenomena [153].

Recurrent neural networks (RNN), designed to handle sequential data by incorporating feedback connections, can also be implemented in the context of ultrafast optics. This type of artificial network has been especially important in offering valuable insights into nonlinear dynamics [154]. It can capture temporal dependencies and feedback connections, allowing them to model the evolution of nonlinear effects over time, optimize and control these effects in real-time, and provide a deeper understanding of complex spatiotemporal nonlinear dynamics in single-mode and multimode fiber systems [155].

Noteworthy, unsupervised learning, and especially clustering analysis that aims to group similar data points based on their inherent characteristics has been employed in this field to optimize and understand chaotic data and unstable nonlinear dynamics [156].

In the context of ultrafast photonics, reinforcement learning algorithms can help optimizing the performance of complex photonic systems by enabling the system to adapt and learn optimal strategies for various tasks [157], [158]. For example, recurrent neural networks can also be implemented in reinforcement learning as a large-scale photonic network [159]. In this case, the photonic RNN could optimize its internal dynamics and improve its prediction capabilities.

By providing rewards based on desired performance metrics, such as higher efficiency, faster switching times, or better signal quality, reinforcement learning algorithms can guide the exploration of parameter spaces and discover novel configurations or operating conditions that maximize the desired objectives.

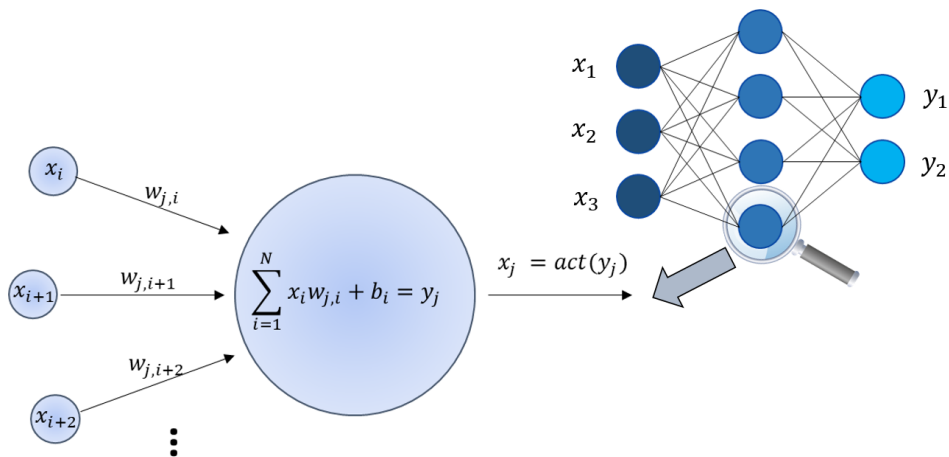


Figure II.8 Representation of a feed-forward neural network architecture, with x_{i+n} the input data $w_{j,i+n}$ are the weights associated with the connections between neurons in different layers, $y_j = \sum_{i=1}^N (x_i w_i + b_i)$ is the weighted sum of inputs with the bias term b_j and $act()$ is the activation function, with $i, j \in \mathbb{N}, n \in \mathbb{Z}^+$.

Search algorithms are another type of machine learning that is widely used and has demonstrated strong potential and recent improvements in an ultrafast optics

context [160], [161], [162]. These are optimization algorithms, that explore a range of possible solutions by evaluating their suitability based on specific criteria and progressively refine the search to converge towards the best or the most optimal solution or parameter values for a given problem. In our studies, these algorithms are the ones that we will mostly use and focus on. Different implementations can be cited in this type of learning.

Genetic algorithms (GA) are one of the most used and effective methodologies and have thus been employed for different optical applications. For example, GAs can be used in the optimization of cavity parameters of mode-locked fiber lasers to achieve autonomous wavelength tuning and the generation of pulses with desired characteristics [163], or to develop automatic mode-locked fiber lasers [164], [165], [166] that can automatically lock onto different operating regimes, such as fundamental mode-locking, second-order harmonic mode-locking, and Q-switching [167], [168]. Moreover, GAs can be used in the context of pulse propagation modeling, to design optical fibers capable of enhancing particular processes or dynamics such as highly-coherent or large bandwidth supercontinuum generation, and therefore opening new possibilities for tailoring fiber properties for specific applications [169], [170]. Overall, genetic algorithms offer powerful means of optimizing and controlling ultrafast photonics systems, enabling for instance laser operation with desired properties, and efficient pulse shaping [130].

An alternative to GA can be particle swarm optimization (PSO). Despite the success of GAs, PSOs can outperform them in certain tasks and converge faster for some problems. As GAs, PSO can among other be used to enable on-the-fly reconfigurability of broadened output spectra by controlling the input pulse parameters and or even more complex optical waveforms generated through optical pulse-shapers (e.g. MZI on-chip cascade). These techniques can be used for different applications, such as the realization of autonomous on-chip waveform generators [130], or multiphoton microscopy optimization via the enhancement of multiphoton absorption [44]. PSO was also applied to the inverse design problem of a fiber 8-figure laser cavity [171], which involved finding the system architecture and design of pulses with specific parameters, such as pulse duration and spectral width, providing the generation of desired laser outputs. Other methodologies can also be cited like the Rosenbrock search [162], [172], and the Toroidal search [160], which have been demonstrated in the context of ultrafast photonics for tasks such as automatic mode-locking in fiber lasers and pulse characterization in mode-locked lasers.

In this thesis work, our approach to machine learning involves the rather straightforward use of search algorithms where we extensively accumulate experimental data by iteratively optimizing the system parameters towards a specific target.

In particular, we relied on algorithms such as GA and PSO to progressively converge towards the best parameters until finding the optimal solution. From a practical viewpoint, this approach consists in heuristic search allowing the exploration of a large parameter space in a limited time. However, in our team, we are also exploring the implementation of artificial neural networks (ANN) for the experimental works presented in Chapter IV.

Our approach involves training such ANNs by provide the systems with a large amount of input and output data obtained respectively before and after nonlinear fiber pulse propagation. In this case, we train the network to mimic the nonlinear transfer function and thus predict the signal output properties from selected input conditions. On the other hand, we can also provide the ANN with output information and train it so it can effectively reverse engineer the input parameters to be used in order to achieve the desired outputs.

While being currently implemented experimentally, this thesis does not explicitly deal with ANN training but rather focus on heuristic search algorithms. This method was deemed effective to eliminate the need for extensive parameters sweep and mitigate long measurements during experimental setups. This attribute offers a remarkable advantage by substantially accelerating the experimentation process and ensuring reasonably good convergence towards the desired target function, especially for the optimization of incoherent MI processes discussed in Chapter IV. Bellow, we succinctly discuss the optimizations algorithms used in our experiments.

II.3.2. Evolutionary algorithms

Evolutionary algorithms are a class of optimization algorithms that are inspired by the process of natural evolution. GA and PSO are examples of evolutionary algorithms [173], [174].

1- Genetic Algorithms (GA):

Genetic algorithms are generally used to optimize solutions for complex problems that have a large search space. GAs mimic the principles of Darwinian evolution by employing a population of candidate solutions and iteratively applying selection, crossover, and mutation operators to evolve the population over multiple generations. The concept of genetic algorithms and the foundation of this problem-solving technique was first introduced by J.H. Holland in 1975 [175].

The algorithm starts with a population of potential solutions, often represented as a set of properties (chromosomes or strings of genetic information). Each set of chromosomes (forming the individual) represents a candidate solution to the problem. The algorithm then evaluates the fitness (or quality) of each individual based on an objective function that quantifies how well it solves the problem. The genetic algorithm iteratively modifies the population by applying genetic operators. Selection is used to favor individuals with higher fitness for reproduction, mimicking the survival of the fittest. Through successive generations, the genetic algorithm explores different combinations of genetic information and gradually converges toward better solutions. The algorithm continues until a stopping condition is met, such as reaching a maximum number of generations or achieving a satisfactory solution. So, we can say the GA models follow the steps [176]: Initialization, selection, genetic operators, and termination (see Figure II.9).

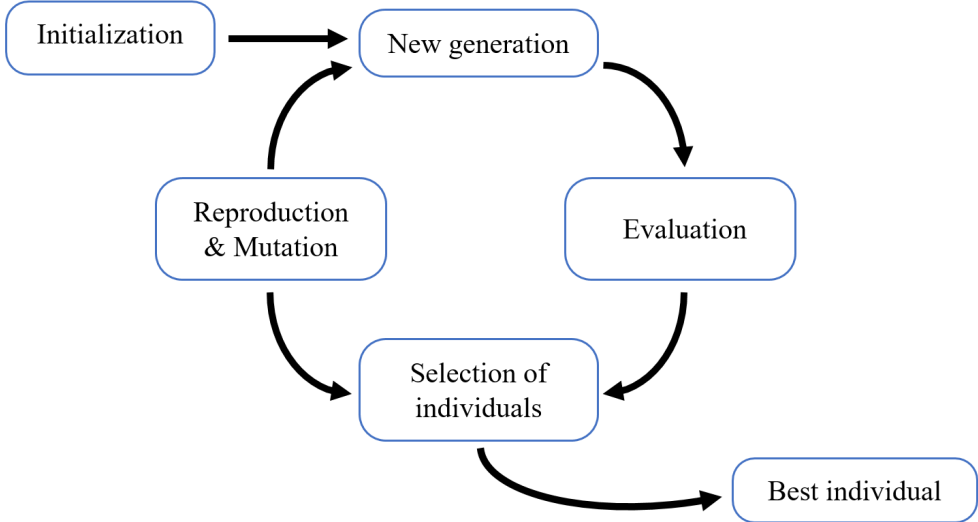


Figure II.9 Schematic representation of a genetic algorithm reproductive cycle.

- Initialization: The initial part begins by creating a set of chromosomes, usually randomly generated, to form the initial population. It is worth mentioning that the quality of the initial population (and its size in term of individuals) can have an impact on the algorithm's performance. If the initial population consists of individuals who are far from the optimal solution, it may take longer for the algorithm to converge. On the other hand, if the initial population is already close to the optimal solution, the algorithm may converge more quickly.
- Selection: The selection step in a genetic algorithm is the process of choosing individuals from the current population to serve as parents for the creation of the next generation. This step is inspired by the natural selection process in evolution, where individuals with favorable traits are more likely to survive and reproduce and it typically follows a probabilistic approach, where individuals with higher fitness have a greater chance of being selected (individuals are selected by filtering solutions using a fitness function). Fitness is a measure of how well an individual solves the problem at hand and is determined by an evaluation metric. There are several selection techniques, including a selection based on an individual's fitness proportion, where a random spin of a roulette wheel determines the chosen individuals (roulette wheel selection), or simultaneous selection by dividing the roulette wheel into slots (stochastic universal sampling). The filtering can also be done by selecting the fittest individual from random subsets (tournament selection) or using a selection based on individual ranks rather than fitness values (rank selection), or even by using a selection based on entropy and sampling methods by selecting individuals based on their probabilities calculated using the Boltzmann distribution.
- Genetic operators: In this step, two main operators can be performed: Crossover and mutation. Both contribute to the exploration and exploitation of the search space. Crossover combines the desirable characteristics of different individuals, potentially creating better solutions. It involves combining the genetic information between two parent individuals to create offspring. Various crossover operators can be used in this step such as single-point crossover, multi-point crossover, uniform crossover, shuffle crossover, order crossover, or partially mapped crossover, ... On the other hand, mutation introduces random changes and new variations in the population, allowing the search algorithm to explore new regions of the parameter space. It helps maintain genetic diversity within the population and prevents settling for suboptimal solutions. The mutation can be a displacement mutation which will move part of the solution randomly for a valid and random mutation, it can be an exchange mutation which will swap parts of the solution, or an insertion mutation which consists of adding a part of the solution to a different location.
- Termination: The termination criterion should be carefully chosen. It can be based on reaching a certain fitness threshold, stagnation of the population, or a predefined maximum number of generations. The termination criterion ensures that the algorithm stops when it has achieved a satisfactory solution or when further iterations are unlikely to yield significant improvements.

2- Particle swarm optimization (PSO):

PSO is another evolutionary algorithm inspired by the behavior of social organisms like birds flocking or fish schooling [173], [177]. In PSO, an initial swarm of particles moves through a multidimensional search space to find the optimal solution as illustrated in Figure II.10. Each

particle's movement is influenced by its own experience and the experience of its neighboring particles.

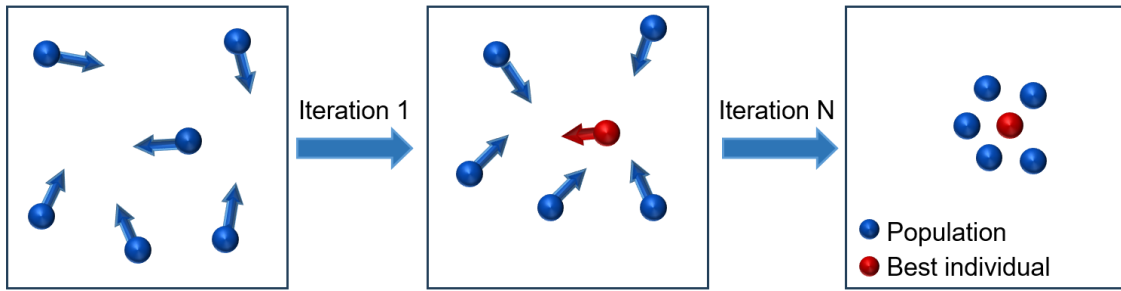


Figure II.10 Schematic representation of PSO evolution within the parameter space.

PSO is a computational optimization technique inspired by the collective behavior of animal swarms. It begins with an initial swarm of particles, each representing a potential solution, dispersed across a multi-dimensional search space. In each iteration, the position of the particles is determined by “swarm intelligence”, based on their current position, their best-known position (personal best), and the best-known position of their neighbors (global best). The velocity of the i -th particle and the k -th iteration can be expressed as [178]:

$$v_i^{k+1} = wv_i^k + c_1r_1(p_{best_i}^k - x_i^k) + c_2r_2(g_{best}^k - x_i^k) \quad (\text{Eq. II.3})$$

Where w is the inertia weight, r_1, r_2 are random numbers between $[0,1]$, and c_1, c_2 are positive constants regulating the respective strength of personal and social influence in the PSO process. x_i^k is the current position of the particle, p_{best} and g_{best} are the personal and global bests, respectively. The first term of the equation (wv_i^k) searches new solutions and explore regions with potentially the best solutions. The second term of the equation explores the previous solutions and find the best solution of a given region by personal influence ($c_1r_1(p_{best_i}^k - x_i^k)$) where the particle returns to a previous position if it proves better than the current one. The third term takes into account the social influence ($c_2r_2(g_{best}^k - x_i^k)$) of the swarm where the particle follows the direction of the best neighbors. These factors are considered to adjust the particle's trajectory in subsequent iterations where this adaptive movement strategy guides particles towards promising regions of the search space. Similar to GAs, PSO iteratively updates particle positions until a termination condition is met, such as reaching a maximum number of iterations or achieving a satisfactory solution.

One key difference between PSO and GA lies in how they determine the next set of individuals or particles. While GA generates new individuals solely from the selected current individuals, PSO constructs the trajectory of each particle based not only on the current particles' positions but also by considering their individual best positions and the overall best position in their neighborhood. This characteristic gives PSO a higher degree of freedom compared to GA by offering greater diversity in particle trajectories and exploration of the parameter space. This broader exploration capability contributes to its potential effectiveness in finding optimal solutions to complex optimization problems.

Both GA and PSO are powerful optimization techniques. The two methods have their strengths and can be fine-tuned for improved performance [130], [44], [179]. The choice between them depends on the specific problem and the desired balance between exploration and exploitation in the search space.

II.4. Characterization techniques

As we explored in section II.2, pulse control methods provide valuable means to manipulate the properties of ultrafast pulses before their propagation. These techniques allow to tailor and optimize in a smart way the characteristics of the desired output after nonlinear propagation. However, while pulse control methods offer significant flexibility, it is equally important to have reliable techniques for accurately measuring and characterizing the resulting pulses. Over the years, many characterization techniques have played a crucial role in analyzing and understanding the fundamental properties of light and proved particularly useful in the measurements of ultra-short pulses associated with extreme and broadband spectral signals.

In the spectral domain, one of the most used characterization devices is the optical spectrum analyzer (OSA). This device relies on spectrally sweeping a monochromator and therefore integrating the spectral intensity at a given wavelengths over multiple pulse periods. While this method enhances the sensitivity, accuracy and stability of the measured spectrum, giving us a smoother and more reliable representation of the signal, averaging multiple successive spectra imposes limitations. OSA measurements washes out the noise components in each individual spectrum, preventing us from performing real-time measurements and detecting the rapid changes and instabilities from shot-to-shot spectra.

In contrast, for direct detection in the temporal domain, one may simply rely on optoelectronic characterization using fast photodiodes associated with an oscilloscope. As these photodiodes have a fast response time, they can capture (in real-time) the rapid variation in intensities of the light signal and send it to the oscilloscope that samples the corresponding electrical signal (at high frequencies) allowing the reconstruction and visualization of the temporal waveform.

However, these techniques still have limitations and prevent us from knowing all the pulse's properties. For example, being able to accurately measure and extract the signal's phase is a crucial aspect for understanding the pulse properties, studying their impact on e.g. phase-matching effects or even analyzing the variations of propagation dynamics due to the pulse chirp. While the previously cited techniques provide a good understanding of the shape, duration, and peak power of the pulse, they do not provide the ability to accede to the pulse's phase. Moreover, the direct real-time characterization techniques are intrinsically bandwidth-limited and thus prevent measuring pulses in the picosecond regime (or below).

II.4.1. Complete pulse properties characterization

Measuring ultra-short pulses has always been a challenging subject, and the time-dependent intensity and phase monitoring of such pulses was hardly solved until 1991. As we know, a pulse is characterized by its electric field E , dependent on the intensity I , the phase ϕ of the pulse in the time domain t and the phase φ in the frequency domain ω :

$$E(t) = \sqrt{I(\omega)} e^{-i\phi(t)} \quad (\text{Eq. II.4})$$

$$\tilde{E}(\omega) = \sqrt{S(\omega)} e^{-i\varphi(\omega)} \quad (\text{Eq. II.5})$$

To measure such a pulse, all we need is to find both its intensity and phase in either the spectral or temporal domain. In the spectral domain, we can easily use a spectrometer to measure the spectra intensity $S(\omega)$. However, being able to measure and study the phase is very important and allows to fine-tune the pulse spectral broadening during nonlinear propagation.

Yet, the spectrum alone is not enough to retrieve the pulse profile without ambiguity, as different complex fields, with different phases, can yield the same spectrum $S(\omega)$. This problem is called a “one-dimension phase-retrieval problem” [180], [181].

In the time domain, researchers commonly rely on the autocorrelation technique. Normally, to measure a pulse, one needs a shorter event with can be used as a reference to resolve the pulse under test (PUT). However, the difficulty arises from the fact that to measure ultra-short pulses, the user does not have direct access to any event or optical reference shorter than the pulse. An alternative approach thus consists in using the PUT to measure and resolve the pulse itself. This idea constitutes the basis of autocorrelation techniques where the measurement is intrinsically self-referenced by the PUT.

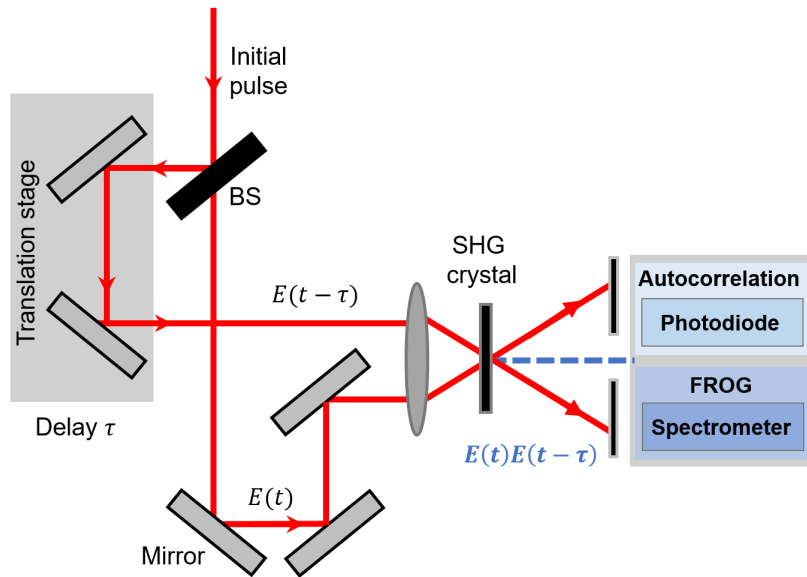


Figure II.11 Setup of an ultrashort pulse measurement via intensity autocorrelation/FROG: The initial pulse $E(t)$ is split and recombined in a SHG crystal with a delayed pulse replica $E(t - \tau)$. The SHG signal can be measured either by a photodiode (to find the autocorrelation trace), or by a spectrometer (for a complete characterization of the pulse and the measurement of the FROG spectrogram).

Specifically, autocorrelation consists in splitting the pulse $E(t)$ into identical copies that follow two different optical paths (see Figure II.11). One of them is called the “gate function” $G(t - \tau)$, which is delayed in time, with a time delay τ using a variable delay line. The two pulses $E(t)$ and $G(t - \tau)$, will then be combined to create an interference pattern that depends on the time delay. The resulting signal can be measured directly using a photodiode (i.e. field autocorrelation), or can for instance be mixed $E_{AC}(t, \tau) \sim E(t)G(t - \tau)$ in a nonlinear medium or via two-photon absorption processes prior to detection (i.e. intensity autocorrelation).

This latter case is usually referred to as intensity autocorrelation because both signal intensities are multiplied in the nonlinear crystal via a second harmonic generation (SHG) process (typically implemented in a non-collinear setup as illustrated in Figure II.11). SHG is a second-order nonlinear process in which two photons of a specific frequency interact with a nonlinear material, leading to the generation of a new photon at precisely twice the frequency. In this context, if we use an SHG crystal, we obtain the autocorrelated signal $E_{AC}(t, \tau) \sim E(t)E(t - \tau)$, where $G(t, \tau) = E(t, \tau)$. In this case, the autocorrelation intensity is a representation of the resulting SHG signal intensity I as a function of the delay: $I_{AC}(\tau) \sim \int_{-\infty}^{+\infty} I(t)I(t - \tau)dt$. The autocorrelation functions can also provide spectral information

through the Wiener-Kinchin theorem [182], which indicates that the Fourier transform of the autocorrelation is the magnitude square of the Fourier transform of the intensity in the frequency domain, i.e. $\widetilde{I}_{AC}(\omega) = |\widetilde{I}(\omega)|^2$.

Even if the autocorrelation function $I_{AC}(\tau)$ does not directly provide the exact pulse duration, it provides valuable information about the pulse shape and the autocorrelation duration $\Delta\tau$. Knowing these two parameters we can then infer the pulse duration Δt . For example, in the case of a Gaussian pulse, $\Delta\tau/\Delta t = 1.414$, and for a hyperbolic secant pulse, $\Delta\tau/\Delta t = 1.543$ [183].

However, autocorrelation still does not provide any information about the phase, which ultimately lead to another one-dimensional phase retrieval problem. Over the years, many techniques tried to overcome these problems by combining both the autocorrelation and the spectral information (e.g. temporal information via intensity (TIVI), fringe-resolved autocorrelation (FRAC), and cross-correlation...), however, they still encounter several limitations, work only for some conditions, and may not be suitable for pulses with more complex temporal profiles especially when complex noise features interfere with the pulse.

To overcome these limitations and obtain more detailed information for a successful pulse retrieval, one must measure the corresponding pulse spectrogram, that provide both spectral and temporal information on the SHG signal measured by autocorrelation [180]. Its representation takes the form of a three-dimensional intensity plot that simultaneously shows the time and frequency projection of the generated SHG signal. This tool allows us to understand how the signal's spectral components are changing over different time convolution intervals (when considering intensity autocorrelation). Indirectly, it can also reveal changes in the pulse spectral content, such as frequency shifts, modulations, or the presence of transient events. Using different existing algorithms, one may also retrieve the temporal field $E(t)$ from the spectrogram and thus determine the waveform intensity $I(t)$ and the phase $\phi(t)$ in the temporal domain, or equivalently, its counterpart in the spectral domain $E(\omega)$, $S(\omega)$ and $\phi(\omega)$.

To measure an intensity spectrogram (based on SHG), one can use the frequency-resolved optical gating technique (FROG). In simple words, FROG is an autocorrelation followed by a spectrometer that allows spectral analysis (Figure II.11). The pulse is gated by itself (so the gate is unknown) so that $E_{AC}(t, \tau) \sim E(t)G(t - \tau)$, where $G(t - \tau)$ is the delayed gate function. Using a suitable nonlinear-optical medium, the optical pulse will then interact with the medium to generate the SHG spectrogram signal that carries information about the pulse's temporal and spectral characteristics.

Unlike autocorrelation that measures the temporal intensity of the intensity autocorrelation signal as a function of the delay between pulses, in FROG, we take it a step further by measuring the spectrum of the autocorrelation signal as a function of the delay ($I_{FROG} = |E_{AC}(\omega, \tau)|^2$), and with this new information, we obtain a two-dimensional phase-retrieval problem that can be solved once one applies suitable deconvolution algorithms [184], [185], [186].

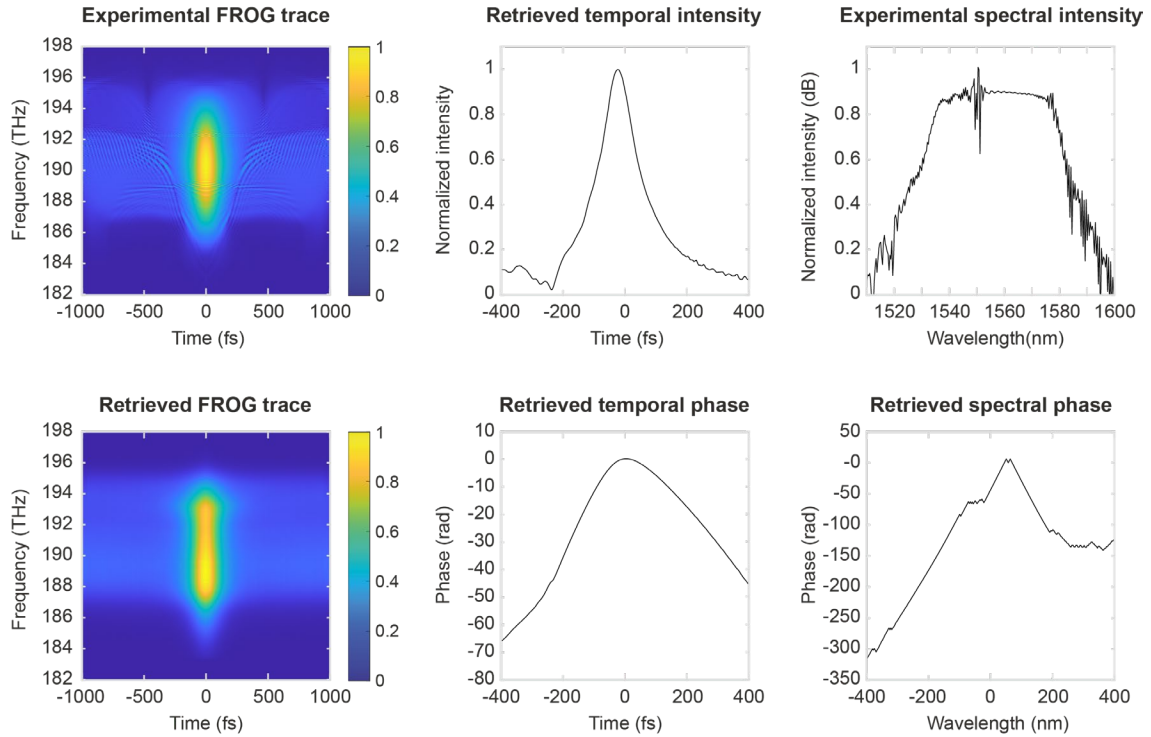


Figure II.12 Experimental FROG trace of a laser pulse centered at 1550 nm with an average input power $P_{avg} = 40$ mW. The experimental trace is represented along the reconstructed FROG trace and the corresponding retrieved intensity and phase (in both time and frequency domains).

FROG algorithms: FROG deconvolution algorithms aim at retrieving both the intensity and phase information of a pulse from its spectrogram (which is also called the FROG trace).

Most of the used algorithms that enable this deconvolution are based on iterative Fourier-transform phase-retrieval techniques, such as alternate projection methods. The objective is to iteratively refine the retrieved pulse until a satisfactory solution is achieved [186].

A generic FROG algorithm consists of starting with an initial guess for the electric field $E(t)$ of the pulse. Using this initial guess, a signal field $E_{AC}(t, \tau)$ is generated from the convoluted gate function [184], [187] and represents the interaction between different components of the pulse's electric field. It is then transformed into the frequency domain via a Fourier transform resulting in the signal field $\tilde{E}_{AC}(\omega, \tau)$. To evaluate the accuracy of the guess, the measured trace $I_{FROG}(\omega, \tau)$ is compared to $|\tilde{E}_{AC}(\omega, \tau)|^2$ to determine the mean square deviation between the traces (i.e. the so-called FROG error). These should ideally be equal and the FROG error is null. However, there will likely be discrepancies between the measured trace and the calculated magnitude.

In order to improve the signal field, a newly updated signal field $\tilde{E}'_{AC}(\omega, \tau)$ is generated, following an adjustment of $|\tilde{E}_{AC}(\omega, \tau)| \sim \sqrt{I_{FROG}(\omega, \tau)}$. This adjustment aims to bring the calculated magnitude closer to the measured values. Next, the updated signal field is transformed back into the time domain by applying an inverse Fourier transform, to get $E'_{AC}(t, \tau)$. Using this latter quantity, a new guess for the electric field $E(t)$ is generated, which takes into account the refined information obtained from the previous iterations. The process described above is repeated iteratively, where at each iteration, the algorithm generates a better guess that gets closer to the true complex electric field of the pulse. This

iterative process (and several other variations) aims to retrieve the accurate intensity and phase information of the pulse, ultimately providing a comprehensive characterization of the pulse's temporal and spectral properties.

In Figure II.12, using a homemade MATLAB retrieval algorithm based on an alternate projection method, we present an experimental FROG trace and the retrieved intensity and phase of the pulse in both temporal and frequency domains, with a corresponding FROG error of 1.98%. These traces allowed us to verify the pulse duration (FWHM) as $\Delta\tau \sim 180$ fs and the time-bandwidth-product was $TBP \sim 0.99$ so that the pulse appears close enough from being transform-limited.

While the quality of this pulse retrieval is up for debate, Figure II.12 is provided for illustrative purposes and several refined signal preprocessing/deconvolution techniques can be employed along with alternative commercial solutions for pulse retrieval (e.g. *Femtisoft FROG* [188]). In our case, for the generation of several hundreds of highly separated femtosecond pulse patterns (see Appendix 2) having a clear FROG trace as a qualitative measurement of the pattern spectrogram is usually sufficient to assess the signal key properties.

However, from a general viewpoint, FROG offers a range of useful properties and advantages [180] that make it an excellent tool for accurately characterizing ultrashort laser pulses. One notable advantage is its high accuracy, as it makes minimal assumptions about the pulse and allows for precise estimation of pulse intensity and phase. As the FROG trace is measured by removing the noise background, the retrieved pulse may be rigorously determined. The off-scale delays and frequency offsets have negligible impact on the retrieved pulse and FROG can account for known systematic errors in the measurement through the pulse-retrieval algorithm. Preprocessing techniques can also be employed to remove systematic errors, enhancing the accuracy of the measurement.

Unlike most ultrashort pulse measurement methods, FROG provides means to assess the reliability and accuracy of the obtained results. FROG provides the presence of two feedbacks, which can be divided into two types: The first type is probabilistic and results from the over-determination of pulse intensity and phase. The FROG trace contains more information than what is needed to determine the pulse, allowing for a check on the reliability of the results. The second type is deterministic and helps identify systematic errors. In this case the technique not only provides information about the pulse shape but also can detect and potentially rectify errors or inconsistencies in the measurements caused by various factors, including instrument calibration issues or environmental conditions. Another FROG feature is that it ensures infinite temporal resolution by combining information from both the time and frequency domains and determining the pulse characteristics with high precision. As the short-time information is extracted from large frequency-offset measurements, we can use delay increments that can be as large as the time scale of the pulse structure and thus indirectly obtain a high temporal resolution. This however requires a careful selection between spectral resolution/temporal span and spectral bandwidth/temporal resolution that should be balanced adequately depending on the experimental constraints and the properties of the PUT (see below).

As we noted before, during a FROG measurement, different nonlinear processes can occur depending on the type and experimental configuration of the nonlinear medium. SHG, based on $\chi^{(2)}$ nonlinearity, is one of the most used autocorrelation processes. However, we can also rely on other configurations or third-order autocorrelation based on $\chi^{(3)}$. In this case, we can mostly cite the polarization gate beam geometry (PG), self-diffraction autocorrelation (SD), or third harmonic generation FROG (THG), where each one of them has a slightly different FROG

setup and results in a different electric field equals to $E(t)|E(t - \tau)|^2$, $E^2(t)E^*(t - \tau)$, and $E^2(t)E(t - \tau)$, respectively.

Among these various correlation processes available, the non-collinear SHG-FROG is still one of the simplest methods to set, and, at the same time, presents advantages in terms of sensitivity and excellent signal-to-noise ratio. It is therefore the implementation I have installed and worked with in the laboratory.

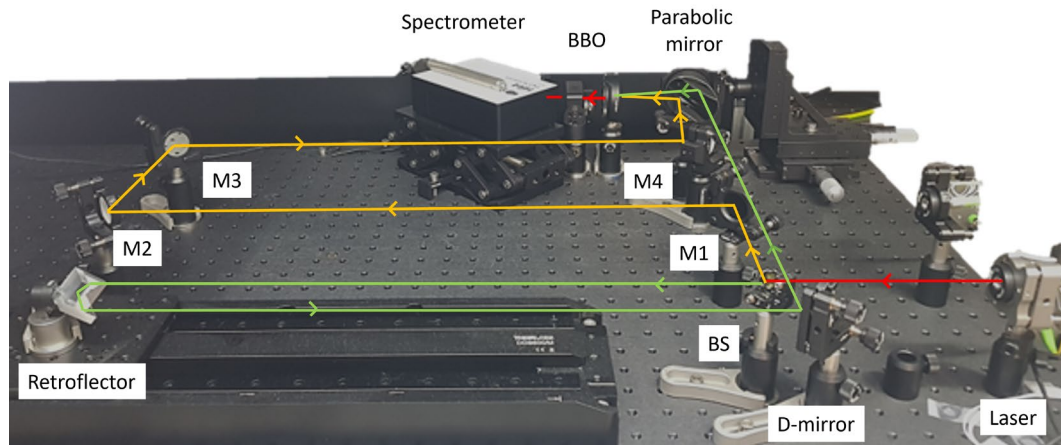


Figure II.13 'Home-made' FROG, set in our laboratory, constituted from a collimator to focus a 1550 nm laser pulse into a beam splitter, where it is divided into two optical paths: The first beam (in green) passes through a reflectometer and arrives into a D-mirror where it reflects towards an elliptical mirror.

The second beam (in orange) is reflected by 4 different mirrors before arriving at the elliptical mirror.

Both beams are focused into the BBO and their SHG signal is measured with a spectrometer.

For our studies, in order to measure the initial pulse properties before nonlinear propagation, we built up a "home-made" FROG system represented in Figure II.13.

Starting with a fiber collimator (Thorlabs - F260APC-1550) that converts the fibered pulse centered around 1550 nm into a free space beam of 3 mm diameter with minimal diffraction, the laser beam is then divided into two different paths using a thin film non-polarizing beam splitter (BS – Thorlabs - BP545B3). The first beam is reflected through four 6 mm silver mirrors (M1, M2, M3, and M4) before hitting a 90° off-axis parabolic mirror (Thorlabs - MPD239-P01). The second beam is the delayed one. After the beam splitter, it passes through a silver retroreflector used to reflect the incident beam back to its source at the same angle but with a spatial offset. The retroreflector is here mounted on a 600 mm linear translation stage (Thorlabs - DDS600), monitored by a channel controller (Thorlabs - BBD201 benchtop controller) that allows adjusting the delay over a span of 4 ns with a 0.6 fs resolution (i.e. 50 nm minimal step size). After reflecting from the mirror, the beam continues its path and hits a D-mirror where it gets directed towards the parabolic mirror.

We should note that for the point where the optical path lengths are the same (i.e. zero delay so that $\tau = 0$) so that the SHG signal power is at its maximum (in our case, where the delay line is centered at $z_0 = 300$ mm), we obtain the same optical power for both beams paths.

After being reflected by the mirror with a focal length 38.1 mm, the two beams are focused onto a BBO crystal (Beta-Barium Borate), whose thickness is 2 mm (but can be lowered down to 100 μm to improve the bandwidth acceptance of the PUT required for very short pulses). This $\chi^{(2)}$ nonlinear medium enables the SHG and convert the two (non-collinear) incoming beams into a new beam with twice the frequency (at ~ 775 nm). At the exit of the BBO, we use

a spectrometer (Ocean Insight - HR4 Pro Custom) to collect the generated signal along the optical axis (and filter out the non-collinear SHG signals generated from independent paths) and thus record the FROG spectrum with a resolution of < 0.7 nm.

By successively changing the delay and recording the information from the spectrometer, we can then create the spectrogram constituted from the different recorded spectra as a function of the delay. With suitable algorithms, we can then retrieve the needed information from the spectrogram and access the phase and intensity of the initial pulse.

In this setup, we use fibered injection, and the polarization state of the PUT is adjusted by a fibered polarization controller (FPC) to maximize the SHG signal peak power and temporal symmetry for our measurements. The intensity autocorrelation can be also directly extracted via a foldaway photodiode (Thorlabs - DET10A2) where the signal can be detected with synchronous detection using a lock-in amplification to gain temporal information (only) on the weakest/longest pulse that can be hard to resolve with the sensitivity of the FROG spectrometer.

Importantly, while we here focus on FROG due to its relative simplicity and versatility in terms of pulse properties, we note that other alternative methods for short pulses characterization have been implemented. One such method, known as "GRENOUILLE," is a simplified and compact variant of SHG-FROG [189]. It replaces multiple components with a single Fresnel biprism, offering cost-effective implementation and improved sensitivity by using thicker crystals. Additionally, we can cite the spectral phase interferometry for direct electric-field reconstruction (SPIDER) that is widely used to complete characterization of short pulses without iterative reconstruction algorithms [190], [191], or an alternative for SPIDER, SPIRIT (spectral interferometry resolved in time) [192] which has the potential for improved performance compared to SPIDER in terms of flexibility, adaptability, and the ability to characterize a wide range of pulses.

As we saw, FROG is one of the most successful methods for pulse characterization. It allows for the complete temporal and spectral characterization of ultrashort laser pulses. It provides detailed information about pulse duration, phase, chirp, and spectral content, enabling precise monitoring of pulse properties in different areas such as laser pulse compression, where FROG was widely implemented for the optimization of compressor setups [193], or for ultrafast spectroscopy applications [180], by accurately measuring the temporal and spectral characteristics of ultrafast laser pulses and assisting in understanding ultrafast dynamics in various systems, including molecular dynamics, chemical reactions, and material characterization. In fiber optics, FROG is a crucial tool used in the characterization of ultrashort pulses. It helps analyze the effects of dispersion and nonlinearity on pulse propagation [194], but also facilitates the design and optimization of fiber-based devices and systems for applications such as telecommunications, nonlinear optics, and optical fiber sensing [195], [196].

II.4.2. Real-time temporal characterization techniques

While the optical interferometry techniques cited above can provide a complete measurement of ultrashort pulses in phase and intensity, they have certain limitations. As FROG works by scanning or measuring pulses over multiple laser periods, the measurements are integrated over time, and does not provide a real-time measurement of the pulse properties. Although other FROG derivatives methods were developed to capture measurements in a single shot regime, such as cross-correlation FROG (X-FROG) [195], they require extremely high power

and are typically less practical for sup-picosecond pulses. SPIDER and SPIRIT can also access single-shot pulse properties, but they are usually more complex to put in place, especially in terms of alignment, pulse synchronization, and signal retrieval, thus hampering their applicability to versatile and/or continuous signal monitoring.

Other techniques for real-time measurement have been implemented and developed over the years in both the temporal and frequency domains. In the time domain, we can introduce the so-called “time-lens” technique, which leverages the concept of space-time, based on the principle of temporal magnification and reshaping of optical pulses using a time-lens device [197], [198]. Just as a lens helps us see things more clearly in space, a time lens can magnify the temporal waveform making it easier to study and measure light over very short timescales.

It consists in sending the signal into a dispersive optical element followed by a time-modulating element imposing a quadratic phase shift (often generated by a phase modulator or a nonlinear effect used to impart a temporal phase shift onto the dispersed signal) before propagation into another dispersive optical element. This phase modulation, analogous to the spatial phase imprinted by a lens on a light beam, is key to achieving the magnification effect of the time lens $M = D_{out}/D_{in}$ (Figure II.14.a), where D_{in} and D_{out} are the fibers corresponding dispersion factors [197], [199], [200], [201]. The time-lens method is particularly useful for the characterization of short laser pulses, typically in the femtosecond or picosecond range. It enables the real-time measurement of non-repetitive waveforms or the monitoring of fluctuating pulse temporal profile or duration, providing valuable insights into the temporal behavior of ultrafast optical signals [200], [201], [202].

On the other side, a well-known technique in the frequency domain is the dispersive Fourier transform (DFT) illustrated in Figure II.14.b. Drawing an analogy to the diffraction of light through a circular aperture, we can understand that similar to how a circular aperture causes the spreading of light waves and generates a spatial diffraction pattern, DFT exploits pure linear dispersive effects, typically through a dispersion compensating fiber (DCF), to transform the spectral information of an optical signal into a corresponding temporal waveform. This transformation allows for a detailed analysis and characterization of the signal spectrum in the time domain [199]. DFT achieves frequency-to-time mapping by time-stretching broadband pulses through group-velocity dispersion: When an optical waveform propagates through a DCF, different spectral components experience different delays due to dispersion.

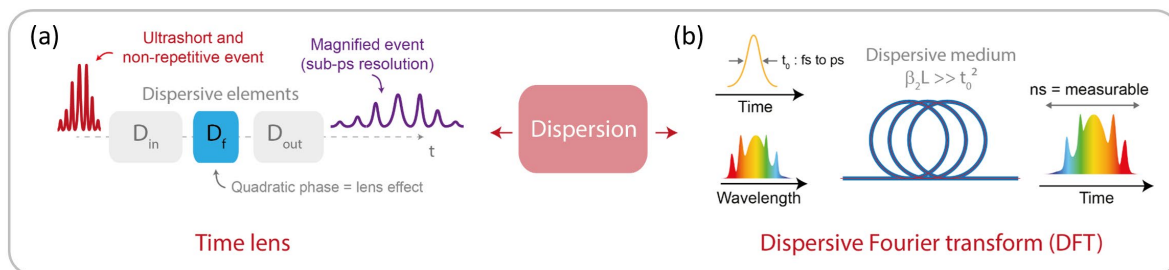


Figure II.14 Principle of (a) the time-lens technique and (b) the DFT technique.

By analyzing these delays, under suitable conditions, it becomes possible to reconstruct the original spectrum of the waveform in the time domain. DFT is mostly used in the far-field region, where the length/dispersion of the DCF is long enough and the conditions of the spatial Fraunhofer dispersion are met [203], [204]. In this case, after propagating through the DCF

with a length L and a dispersion of β_2 , the resulting temporal waveform can then be represented as:

$$|U_{DFT}(t)|^2 = |\tilde{U}(t/\beta_2 L)|^2 \quad (\text{Eq. II.6})$$

where ω represents the frequency and t denotes the time. The dispersed output pulse yields the pulse spectrum subject to the mapping of the time coordinate, so that:

$$\omega = 2\pi\nu = \frac{t}{\beta_2 L} \quad (\text{Eq. II.7})$$

The principle of DFT is described in Figure II.15, where a laser pulse entering a HNLF and experiencing spectral broadening is then sent into a DCF. Due to purely linear dispersive effects, the optical signal is stretched into an exact waveform replica in the temporal domain [199], [205], [206], [207].

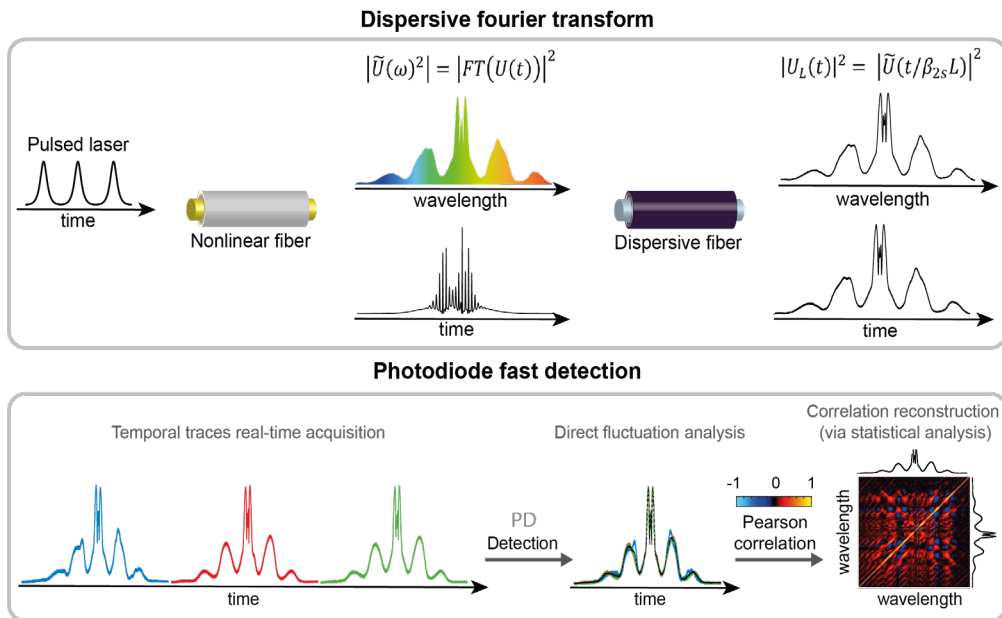


Figure II.15 (Top) Principle of DFT: A broadband optical signal is temporally stretched after linear propagation in a highly dispersive fiber. The various spectral components of the optical signal are directly mapped in the temporal domain. (Bottom) Real-time spectra acquired from PD measurements by readily analyzing shot-to-shot fluctuations from successive traces.

This mapping of the spectrum into a time-domain waveform replica indeed allows for the direct real-time measurement of the temporal intensity profiles. The standard optoelectronic detection process, which can be seen in Figure II.15, involves using high-speed photodiodes and ultrafast oscilloscopes to capture shot-to-shot fluctuations of the spectrum and perform real-time acquisition of successive temporal traces, to directly measure the variation of the signal's intensity profile as a function of time [199], [205], [208].

The DFT technique plays a crucial role in this thesis to study and characterize nonlinear dynamics phenomena, such as modulation instability and four-wave mixing processes, in ultrafast optical systems [207], [209], [210]. These processes generate new frequencies and complex spectral patterns and are often accompanied by fluctuations and intricate behaviors that are essential to understand the underlying physics [211], [212]. They are incoherent, noise-driven, and fluctuate between two time-events (i.e. from one pulse to another) which

makes it necessary to apply real-time characterization techniques to suitably measure these dynamics [205], [207], [208].

To illustrate this point, in Figure II.16, we show numerical results obtained by considering a 34 ps Gaussian pulse propagating into a HNLF and experiencing spontaneous modulation instability. The four output spectra presented are obtained from Monte-Carlo simulations where each numerical realization is simulated with the same exact input parameters, apart from different noise seeds (i.e. 1 photon per spectral mode with random phase). The incoherent nature of such noise-driven spectral broadening can be seen when comparing the different output profiles from each realization. In contrast, the mean output spectrum (red line), averaged from 1000 different realizations, displays an artificially smooth shape as one would observe experimentally from “slow” OSA measurements (typically integrating the spectrum from several millions of subsequent optical waveforms). Experimentally, to measure these fluctuations without losing information (besides the phase), we need to perform shot-to-shot detection, which can be provided by the DFT technique.

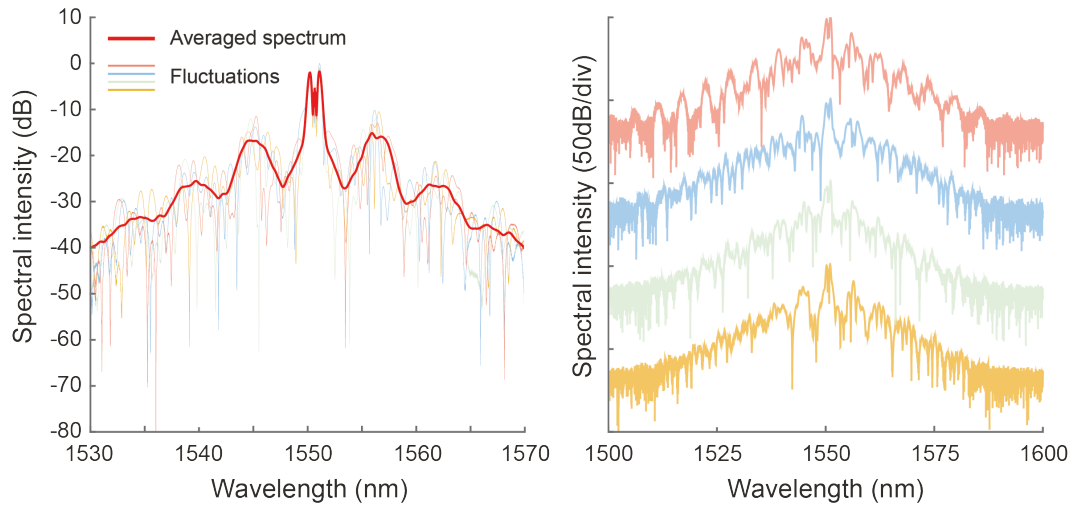


Figure II.16 Stochastic simulations of a 30 ps Gaussian pulse with $P_0 = 2.5$ W propagating in 485 m of HNLF ($\beta_2 = -1.78$ ps².km⁻¹, $\beta_3 = 0.07$ ps³.km⁻¹, $\gamma = 8.4$ W⁻¹.km⁻¹). The figure shows the four fluctuating MI output spectra simulated with the same parameters apart from a different initial noise seed. These spectra can be measured using real-time detection with the DFT technique. The average spectrum of 1000 realizations is shown in red, as a smooth artificial spectrum, preventing us from accessing to the incoherent shot-to-shot fluctuations of the noise-driven nonlinear dynamics.

To be fully leveraged, DFT is often followed by a statistical analysis, such as the retrieval of correlation between different spectral components. These correlations are usually represented by spectral correlation maps, calculated using Pearson’s correlation coefficient. Defined as $\rho_{(\lambda_1, \lambda_2)}$, it quantifies the linear dependencies between two wavelengths (λ_1, λ_2) based on the fluctuation of their respective spectral intensity I . This calculation is given by:

$$\rho_{(\lambda_1, \lambda_2)} = \frac{\langle I(\lambda_1) I(\lambda_2) \rangle - \langle I(\lambda_1) \rangle \langle I(\lambda_2) \rangle}{\sqrt{\langle I^2(\lambda_1) \rangle - \langle I(\lambda_1) \rangle^2} \sqrt{\langle I^2(\lambda_2) \rangle - \langle I(\lambda_2) \rangle^2}} \quad (\text{Eq. II.8})$$

The resulting values of $\rho_{(\lambda_1, \lambda_2)}$ lying between -1 and 1, allow us to determine the correlation status between the corresponding wavelengths and understand their behavior relative to each other. A correlation value of $\rho_{(\lambda_1, \lambda_2)} = 0$ indicates that there is no correlation between the two

wavelengths. As the value approaches 1 or -1, the correlation gradually increases or decreases, respectively, indicating a positive or negative correlation between the corresponding wavelengths.

The simplicity and ease of DFT implementation, and its ability to provide valuable information have led to its widespread use in numerous studies and applications over the years [213], [214], [215]. Specifically, in the understanding of nonlinear processes such as FWM and MI, DFT techniques can reveal hidden features and patterns in the spectral domain that may not be apparent in ensemble measurements or averaged data. DFT has nowadays become a standard approach for detailed real-time measurements of noise across a full spectral range such as supercontinua, providing insight into fluctuation statistics [205], [208], [216]. It offered a significant advancement in this field of ultrafast photonics, and the extraction of correlation metrics made it a valuable tool for analyzing noise-driven processes in nonlinear fiber propagation.

To summarize, we emphasize that pulse properties control and characterization is a complex subject. It necessitates an understanding not only of the interplay between temporal and spectral parameters but also of their distinct influences on nonlinear dynamics propagation and the generation of new frequency components during spectral broadening. A wide array of tools and combinations of approaches exist for managing these properties or even controlling them using machine learning techniques. The more comprehensive our access and manipulation of pulse properties, the greater our degree of control and precision in fine-tuning nonlinear dynamics and output waveform properties.

Various methods exist to study and understand the behavior of both the input output optical signals, each associated with unique advantages and limitations. Among these, the DFT technique is a well-known method enabling real-time characterization and comprehensive access to spectral attributes. DFT has been extensively studied over the years for different applications and has been refined through diverse approaches, which will be thoroughly examined in Chapter III. However, depending on our specific objectives and applications, each technique might carry some limitations, thus making important the exploration of new characterization approaches.

Chapter III. Ultrasensitive DFT-based characterization technique

The dispersive Fourier-transform is a well-known characterization technique used in various applications due to its potential in studying complex nonlinear phenomena within the field of photonics and nonlinear optics. To explore this technique and understand its various implementations, we propose in **Section III.1** an overview explaining the advantages and limitations of this technique. Over the years, several DFT-based characterization approaches have been implemented to overcome these limitations and answer particular application requirements. We delve into its multifaceted applications, showing how it has become a cornerstone in diverse fields such as laser development, ultrafast optics, and imaging applications. Specifically, the section explains how DFT has been used to characterize incoherent nonlinear processes such as modulation instability and frequency conversion phenomena, enabling a deeper understanding of complex noise-driven dynamics during nonlinear propagation. In **Section III.2**, we focus on the employment of such frequency-to-time techniques in the world of quantum science. Combined with single-photon detectors (SPDs), these techniques play an important role in characterizing non-classical states of light through the measurement of joint spectral intensity or second-order autocorrelation functions. Taking advantage of the frequency-to-time mapping DFT technique by leveraging multiple single photon detectors, we present in **Section III.3** a new DFT-based approach at the boundary between nonlinear and quantum optics to characterize complex nonlinear phenomena, specifically modulation instability, with unprecedented sensitivity, dynamic range, and resolution. In this section, we explain the methodology of our approach, describing the developed experimental setup and how it allows for a direct access to inter- and intra-pulse dynamics during MI measurements. Such technique provides an ultrasensitive characterization using mutual information analysis to reconstruct the correlation maps and study different behaviors of nonlinear instabilities. In this framework, a comparative study of different DFT implementations and statistical analysis methods is presented in this section, allowing to highlight the improvements of our new approach regarding “standard” DFT detection. The section highlights the advantages of our approach, showing experimental results that demonstrate the efficacy of our technique in detecting and characterizing modulation instability observed under challenging experimental conditions.

III.1. The dispersive Fourier-transform technique: Overview & applications

As already briefly discussed in section II.4.2, DFT is a widely used technique that allows us to perform real-time detection of temporal spectra and has become a standard characterization tool in a wide range of applications [199], [217]. It has been extensively used in laser development, allowing for precise characterization of laser pulses and their spectral properties [213]. DFT has also found applications in ultrafast microscopy and contributed to the development of better resolution, broadband, and real-time spectroscopy techniques [218], [219]. Additionally, DFT can be employed for velocimetry applications by enabling high-speed imaging, tracking, and measurement of vibrations and shockwaves, providing real-time analysis and characterization of their dynamics and interactions [220], [221]. In nonlinear fiber optics, the deployment of DFT has brought about significant advancements in the measurement and analysis of diverse phenomena [80], [208], [222].

One notable application lies in the characterization of supercontinuum generation and the formation of optical rogue waves [80]. By directly accessing single-shot fluctuations across the

full spectrum (see section II.4.2), DFT allows for the identification of the optical process statistics and the detection of outliers within the broadband spectrum. Furthermore, DFT plays a pivotal role in studying complex fluctuating noise-driven dynamics during nonlinear propagation processes, such as broadband incoherent supercontinua, or modulation instability dynamics [223]. The technique enables the monitoring of the spectral fluctuations and the quantification of correlation functions (such as Pearson's Correlation) which offers insights into spectral stability and the impact of external factors on the process dynamics [210], [205].

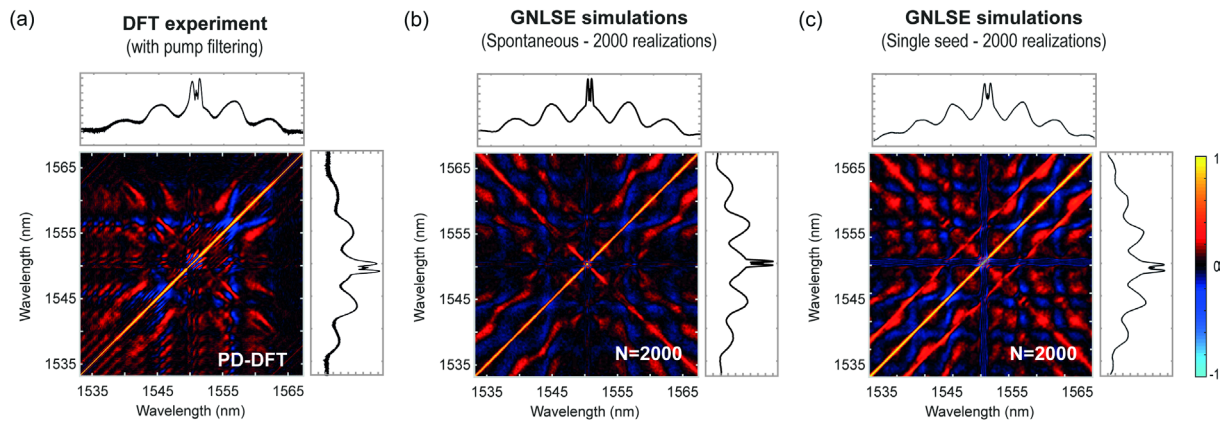


Figure III.1 (a) Average OSA spectrum and Pearson's correlation map extracted from a DFT measurement using a DCF with a dispersion $D_{DFT} = 478 \text{ ps/nm}$, of 500 fluctuating spectra in a spontaneous MI regime. (b) Corresponding numerical results using GNLSE simulations with 2000 random Monte Carlo realizations with different noise seeds. (c) Same numerical results as (b) but adding an incoherent weak seed (-35 dB) to the pump before nonlinear propagation (seed with a frequency detuning of 800 GHz and a relative spectral phase $\phi=0$).

For example, in Figure III.1.a, we show the statistical analysis of a DFT measurement of a 60 ps Gaussian pulse propagating in a 500 m - HNLF. The DFT spectra were recorded experimentally with a photodiode and an oscilloscope with pump filtering to gain a better dynamic range on the spectral fluctuations of the MI sidebands. The correlation maps are extracted using Pearson's correlation equation (Eq. II.8). For comparison, the same conditions were simulated numerically using the GNLSE equation (section I.3.2 and section I.3.3) with 2000 realizations, each with a different input noise seed (Figure III.1.b). The averaged output spectrum is displayed for both cases, and the fluctuating spectra are used to construct the corresponding correlation maps.

The correlation maps offer detailed statistical insights into the links and relationships among various spectral components within the analyzed incoherent spectrum. In this instance, they facilitate the examination of the effects of noise on the MI dynamics, the FWM cascades, and nonlinear broadening characteristics. Moreover, they have broader application in identifying significant attributes in nonlinear optics, encompassing phenomena like soliton spectral variations, pulse interactions, localized energy depletion, and spontaneous/stimulated conversion processes [208], [210], [205], [207], [224].

Additionally, DFT can serve as a means to quantify the impact of external factors on the spectral stability of nonlinear fiber systems. For example, by assessing variables such as optical seeding (Figure III.1.c), DFT-based monitoring offers a quantitative approach to understand how these factors influence the spectral behavior [225], [226], [227]. Here, we added an extremely weak optical seed (35 dB spectra attenuation compared to the pump) with an 800 GHz frequency detuning from the pump. As we can see, even though the seed has a very low

intensity regarding the pump, the correlation maps were modified due to the effect of the added signal on the nonlinear propagation dynamics in the fiber and thus, on the resulting spectral broadening.

In this example, the impact of such an extremely weak optical seed is fairly moderate, and the spectral correlation signatures remain qualitatively similar. Still, this effect is noticeable (at least from a numerical viewpoint) and understanding how the parameters of these factors can change the output spectrum and the correlations between the spectral components is a key to enable fine control and tailor the dynamics towards the desired properties. DFT is, in this context, an excellent experimental tool to assess the impact of optical pulse shaping and control methods described in Chapter II on adjusting relevant spectral broadening dynamics.

However, as all other techniques, DFT has some limitations, mainly related to the optoelectronic devices used for detection. Despite important technological advancements, ultrafast photodiodes and high-speed oscilloscopes are typically limited to a few tens of GHz in terms of their detection bandwidth, which imposes a constraint on the overall system, impacting the maximum spectral resolution achievable with respect to the signal bandwidth and repetition rate. Additionally, photodiodes exhibit limited sensitivity with poor noise figures, and high-speed oscilloscopes, typically equipped with 8-12 bits digitalization, suffer from a reduced dynamic range [197]. The combination of limited sensitivity and dynamic range leads to restricted real-time spectra with typically less than 30 dB contrast, which falls short of the requirements for characterizing incoherent broadband pulses in demanding signal processing applications [147], [228].

Several improvements in DFT techniques have been implemented over the years to address these challenges (see Figure III.2). For example, in order to adjust the spectral resolution, the amount of dispersion can be adjusted before measuring the temporal profile of the optical signal. This can be achieved by using different fiber dispersions/lengths or employing (switchable) recirculating fiber cavity loops, as illustrated in Figure III.2.b. By adjusting the amount of dispersion, one can effectively control the extent of temporal broadening and, consequently, the equivalent spectral resolution of the DFT measurements. Additionally, advanced processing techniques and the use of more sophisticated algorithms can help extract more information from the measured data, enhancing the accuracy and resolution of DFT measurements [222], [224]. However, even with these adjustments, DFT still encounters limitations imposed by the spectral bandwidth of the optical signal and its repetition rate (that may lead to temporal overlap between successive DFT signals).

In this context, one can also rely on pulse picking and/or selective spectral filtering to avoid the overlap of successive time-stretched waveforms and achieve extremely high spectral resolution (see Figure III.2.c). With such approaches, extreme DFT temporal stretching leads to a drastic decrease of the “power temporal density” of the stretched pulse (i.e. the “local” temporal intensity of the DFT stretched spectrum): the energy of the pulse is further spread temporally, making it necessary to have an improved detection sensitivity to accurately measure the weakest pulses or spectral components. It is important to acknowledge that DFT relies on a linear dispersive process. This means that the achievable detection quality is inherently limited by the available power (to avoid undesirable nonlinear effects). Therefore, there exists a tradeoff between the limited spectral power density and sensitivity versus the bandwidth and spectral resolution in DFT measurement schemes.

To address the decreased measurable power levels resulting from the substantial spectral time-stretching, amplified DFT approaches have emerged as an alternative. This involves

integrating an active amplification scheme into the DFT setup, effectively amplifying the optical signal conjointly with the time-stretching process [229]. These schemes mitigate power reduction and compensate for the overall system losses caused by temporal elongation. This is accomplished by enhancing the signal strength, therefore enabling more robust spectral analysis.

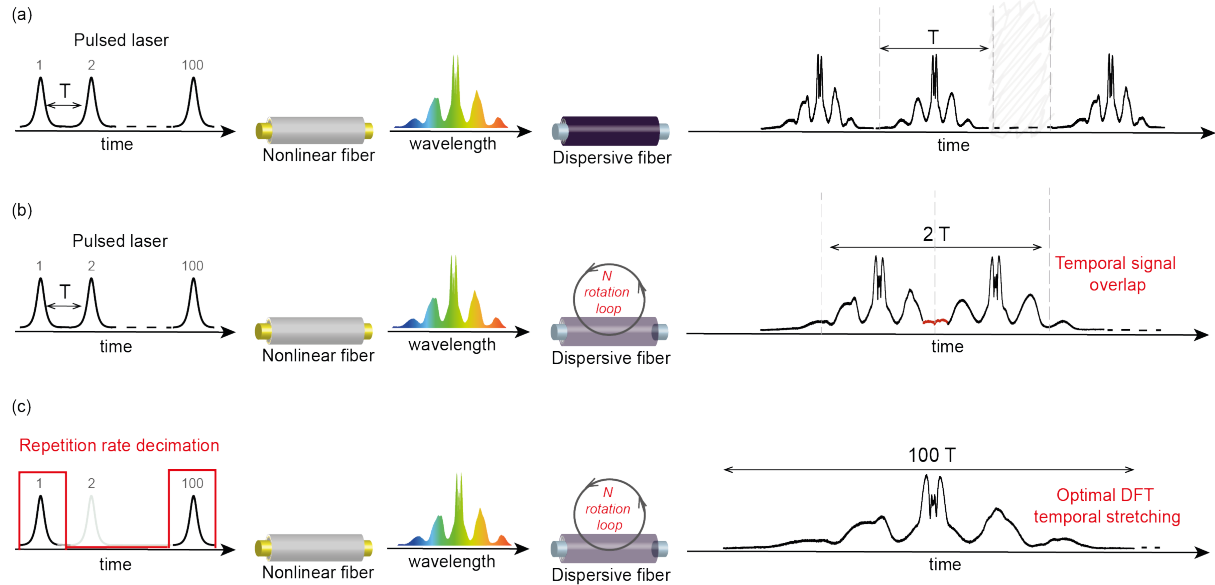


Figure III.2 Example of DFT schemes and mitigation techniques for achieving enhanced spectral resolutions (a) Schematic of the DFT of a pulse train broadened after propagation in an HNLF. (b) Enhancement of the equivalent spectral resolution of DFT measurements by tuning the amount of dispersion. This can lead to a temporal overlap between successive time-stretched waveforms. (c) Pulse picking can be employed on the initial pulse train, to mitigate pulse temporal overlap and enable extremely high resolution. This comes at the expense of reducing temporal intensity of the DFT stretched waveform.

In addition, the inherent repetition rate limitation of DFT poses challenges when studying high-repetition laser sources due to the temporal overlap of stretched pulses in dispersive fibers. Although methods like compressive sensing have been used to address this, they can be complex and require extensive post-processing [230]. Consequently, DFT has found its primary use in sources with lower repetition rates, typically in the MHz range. However, emerging laser cavity solitons in microcavities provide a new approach for generating high repetition-rate frequency combs [231]. These microcombs offer distinct advantages such as broad spectral ranges and enhanced mode efficiency. Their setup involves nonlinear Kerr micro-cavities seeded externally or typically integrated within fiber loops. Yet, the intrinsic repetition rate of these microcombs is often incompatible with DFT. To bridge this gap, optical sampling via an electro-optical modulator and a pulse generator may be used to decimate (i.e. lower) the repetition rate of the signal, creating manageable temporal stretches that avoid overlap [232], [233]. This modulation strategy generates groups of pulse(s), each treated as a single unit for temporal analysis. A DFT diagnostic is then applied to these modulated pulse groups, providing insight into the system's dynamic behavior.

Despite the limitations and challenges associated with DFT, it has still been found to be beneficial in various applications. For example, laser systems, particularly mode-locked lasers, exhibit intricate dynamics like chaotic behaviors and nonlinear effects. DFT, along with high-speed digitizers, has enabled a detailed exploration of these dynamics in mode-locked lasers,

which have significant roles in optical technologies. It offers insights into the instabilities and interactions of dissipative solitons [214], and allows in-depth analysis of pulse evolution, contributing to applications like multiphoton microscopy and frequency combs [217], [234]. DFT helps track the transition from noisy to steady-state regimes and even retrieves field autocorrelation information [213], [235]. This technique has revealed intricate behaviors like soliton explosion and bound state formation, where multiple solitons create a “soliton molecule” [236]. DFT-based spectral interferometry can be used to characterize these molecules, their binding properties, and complex dynamics like break-up and collisions. Beyond solitons, DFT has allowed broader studies of nonlinear phenomena like extreme events formation in fiber optics and the optical Sagnac effect in laser oscillators [236].

DFT-based techniques were also leveraged in imaging applications as they enable capturing ultrafast phenomena [237], [238]. Serial time-encoded amplified microscopy (STEAM), which is an amplified time-stretch imaging technique, that has been developed to replace convolutional imaging methods which fall short of capturing such events [220], [229]. STEAM is a real-time imaging technique that encodes temporal information onto ultrashort pulses' spectral profiles, and then maps this information into the time domain using DFT. The resulting data is recorded using high-speed digitizers and relies on substantial signal amplification to compensate for losses due to time-stretching. A specific application of this technique was for instance demonstrated to track laser-induced supersonic shock waves (SWs). Time-stretch imaging was used to capture the entire dynamics of individual SWs and gather statistical insights into their fluctuations [239]. This study for instance provided a deep understanding of these dynamics and how they change over a short period of time.

While not exhaustively listed here, these demonstrations highlighted that, with different implementations of DFT tailored to specific needs, DFT has proved useful in providing valuable insights and monitoring capabilities in multiple areas of physics and beyond. Despite its limitations, DFT continues to find relevance and offers potential for improvement to further enhance monitoring capabilities and overcome the next challenges in demanding optical characterization.

III.2. Frequency-to-time mapping in quantum science

The importance of frequency-to-time mapping techniques, harnessing the concept of mapping frequency information onto the time domain, has emerged as a powerful tool in the field of quantum applications. Among others, it allows for the detailed analysis of quantum states and spectral properties and enables the precise measurement and characterization of specific quantum phenomena.

In this context, researchers have combined frequency-to-time mapping techniques with quantum technology to perform extremely sensitive measurements at the level of individual photons [199]. This involves sending a quantum optical signal, such as a single photon or photon pairs, into optical fibers using chromatic group velocity dispersion to associate spectral information with the arrival time of a photon at a detector. By measuring the photon's arrival time with high temporal resolution, it becomes possible to extract the photon spectral properties in a simple and straightforward manner [238]. This was applied, for example, in the analysis of spectral features of non-classical light sources, such as those generated through parametric down-conversion processes [240]. Moreover, this approach has overcome the traditional single photon coincidence into measuring high-resolution spectral characterization of two-

photon states [241], offering improved accuracy and resolution in characterizing photon pairs emitted from spontaneous parametric processes.

For instance, in many quantum applications, the *joint spectral intensity* (JSI) is a valuable property that provides insights into the quantification of probability distributions for photon pairs and the spectral correlations between photons in quantum systems. Such information can be measured indirectly using Fourier-transform spectroscopy, recording interference patterns between photon pairs as a function of an adjustable optical delay. This approach enables extracting valuable information about the spectral correlations between photons [242] but however experimentally requires sweeping the optical delay within impractical setup.

In contrast, direct measurements of this metric can be achieved by pairing frequency-to-time techniques with single photon detectors in order to study non-classical states of light in a time-of-flight (TOF) spectrometer configuration. This approach can not only enhance the precision and repeatability of spectral correlation measurements, but also allows for tailoring spectral properties of photon pairs to suit diverse quantum applications in experimental configurations like Hong-Ou-Mandel interference and two-photon spectral interferometry [243], [244]. Other frequency-to-time mapping techniques such as electro-optic time lenses [245] have enabled the manipulation of quantum light's spectral-temporal waveform. This manipulation has for instance implications for enhancing single-photon flux into spectrally narrowband absorbers and enables spectral-temporal photonic quantum information processing.

From a technical viewpoint, we note that avalanche photodetectors (APD) are the most widespread systems to detect individual photons in quantum experiments, and are usually complemented by time correlated single photon counting (TCSPD) module to measure coincidences between detectors — when e.g. two photons arrive at the same time. Importantly, over the last decades, APDs typically offering 100-200 ps resolution have been supplanted by superconducting nanowire single-photon detectors (SNSPD) providing excellent detection efficiency and temporal resolutions reaching below 50 ps.

Recently, we have leveraged this technological advantage with our collaborators at the Leibniz University of Hannover [246] and employed the dispersive Fourier-transform technique to directly map the spectral information of non-classical states of light.

Specifically, the joint spectral intensity of a biphoton state, generated through pulsed spontaneous parametric down-conversion (SPDC) within a periodically-poled lithium niobate (PPLN) waveguide, was directly characterize by means of the DFT technique. In this scanless delay configuration, time-resolved intra- and inter-pulse coincidence detections were achieved using low-jitter SNSPDs (25 ps) (see Figure III.3.a).

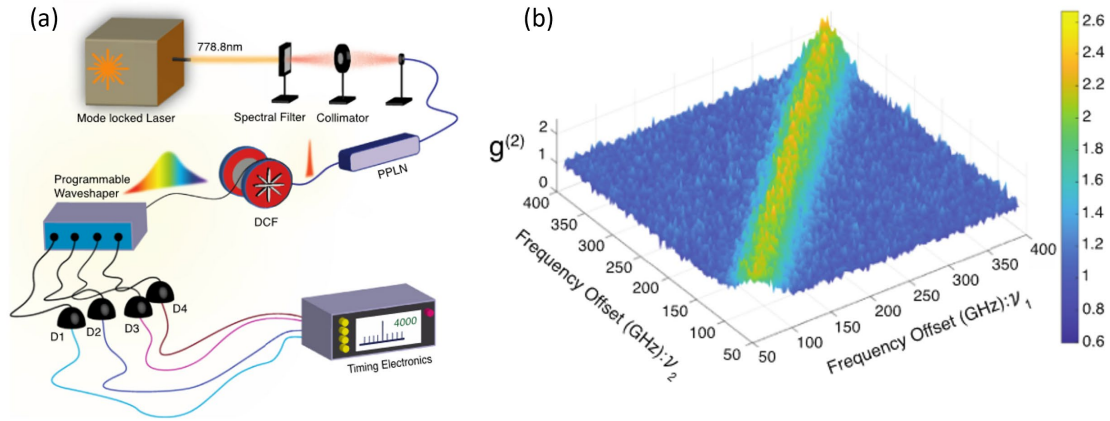


Figure III.3 (a) Experimental setup for SPDC spectral properties characterization in the temporal domain using the DFT technique and multiple single-photon detection (D1-D4): A $10 \mu\text{W}$ laser pulse centered at 778.8 nm with 50 MHz repetition rate, enters a PPLN waveguide. After down-conversion, the SPDC spectrum is time-stretched and converted in the temporal domain using the DFT technique via a DCF with a dispersion of $D_{DFT} = 960 \text{ ps/nm}$. Using a Waveshaper, the SPDC spectrum was then filtered within an 800 GHz bandwidth window (400 GHz for the signal, and 400 GHz for the idler regarding the degeneracy wavelength 1557.6 nm). Each 400 GHz - spectrum is then divided by a $50:50$ splitter and respectively sent into two single photon detectors (D1-D2, and D3-D4). (b) Reconstructed second-order autocorrelation function $g^{(2)}$, experimentally measured between the frequency offsets ν_1, ν_2 , with respect to the degeneracy wavelength (1557.6 nm), starting from $\nu_1 = \nu_2 = 50 \text{ GHz}$.

The setup was implemented through a Hanbury-Brown and Twiss (HBT) interferometry technique [247], [248] and resolved via the frequency-to-time mapping framework as described in Figure III.3. This setup allowed us to directly characterize the single frequency-mode bandwidth and for the first time, to show a direct measurement of the spectral second-order autocorrelation function $g^{(2)}$ (see Figure III.3.b) [246].

This concept is essential for studying the degree of quantum correlations, characterizing the quality of the generated quantum states, and ensuring their suitability for a variety of quantum applications. More importantly, such approach allowed to determine the single frequency-mode bandwidth $\delta\nu = 57.18 \pm 0.94 \text{ GHz}$ through the collected intra-pulse events, as well as the direct measurement of the JSI and the coincidence to accidental ratio (CAR) of the photon-pair source by collecting the time-resolved coincidence events corresponding to high-purity signal-idler photon pairs. This frequency-to-time mapping approach was demonstrated as an efficient and reliable method for the direct spectral characterization of biphoton states with high frequency resolution of $\nu_r = 3.03 \text{ GHz}$, which is at least 10 times higher than those reported in previous studies (see for e.g. [240], [241]).

In summary, the combination of both frequency-to-time mapping techniques and advances in single photon detector performances has paved the way for new studies and development in the field of quantum science, enabling the measurement and characterization of non-classical states of light with novel and potentially simplified/scalable experimental configurations.

It is worth noting that this experiment was performed at Leibniz University and that my contribution mostly remained on the study of the DFT signal processing and conversion rather than the quantum state characterization part of this study. However, this work was performed

hand-to-hand with the experimental study presented in the next section, and thus provided the theoretical foundation for the quantum-inspired DFT characterization of incoherent processes.

In this manuscript, I indeed focus on transposing this DFT approach for the analysis of nonlinear instabilities, which explores novel applications of these measurement techniques beyond fundamental research in quantum optics.

III.3. Ultra-sensitive DFT: Case study of MI in nonlinear fiber optics

In ultrafast optics, real-time characterization techniques have been widely used to study complex dynamics and phenomena with applications spanning diverse fields. In the preceding sections, we explored the importance of these techniques, especially the DFT technique, and the role they play in our understanding of nonlinear optical dynamics, via e.g. the analysis of spectral correlation features. We have also acknowledged the limitations inherent to traditional DFT implementations, stemming from the sensitivity cutoff and dynamic range constraints of the optoelectronic devices used for detection.

In this section, we present a novel approach that exploits the power of frequency-to-time mapping and the advantages of single-photon detection introduced in section III.2. Specifically, we implement a DFT-based technique through the use of low-jitter single-photon detectors for ultrasensitive characterization of nonlinear instabilities [222]. We delve into one specific phenomenon that has garnered considerable attention in nonlinear optics over the last decades: modulation instability, a complex noise-driven process that can significantly impact the behavior of optical pulses during propagation (see section I.5.2). In section II.4.2, we showed the need to accurately characterize such noise-driven dynamics using real-time characterization techniques. By combining the well-established concepts of DFT and single-photon detection (SPD-DFT) within the study of nonlinear optical processes, we stand at the boundary between nonlinear and quantum optics. Unlike traditional DFT implementations, this approach enables measurements at the single-photon level without the sensitivity and dynamic range limitations. Through experimental analysis, we highlight the advantages of this technique for the characterization of nonlinear noise-driven dynamics with ultra-high sensibility, resolution, and a theoretically unlimited dynamic range.

As discussed earlier, DFT-based techniques provide the capability for real-time spectral fluctuation measurements, usually followed by a comprehensive statistical analysis that involves the examination of correlation among distinct spectral components using Pearson's correlation coefficient (Eq. II.8).

Here, the SPD-DFT-based method brings forth a different but advanced capability for correlation measurements: Employing a pair of single photon detectors (SPDs) enables the investigation of both inter and intra-pulse dynamics as required for incoherent optical signal analysis. With an associated timing module (time-tagger), we can perform a time stamp acquisition of each detected photon by recording the precise arrival time of each photo-event registered by the time-tagger. Combined with DFT, the SPD detection is analogous to an ultra-sensitive spectrometer, where the probability of detecting a photon within a specific time interval, known as a time-bin, is directly connected to the spectral intensity $I(\lambda)$ of the signal being studied. In this context, after applying the time-to-frequency conversion provided by DFT (Eq. II.7), the probability of detecting a photon at a particular wavelength λ_i can be deduced from the analysis of these recorded time stamps (t_k). This allows to construct a probability density function for the overall N detected photons, given by:

$$P_{\lambda_i} \equiv P_{t_i \pm \frac{\Delta\tau}{2}} = \frac{1}{N} \sum_{k=1}^N t_k \in \left[t_i - \frac{\Delta\tau}{2}; t_i + \frac{\Delta\tau}{2} \right] \quad (\text{Eq. III.1})$$

(Eq. III.1) introduces $\Delta\tau$ as the width of the time interval in the time-tagger analysis. The time-stamp t_k corresponds to the timing of the k -th event relative to the laser period t_{laser} , within an integration time, spanning multiple laser pulses with indices n_k . The absolute event time, $t = n_k t_{laser} + t_k$, is influenced by the joint timing jitter [222] of the SPD and time-tagger, which is here approximate to $\sigma_t = 25 \text{ ps}$. To rigorously account for timing uncertainty, the actual probability distribution P_{t_i} is convolved with a Gaussian distribution of standard deviation σ_t . This analysis yields to the spectral resolution σ_λ of the quantum-inspired DFT measurement, linked to the dispersion D_{DFT} of the dispersive fiber by the relation $D_{DFT} = \sigma_t / \sigma_\lambda$, and guides the choice of the minimum time-bin width $\Delta\tau$ achievable for the DFT signal analysis.

To demonstrate how our proposed approach works, we illustrate in Figure III.4, the photon detection process recorded from each single photon detector to calculate the joint probability denoted as $P_{\lambda_1, \lambda_2} = P(\lambda_1, \lambda_2) = P(\{\lambda_{SPD1} = \lambda_1\} \cap \{\lambda_{SPD2} = \lambda_2\})$, which represents the possibility of detecting at the same time a photon with a wavelength λ_1 by the first detector (SPD1) and a photon with a wavelength λ_2 by the second detector (SPD2). The coincidence detection can be selectively applied to analyze two types of photon events: Intra-pulse events (blue arrows), where the detected photons originated from the same laser pulse ($n_{k, \lambda_1} = n_{k, \lambda_2}$); or inter-pulse events (red arrows), where the detected photons come from different laser pulses so that $n_{k, \lambda_1} \neq n_{k, \lambda_2}$.

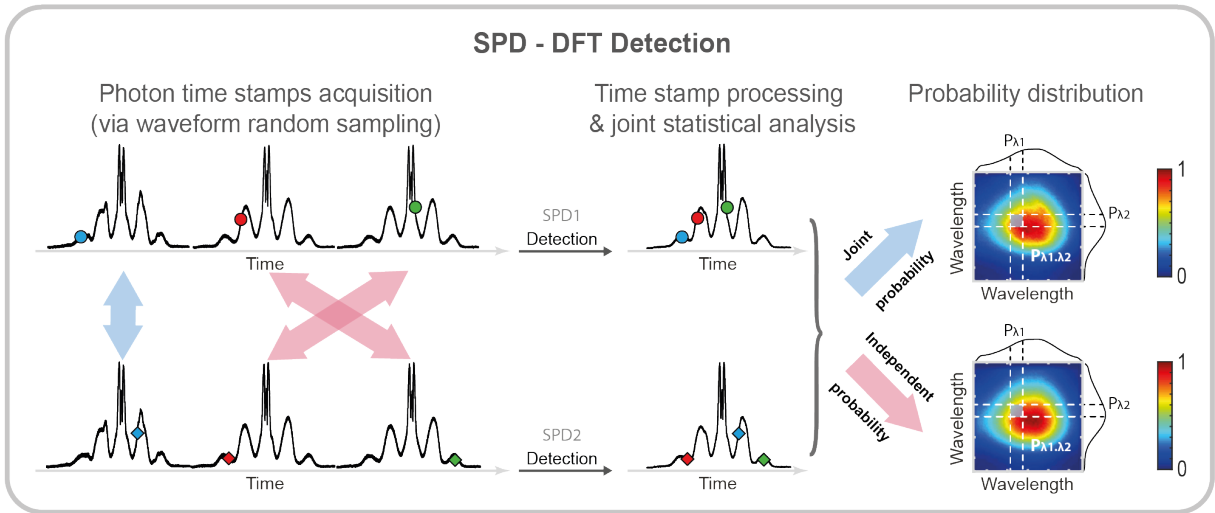


Figure III.4 Principle of DFT detection via two single photon detectors (SPD-DFT): The intra-pulse and inter-pulse dynamics are differentiated by blue and red arrows, respectively. The corresponding joint and independent probabilities between the detected photo-events in the spectral domain (λ_1 and λ_2), represented with 2D maps allow for the reconstruction of mutual information correlation maps.

To extract spectral correlation features with this approach, and access to both inter- and intra-pulse dynamics, we use a statistical tool called *mutual information analysis* (MIA) [224]. Here, the MIA allows us to statistically quantify the relationships between the spectral components, considering both linear and nonlinear dependencies. This approach has proven valuable in understanding various complex processes such as parametric phenomena in laser physics (as already explained in section III.2). In our system, by employing the MIA (i.e. a differential/

relative metric), we can overcome potential biases and uncertainties present in (Eq. III.1), arising from factors like the SPD deadtime, quantum efficiency, and wavelength dependence. The combination of SPD-DFT and MIA provides highly-sensitive measurements while ensuring unbiased statistical analysis of conditional probabilities and spectral correlations of incoherent nonlinear dynamics. To calculate the MIA between two wavelengths λ_1 and λ_2 we rely on both the joint and marginal probabilities following the equation:

$$\mu_{(\lambda_1, \lambda_2)} = P_{\lambda_1, \lambda_2} \log \left(\frac{P_{\lambda_1, \lambda_2}}{P_{\lambda_1} P_{\lambda_2}} \right) \quad (\text{Eq. III.2})$$

To validate our approach, we developed at Leibniz University Hanover (group of Prof. Kues at the Institute of Photonics), the experimental setup illustrated in Figure III.5. A 50 MHz laser (Menlo Systems – C-fiber) emitting 80 femtosecond hyperbolic secant pulses at 1550.65 nm is sent into a spectral programmable filter (Finisar, Waveshaper 4000A). The broadband signal is filtered -with a 15 GHz bandpass filter (FWHM \sim 0.12 nm)- into a 55 ps pump with adjustable peak power values ranging from 0.8 to 2 mW (via controlled Waveshaper attenuation), ie, an average power ranging from 2.4 μ W to 5.7 μ W. After spectral filtering, this picosecond pulse is then amplified using an EDFA with a constant laser pump current of 880 mA to attain up to \sim 25 mW average power (\sim 2.7 W peak power), while the intrinsic ASE noise of the EDFA is filtered via a bandpass filter of \sim 0.8 nm bandwidth (Newport TBF-1550-1.0). The signal is then sent into a 485 m HNLF where it experiences a nonlinear spectral broadening typically associated with spontaneous MI dynamics (see section I.5.2.2).

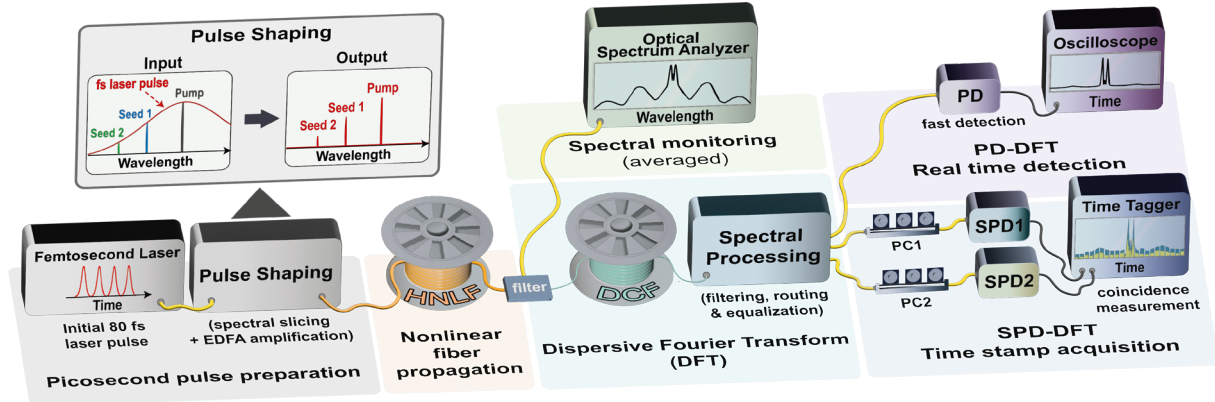


Figure III.5 Experimental setup showing the comparison between standard DFT with fast photodiode (PD) and our novel approach using ultra-sensitive single photon detectors (SPDs) for the spectral characterization of incoherent MI dynamics.

After fiber propagation, the incoherent broadband signal was analyzed by either an averaged OSA measurement, or a DFT characterization using a DCF fiber of a dispersion $D_{DFT} = 468 \text{ ps/nm}$. Here we note that, to get a better dynamic range, we employ a notch filter to remove most of the pump before injection in the DCF. After DCF propagation, the temporally stretched spectrum extends over a temporal span of almost 19 ps, which corresponds to a spectral bandwidth at 35 dB ranging between 1530 nm and 1570 nm.

To demonstrate the improvement of this DFT-based approach, we here perform an experimental comparison between the standard DFT using a fast photodiode and an oscilloscope featuring a 6 GHz detection bandwidth (PD-DFT), and our new approach through the use of two single photon detectors (Single Quantum, Multi-channel SNSPD) and

associated with a time tagger (Swabian Instruments, Time Tagger Ultra) with 25 ps jitter, which would correspond to a 40 GHz bandwidth (SPD-DFT). In this case, both DFT implementations were synchronized with the 50 MHz laser to facilitate a direct comparison between the two measurement techniques. An additional programmable filter (Finisar, Waveshaper 4000A/X) is also placed after the DCF, having the capability to selectively filter specific sections of the output spectrum (see Figure III.7), or equalize different spectral components of the DFT detected signal (see Figure III.13).

As in this work, our goal is to study the nonlinear dynamics of modulation instability, it is important to understand the behavior of MI in our experimental configuration. In our experiment, a 55 ps laser pulse propagates in the anomalous regime of a custom-designed HNLF (Germanium-doped silica fiber). In such conditions, the pulse will experience a nonlinear spectral broadening, governed by the self-focusing nonlinear Schrödinger equation (NLSE) [212] and typically lead to the generation of incoherent supercontinuum [249]. Modulation instability is here considered as the initial stage of such SCG, which will occupy our main studies for now.

To visualize the realistic pulse evolution and associated MI formation, the pulse propagation within our experimental conditions is modeled using the generalized nonlinear Schrödinger equation (GNLSE), numerically solved with a split-step Fourier method [249] (see Figure III.6). The 55 ps pulse centered at $\lambda_0 = 1550.65$ nm and with a peak power $P_0 = 2.7$ W propagates within a 485 m of HNLF with dispersion parameters $\beta_2 = -1.78$ ps².km⁻¹, and $\beta_3 = 0.07$ ps³.km⁻¹ and a nonlinear parameter is $\gamma = 8.4$ W⁻¹.km⁻¹.

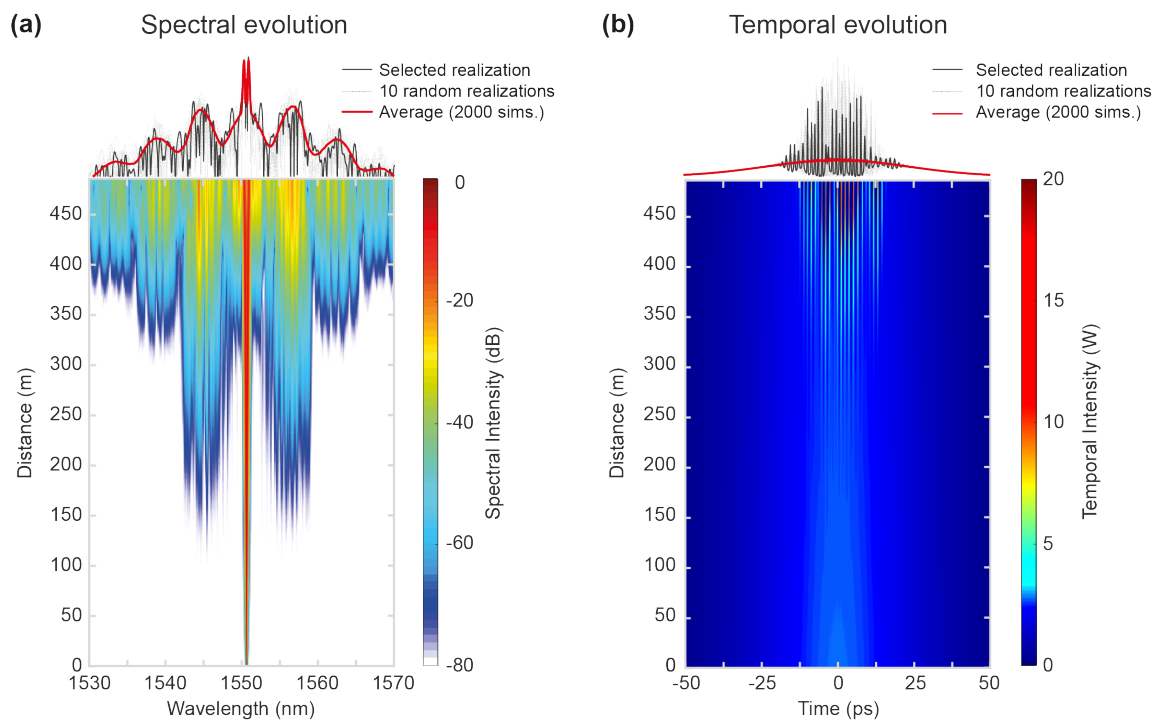


Figure III.6 Pulse spectrum broadening through noise-driven MI in both (a) spectral and (b) temporal domains. Top panels: Results of Monte-Carlo simulations with 2000 different noise seeds (i.e. vacuum noise with one photon with random phase per spectral bin) showing spectral and temporal fluctuations for 10 realizations (grey traces), and one randomly selected realization (black trace), compared to averaged spectra (red) representative of an OSA measurement. Bottom panels: Corresponding spectral and temporal pulse evolutions of a randomly selected realization (i.e. black traces on the top panel).

The figure above shows the numerically computed evolution of the pulse in both the spectral domain (Figure III.6.a) and the temporal domain (Figure III.6.b), with a spectral broadening mediated by spontaneous MI. Initially, at around ~ 120 m of propagation, the first sidebands of the MI start to appear. These sidebands originate due to noise amplification within the MI gain region, symmetrically surrounding the pump frequency. Progressing through propagation, the pump pulse undergoes self-phase modulation effects [24]. Beyond approximately ~ 310 m of propagation, cascaded four-wave mixing (FWM) takes place, leading to the development of higher-order MI sidebands (which can act as secondary pump sources for FWM conversion [212], [250], [66]). Temporally, this cascaded MI process triggers the growth of localized femtosecond structures onto the envelope of the initial picosecond pulse [200]. This behavior corresponds to the onset of soliton fission phenomenon, which precedes and condition incoherent supercontinuum formation in a regime characterized by weakly anomalous dispersion [249].

In the top panels of Figure III.6, numerical Monte-Carlo simulations stemming from 2000 different initial noise seeds capture the shot-to-shot spectral and temporal fluctuations associated with the pulse incoherent propagation. These fluctuations are illustrated by the grey traces for 10 realizations and, in black, for one randomly selected realization, which propagation dynamics corresponds to the one shown in the MI evolution maps. In red, we added the averaged spectrum and temporal intensity profiles which highlight the limitations of practical experimental methods, such as optical spectrum analyzers, with extended integration times that intrinsically smooth out output fluctuations over numerous pulse periods.

III.3.1. Comparison of DFT characterization techniques and statistical analysis

To compare the outcomes from different approaches and embark on a comprehensive examination of spectral variations tied to modulation instability (MI), we rely on three distinct methods: OSA, PD-DFT, and our proposed SPD-DFT, as illustrated in Figure III.7.

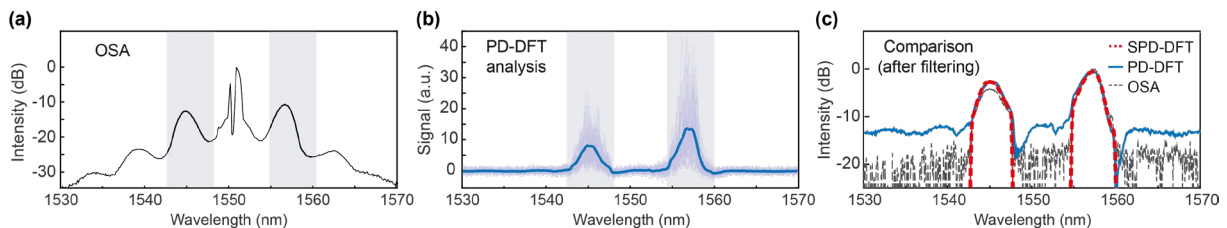


Figure III.7 Output MI spectrum detected by various detection methods: (a) OSA spectrum with the first MI sidebands highlighted in grey, (b) 500 fluctuating spectra (light dotted lines) obtained from PD-DFT detection and the resulting average spectrum (thick solid blue line), achieved by filtering the first MI sidebands (grey-shaded), (c) Comparison between the average SPD-DFT (dashed red), the average PD-DFT (solid blue) and an OSA (dotted grey) measurement of the 1st sidebands MI output spectrum. The figure underscores a good agreement between these methods within a limited dynamic range above the detection noise floor.

In particular, we focus on a specific spectral region: the initial MI sidebands adjacent to the pump (see section I.5.2 – the MI gain $G_{MI}(\omega_{mod})$). The symmetrical 1st MI sidebands, centered at 1545 nm and 1557 nm, and highlighted in grey on the obtained OSA spectrum (Figure III.7.a), lie within an intensity range of approximately 13 dB. When applying the PD-DFT technique, as illustrated in Figure III.7.b, and by filtering only these sidebands for the analysis, we exploit the optimal dynamic range provided by our 8-bit optoelectronic detection system. This ensures that the captured fluctuations (light dotted lines) remain within a non-saturating range, reaching up to 24 dB in an ideal 8-bit digitization scenario. However, the most significant

aspect here comes from the agreement between the average spectrum obtained from the SPD-DFT measurements with the spectra obtained through experimental OSA and PD-DFT measurements as can be seen in Figure III.7.c. This compelling agreement underlines the validity of our SPD-DFT technique and showcases its ability to accurately capture the fluctuations associated with the MI spectral broadening phenomenon.

To further investigate the performances of our approach, we rely on the analysis of the spectral correlation maps. Overlong this chapter, we mentioned different statistical analysis methods that allow us to extract the correlation maps and understand the relation between the spectral components of the MI spectra and their different behavior during propagation.

In particular, we explained how, by performing a real-time DFT detection, we can detect the nonlinearly induced spectral fluctuations using fast optoelectronic devices and extract the correlation maps using Pearson's correlation method (see section II.4.2). For quantum applications (section III.2), we saw how the second-order correlation function $g^{(2)}$ is widely used to study the statistical properties of light [251] (indicating e.g. photon bunching ($g^{(2)} > 1$) or anti-bunching ($g^{(2)} < 1$) behavior) and to provide insight into the coherence properties of non-classical states of light [248]. Finally, for the DFT detection via SPDs, leveraging two single-photon detectors allowed for direct access between both inter- and intra-pulse dynamics, which further requires mutual information computing to obtain analogous correlation maps (see Figure III.4). Here, we extract the correlation maps corresponding to the first MI sidebands using different statistical methods:

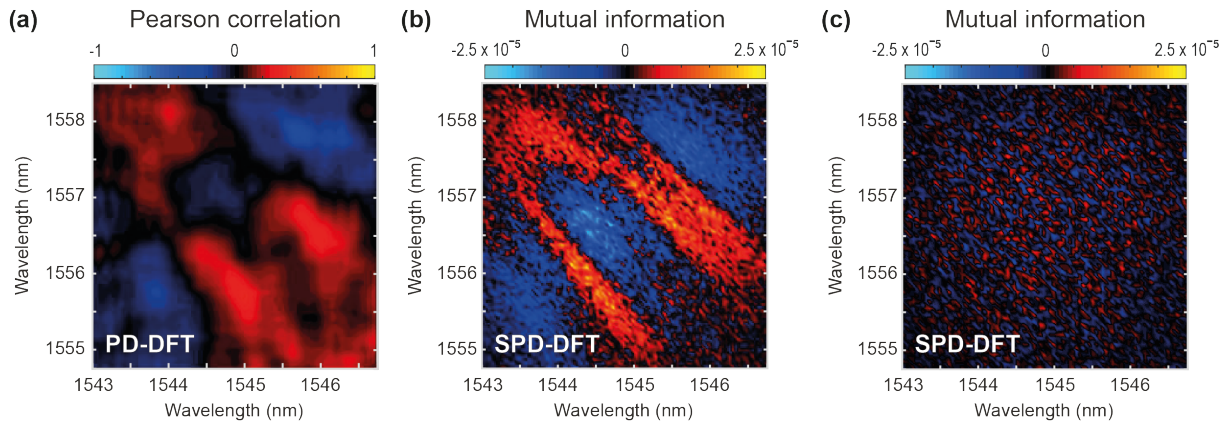


Figure III.8 Correlation analysis of the first MI sidebands. (a) Pearson's correlation map of the MI sidebands obtained from PD-DFT analysis. (b) Mutual information map of the MI sidebands obtained from SPD-DFT analysis (when considering intra-pulse events). (c) Mutual information map of the MI sidebands from SPD-DFT analysis (when considering inter-pulse events).

Starting with the standard DFT approach, we measure 500 shot-to-shot traces captured with PD-DFT using the 6 GHz photodiode and oscilloscope detection. The statistical analysis of the spectral correlation between the 1st MI sidebands was performed using the Pearson formula given in (Eq. II.8). As illustrated in Figure III.8.a, the reconstructed correlation map demonstrates characteristics of spontaneous MI phenomena [208], [205]. Within this map, we can analyze the effects of nonlinear spectral reshaping of the pump caused by SPM and the formation of cascaded sidelobes.

In Figure III.8.b, we show the SPD-DFT results, detected with the two SPDS via mutual information processing as provided in (Eq. III.2). Here, we can notice similar qualitative features between the two approaches, but with finer structures only visible with the SPD

detection and significantly enhanced spectral resolution. While with the PD-DFT we can get a 0.25 nm spectral resolution, the value is reduced to ~ 53 pm with the SPD-DFT technique.

In fact, for the MIA measurements, we calculated the joint probability P_{λ_1, λ_2} , by examining 8.5 million coincident photon detections between the two detectors within specific wavelength bins. This calculation was carried out while selecting photo events originating from the same input laser pulse. To obtain the independent probabilities P_{λ_1} and P_{λ_2} we computed the marginal of this joint probability distribution $P_{\lambda_1, \lambda_2}(n_{k, \lambda_1} = n_{k, \lambda_2})$. Importantly, we ensured the unbiased nature of this approach by calculating P_{λ_1, λ_2} based on the post-selection of coincident photo-events originating from inter-pulse events, where $n_{k, \lambda_1} \neq n_{k, \lambda_2}$. This study revealed that the corresponding mutual information was essentially negligible across the entire spectral map in this case, as shown in Figure III.8.c. Thus, we can confirm the absence of mutual information between inter-pulse events, ensuring that $P_{\lambda_1, \lambda_2}(n_{k, \lambda_1} \neq n_{k, \lambda_2}) \sim P_{\lambda_1} P_{\lambda_2}$.

In addition to its comparability with linear Pearson correlations, the MIA presents similarities with the second-order correlation function $g^{(2)}$, which serves as the intensity equivalent of the first-order correlation function, consisting in a standard tool for quantifying the coherence of classical optical signals [89]. Both SPD and PD-based DFT measurements enable the computation of the $g^{(2)}$ function and can be defined as follows:

$$g_{PD-DFT}^{(2)}(\lambda_1, \lambda_2) = \frac{\langle I_i(\lambda_1, \lambda_2) I_j(\lambda_1, \lambda_2) \rangle_{i \neq j}}{\langle |I(\lambda_1, \lambda_2)|^2 \rangle} \quad (\text{Eq. III.3})$$

$$g_{SPD-DFT}^{(2)}(\lambda_1, \lambda_2) = \frac{P_{\lambda_1, \lambda_2}(n_{k, \lambda_1} = n_{k, \lambda_2})}{P_{\lambda_1, \lambda_2}(n_{k, \lambda_1} \neq n_{k, \lambda_2})} \quad (\text{Eq. III.4})$$

Figure III.9 shows the results of the $g^{(2)}$ measurements for both cases, accompanied by a map representing the relative error computed between each DFT approach. This direct comparison between the two DFT techniques allows us to validate that not only do we have a qualitative similarity between the two, but also a quantitative agreement: The average root-mean-square error (RMSE) between the maps is 3.2%. This methodology proves valuable for examining linear and nonlinear correlations within broadband FWM, enabling to explore spectral bunching and anti-bunching within frequency conversion processes.

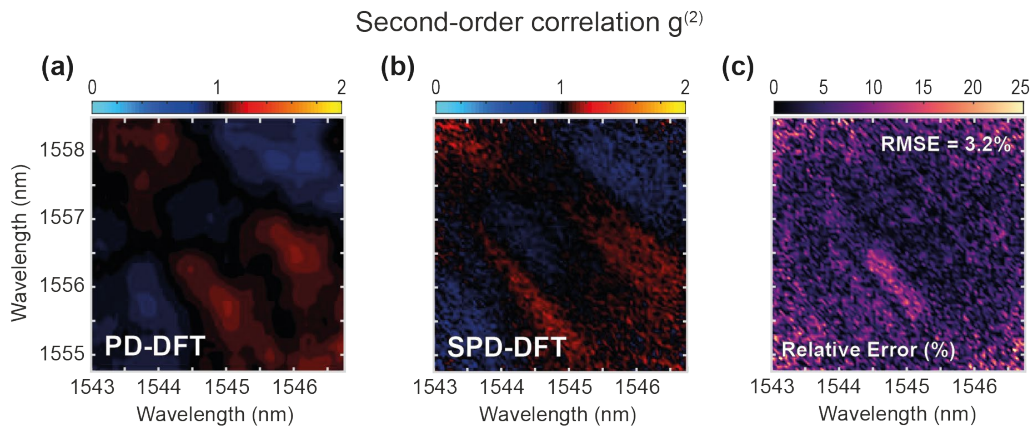


Figure III.9 Second-order correlation map $g^{(2)}$ derived from both (a) PD-DFT and (b) SPD-DFT measurements, along with (c) the relative error comparison.

Our SPD-DFT technique paired via mutual information analysis, enhances insights into noise-driven frequency conversion processes of nonlinear physics, leveraging quantum-inspired measurement techniques for improved sensitivity and spectral resolution beyond standard DFT approaches. In addition, it provides a valuable means to measure and understand intricate nonlinear correlation features within the incoherent broadband signal. For example, in Figure III.10, we represent the changes in the mutual information within the MI sidebands in response to varying optical pump power. When increasing the input pump power, we can see a shift in the spectral domain of the MI sidebands, accompanied by a nonlinear transformation of the pump pulse's shape during its propagation through the HNLF, which is a phenomenon attributed to the SPM effect. These alterations induced by the optical power change cause the spectral mutual information maps from featuring a single sideband to displaying complex correlation features and subsequent cascaded FWM processes in the higher-order MI sidebands.

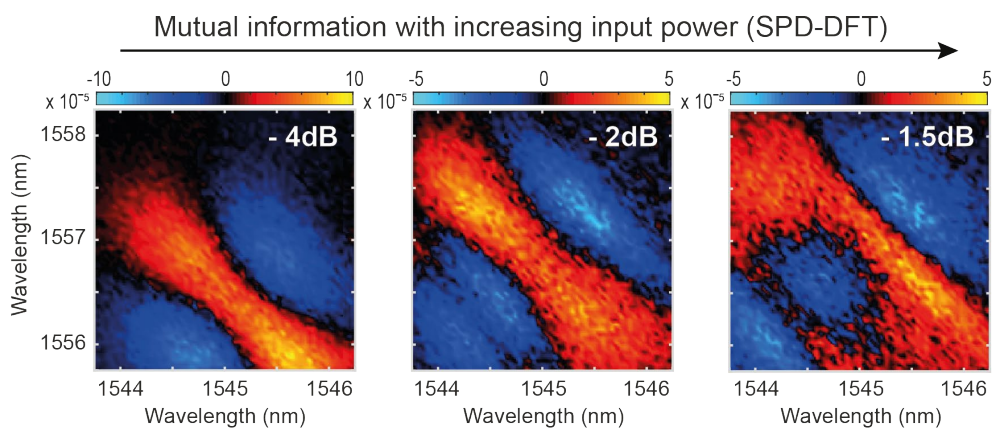


Figure III.10 Evolution of mutual information spectral maps within the MI sidebands with different input pump power adjusted by attenuating the input pump signal using the Waveshaper from -4 to -1.5 dB. The transition from a single sideband to more intricate correlation patterns reflects the emergence of nonlinear processes and cascaded FWM.

To thoroughly examine the differences and illustrate the potential limitations among various DFT architectures, we conducted a detailed experimental analysis shown in Figure III.11. In order to have a fair comparison between the two DFT approaches, we implemented a new setup by increasing the detection bandwidth of the PD-DFT system from ~ 5 GHz to 45 GHz. This bandwidth enhancement naturally improves the ability to resolve finer spectral details, but also simultaneously impacts the sensitivity, the signal-to-noise ratio (SNR), and the overall quality of the PD-DFT measurements.

It is important to note that these effects are of course more noticeable when dealing with the less prominent components of the MI spectrum. To examine this potential impact, we carefully set-up a new experiment with similar conditions to the ones described in Figure III.5. While we made several changes in terms of the laser source and EDFA amplification for the spontaneous MI spectral broadening, we made sure that the resulting output spectrum after nonlinear propagation matched qualitatively with the results of the initial setup, as seen in Figure III.7.a (here, achieved with a 21 mW input power).

In this case, our approach for the DFT time stretch involved using two different lengths of DCF, which provided distinct stretching factors: 403 ps/nm and 565 ps/nm, respectively. After temporal stretching and pump filtering, we achieved average powers of 320 μ W and 150 μ W, associated to the respective stretching factors (and linear attenuation) of the two different DCFs. In addition, an important aspect of our study was the PD-DFT detection using two

different experimental setups, each with a unique detection bandwidth. These setups were based on real-time oscilloscopes paired with photodetectors with specific characteristics outlined in Table III.1 Specifications of PDs, oscilloscopes, and total spectral resolution for different detection setups.. By considering these different detection conditions, we could determine the DFT spectral resolution based on the detection bandwidth and the chosen stretching factor.

PD-DFT setup characteristics		Detection #1 (low bandwidth)	Detection #2 (high bandwidth)
PD Specifications	PD model	Thorlabs (DET08CFC/M)	Newport (1014 InGaAs)
	PD detection bandwidth	5 GHz	45 GHz
	PD peak responsivity	0.9 A/W	0.45 A/W
	Noise equivalent power (NEP)	2 fW/ $\sqrt{\text{Hz}}$	45 fW/ $\sqrt{\text{Hz}}$
Scope specifications	Associated oscilloscope model	Rhode & Schwarz (RTO2064)	Tektronix (DPO77002SX)
	Oscilloscope detection bandwidth	6 GHz	70 GHz
	Oscilloscope ENOB	7.6 (for 22 dB dynamic range)	4.7 (for 14 dB dynamic range)
	Equivalent temporal resolution	200 ps	22 ps
Total spectral resolution	Spectral resolution with stretching factor $D_{DFT} = 403 \text{ ps/nm}$	0.496 nm	0.055 nm
	Spectral resolution with stretching factor $D_{DFT} = 565 \text{ ps/nm}$	0.354 nm	0.039 nm

Table III.1 Specifications of PDs, oscilloscopes, and total spectral resolution for different detection setups.

In each situation, we measured 500 fluctuating MI spectra and then used the data to create Pearson spectral correlation maps. We first only filter the pump signal and show the results in Figure III.11.a-b. These figures clearly demonstrate how the quality of the signal changes for the different setup conditions. For a meaningful comparison with Figure III.8.a, we also looked into measuring correlation maps after filtering only the first symmetrical MI sidebands, as shown in Figure III.11.c-d.

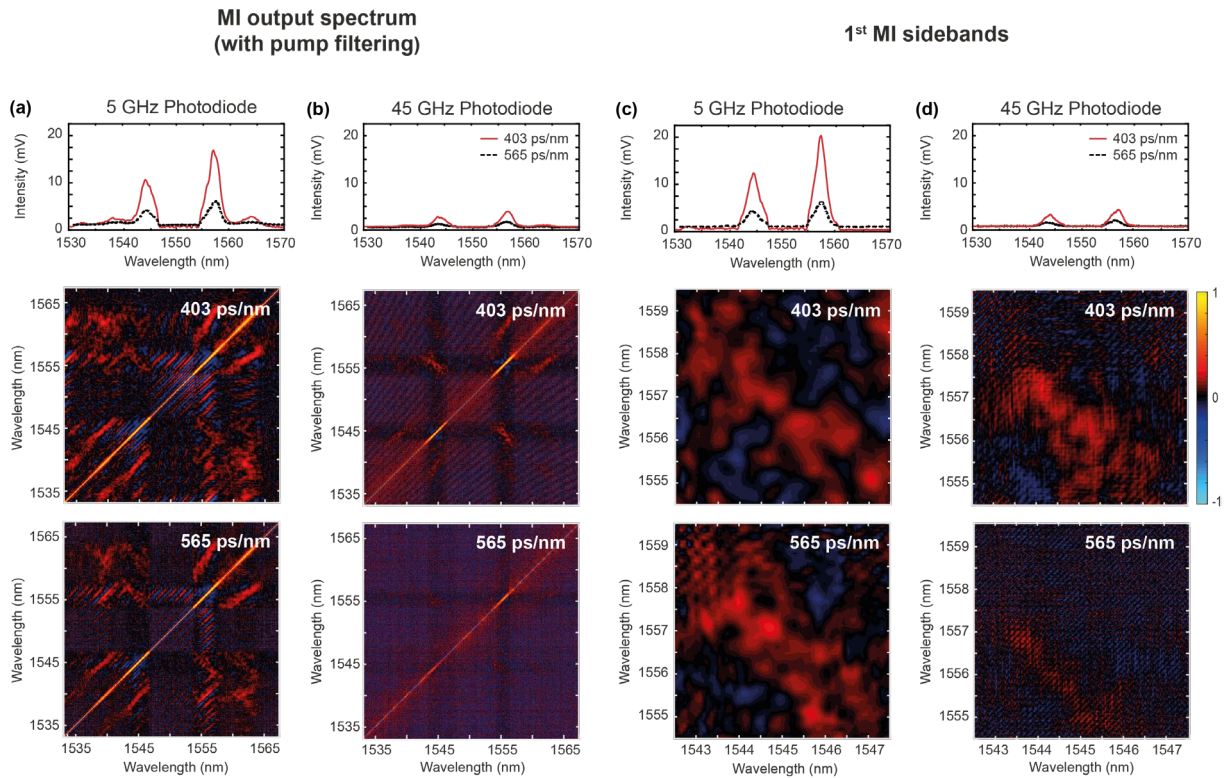


Figure III.11 Comparison of Pearson's correlation for MI spectrum measurements with different PD-DFT detection schemes: Top panels: Average spectra of 500 traces collected via PD-DFT detection using two different DCFs with a dispersive factor of respectively 403 ps/nm (solid red) and 565 ps/nm (dashed black). In (a) and (b), we represent the average spectra as well as Pearson's correlation maps of the DFT measurements with both DCFs, obtained from the MI spectrum with pump filtering, using a 5 GHz PD and a 45 GHz PD, respectively. In (c) and (d), we represent the average spectra and the zoomed-in correlation maps of the DFT measurements with both DCFs, obtained for filtering the 1st MI sidebands only, using a 5 GHz PD and a 45 GHz PD, respectively.

Through a careful comparison, a clear picture of the differences among the PD-DFT detections emerged. Notably, when we look at the average DFT output spectra, we deduced that the lower sensitivity of ultrafast photodiodes (45 GHz), resulted in a nearly fourfold decrease in the detected signal compared to the 5 GHz PD detection. The 45 GHz photodiode, while offering a wider bandwidth for improved temporal resolution, also yield a significantly higher noise equivalent power (NEP) compared to the 5 GHz photodiode, with the difference exceeding one order of magnitude. Additionally, the dynamic range of the 70 GHz oscilloscope experienced an approximately 8 dB reduction compared to its 6 GHz counterpart. This reduction was due to limitations related to the equivalent number of bits (ENOB) during high-speed analog-to-digital conversion. As a result, the 45 GHz detection approach faced a substantial challenge in obtaining sufficient signal magnitudes for effective analysis. This challenge led to a reduced SNR for signals with the lower intensity, thereby impacting the quality of analysis of such signals.

These limitations become particularly noticeable within the correlation maps displayed in Figure III.11.a-b. The 45 GHz detection setup demonstrates an admirable capability to reduce artifacts linked to the relatively slower impulse response of the 5 GHz photodiode. However, the compromises made in terms of sensitivity, responsivity, and dynamic range within our 45 GHz detection approach hindered the clear visualization of the MI patterns when examining the reconstructed correlation maps. When only focusing on the first sidebands (Figure III.11.c-

d), we observe traces of MI patterns with the 45 GHz detection, nevertheless, the signal intensity and the resulting SNR remain less than optimal for extracting correlation patterns related to the 1st MI sidebands.

In addition, the reduced sensitivity becomes quite evident when we compare different DFT stretching factors. Notably, with the increase in the temporal stretching, along with the associated losses that come with longer DCF there is a noticeable drop in peak power for PD-DFT signal detection (here, by a factor ~ 3). While this decrease has relatively minor consequences for the 5 GHz PD-DFT detection, it becomes much more significant for its 45 GHz counterpart. In fact, in the case of 45 GHz detection, it approaches the sensitivity threshold (i.e. noise floor) of such detection methods.

The limitations relevant to higher-speed PD-DFT, are also visible in the correlation maps, obtained when filtering only the first MI sidebands (Figure III.11.c-d). Despite the 45 GHz bandwidth offering improved DFT spectral resolution, the intricate correlation patterns of MI are somewhat washed out within the noise, due to the compromised overall SNR within the detection process.

From this analysis, we can deduce that the choice of an optimal bandwidth for PD-DFT requires a delicate balance between DFT spectral resolution and signal quality. While a wider bandwidth enhances temporal resolution, it inevitably brings about a decrease in sensitivity and dynamic range.

In addition, when we compare the maps obtained through PD-DFT and SPD-DFT, both carefully collected under identical conditions of detection bandwidth and spectral resolution (see Figure III.8.b and Figure III.11.d), the advantages of our approach over traditional DFT methods remain evident. This contrast emphasizes the benefits provided by SPD-DFT: an impressive combination of a high spectral resolution, sensitivity, and dynamic range. Notably, increasing the PD-DFT detection bandwidth with the 45 GHz bandwidth to align with our SPD-DFT configuration resulted in only marginal enhancements, and did not significantly improve the detection efficiency of the PD-DFT.

III.3.2. Analysis and control of cascaded FWM processes in noise-driven MI

To go further in the study of MI dynamics using DFT, we also investigated the mutual information maps obtained as a result of nonlinear broadening under two different input power conditions (i.e. at the maximum input power of the pump, and by attenuating the pump power using the Waveshaper with -2 dB). These mutual information maps, illustrated in Figure III.12, were acquired using the SPD-DFT technique and involved filtering different sideband combinations, thus providing insights into the correlation dynamics (within higher-order sidebands) resulting from cascaded FWM processes. The figure presents three different regions of interest, highlighted (in grey) on the OSA spectra, and selectively chosen for examination at different input power, i.e. with pump attenuation of 0 dB (solid red line) and -2 dB (dashed black line). In the first highlighted region (Figure III.12.a), we present a combination of the first and second MI sidebands on the long-wavelength edge of the spectrum. Here, the interaction strength between adjacent sidebands decreases as the input power increases,

potentially due to the influence of cascaded FWM process [207], [212], [250]. Despite this, the overall mutual information map experiences only marginal qualitative changes.

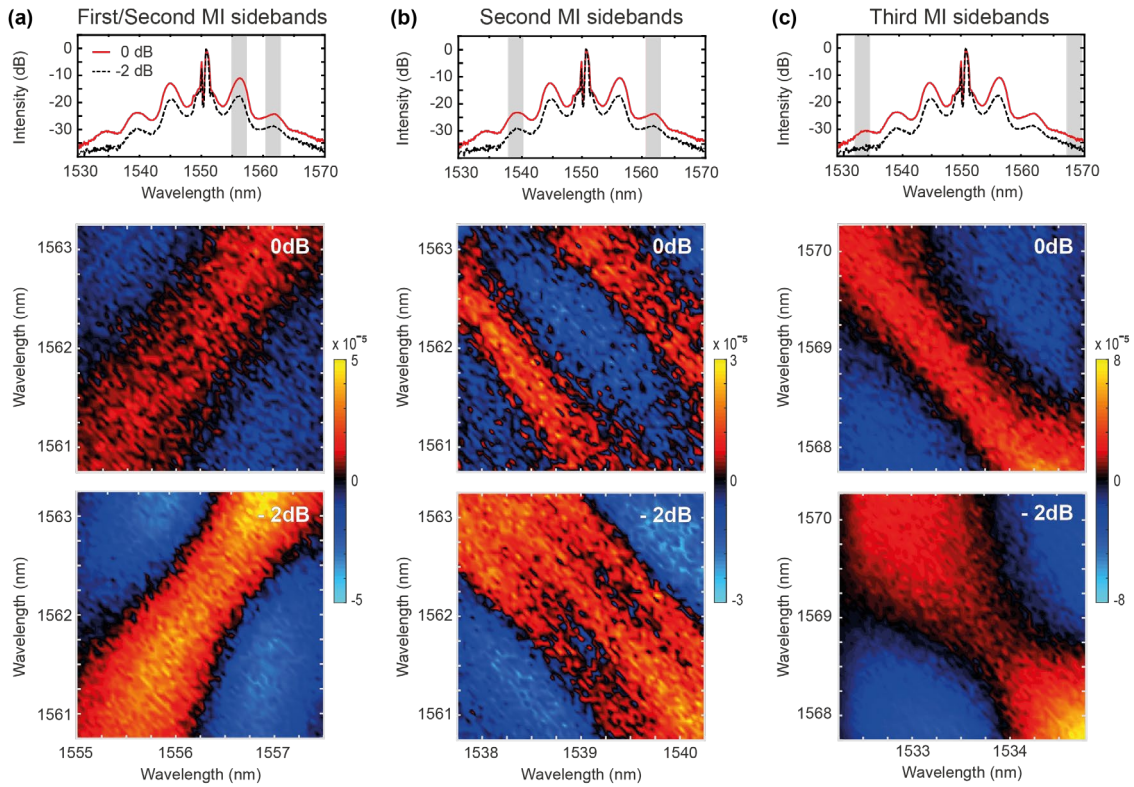


Figure III.12 (a) First and second MI sidebands located at the long wavelength edge of the spectrum, (b) symmetrical second MI sidebands, (c) and symmetrical third MI sidebands, are represented by their spectral mutual information correlation maps, derived from experimental SPD-DFT measurements (selectively filtered and transmitted to each SPD). The corresponding OSA spectra for each sidebands' combination are captured for two different input power levels before HNLF propagation and represented in the top panel: 0 dB attenuation are solid red lines, -2 dB attenuation are dashed black lines, while the sideband locations are highlighted in grey.

If we focus on the symmetrical second MI sidebands (located at 1539 nm and 1562 nm), as in Figure III.12.b, the mutual information maps exhibit distinct reshaping patterns as the input power increases. The SPM-like shape in these spectral maps likely arises from more complex phenomena such as non-degenerated FWM interactions involving the first sidebands or even reverse energy flow towards the pump, as there is no straightforward direct FWM process anticipated in this scenario. For higher-order sidebands (third MI sidebands located at 1533.5 nm and 1569 nm), resulting from multiple cascaded FWM conversions, the mutual information correlations in this case are surprisingly more pronounced (Figure III.12.c), despite the very low intensity of these sidebands (see MIA scale of the maps). Even though the reshaping of the correlations is not clear in this case, the map mostly retains a diagonal pattern. This symmetry in correlation features can be associated with spontaneous processes, indicating that energy conservation signatures are statistically preserved despite the multi-step FWM interactions.

With this analysis, we demonstrate that for the complex interplay of spectral correlations within MI sidebands, the SPD-DFT technique offers a window into the intricate dynamics of these nonlinear processes, shedding light on various mechanisms such as cascaded FWM and SPM

effects that shape the observed mutual information patterns (and into the statistical distribution of energy transfer occurring between weak spectral components). In contradiction with PD-DFT measurements which face inherent constraints to detect information at low intensities, SPD-DFT proved useful to overcome these limitations and allow for high-sensitivity correlation measurements with low-noise figures between weak spectral components.

In addition, considering the high sensitivity (and resolution) that we presented in the previous analysis, the SPD-DFT approach stands out for its capability to feature a dynamic range well above 70 dB (depending on the count rate saturation characteristics of the detectors in use). As long as the signal is above the noise floor of the SPDs (typically around -130 dBm), it is possible to accumulate instances of photon events over an extended timeframe. The main concept here is to integrate instances of photon detection over a duration that is sufficient to capture useful coincidental detections spanning all frequency components (further explained in Figure III.15). To empirically confirm the agreement and versatility of the two DFT detection methods across the complete spectrum of MI, we conducted further measurements which results are summarized in Figure III.13.

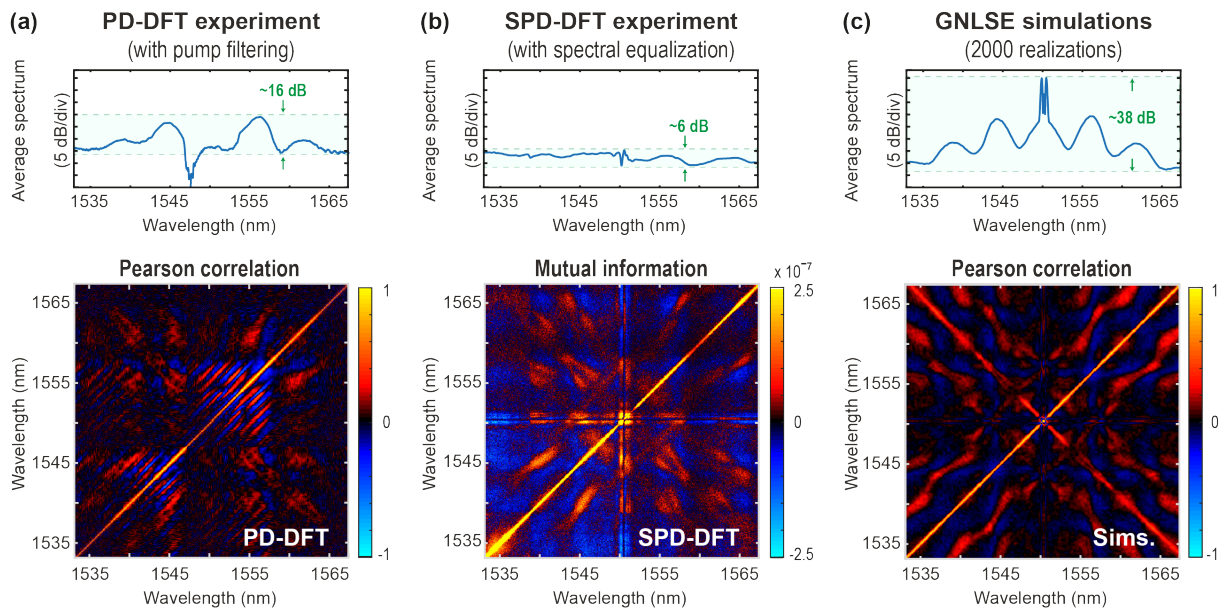


Figure III.13 Comparison of the averaged OSA spectra (top panels) and correlation maps (bottom panels) of the complete MI spectrum over a spectral range between 1532 nm and 1568 nm, using distinct approaches: (a) PD-DFT measurements after pump filtering based on 500 experimental measurements. (b) SPD-DFT measurements via spectral signal equalization. (c) GNLSE simulations with 2000 numerical realizations. The green shadings in the average spectra highlight the signal's dynamic range after processing, respectively indicating 16 dB, 6 dB, and 38 dB, for each case.

We first present, in Figure III.13.a, the Pearson's correlation map of a PD-DFT measurement capturing 500 distinct shot-to-shot traces. To effectively identify the MI sidebands and maintain a favorable dynamic range of about 16 dB in the average spectrum, the pump signal (centered at 1550.65 nm) is carefully filtered out. However, as we can see here, the statistical analysis is susceptible to certain factors. Firstly, the notable impulse response of the photodiode significantly influences the results. This leads to visible artifacts, including noticeable dips in the average DFT spectrum and diagonal correlation patterns clearly observed within the correlation map. Additionally, a notable limitation arises from the detection sensitivity,

especially when dealing with higher-order MI sidebands whose correlation features are hardly resolved. This constraint emphasizes the nuanced challenges linked to identifying and accurately characterizing components further away in the spectrum.

When using the SPD-DFT detection, it is important to note that the dynamic range can exceed 70 dB, and it is only limited by the detectors' count rate saturation. As long as the signal is above the noise floor (around -130 dBm), we can accumulate coincident detections across various frequency components by registering photo-events for a longer integration time. However, the quadratic nature of 2-photon coincidence, makes that, for a signal with spectral components with different intensities, we need longer integration times to accumulate the same number of coincidence counts (for example, 100 times longer if we have spectral components with a 10 dB lower intensity, and 10 000 times longer if we have 20 dB lower intensity). This makes SPD-DFT less practical for high-resolution analysis of broadband spectral fluctuations with significant intensity contrast.

Nonetheless, the use of mutual information analysis provides a relative measurement of the correlation between two wavelengths, independent of the absolute photon detection probability, which means that we can assess the relationship between spectral components without being highly dependent on the absolute intensity levels.

For this reason, to study the whole MI spectrum using SPD-DFT measurements, spectral equalization was employed. Using the second Waveshaper (in Figure III.5), we apply an inverse attenuation profile to the DFT signal before the SPD detection, aligning it with the intensity level of the lowest spectral components within the MI spectrum (-35 dB with respect to the maximal spectral intensity), to limit the overall measurement time. Even though this approach led to a significant reduction in the spectral intensity contrast of the spectrum (below 6 dB), it still provided the necessary coincident detections for a successful analysis of the mutual information features over the full 35 nm spectral bandwidth, and within a relatively short integration time (see below). What differentiates these results, is that the detections occurred without encountering neither the impact of impulse response nor a sensitivity cutoff as observed for the standard DFT detection. The maps illustrated in Figure III.13.b, retrieved with an integration time of 300 mins, confirm the effectiveness of the SPD-DFT methodology across the whole spectral frequencies and the maximum needed dynamic range.

Spectral equalization, as employed in the SPD-DFT technique, cannot be applied to the PD-DFT technique. This is primarily due to the fact that equalizing the spectral components for PD-DFT would lead to signal levels falling below the detection noise floor and becoming too weak to be reliably detected. In addition, this analysis demonstrates that when using SPD-DFT with spectral equalization, we can reduce the measurement time without significant deterioration of the mutual information maps. In addition, the mutual information maps in this case show a symmetry along their diagonals, meaning that the correlation between $\mu_{(\lambda_1, \lambda_2)}$ and $\mu_{(\lambda_2, \lambda_1)}$ is the same. By using this expected symmetry, when measuring across the entire spectrum with both SPDs, we can directly calculate a compound (symmetric) value for the mutual information map. This helps reduce measurement noise and statistical biases in our analysis.

Both Pearson's correlation and the mutual information allow to study and measure the fluctuations of noise-driven MI dynamics after nonlinear propagation. However, the mutual information offers a clearer representation of the dynamics of this frequency conversion

process. To further validate this result, we numerically generate using GNLSE simulations, Pearson's correlation maps, created from 2000 Monte Carlo realizations based on random input noise (corresponding to the method used for Figure III.6). Compared with the mutual information analysis, the results of Figure III.13.c show similar patterns and features. While the contrast is different, the overall agreement between the two statistical approaches illustrates the usefulness of MIA via SPD detection, making it an important tool in analyzing the spectral fluctuations with good fidelity, while identifying key dynamics and physical processes during nonlinear propagation.

A more powerful application of our new approach is its role in helping to control and tune the correlations between different spectral components of the MI spectrum. To investigate this property, we consider a more complex frequency conversion process associated with modulation instability. Specifically, using the Waveshaper for the initial pulse preparation (see Figure III.5), we filter the femtosecond pulse into a 55 ps pump centered at 1550.65 nm, and two additional weak 55 ps seeds (i.e. 28 dB attenuation regarding the pump), each with and adjustable phase and frequency detuning. In this case, the pump and the seeds will propagate together in the HNLF and generate new nonlinear frequency conversion processes and yield more propagation dynamics.

It is important to note that here, the spectral intensities of the seeds are intentionally set at a level comparable to the ASE of the EDFA. This balance sets the stage for direct competition between a noise-driven spontaneous MI process and a (weakly) induced MI process.

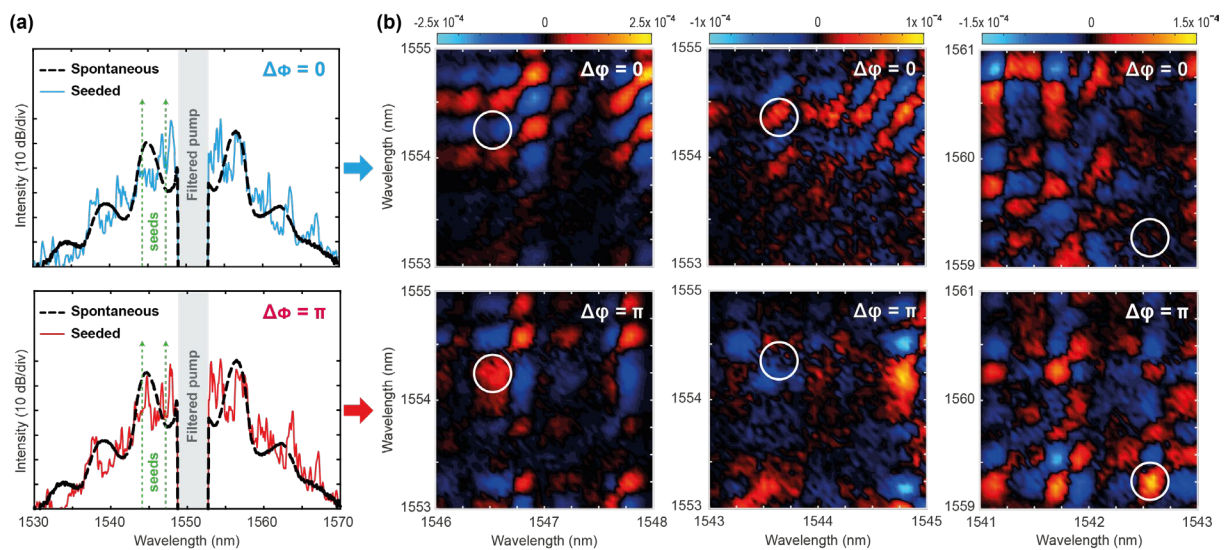


Figure III.14 (a) Output MI spectra with controlled seeding: MI spectra resulting from spontaneous MI (in black dashes) and the introduction of two coherent input seeds at frequency detuning of 400 GHz and 800 GHz (green arrows). These input seeds have distinct spectral phase differences: $\Delta\phi = 0$ (blue) and $\Delta\phi = \pi$ (red). (b) Spectral mutual information maps with seeded MI: Correlation maps obtained from SPD-DFT measurements with two weak coherent seeds added to the pump for three different selected spectral regions. Inverting the phases of the seeds can modify the sign (and shape) of the mutual information map highlighted in the white-circled areas within the maps.

In Figure III.14, we consider the case where the frequency detuning of the two seeds is respectively equal to $\Delta\nu_1 = 400 \text{ GHz}$ and $\Delta\nu_2 = 800 \text{ GHz}$, corresponding to the wavelengths of 1547.4 nm and 1544.3 nm, respectively. This configuration places both seeds within the MI gain region and employs harmonic detuning ($\Delta\nu_2 = 2\Delta\nu_1$), indicating intricate degenerate and

cascaded FWM processes. In this case, the relative spectral phase between the seeds is a critical parameter. For this reason, we choose the relative phases of the seeds regarding the phase matching defined by $\Delta\phi = 2\phi_0 + \phi_1 + \phi_2$ (see (Eq. 1.57)) with $\phi_0 = 0$ being the phase of the pump. Two cases were studied: When $\Delta\phi = 0$ (with $\phi_1 = \phi_2 = 0$) and when $\Delta\phi = \pi$ (by choosing $\phi_1 = 0, \phi_2 = \pi$).

As we can see from Figure III.14.a, optical seeding can drastically impact the MI broadening dynamics after nonlinear propagation (blue and red traces). Even when the seeds are weak with respect to the pump, these modulations can still significantly reshape the frequency conversion dynamics. In addition, these changes are evident when extracting the mutual information correlation maps between spectral component combinations close to the pump (i.e. 1547 and 1554 nm), or further away (e.g. 1542 and 1560 nm) as arising from cascaded FWM processes (Figure III.14.b). The analysis in Figure III.14 reveals that the input phase of optical seeds can indeed alter both the spectrum and the features of mutual information maps at specific wavelengths. This is particularly visible in the white-circled areas in the maps. These results highlight the capability of SPD-DFT and mutual information analysis in gaining insight into complex incoherent dynamics and cascaded frequency conversion processes that are challenging to explore using traditional methods.

The overall results presented in this chapter have validated a new quantum-inspired technique to understand the instabilities of nonlinear processes in fiber optics such as modulation instability. Taking advantage of the concept of dispersive Fourier-transform through the use of multiple single-photon detectors, we were able to achieve a high resolution of around 53 pm, a sensitivity reaching below the femtowatt, and a high dynamic range of over 80 dB.

Compared with other real-time technique, such as PD-DFT, which also allow to measure shot-to-shot fluctuations and conduct statistical analysis to extract relevant spectral correlation signatures, this SPD-DFT technique provides similar analysis of these instabilities without any sensitivity cutoff or dynamic range limitations, allowing to understand the behavior of the nonlinear processes of interest even at very low intensities. The main limitation that our approach can however face is measurement integration time.

In this work, for the measurements of the PD-DFT correlation maps, we combined data from 500 shot-to-shot spectra from the oscilloscope. Such analysis required a total measurement time of ~ 5 minutes, with each spectrum being measured in about ~ 600 ms. However, this measurement time can be improved with faster data transfer rates.

On the other hand, for the SPD-DFT, we generated mutual information maps obtained by concatenating 100 dataset files. Each of the dataset file contains 25 million time tags, including both SPD1 and SPD2 time tags, as well as the 50 MHz laser trigger time tags. Here, collecting each dataset took about 18 seconds, which led to a 30-minutes measurement. In the specific case where we focused on the broadband mutual information map (see Figure III.13.b - using SPD-DFT detection after spectral equalization), we combined data from 1000 time-tag dataset files. This increased the integration time to ~ 5 hours (i.e. 300 mins).

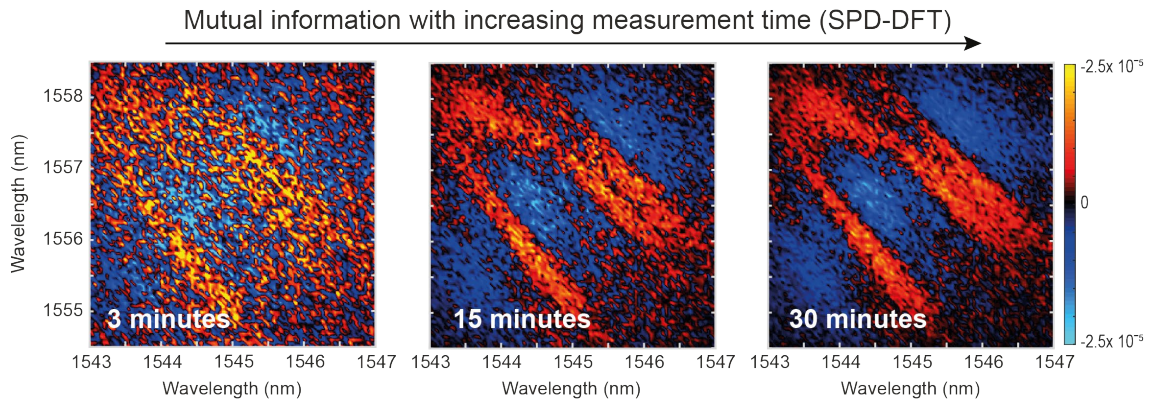


Figure III.15 Mutual information correlation maps of the first symmetrical MI sidebands acquired through SPD detection for different measurement integration times: 3, 15, and 30 minutes.

It is important to note that the total integration time used for such detection was chosen to ensure a sufficiently large number of detected photon-events for a meaningful statistical analysis, without refining the setups towards optimal measurement time. However, clear mutual information signatures can be readily observed with fewer detected photon events and shorter integration times. For example, in Figure III.15, we show the evolution of the mutual information map (for the first MI sidebands) over various integration times of SPD-DFT measurement. Within 3 minutes, the initial correlation features begin to emerge, until becoming clearly defined within only 15 minutes of integration. Additional integration time (up to a total of 30 minutes) only slightly improved the correlation features.

As writing the datafiles occupies most of the measurement time, it results in a significant reduction in the acquisition data rate due to the time-consuming nature of off-line data handling. We then anticipate that implementing online photon-event detection, along with appropriate selection rules and signal processing, can lead to an improvement in the data collection rate of the SPD-DFT measurements. Additionally, in this framework, the use of multiple SPDs (more than two) in the detection scheme is expected to yield improved integration time in the SPD-DFT while at the same time opening the path towards the measurement of both higher-order and multidimensional (e.g. spectro-temporal) metrics and correlation functions, allowing to explore the formation mechanisms of more complex waveforms.

In conclusion, these research findings show that our novel DFT-based approach allows for statistical analysis of fundamentally complex ultrafast optical phenomena, and for extracting correlation signatures between weak spectral components at very low intensities (e.g. between MI cascading processes up to the third sidebands). We envision significant improvements in the realm of advanced all-optical signal processing, holding potential for applications ranging from phase-sensitive amplification to quantum state manipulation. Furthermore, the potential of our DFT technique extends to imaging and microscopy applications that demand both high sensitivity and powerful spectral detection capabilities. The fields of computational imaging, correlated microscopy, and multiphoton spectroscopy stand to gain direct benefits from the SPD-DFT tool.

In the context of this thesis, these results have demonstrated the ability to finely adjust correlations between specific wavelengths by the addition of weak optical seeds to the initial pulse before propagation. We expect this method to pave the way toward controlling noise-driven processes at the boundary between quantum and nonlinear optics and tailoring nonlinear interactions in fiber optics. This technique should also enable machine learning strategies towards controlling multidimensional optical properties via dedicated optimization algorithms. These particular aspects are key components of this PhD work, and will be detailed and experimentally demonstrated in Chapter IV, proving our ability to apply a ‘smart’ control to tune and optimize the spectral properties of broadband spectra obtained from nonlinear processes during fiber optics propagation.

Chapter IV. Smart control of modulation instability

The exploration of the nonlinear dynamics and real-time characterization techniques discussed in the first three chapters of this thesis, allowed us to better understand the unstable behavior and fluctuating processes generated from the complex interplay between the dispersion and nonlinear effects in optical fibers. While these fluctuations present challenges in terms of characterization, they also provide an essential understanding of the principles of incoherent supercontinuum generation [62]. In fact, in addition to underlying physical mechanisms driving spectral broadening in supercontinuum generation, studies have also investigated the instability properties inherent to this phenomenon. This examination has established interesting connections between supercontinuum noise and extreme instabilities observed in other physical domains usually referred as extreme events and rogue waves [252], [80], [78]. One such manifestation of noise's influence is modulation instability, which we will focus on in this chapter with the target to understand and control such noise-driven and fluctuating spectra [253].

Over the years, several approaches were set in place to control nonlinear effects in optical fibers (section II.2 and section II.3). For example, control of the dynamics of optical rogue wave formation have been reported by applying modifications to the input pulse. By adding a small modulation across the pulse envelope, one could enhance the generation of rogue waves and observe significant spectral broadening [68], [254]. In contrast, extreme frequency shifts associated with rogue wave generation were suppressed by attenuating such spectral components using a sliding frequency filter (while minimizing the overall bandwidth and power reduction during spectral broadening) [82]. Programmable spectral filters (like Waveshapers) were applied in such MI-associated studies to generate specific nonlinear phenomena. For example, Frisquet et al., have demonstrated that, by generating two additional signals to the initial pulse, they can create Akhmediev breathers when these two modulations superpose. By carefully controlling the signal's spectral intensity and phase characteristics, they created specific conditions where the two ABs would collide efficiently [77] to generate highly localized temporal structures.

In fact, relying on optical seeding to tune the conditions of the input pulse and control the subsequent dynamics in nonlinearly broadened spectra has been studied and employed in a variety of scenarios [254], [82]. By carefully adjusting the various parameters of the input signal (frequency, phase, amplitude, bandwidth, ...), we are able to create or suppress new frequencies, enhance specific phenomena, and ultimately achieve personalized output spectra [82], [255], [256]. Coherent and incoherent seeding were explored in the context of induced modulation instability, allowing to enhance the resulting MI spectrum in terms of spectral bandwidth, signal-to-noise ratio, and degree of coherence [253], [225] – to only name a few examples. However, as already mentioned in section II.3, as these dynamics are often complex, unpredictable and sensitive to the initial conditions, it can be beneficial to leverage machine learning strategies [8], [147], allowing for smarter, and faster control and optimization (especially in an experimental context).

In this chapter, we demonstrate and apply a control strategy using both tailored optical seeding and machine learning algorithms to finely-tune the properties of different spectral components in the output spectrum and optimize their correlations.

To delve into such a study, we start in **Section IV.1** with a brief reminder of the impact of the input parameters on nonlinear instabilities in both the spontaneous and induced MI regimes.

In our studies, however, we explore a regime situated at the boundary between these two purely coherent and incoherent processes, respectively. In **Section IV.2**, we therefore present a numerical study showing the impact of optical seeding on the generation of MI in this hybrid regime. Our investigation covers a range of scenarios using both coherent and quasi-coherent seeds, with a comparison between the different initial parameters and their impact. To precisely tune the broadening dynamics, we introduce and implement experimental MI control using reconfigurable optical seeding iteratively tuned by machine learning strategies, especially genetic algorithms. **Section IV.3**, presents the results of this research, highlighting the effectiveness of our algorithm in enhancing the correlation between various spectral components and correspondingly altering the MI spectrum. We also present some complementary studies that can be accomplished in this context. As we go further in our analysis, we discuss potential relationships between the optimal seeds' parameters and the nonlinear processes involved during fiber propagation, which will be detailed in **Section IV.4**.

IV.1. Influential factors in MI spectral broadening

As seen in the previous sections, MI spectral broadening can occur from noise without adding any modulation to the pulse (spontaneous MI). In this case, the properties of both the pump laser and the fiber [257] can have a significant impact on the waveguide propagation within the waveguide, where the dispersion and the nonlinear effects interact to create new frequencies and generate a broader spectrum. Increasing the input power before entering the HNLN is an effective and easy way that allows tuning the MI gain region and the equivalent nonlinear propagation length to thus modify the output spectrum. In this context, we show in Figure IV.1 an example, using numerical simulations and Pearson's correlation maps, to illustrate how the increase of the input average power P_{in} can modify the nonlinear dynamics in a spontaneous MI regime, and results in different correlation features.

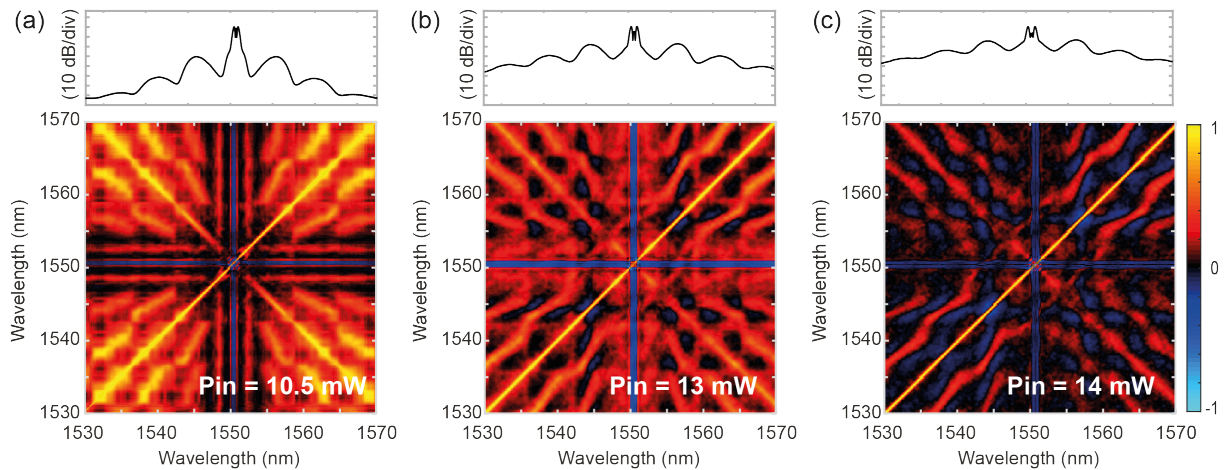


Figure IV.1 Numerical simulations showing the average spectra (top panels) and Pearson's correlation maps (bottom panels) of a 30 ps laser pulse centered a 1550.65 nm propagating into 385 m of HNLN, whose parameters are $\beta_2 = -2.15 \text{ ps}^2 \cdot \text{km}^{-1}$; $\beta_3 = 0.07 \text{ ps}^3 \cdot \text{km}^{-1}$; and $\gamma = 3.5 \text{ W}^{-1} \cdot \text{km}^{-1}$. The figure illustrates the evolution of the MI process with various input peak powers with (a) 10 mW, (b) 13 mW, and (c) 14 mW.

When the input power is $P_{in} = 10.5 \text{ mW}$ (Figure IV.1.a), corresponding to the onset of MI broadening, we can see that the correlations between the different components have mostly positive values, as the energy is simply transferred from the pump to the sidebands. However,

when we increase the power, we obtain complex interactions between the various and competing frequency conversion effects in Figure IV.1.b. For $P_{in} = 14$ mW, for a fully extended MI spectrum, multiple cascaded process and reverse energy flows appears and yields anti-correlation features seen in the map in Figure IV.1.c.

However, spectral broadening dynamics are not only governed by the input power. While increasing the power can indeed intensify nonlinear effects, other critical factors play significant roles. The characteristics of the fiber, mainly the dispersion parameter β_2 and the nonlinear coefficient γ can largely affect the nonlinear behaviors (and depending on the sign of β_2 , the overall interaction between these two parameters will lead to very different broadening regimes and dynamics – see section I.5). Higher-order dispersion and scattering effects can also play a role in the shaping dynamics (via e.g. NLSE symmetry breaking terms) and the corresponding output spectrum [62], [258], [259]. The introduction of these additional nonlinear effects can affect the recurrence behavior observed in the system, specifically the FPU recurrence in MI, which may be compromised or lost in the presence of these terms, and which reinforces the need for idealized FWM experiments to comprehensively study and control nonlinear optical dynamics [71], [260], [261].

If dispersion parameters are carefully controlled, their manipulation [262], [263], in conjunction with power adjustment, allows for the precise engineering of nonlinear effects. Understanding the resulting processes, such as modulation instability or subsequent supercontinuum generation, is therefore crucial for enabling advance spectral tailoring in various applications.

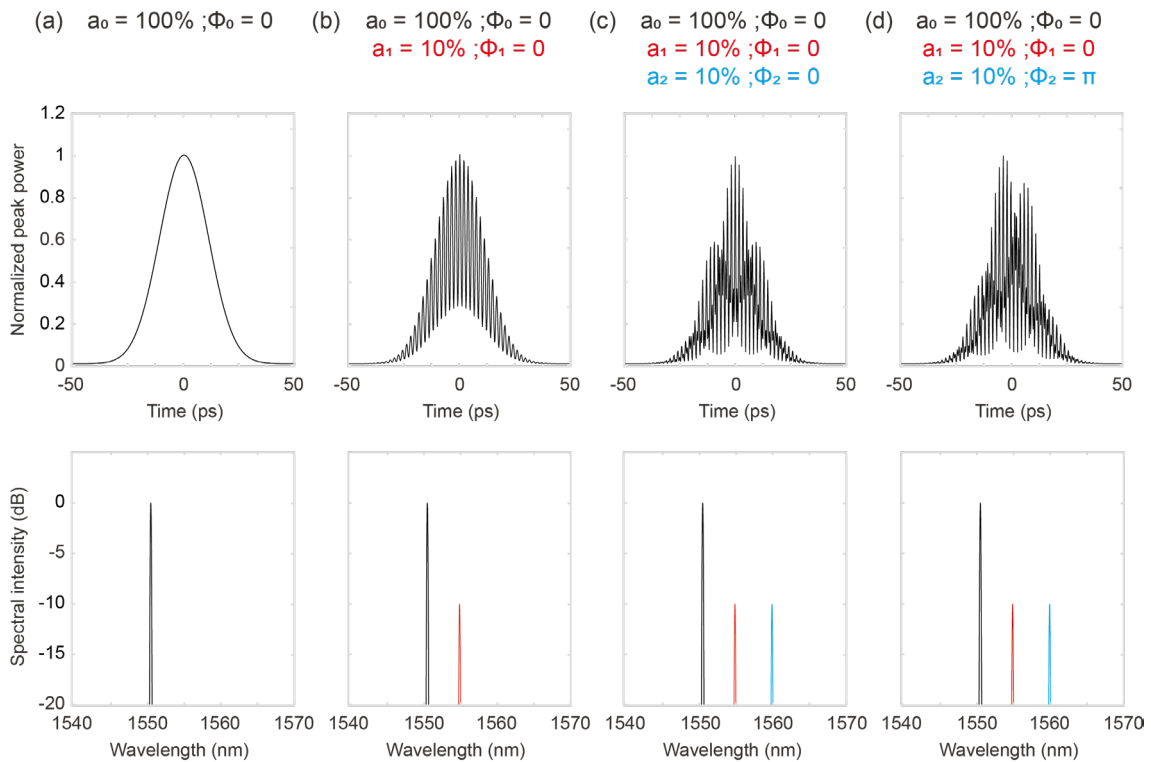


Figure IV.2 Visual representation in both the temporal (top panels) and spectral (bottom panels) domains of (a) a Gaussian 30 ps laser pump centered at 1550.6 nm, (b) the pump signal with an added weak modulation at 1555 nm (in red) with 10 dB attenuation ($a_1 = 10\%$) and a phase $\phi_1 = 0$, (c) the signal with an additional modulation (in blue) centered at 1560 nm, with $a_2 = 10\%$ and $\phi_2 = 0$, (d) Total signal achieved by adjusting the phase $\phi_2 = \pi$.

On the other hand, we have discussed in section I.5.2.1 how the addition of modulations to the pump pulse can profoundly alter the behavior of nonlinear broadening effects [74], [67]. In Figure IV.2.a, we provide a visual representation, in both the temporal and spectral domains, of an initial Gaussian 30 ps laser pulse centered at 1550.6 nm. When a weak modulation (in red) at 1555 nm is introduced with an attenuation of 10 dB ($a_1 = 10\%$ of the intensity), notable changes emerge. In the spectral domain (Figure IV.2.b), the modulation appears as a peak alongside the pump, while in the temporal domain, the previously uniform pulse envelope now exhibits a clear modulation (see also Figure I.17). Figure IV.2.c extends this exploration by incorporating an additional modulation (shown in blue) centered at 1560 nm, featuring $a_2 = 10\%$ and a phase $\phi_2 = 0$. This introduces a transformation of the input pulse by changing its temporal form and resulting in the generation of a new signal seen with a dual modulation in the spectral domain.

An important aspect to consider here is the modulation's parameters. In a trivial fashion, increasing the seed signals (i.e. decreasing the attenuation), amplifies the modulation on the input pulse.

More importantly, the input pulse changes of shape and characteristics are largely dependent on the frequency and phase values of the modulations that can lead to more complex interference patterns. To illustrate this point further, in Figure IV.2.d, we provide an example where the phase of the second modulation is tuned to a value of π . This adjustment demonstrates how altering a single phase parameter can impact the symmetry of the pulse temporal profile. In the following sections, we analyze of how such modulations applied to the input pulse can significantly impact nonlinear propagation and influence the resulting MI output spectrum.

IV.2. Numerical study: Modulation instability control via optical seeding

Spontaneous and induced MI regimes have been studied for different applications and in different scenarios [253], [68], [225], [74]. Here, we work at the frontier between these two regimes. The objective is to study the competition between weak optical seeds (added to the initial pulse) and broadband ASE noise (occurring from amplification) through their contribution to the MI broadening process, in order to gain insight on the impact of the seeds' parameters during nonlinear propagation.

First, we report a numerical study using GNLSE simulations (section I.3.3) based on a realistic experimental setup. We used the 80 fs pulsed laser, with a 50 MHz repetition rate and centered at 1550.65 nm (see Figure III.5), and we applied a spectral filter (Waveshaper) on the broadband signal to transform the initial fs pulse into a ~ 30 ps Gaussian pump.

The noise-driven MI regime (spontaneous MI) can be simply excited by sufficiently amplifying the pump signal (through an EDFA) and employing a super-Gaussian bandpass filter (BPF) of ~ 1 nm to strongly limit the ASE noise in the system (see Figure IV.3.a).

In this section, the nonlinear dynamics are studied during the propagation in a 385 m-long HNLF with $\beta_2 = -2.15 \text{ ps}^2 \cdot \text{km}^{-1}$; $\beta_3 = 0.07 \text{ ps}^3 \cdot \text{km}^{-1}$; and $\gamma = 3.5 \text{ W}^{-1} \cdot \text{km}^{-1}$. The conditions were selected so that typical spontaneous MI spectral broadening could be excited, along with a cascaded process depending on the input power (typically up to the distance of maximal spectral expansion (i.e. first FPU compression before recurrence [264], [265])).

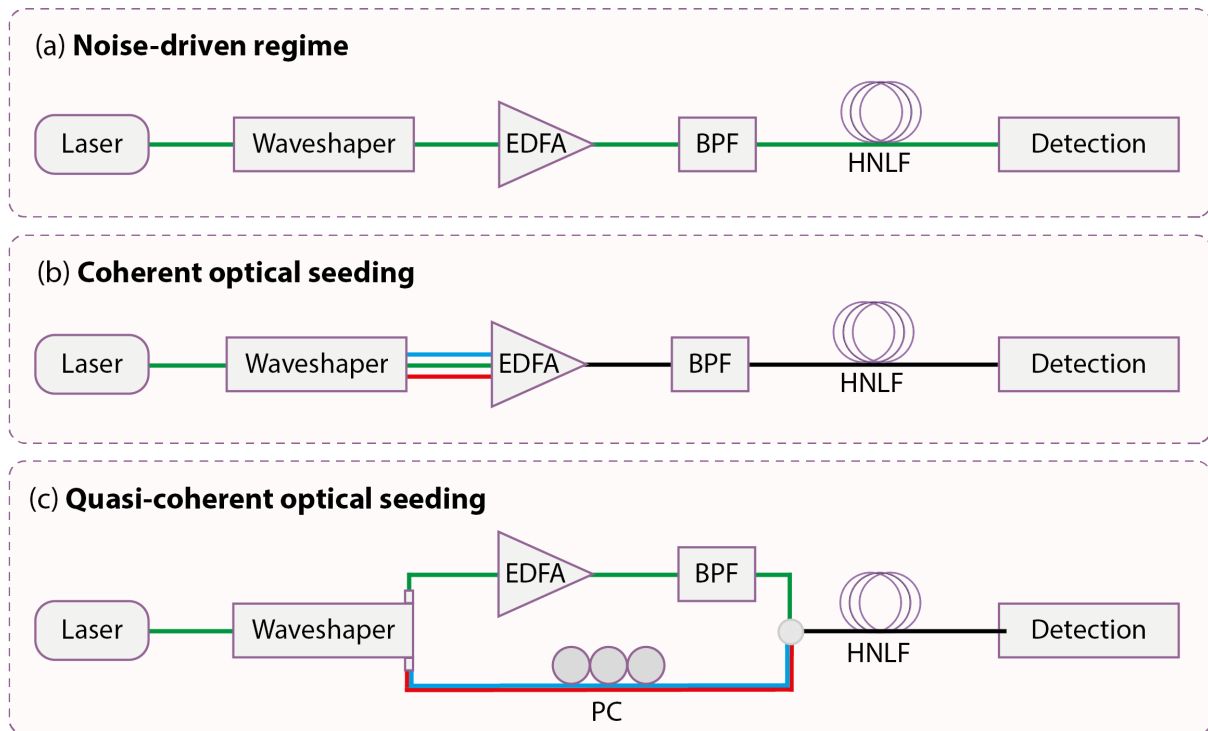


Figure IV.3 Illustration of the experimental setups and numerical scenarios studied in this chapter within the framework of MI control. (a) Noise-driven MI regime (spontaneous MI) achieved by amplifying a filtered 30 ps pump with an EDFA and applying a bandpass filter (BPF) to limit the impact of ASE noise before propagation in a HNLF. (b) MI regime with coherent optical seeding, using a single output of a Waveshaper to filter additional weak signals combined with the pump. (c) Quasi-coherent optical seeded MI regime, using two distinct Waveshaper outputs: one for the pump which will be amplified, and the other for the generation of the seeds. The three signals are in this case combined before nonlinear propagation but experience partial propagation along different optical paths.

In parallel, two scenarios were studied: The first setup, illustrated in Figure IV.3.b, describes an MI regime using coherent optical seeding. In addition to the pump, we use the same Waveshaper to filter one or two weak seeds with the same bandwidth as the pump, but with adjustable attenuation, frequency detuning, and an adjustable spectral phase between 0 and 2π . All the signals are then combined, and jointly amplified, before propagating in the HNLF.

The second setup, illustrated in Figure IV.3.c, describes a quasi-coherent optical seeded MI regime. In fact, the Waveshapers we experimentally use possess multiple output ports, which provide the ability to split an input signal with an equivalent (or differential) power across all frequencies and ports (see section II.2.1). For each signal, we are able to define a filtering profile with adjustable power, attenuation, and phase. This interesting property allows us to generate “quasi-coherent” seeds. Instead of filtering the pump and the seeds and sending the combined signal into the EDFA (so that all optical signals follow the same optical path), the pump is here filtered through one output of the Waveshaper where it will be amplified. Conversely, the seeds (one or more) will exit from another output of the Waveshaper. After adjusting the delay between the pump and the seeds, these optical pump and seed signals are sent into the HNLF where they jointly experience MI spectral broadening. In this case, however, the seeds are very weak compared to the pump, at a level similar to the ASE noise generated from amplification.

In this study, we will explore how these weak optical seeds can affect noise-driven MI dynamics depending on their input parameters and the decoherence level. In the next section, we first present the numerical results for both cases presented above and analyze the spectral fluctuations of these hybrid MI regimes through Pearson's correlation maps.

IV.2.1. Coherent optical seeding

The introduction of coherent seeds into the MI process presents a simple way to control incoherent MI dynamics. By precisely tuning the properties of the seed, such as its frequency, phase, and amplitude, we obtain a unique tool for adjusting desired spectral features and correlations within the spectrum, especially when compared to classical modulation techniques [68], [266] that can be limited in terms of coherence and/or potential for scalability.

Figure IV.4, presents an illustrative view of this effect, by showing the average spectra and the spectral correlations resulting from the propagation of a coherent seed added to the pump with 22 dB relative attenuation (i.e. less than 1% modulation) using 500 simulations with random initial noise seeds. Comparing with the MI regimes (illustrated in Figure I.17 and Figure I.18), we observe that the output spectra present behaviors that place them between induced and spontaneous MI regimes. However, in this context, the seed exhibits a more pronounced influence on the nonlinear dynamics than does the noise, which makes the characteristics of the propagation closer to the induced regime. It is important to note, that as explained previously, the parameters of the seed play an important role in shaping the propagation dynamics.

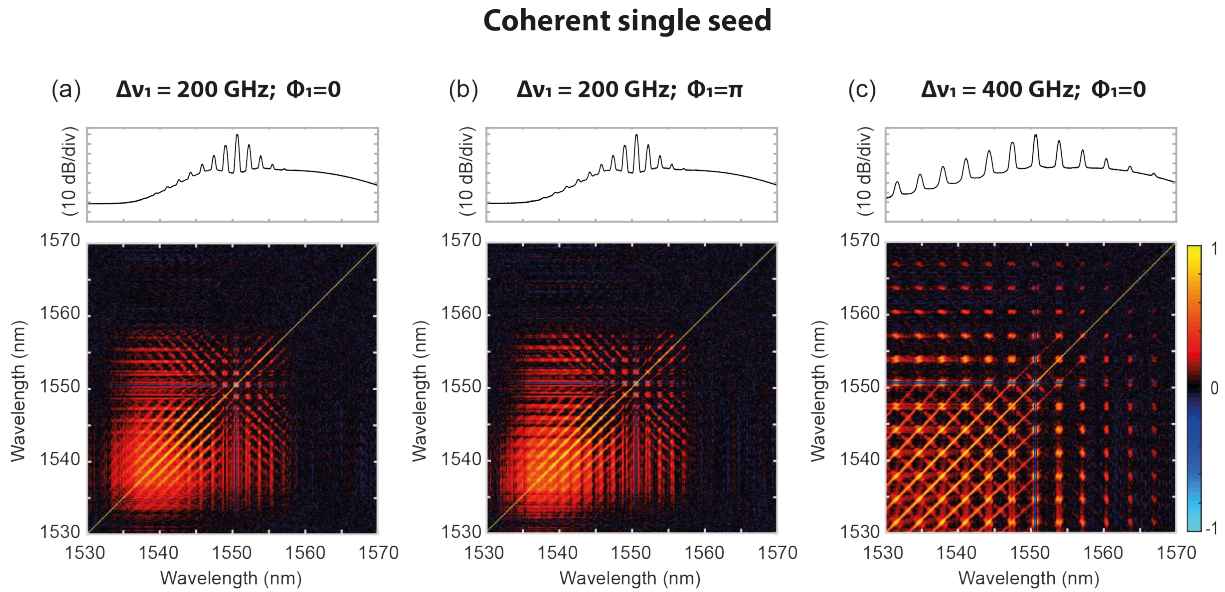


Figure IV.4 Average spectra (top panels) and Pearson's correlation maps (bottom panels) obtained after HNLF propagation and resulting from a coherent seed added to the pump with 22 dB attenuation and adjustable parameters by (a) detuning the seed by $\Delta\nu_1 = 200 \text{ GHz}$, (b) varying its phase from 0 to $\phi_2 = \pi$, (c) increasing the frequency detuning to $\Delta\nu_1 = 400 \text{ GHz}$ with $\phi_1 = 0$.

As demonstrated in Figure IV.4.a-b, when the seed is detuned from the pump by $\Delta\nu_1 = 200 \text{ GHz}$, varying its phase from 0 to π , leads to a marginal change in the output spectra. This variation however drives slightly different propagation dynamics and results in modified correlation features between the MI spectral components. Yet, a noteworthy observation here is the significant impact of the frequency detuning on the MI spectrum, as expected from the

excitation of different MI gain from different seed frequency. In Figure IV.4.c, when we increase the frequency detuning of the seed (to reach the region close to the maximal MI gain ~ 475 GHz – see $Gain_{MI}$ in section I.5.2), the optical seed grows faster during propagation and lead to a cascaded MI process appearing on both sides of the pump. This yields in a drastically broadened MI spectrum and the generation of new correlation features among these spectral components emerging from the noise.

To go further in this study, we extended our analysis by considering the case where an additional seed is introduced into the MI process. The interaction between multiple seeds adds another layer of complexity and thus leads to nonlinear dynamics that depend on a broader range of parameters [74]. Nonetheless, with such an environment, the ability to tune the seed parameters provides us with a larger degree of control to stabilize the MI spectrum and achieve desired correlations between various spectral components. In fact, dual-seed interactions can lead to the formation of intricate spectral patterns, often characterized by additional sidebands and unique correlation features. Figure IV.5, illustrates the impact of both the frequency and phase of the input coherent seeds on the output spectral correlations.

Coherent dual seeds

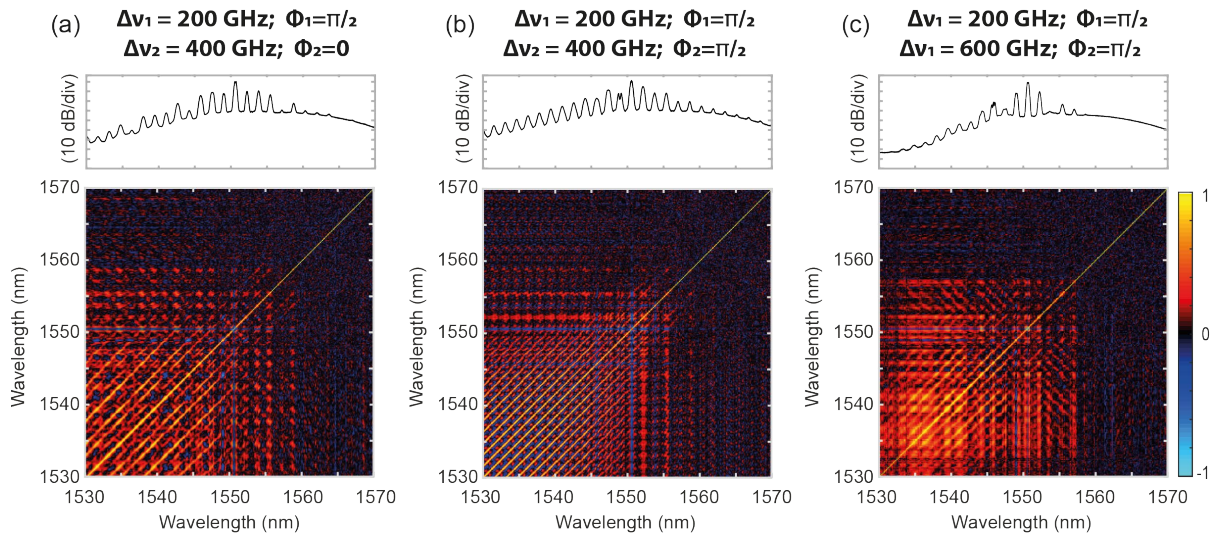


Figure IV.5 Influence of dual seed parameters on the MI output spectrum (top panels) and the correlation maps (bottom panels) obtained from 200 simulations with random initial noise seeds. The figure explores the effects of varying the frequency and phase of coherent seeds (ν_1, ϕ_1) and (ν_2, ϕ_2) , with a 22 dB attenuation, on the resulting MI dynamics: (a) for a frequency detuning $\Delta\nu_2 = 2\Delta\nu_1$ with $\phi_1 = \pi/2$ and $\phi_2 = 0$; (b) by varying the phase to $\phi_2 = \pi/2$; (c) by shifting the frequency of the second seed by $\Delta\nu_2 = 3\Delta\nu_1$, with $\phi_1 = \pi/2$ and $\phi_2 = \pi/2$.

In Figure IV.5.a, we first study the impact of the interaction between two coherent seeds (ν_1, ϕ_1) and (ν_2, ϕ_2) with the pump, introduced with a 22 dB attenuation and a frequency detuning $\Delta\nu_2 = 2\Delta\nu_1$. The output spectrum in this case experiences a complex degenerate FWM process and the generation of additional sidebands, due to the increased number of seeds. In addition, in Figure IV.5.b, we demonstrate that simply changing the phase of one seed (ϕ_2), while maintaining the other parameters exactly the same, yields new dynamics and substantial modifications in the correlation map. This can be explained by different and competing phase-matching conditions in the FWM processes as introduced in (Eq. I.58). In Figure IV.5.c, we also show the significance of altering only the frequency of one of the seeds in order to change the spectrum. However, depending on the relation between the seeds (as seen here between

$\Delta\nu_2 = 2\Delta\nu_1$ and $\Delta\nu_2 = 3\Delta\nu_1$) and the FWM processes involved during the MI, we can significantly modify (increase or decrease) these correlations, enabling us to both control the relation between selected spectral components and reach a desired output spectrum shape.

IV.2.2. Quasi-coherent optical seeding

Our exploration of the influence of optical seeds on MI dynamics led us to also investigate the scenario where nonlinear effects are primarily driven by noise, and the seeds are very weak compared to the pump. In this case, the pump and the seeds follow two different optical paths, where the seeds have a random phase fluctuation that we assume to follow a normal distribution $\mathcal{N}(\phi, g\pi)$ centered on a phase ϕ and with a standard deviation $g\pi$, where g defines the degree of decoherence of affecting the seed. We can then rewrite the spectral seed formula used for each Monte-Carlo simulation as:

$$\tilde{A}(\lambda_i, \phi_i) = |\tilde{A}(\lambda_i)| e^{iN(\phi_i, g\pi)} \quad (\text{Eq. IV.1})$$

Where $i = \{1,2\}$ is the index of the seeds.

After amplifying the pump signal, we add the seed and study its influence during nonlinear propagation when modifying its attenuation, phase and decoherence. In this scenario, we first employ numerical simulations describing the realistic experimental setup depicted in Figure IV.3.c, where a single seed with an attenuation of 35 dB (in comparison to the pump) was added at the fiber input, considering $g = 0.3$ to match experimental observations (see section IV.3.5 for details).

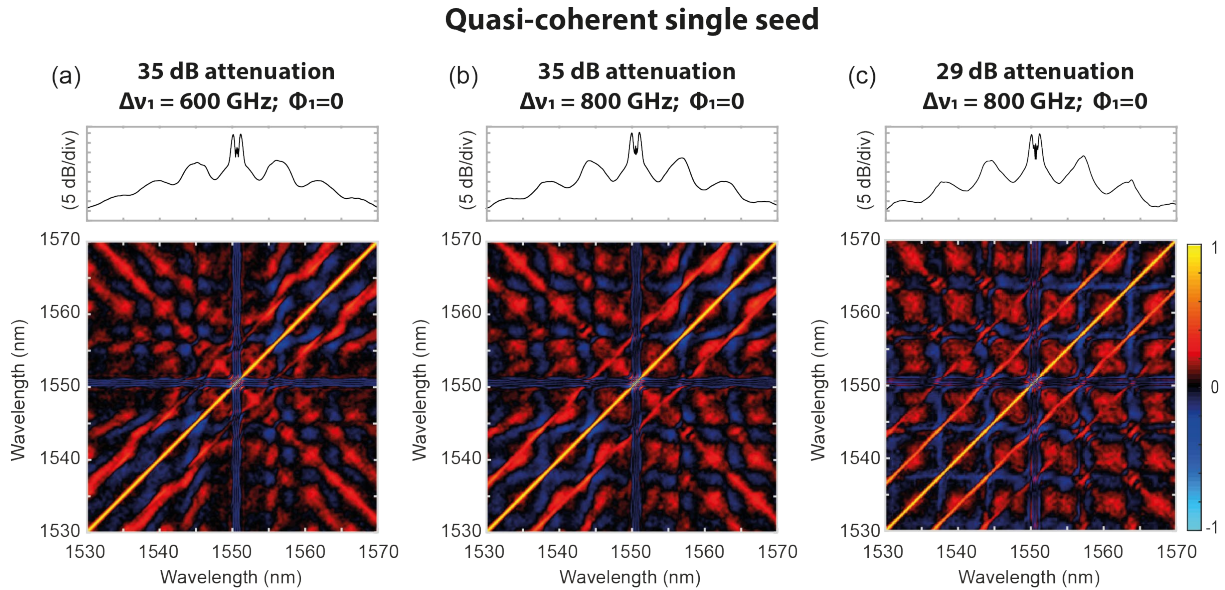


Figure IV.6 Average spectra (top panel) and correlation maps (bottom panel) obtained from 1500 simulations with random initial seeds, demonstrating the effect of a quasi-coherent single seeds added to the pump when considering $g = 0.3$. The results are primarily driven by noise, with slight variations based on the weak seed parameters: (a) 35 dB attenuation and a frequency detuning of $\Delta\nu_1 = 600$ GHz, (b) 35 dB attenuation and a frequency detuning of $\Delta\nu_1 = 800$ GHz, and (c) lower attenuation at 29 dB with a frequency detuning of $\Delta\nu_1 = 800$ GHz.

In Figure IV.6.a, which represents the dynamics of a seed detuned from the pump by $\Delta\nu_1 = 600$ GHz and with a spectral phase $\phi_1 = 0$, the correlation map exhibits remarkable similarities to the one obtained from the spontaneous MI regime, as demonstrated in Figure IV.1.c. This

resemblance can be primarily attributed to the weak power and decoherence of the additional seed, which can essentially be considered as a noise component. However, even though the impact of the seed on the final output is relatively minor, it still possesses the capacity to alter the MI fluctuations and the resulting correlation signatures. This can be seen in Figure IV.6.b, where the seed is shifted to $\Delta\nu_1 = 800$ GHz from the pump and the spectral phase remains the same. While the overall dynamics may appear similar, there are observable changes in the features of the correlation maps. Yet, in this case, the seed spectral phase has a relatively low effect on the output spectral properties, and as the distinctions between the correlations are hardly noticeable, the results are not presented in this thesis.

In Figure IV.6.c, we repeated the simulations by using a slightly stronger seeds (i.e. reducing its attenuation to 29 dB). It is worth noting that despite the 6 dB seed intensity increase, the results do not display drastic changes. In both cases, MI predominantly arises from the noise inherent in the system and the key correlation signature remain similar. However, some differences between the two figures can still be noticeable, indicating the relative impact of the seed strength on the correlation maps.

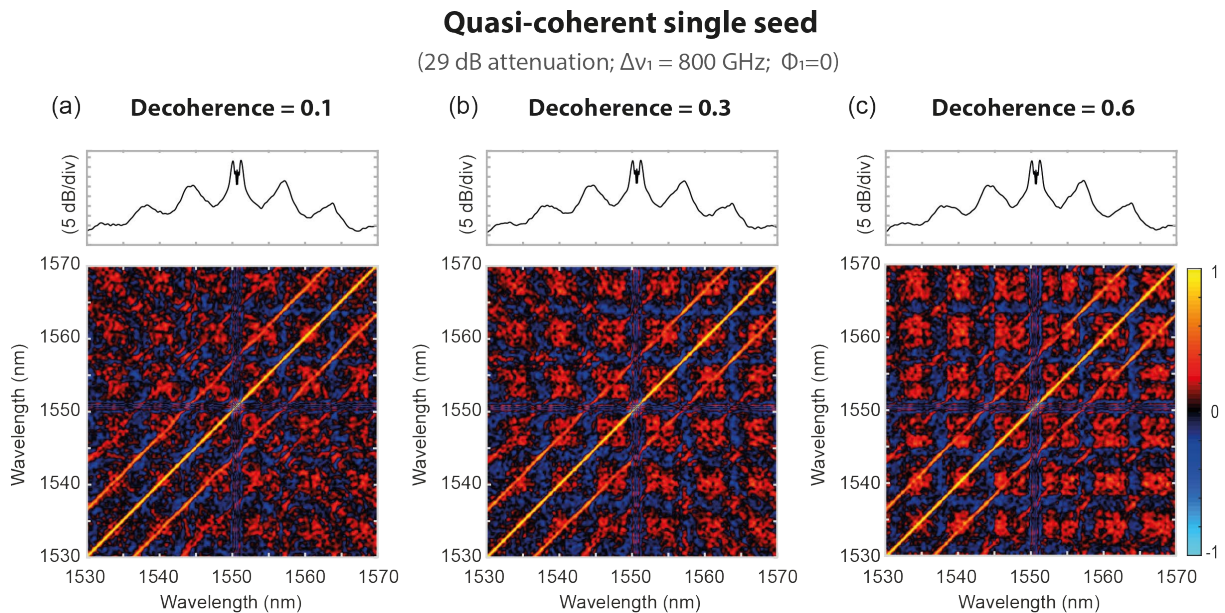


Figure IV.7 Average spectra (top panel) and correlation maps (bottom panel) obtained from 500 simulations with random initial seeds, demonstrating the effect of a weak quasi-coherent single seed with 29 dB attenuation added to the pump when considering a frequency detuning $\Delta\nu_1 = 800$ GHz. The results are shown for 3 different decoherence parameters (a) for $g = 0.1$, (b) $g = 0.3$ and (c) $g = 0.6$.

To understand the effects of the seed(s) coherence during nonlinear propagation, we present in Figure IV.7 a comparison between the average spectra and the correlation maps obtained using different decoherence degree g (see (Eq. IV.1)) for a single quasi-coherent seed with a frequency detuning $\Delta\nu_1 = 800$ GHz, and an attenuation of 29 dB regarding the pump. As we can see, when the degree of decoherence increases, we tend to obtain “square” correlation patterns owing to the growing impact of spontaneous noise being broadly amplified in the whole MI sidebands.

For this regime, we also conducted additional studies by analyzing the MI fluctuations observed when adding two weak quasi-coherent seeds (ν_1, ϕ_1) and (ν_2, ϕ_2) to the pump using (Eq. IV.1) with a decoherence degree $g = 0.3$. The seeds were added with 32 dB attenuation, so that the

induced modulation power remain the same as the single seed case. We then varied their frequency detuning and phase so that $\Delta\nu_2 = 2\Delta\nu_1$. As illustrated in Figure IV.8.a, such conditions lead to more complex dynamics and the emergence of distinct correlation features. Following the same analysis as the previous regimes to manipulate the seed parameters, we started by shifting the detuning of the seeds. In Figure IV.8.b we show the results obtained for $\Delta\nu_1 = 600$ GHz and $\Delta\nu_2 = 1200$ GHz with $\phi_1 = 0$ and $\phi_2 = \pi/2$, respectively. As expected, this modification may not induce as many changes as observed in the case of coherent dual seeding in Figure IV.5.c. Nevertheless, it does tweak the associated propagation dynamics that can be seen in the output correlation maps and cause slight alterations in the average spectrum. However, in comparison to the quasi-coherent single-seed scenario, the impact of the seed phase phases is in this case slightly more significant, especially as it influences SPM pump reshaping and therefore, the MI broadening dynamics. In summary, even in this quasi-coherent regime, the seeded FWM process plays an important role in the generation of the MI output spectrum depending on both the frequency and phase of the seeding signals.

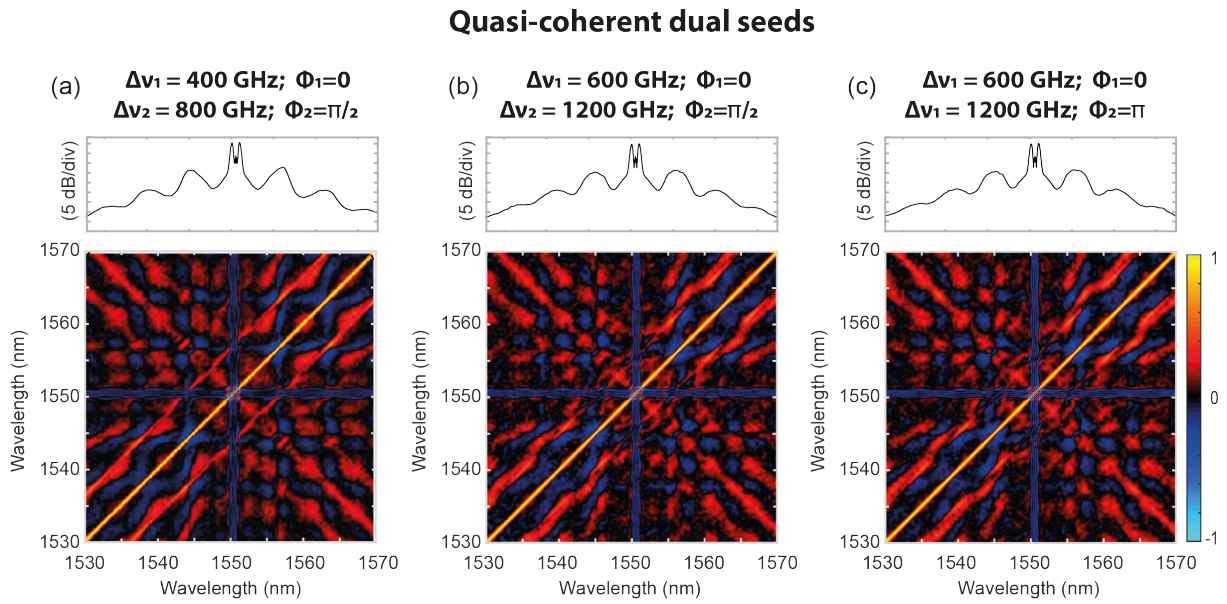


Figure IV.8 Illustration of the effect of introducing two weak quasi-coherent seeds to copropagate with the pump. Both the average spectrum (top panels) and the correlations (bottom panels) obtained from 500 simulations with random initial noise, are represented for 32 dB attenuated input seeds with frequency detunings $\Delta\nu_2 = 2\Delta\nu_1$, and a decoherence degree $g = 0.3$. The results are shown for three different cases: (a) $\Delta\nu_1 = 400$ GHz with $\phi_1 = 0$ and $\phi_2 = \pi/2$, (b) a shift in the frequency by $\Delta\nu_1 = 600$ GHz, and (c) a variation of the phase using ($\Delta\nu_1 = 600$ GHz, $\phi_1 = 0$), and ($\Delta\nu_2 = 1200$ GHz, $\phi_2 = \pi$).

IV.3. Experimental demonstration: Optimization of noise-driven MI dynamics

In the previous section, we have seen that optical seeding with different regimes and parameters allows us to modify and adjust the MI broadened spectra properties depending on the potential user requirements. However, from an experimental viewpoint, this analysis lacks fine-tuning and necessitates a large amount of time to probe the parameter space and find the optimal input seed(s) properties. To overcome these limitations, we here propose an experimental MI control using both optical seeding and machine learning strategies to iteratively adjust the initial conditions.

IV.3.1. Experimental setup

The overall setup used for this MI optimization study is depicted in Figure IV.9 and based on DFT measurements for experimentally assessing MI spectral fluctuations depending on the seed parameters.

Using the Waveshaper (Finisar, Waveshaper 4000A), we first filter a 80 fs laser pulse (60 mW input power) with a 12 GHz Gaussian filter centered at 1560 nm. We then add two coherent optical seeds to the pump with controllable central wavelengths and phase $((\lambda_1, \phi_1)$ and $(\lambda_2, \phi_2))$. In this experiment, the seeds have the same FWHM as the pump (34 ps Gaussian pulse) but with a 35 dB power reduction (as set in the Waveshaper filtering). The three signals are then amplified using an EDFA. To reduce the impact of the ASE generated during the amplification process (and suitably analyze the effects of the two weak seeds on the output spectrum), we only keep the signal between 1559.42 nm and 1564.63 nm using a bandpass filter (which corresponds to ~ 5 nm spectral span covering the first MI gain sideband on the long wavelength edge of the pump).

For nonlinear propagation, we use the same 485 m - HNLF as in section III.3. The average spectrum is collected with an OSA, and real-time fluctuations are analyzed using the DFT technique implemented via a DCF of a dispersion factor $D_{DFT} = 407$ ps/nm. After the DCF a second Waveshaper is used (Finisar, Waveshaper 4000A/X), to filter out the pump and get a better dynamic range on a 20 GHz photodiode (Thorlabs – DXM20AF) and a 6 GHz real-time oscilloscope (Rhode & Schwarz - RTO2064).

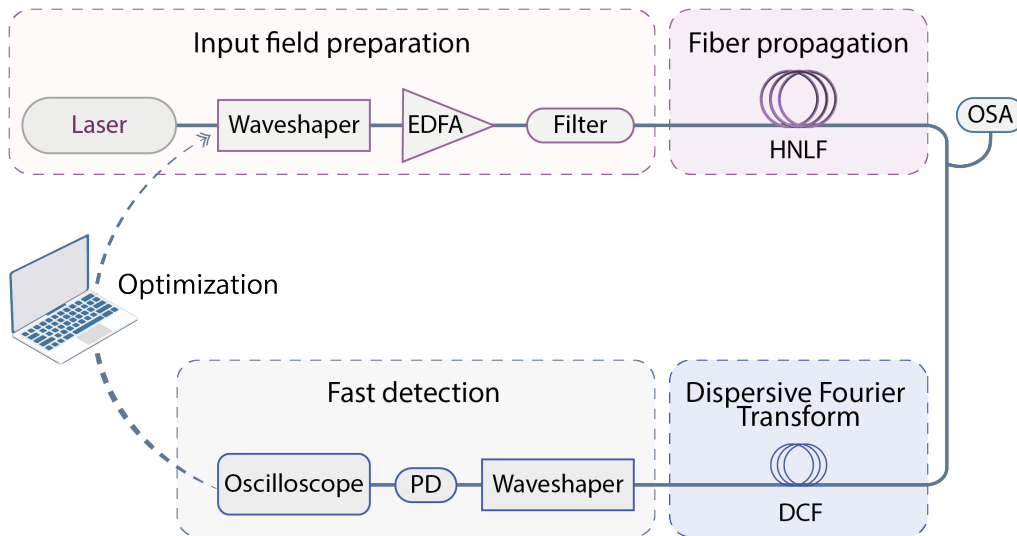


Figure IV.9 An 80 fs laser pulse centered at 1560 nm is reshaped using a programmable spectral filter (Waveshaper) into a picosecond pump and two seeds with adjustable spectral detuning and phase. The signals are then amplified using an EDFA and filtered between 1559.42 nm and 1564.63 nm to reduce the ASE. After propagation in a HNLF, we can either visualize the output with an OSA or perform a real-time detection using the DFT technique. A genetic algorithm is used to optimize the correlation between two specific wavelengths in the output spectrum by iteratively adjusting the input seed parameters.

Our study aims at trying to find the best seeds parameters to either maximize or minimize the correlation coefficient ρ between two frequency targets (ν_a and ν_b) located in the MI gain region on the short wavelength side of the pump (see Figure IV.10.a-b). On the other side of the pump, the seeds were configured to have a variable wavelength from 1560.5 nm to 1564.6 nm

corresponding to the first sideband of the MI spectrum, as shown in Figure IV.10.c, and a spectral phase continuously varying from 0 to 2π .

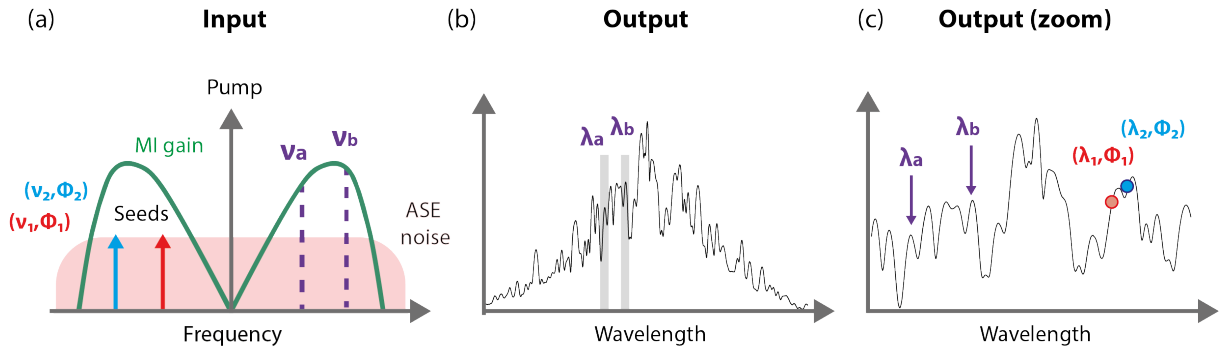


Figure IV.10 Representation of the experimental principles for MI optimization and varying parameters: (a) In the frequency domain, we select two targets ν_a and ν_b , positioned at higher frequencies than the pump. With the GA, we iteratively optimize the correlation between these two target wavelengths by adding coherent dual seeds $((\nu_1, \phi_1)$ and (ν_2, ϕ_2)) on the other side of the pump where the seed will experience MI gain. The seeds are intentionally weak, approximately matching the level of the ASE noise. (b) Spectral representation of the target wavelength on a seeded but fluctuating MI output spectrum. Note that here only the average spectrum is represented for clarity. (c) Representation of the location of both the targets and the seeds in the spectrum. In the case presented here, the seeds have variable central wavelengths that are tunable over only the first MI sideband located across the pump (compared to the target wavelengths).

Here we note that to be able to incorporate automated optimization strategies into this setup, I fully interfaced the instruments of the setup (i.e. two Waveshapers, an OSA, and a real-time oscilloscope) into a MATLAB program jointly driving all the apparatus and the optimization algorithm. Specifically, the real-time spectra of fluctuating MI are sequentially collected with the oscilloscope and processed to derive DFT time-frequency mapping and retrieve the relevant correlation maps from 500 successive DFT traces.

Based on this statistical analysis, we implemented a genetic algorithm to perform a seed parameter search for 30 successive generations of 50 individuals each, thus intending to find the minimum or maximum value of $\rho(\lambda_a, \lambda_b)$. Practically, the program will connect to the Waveshaper and change, for each iteration, the wavelength and phase of the pair of seeds, collect the DFT spectra, and repeat the process until finding the best parameters for an optimal result.

IV.3.2. Experimental results: First MI sideband optimization

For our first experimental campaign, the measurements were done for five different pairs of frequency targets, where the relation between their frequency detuning with respect to the pump varied was defined based on commensurate relationships such as:

- $\Delta\nu_b = 1.5\Delta\nu_a$, with the two cases of $[\Delta\nu_a = 0.3 \text{ THz}; \Delta\nu_b = 0.45 \text{ THz}]$ and $[\Delta\nu_a = 0.225 \text{ THz}; \Delta\nu_b = 0.3375 \text{ THz}]$
- $\Delta\nu_b = 2\Delta\nu_a$, with the case of $[\Delta\nu_a = 0.225 \text{ THz}; \Delta\nu_b = 0.45 \text{ THz}]$
- $\Delta\nu_b = 3\Delta\nu_a$, with the case of $[\Delta\nu_a = 0.2 \text{ THz}; \Delta\nu_b = 0.6 \text{ THz}]$
- $\Delta\nu_b = -\Delta\nu_a$, with the case of $[\Delta\nu_a = 0.45 \text{ THz}; \Delta\nu_b = -0.45 \text{ THz}]$

The results indicating the best seeds parameters and the optimal correlation value for the maximization and minimization of each pair of targets wavelengths are shown in Table IV.1.

$\Delta\nu_a$	$\Delta\nu_b$		λ_1	$\phi_1[\pi]$	λ_2	$\phi_2[\pi]$	$\rho(\lambda_1, \lambda_2)$
0.3 THz	0.45 THz	maximize	1561 nm	1.6039	1562.9 nm	0.01562	0.78
		minimize	1562.9 nm	0.48422	1564.2 nm	0.91023	-0.59
0.225 THz	0.3375 THz	maximize	1561 nm	1.985	1564.3 nm	0.47521	0.66
		minimize	1560.7 nm	1.9346	1562.4 nm	0.6752	-0.82
0.225 THz	0.45 THz	maximize	1562.6 nm	1.0507	1562.9 nm	0.60345	0.73
		minimize	1562.5 nm	0.026499	1564.3 nm	1.3264	-0.69
0.2 THz	0.6 THz	maximize	1561.8 nm	1.2721	1563.6 nm	1.3736	0.63
		minimize	1561.5 nm	0.86217	1562.7 nm	0.16764	-0.81
0.45 THz	-0.45 THz	maximize	1562.5 nm	0.79957	1563 nm	1.5605	0.56
		minimize	1563.2 nm	1.0007	1564 nm	0.82537	-0.54

Table IV.1 Quantitative analysis of the experimental results obtained for seeded MI optimization. The table indicates the optimal seeds parameters and correlation coefficients obtained after GA optimization, when either maximizing or minimizing the correlation coefficient $\rho(\lambda_1, \lambda_2)$ between the five different pairs of target wavelengths. Note that the phases are here given in units of π .

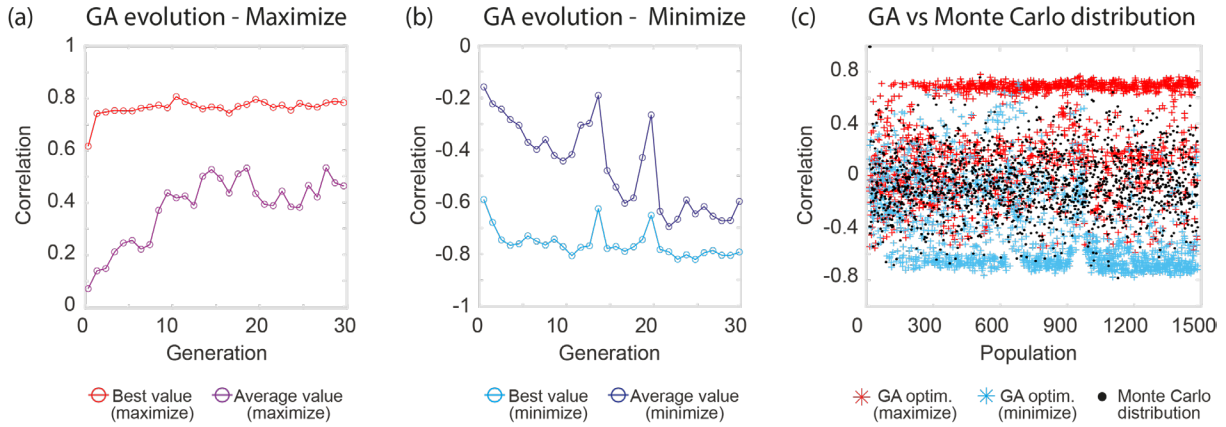
As an example, we analyze in more details two specific cases: When the frequency detuning of ν_a and ν_b are directly proportional to each other ($\Delta\nu_a = 0.225$ THz; $\Delta\nu_b = 0.45$ THz) and on the other hand, when $\Delta\nu_a = 0.3$ THz; $\Delta\nu_b = 0.45$ THz. The experimental results displayed in Figure IV.10, show that the GA can effectively optimize the correlation between the chosen spectral components in the output spectrum.

For instance, as we can see in Figure IV.11.a-b for the case of $\Delta\nu_b = 2\Delta\nu_a$, our algorithm achieved a maximum correlation of $\rho(\lambda_a, \lambda_b) = 0.73$ and, interestingly, managed to quickly converge and recognized the best seeds parameters within the first generations. Similarly, for the minimization case, even though the correlation evolution was not as stable along the optimization process, it still attained a minimal correlation of $\rho(\lambda_a, \lambda_b) \sim -0.7$.

For the case of $\Delta\nu_b = 1.5\Delta\nu_a$, shown in Figure IV.11.d-e, the optimization is not so obvious (at least from a physical viewpoint). As the frequency detuning of the spectral targets are not explicitly linked by a direct (or cascaded) FWM process, the relationship between these spectral components is more complicated and harder to optimize. Even then, our GA algorithm achieved a well-optimized correlation coefficient, however, it is clear that maximizing the correlations in such a regime proved to be easier than minimizing them.

To assess the efficiency of our optimization, we also performed correlation measurements using the Monte Carlo (MC) method, where at each iteration, the seeds' wavelength and phase, (λ_1, ϕ_1) and (λ_2, ϕ_2) are randomly modified. For both the cases discussed above, the comparison with GA optimization is provided in Figure IV.11.c-d. We clearly see that the GA's approach provided better results, allowing for a more efficient probing of the parameter space and an optimization robust to experimental perturbation.

$$\Delta v_a = 0.225 \text{ THz} ; \Delta v_b = 0.45 \text{ THz} \quad (\Delta v_b = 2\Delta v_a)$$



$$\Delta v_a = 0.3 \text{ THz} ; \Delta v_b = 0.45 \text{ THz} \quad (\Delta v_b = 1.5\Delta v_a)$$

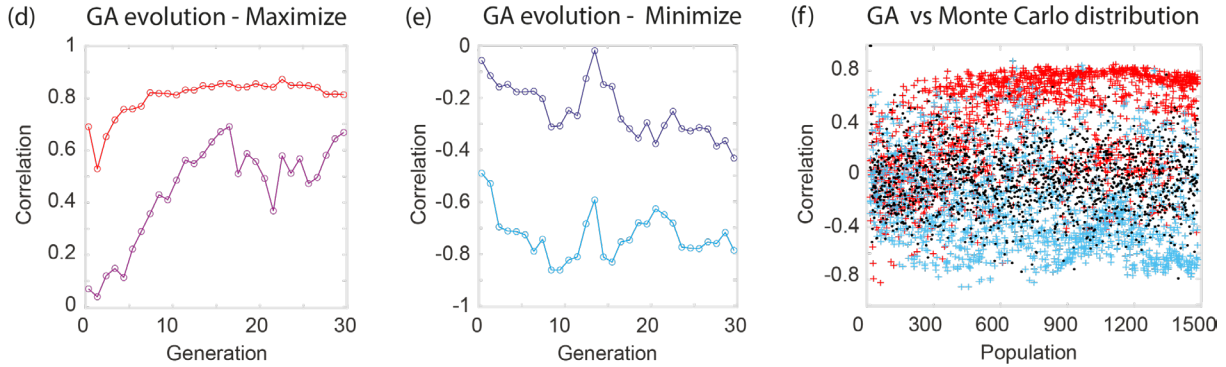
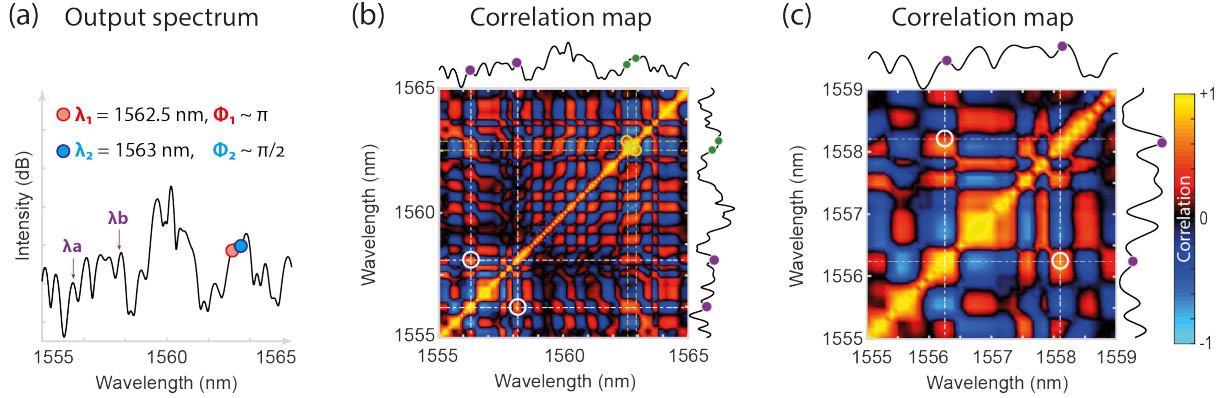


Figure IV.11 GA optimization of the correlation between two frequency targets ν_a and ν_b , when (a-c) $\Delta v_b = 2\Delta v_a$ and (d-f) $\Delta v_b = 1.5\Delta v_a$. For both cases, we present the GA evolution of the best and average values obtained in each generation when (a,d) maximizing the correlation and (b,e) minimizing the correlation. (c,f) Comparison of the distribution of the GA results with the ones obtained from Monte-Carlo measurements for iteratively generating random seed parameters.

For a better visualization of these achievable incoherent MI spectral adjustments, we also computed the Pearson's correlation maps (Eq. II.8) obtained after GA optimization for both of cases (see Figure IV.11).

Maximum correlation

$$(\Delta\nu_a = 0.225 \text{ THz} - \Delta\nu_b = 0.45 \text{ THz})$$



Minimum correlation

$$(\Delta\nu_a = 0.225 \text{ THz} - \Delta\nu_b = 0.45 \text{ THz})$$

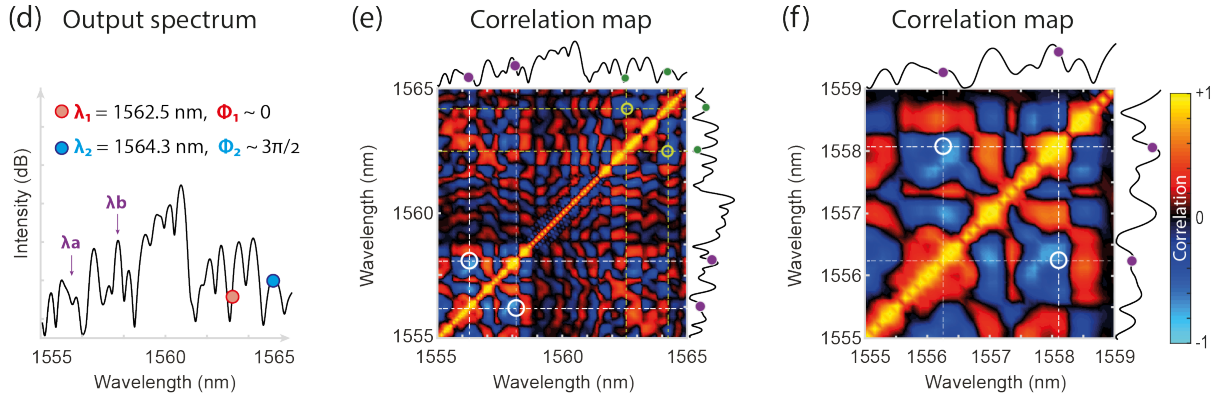


Figure IV.12 GA-optimized spectrum (a) and correlation maps (b,c) with the seed parameters (λ_1, ϕ_1) and (λ_2, ϕ_2) obtained for a maximal correlation between two frequency targets ν_a and ν_b with $\Delta\nu_a = 0.225 \text{ THz}$ and $\Delta\nu_b = 0.45 \text{ THz}$. The targets wavelengths are shown with white circles on the correlation maps indicating a positive correlation. (d-f) The same results for a minimal correlation between ν_a and ν_b . In the output spectra of (a) and (d), the frequency targets ν_a and ν_b are shown with purple arrows and the optimized seed parameters (and spectral locations) are shown, for each case, with blue and red dots. In the correlation maps (b) and (e), the seed locations are shown with green circles.

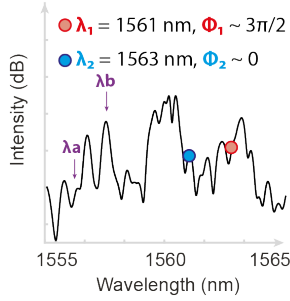
In the case of $\Delta\nu_b = 2\Delta\nu_a$, we found the best seeds parameters with $(\lambda_1, \phi_1) = (1562.5 \text{ nm}, \pi)$ and $(\lambda_2, \phi_2) = (1563 \text{ nm}, \pi/2)$, yielding a maximal correlation of $\rho(\lambda_a, \lambda_b) \sim 0.7$, as indicated in Figure IV.12.a. When looking at Figure IV.12.b-c, we can clearly see how the correlation between the two wavelength targets (λ_a, λ_b) , indicated in white circles is drastically increased (red colors of the map). In contrast, when looking at Figure IV.12.d-f, we can see how the correlation features in the map gain an opposite sign, and the correlation between the target wavelengths becomes minimal.

For comparison, in Figure IV.13, we also show the results of GA optimization for the case $\Delta\nu_b = 1.5\Delta\nu_a$. As above, we can prove the validity of our GA optimization by analyzing the correlations at the locations of the target wavelength. This value goes from $\rho(\lambda_a, \lambda_b) \sim 0.8$ for the maximization, to $\rho(\lambda_a, \lambda_b) \sim -0.6$ for the minimization.

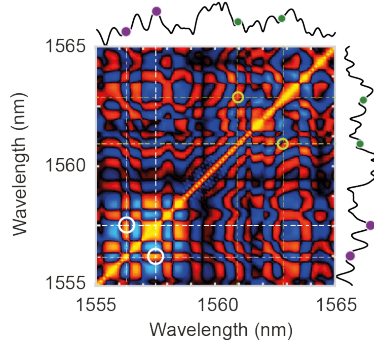
Maximum correlation

($\Delta\nu_a = 0.3$ THz - $\Delta\nu_b = 0.45$ THz)

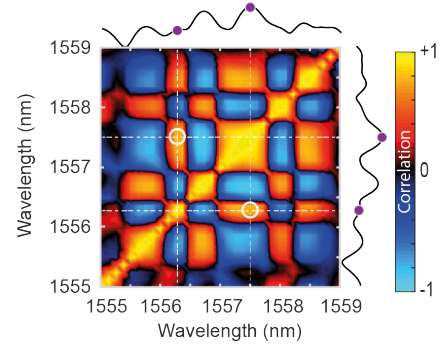
(a) Output spectrum



(b) Correlation map



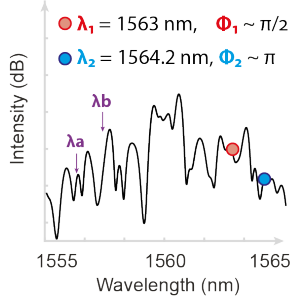
(c) Correlation map



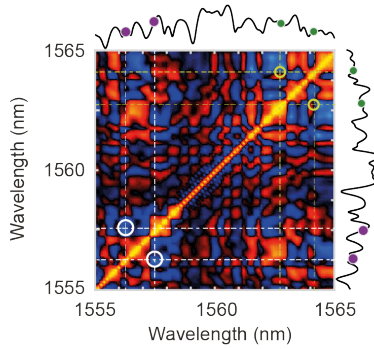
Minimum correlation

($\Delta\nu_a = 0.3$ THz - $\Delta\nu_b = 0.45$ THz)

(d) Output spectrum



(e) Correlation map



(f) Correlation map

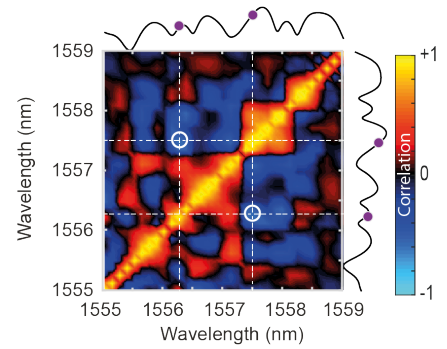


Figure IV.13 GA-optimized spectrum (a) and correlation maps (b,c) with the seed parameters (λ_1, ϕ_1) and (λ_2, ϕ_2) obtained for a maximal correlation between two frequency targets ν_a and ν_b with $\Delta\nu_a = 0.3$ THz and $\Delta\nu_b = 0.45$ THz. The targets wavelengths are shown with white circles on the correlation maps indicating a positive correlation. (d-f) The same results for a minimal correlation between ν_a and ν_b . In the output spectra of (a) and (d), the frequency targets ν_a and ν_b are shown with purple arrows and the optimized seed parameters (and spectral locations) are shown, for each case, with blue and red dots. In the correlation maps (b) and (e), the seed locations are shown with green circles.

As we can notice from Figure IV.12 and Figure IV.13, the wavelength and phase of the optimized seeds (for either maximum or minimum target correlations) are obtained at relatively well-defined values. However, looking closely at the seeds' parameters, we observe a great variability depending on the optimization target, and can also deduce that we have more complex dynamics involving both seed wavelength and phase adjustments to suitably tailor incoherent nonlinear effects during fiber propagation. In this case, the achieved optimization may help gaining insight into these noise-driven MI dynamics in realistic experimental regimes. While a complete analysis falls outside the scope of this thesis, in section IV.4, we also discuss the physical FWM mechanisms at play, and that can potentially underly the control of MI spectral broadening.

IV.3.3. Complementary studies: MI optimization extended to the second sideband

The optimization of the correlation using the experimental setup shown in Figure IV.9, proved successful all along the study, for a variety of experimental conditions. However additional analysis can be considered, for example by configuring the seeds to be selected on a range covering only the first MI sideband, but the target frequency for optimization located in the second sidebands of the MI spectrum. As an example, we present a result where the GA is limited to choosing the seeds between 1560.5 nm and 1564.6 nm (i.e. $|\Delta\nu_{1,2}| < 0.5$ THz) and analyzing frequency targets with $\Delta\nu_b = -\Delta\nu_a = 0.9$ THz.

Figure IV.14.a illustrates the evolution of the correlation algorithm for such optimization aiming at maximizing the correlation between on the second MI sidebands (via cascaded MI processes). The GA shows a stable increase towards a maximal correlation $\rho(\lambda_a, \lambda_b) \sim 0.6$, however, the GA seems to still evolve and may need a higher number of generations to fully converge and achieve better results in this particular case. The correlation map corresponding to the MI fluctuations generated from the optimal seeds (for a maximal correlation between ν_a and ν_2) is shown in Figure IV.14.b. The targets' positions are indicated in white circles and the seeds' locations are shown with the green circles.

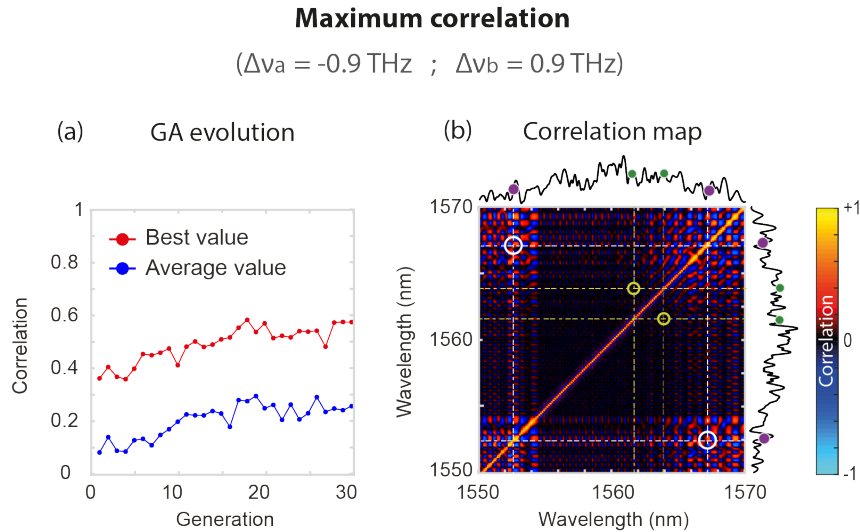


Figure IV.14 (a) GA evolution of the correlation between $\Delta\nu_a = -0.9$ THz and $\Delta\nu_b = 0.9$ THz along 30 generations with 50 individuals each. (b) MI average spectrum and the correlation map obtained after nonlinear propagation with the best seeds' parameters.

IV.3.4. Complementary studies: MI control in a high noise level regime

To study the impact of the weak coherent seeds in a chaotic noise-driven regime, we reconfigured the experimental setup by removing the filter after the EDFA, allowing the ASE noise to gain prominence in the dynamics and interact significantly with the seeds during HNLF propagation. A filter was instead added after the DCF, to study the spectral region between 1559.42 nm and 1564.63 nm with the best possible dynamic range during DFT measurements. In this case, the seeds were selected over a range covering the first MI sideband ranging between 1551 nm and 1556 nm (on the blue side of the pump).

Maximum correlation

$$(\Delta\nu_a = -0.225 \text{ THz} ; \Delta\nu_b = -0.45 \text{ THz})$$

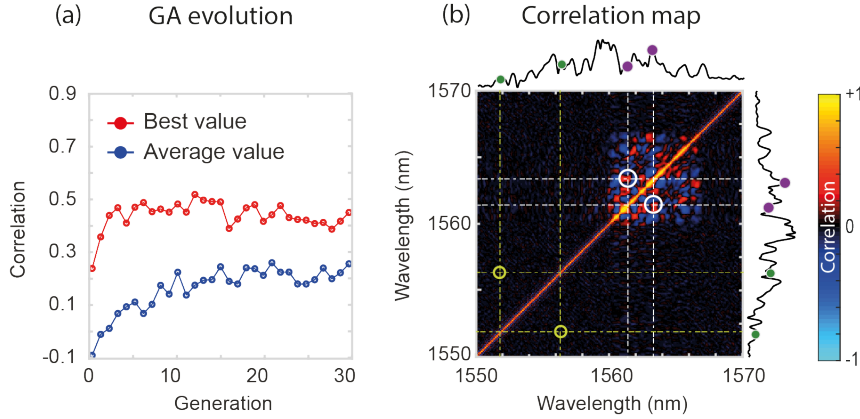


Figure IV.15 (a) GA evolution of the correlation between $\Delta\nu_a = -0.225 \text{ THz}$ and $\Delta\nu_b = -0.45 \text{ THz}$ obtained from the new setup configuration for noisy MI optimization. (b) MI average spectrum and the correlation map obtained after nonlinear propagation with the best seeds' parameters.

The results, displayed in Figure IV.15, show that in such regime, the correlations are harder to optimize due to the highly-fluctuating output spectrum (whose MI dynamics are relatively less impacted by optical seeds compared to the previous case). Figure IV.15.a shows the GA evolution of the correlation coefficient between $\Delta\nu_a = -0.225 \text{ THz}$ and $\Delta\nu_b = -0.45 \text{ THz}$ with a maximal value of only $\rho(\lambda_a, \lambda_b) \sim 0.52$ reached after optimization. This optimization result is illustrated in Figure IV.15.b, where we can see the positive correlation features appearing in the white circles, which represent the location of the targets. These results demonstrate the strong impact of the noise dynamics, the stability of the seeds and of the overall measurements to properly optimize MI correlation features. In this sense, investigating the stability and coherence of the seed signals may be of particular interest for finely-tuning incoherent dynamics with realistic numerical and experimental parameters.

IV.3.5. Complementary studies: On the coherence of optical seeds in experiments

The experimental results presented in section IV.3.2 considered purely coherent seeds, as the pump and the seed(s) follow the same optical path and all signals are combined and amplified together before nonlinear propagation.

However, for many practical applications, multiple signals are required to follow different path to enable suitable signal processing (filtering, amplification, etc.). This corresponds to the case of quasi-coherent seeding described in section IV.2.2. In such case, the impact of phase stability is important in the MI regime, as seen in Figure IV.7.

Currently, we are conducting ongoing experimental studies in a quasi-coherent regime, considering signals from the same laser source but practically experiencing decoherence.

Using the same setup configurations illustrated in Figure IV.3.c and Figure IV.9, we generate in our experimental studies optical seeds exiting from another port of the Waveshaper before EDFA amplification and joint nonlinear propagation in the 385 m-long HNLF.

For suitable processing of the input signal, one may require assessing the decoherence imprinted by these experimental systems. Experimentally, it is possible to assess decoherence through interferometric measurements at the fiber input. However, obtaining high fringe

visibility can be challenging when the seeds have over > 20 dB attenuation (resulting in a visibility of 1% at best) and impaired by broadband ASE noise (potentially leading to large experimental uncertainties).

Instead, in our case, we have tried to leverage the DFT technique (Figure IV.9) to detect fluctuating spectra and to indirectly assess this decoherence. To complement our experimental observations, we have thus performed a comparison with numerical simulations. These simulations allow us to empirically fit the decoherence degree of the seeds based on the MI fluctuations obtained at the fiber output, providing valuable insights into the dynamics of our quasi-coherent propagation. Comparing numerical results using different degrees of decoherence (see Figure IV.7), with the spectral correlation map extracted from an experimental measurement, we have identified that a degree of decoherence of $g = 0.3$ exhibits the best fit to our experimental results, and aligns well with the modulation instability dynamics observed in our experiments:

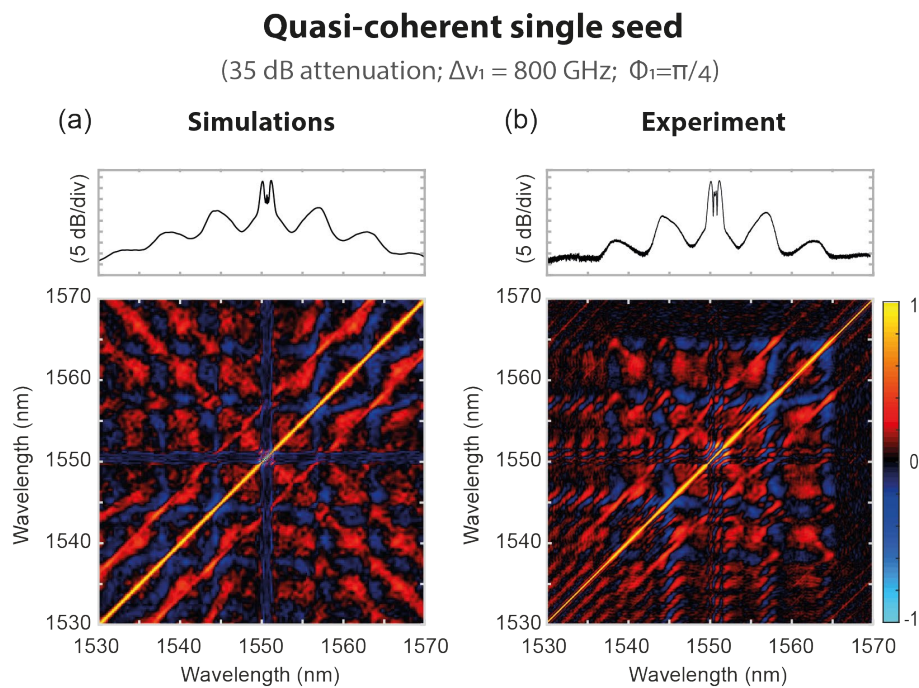


Figure IV.16 Comparison of the average spectra (top panel) and correlation maps (bottom panel) of a quasi-coherent single seed added to the pump with 35 dB attenuation and a frequency detuning of $\Delta\nu_1 = 800$ GHz, and $\phi_1 = 0.25\pi$, obtained (a) numerically from 500 GNLSE simulations with random initial seeds and considering $g = 0.3$, and (b) from 500 fluctuating spectra measurements collected experimentally using the DFT technique.

Figure IV.16, illustrates the comparison between the numerical and the experimental results using a decoherence of 0.3. In this case, we display a particular example obtained using a single quasi-coherent seed with 35 dB attenuation, a frequency detuning of $\Delta\nu_1 = 800$ GHz, and a phase $\phi_1 = \pi/4$. The results obtained here allow us to inform numerical simulations but will also be paramount for assessing the validity of experimental implementations and practical applications of MI-based signal processing and optimization techniques in the near future.

IV.4. Discussion on the MI optimization results

As we saw in the previous sections, MI optimization can be studied in different regimes. In this section, we discuss the experimental results obtained in section IV.3.2, trying to understand the impact of optimization on the underlying the FWM processes that can be excited under these conditions.

IV.4.1. Comparison of optimization algorithms

In section IV.3.2, we presented experimental results showing the optimization of the correlation coefficient between two defined targets via genetic algorithms. However, the choice to apply GA for such optimization was based on a comparison with PSO efficiency.

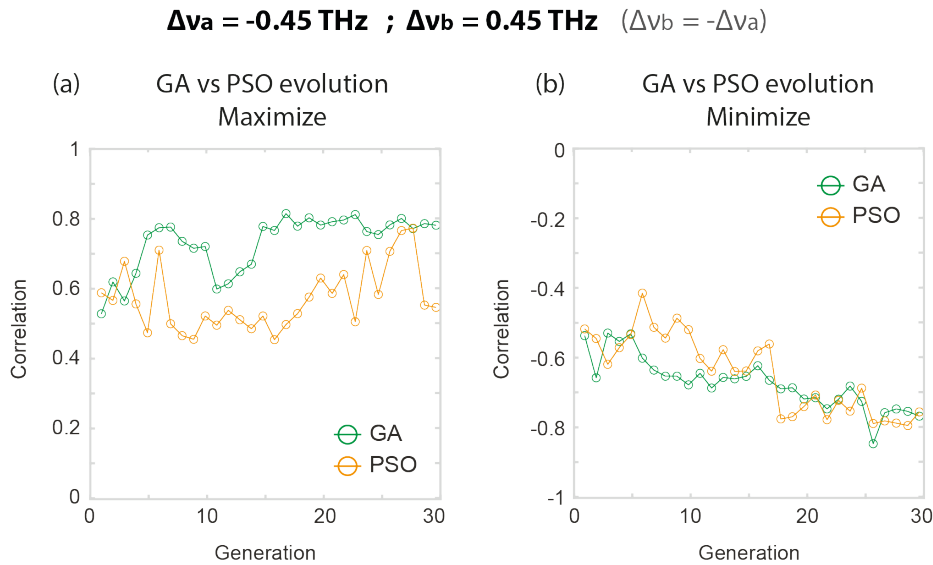


Figure IV.17 Comparison of optimization algorithms: GA (in green) and PSO (in yellow), for a (a) maximal correlation or (b) a minimal correlation between the frequency targets with a detuning of $\Delta\nu_a = -0.45 \text{ THz}$ and $\Delta\nu_b = 0.45 \text{ THz}$.

In Figure IV.17, we show the evolution of the correlation between the two targets (ν_a, ν_b), when $\Delta\nu_a = -0.45 \text{ THz}$ and $\Delta\nu_b = 0.45 \text{ THz}$. In both the maximization and minimization cases, the GA demonstrates a slightly faster convergence, finding optimal values early in the optimization process. Conversely, the PSO exhibits variable behavior along all the generations, eventually converging to similar values as the GA. However, due to this variation and the longer time required for stabilization, PSO may not be the best choice for this study. Obviously, this empirical observation may be put in perspective and further refined by the adjustment of the GA and PSO parameters for the heuristic search performed by the algorithms. Yet, comparing these results with randomly probing the parameter space with a Monte-Carlo approach (see Figure IV.11), it appears that the GA implemented provide a good baseline for an efficient optimization without being stuck with local extrema in the parameters space.

IV.4.2. Insight into the underlying MI conversion processes

In this study, the main crucial parameters are the frequencies and the phases of the seeds. Understanding the evolution and relation between these two parameters during the optimization allows us to discover interesting and important behaviors related to nonlinear processes arising during the HNLF propagation. For this reason, we studied the evolution of

the ratio between the frequency detuning of the two seeds $\Delta v_r = \Delta v_2 / \Delta v_1$ and the corresponding phase difference $\Delta \phi = \phi_2 - \phi_1$.

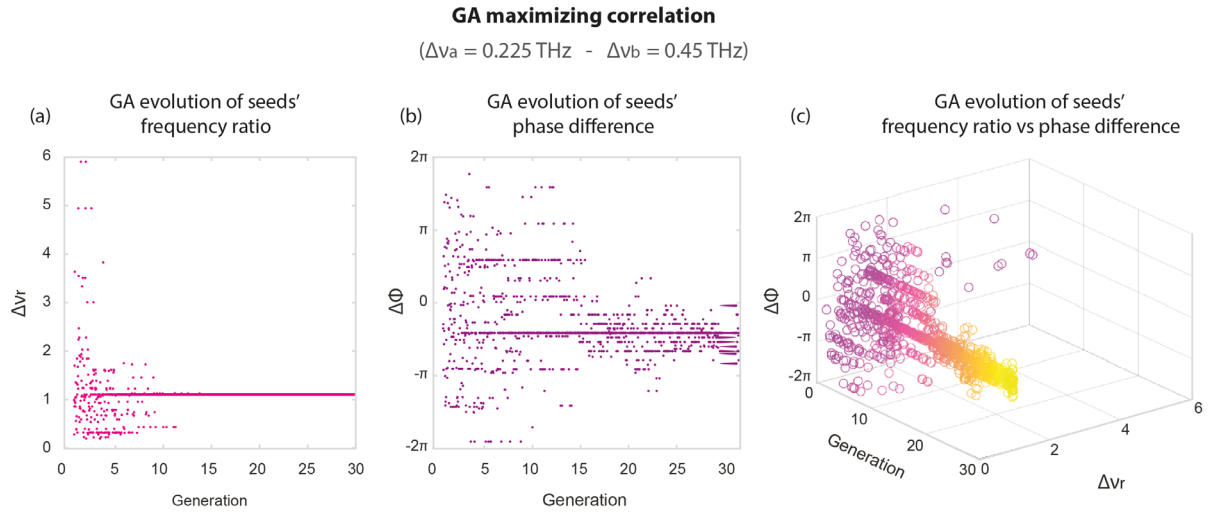


Figure IV.18 Evolution of (a) the frequency detuning ratio Δv_r between v_1 and v_2 , and (b) the phase difference between ϕ_1 and ϕ_2 , during GA correlation maximization between $\Delta v_a = 0.225$ THz; $\Delta v_b = 0.45$ THz. (c) A 3D representation of both the frequency detuning ratio and the phase difference as a function of the GA generation.

In Figure IV.18, we show for $\Delta v_a = 0.225$ THz and $\Delta v_b = 0.45$ THz, the evolution of these two frequency detuning and phase variables over the 30 generations used in our GA algorithm. In Figure IV.18.a, we can see a clear convergence of the frequency detuning ratio towards the best result obtained from the first few generations of the GA. In this case, the optimization yields a case where $\Delta v_r \sim 1$ which is not unexpected as it corresponds approximately to the same frequency detuning ratio of the target frequency (i.e. $\Delta v_r \sim \Delta v_b / \Delta v_a = 1$).

In contrast, in Figure IV.18.b, the evolution of the phase difference is less obvious and starts to converge towards the optimal solution, only after 15 generations. Even though it appears that the difference between the two phases is about $-\frac{\pi}{2}$, the phase optimization remains unstable along the generations. This can also be seen in Figure IV.18.c, which shows how the evolution of both the phase difference and frequency detuning ratio converges with the GA, starting from a random exploration of the seed parameter space towards well-defined parameter values.

While fairly trivial, this analysis is in fact important to understand more complex spontaneous MI mechanisms from simple FWM approaches. For instance, for the case where $\Delta v_b = 1.5\Delta v_a$ presented in Figure IV.19, the convergence is not straightforward:

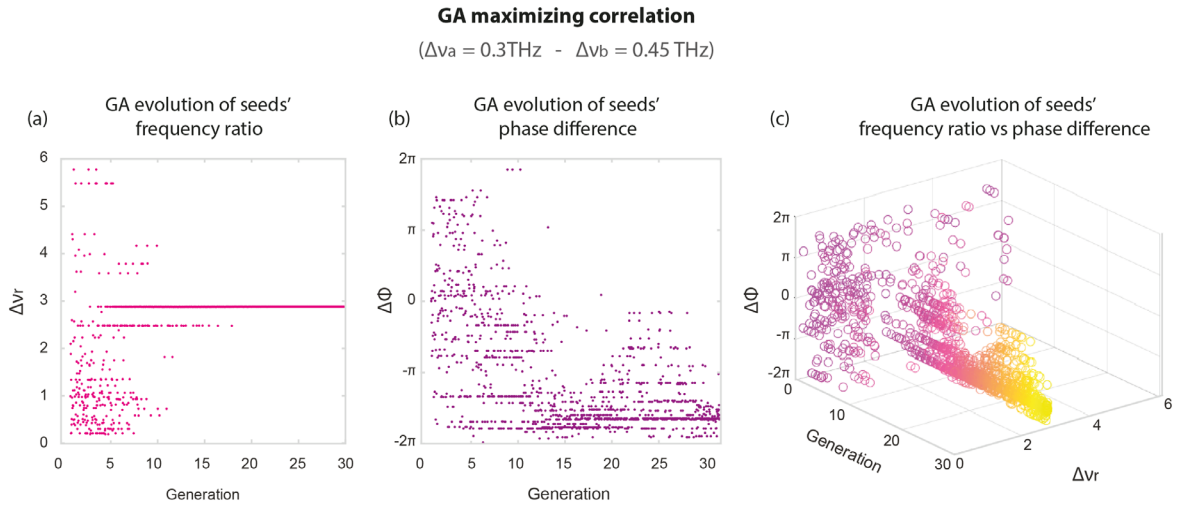


Figure IV.19 Evolution of (a) the frequency detuning ratio between ν_1 and ν_2 , and (b) the phase difference between ϕ_1 and ϕ_2 , during GA correlation maximization between $\Delta v_a = 0.3\text{ THz}$; $\Delta v_b = 0.45\text{ THz}$. (c) A 3D representation of both the frequency detuning ratio and the phase difference as a function of the GA generation.

We can see that for the frequency detuning ratio of the seeds (Figure IV.19.a), does not fully converge before at least 20 generations, eventually reaching a value $\Delta v_r \sim 3$. In addition, the phase difference optimization is very chaotic as illustrated in Figure IV.19.b, and the algorithm needs at least 27 generations to eventually reach optimal values so that $\Delta \phi = \phi_2 - \phi_1 \sim -1.5\pi$. The 3D representation of both the frequency ratio and the phase difference of the seed parameters (Figure IV.19.c) shows how this relation varies along the GA generations, hardly achieve optimal values for over 20 generations.

The two illustrated results presented here are only shown for the maximization case. However, we have observed that for the all the 5 combinations of target frequencies (and for both correlation maximization and minimization), the frequency detuning ratio of the seeds converged quickly over the first tens of GA generations, but the evolution of the seed phase difference demonstrates a more complex optimization.

The reason behind these dependencies, which involve optimizing the seeds' parameters in both frequency and phase towards two defined targets, take obvious roots in the process of four-wave mixing. As we discussed in section I.5.2, modulation instability is a degenerated FWM process, resulting from an energy transfer from the pump, into unstable frequency components, satisfying the energy conservation specified in (Eq. I.58): $2\nu_p - \nu_{pos} - \nu_{neg} = 0$ (and eventually a reversed energy from the modulation frequency components into the pump when the adequate phase matching conditions are met).

To leverage this extremely simple but powerful property, we offer below a qualitative interpretation of potential cascaded FWM processes than can occur during nonlinear propagation to shed light in the GA results obtained for two cases of optimized MI optical seeding (as reported in Figure IV.11).

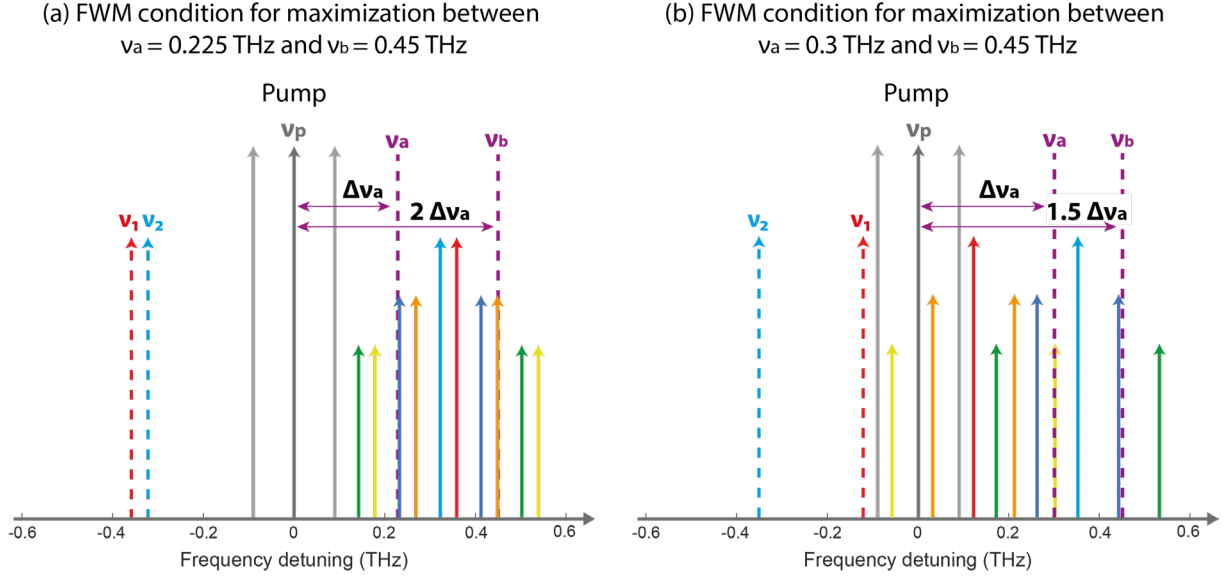


Figure IV.20 Illustration of the FWM processes potentially occurring during MI evolution and resulting from the interaction between the pump and the optimal coherent seeds (v_1, v_2), obtained for a maximal correlation between (a) $\Delta v_a = 0.225$ THz; $\Delta v_b = 0.45$ THz, and (b) $\Delta v_a = 0.3$ THz; $\Delta v_b = 0.45$ THz. Parameters: For (a), the optimized seeds have a detuning $\Delta v_1 = -0.36$ THz and $\Delta v_2 = -0.32$ THz. For (b), the optimized seed detuning's are respectively $\Delta v_1 = -0.12$ THz and $\Delta v_2 = -0.35$ THz.

In Figure IV.20, the pump is represented in dark grey, and the two seeds in dashed red and blue, respectively. We then calculate the new frequencies that may emerge from direct FWM based on energy conservation conditions:

First, we compute the two symmetrical frequencies (in solid red and blue lines) resulting from the interaction between the pump and the seeds, using the relation $v_{i_k} = 2v_p - v_i$, with $i = \{1,2\}$ representing the seed index and where k refers to the FWM process index (here, this direct FWM process is noted $k = 1$).

However, it is important to note that FWM it can arise from the mixing between the seeds and either or both of the pump frequency and/or the small pump sidelobes generated by self-phase modulation (SPM), which are here considered to be at a detuning of ± 0.9 THz. In this case, we obtain $2v_p = v_{SPM^-} + v_{SPM^+}$ and FWM symmetrically distributed around the pump can be attributed to either a degenerate process (with $v_{i_1} = 2v_p - v_i$) or a non-degenerate process (with $v_{i_1} = v_{SPM^-} + v_{SPM^+} - v_i$).

More importantly, in this regime where SPM is non-negligible (and where $\sim 2-3$ sidelobes are generated via a nonlinear phase shift $\pi < \Delta\Phi_{SPM} < 2.5\pi$, see (Eq. I.34) and Figure I.8), FWM can emerge from a pump combination of different SPM lobe components:

In the first non-degenerate case, a new frequency can appear from the interaction with one photon from the central pump and one photon of the pump SPM sidelobe so that $v_{i_2^+} = v_p + v_{SPM^+} - v_i$ and $v_{i_2^-} = v_p + v_{SPM^-} - v_i$ depending if we consider the negative or positive SPM sidelobes. These FWM frequencies are illustrated with orange arrows for $i = 1$ and dark blue arrows for $i = 2$ in Figure IV.20.

Similarly, in a degenerate case, the 3rd FWM can yield a new frequency can appear from the interaction with two photons of either pump SPM sidelobe so that $v_{i_3^+} = 2v_{SPM^+} - v_i$ and

$\nu_{i_3^-} = 2\nu_{SPM^-} - \nu_i$, depending on the SPM sidelobe considered. These FWM processes are represented in yellow for $i = 1$ and in green for $i = 2$ in Figure IV.20.

A particular interest here is the fact that, in Figure IV.20.a, we added the location of the two targets ν_a and ν_b to the diagram when $\Delta\nu_a = 0.225$ THz and $\Delta\nu_b = 0.45$ THz. One can observe that the two targets correspond to a direct FWM combination between the pump, an SPM sidelobe, and the seeds. As the frequencies detuning of the targets are directly proportional to each other, their correlation are expected to be readily by the optimized seed from a similar FWM process. As a comparison, we also show in Figure IV.20.b the case for $\Delta\nu_b = 1.5\Delta\nu_a$. Here, however, the targets seem to correspond to two different FWM process: between the positive SPM sidelobe and the 1st seed (in one case), and between the pump, the positive SPM sidelobe, and the 2nd seed (in one case).

It is important to notice that the seeds chosen by the GA seem to in fact originate from a rather simple FWM process, but here provided by realistic experimental conditions beyond the tree wave mixing approximation. This simple approach thus needs to be taken inconsideration even when dealing with highly incoherent MI dynamics. Whether the targets are directly related to each other or not (and depending on a targeted increase or decrease of the desired spectral correlation), these effects will vary, and the GA will explore more complex combinations to find the optimal parameters for the specified desired tuning of MI spectral fluctuations for the precise experimental settings of the system.

Of course, these nonlinear effects are more complex than simple SPM degenerate/non-degenerate FWM, that and cannot be only explained with such analysis. First, in this regime defined by broadband noise and seed amplification, one may need to consider more complex and cascade FWM process that might excite the same frequency components in a non-trivial manner. Moreover, in addition to the seed frequency (for energy conservation), we must also take into consideration the phase matching explained by (Eq. I.57) that favor specific FWM processes and allow for fine-tuning the statistical energy allocation in a noise-driven MI. However, measuring this parameter experimentally and predicting/forecasting suitable FWM phase matching for adjusting incoherent frequency conversion is expected to be challenging from a theoretical and numerical viewpoint. Yet, the GA seems to empirically converge to specific phase relationship between the seeds are definitely of interest.

Further studies may be used here to gain insight into the behavior of the phase and better understand the relation between the seeds' parameters and the targets. Numerically modeling this experiment may indeed enable a more in-depth analysis of the phase, but it would be difficult to replicate the same initial conditions due to the noise-dependency of our measurements and potential instruments instability (especially the EDFA), preventing us from achieving a good agreement between the numerical and experimental approaches.

The impact of the phase of the seed (and the seed intrinsic coherence with respect to the pump signals) is an aspect that is currently being investigated from both an experimental and numerical point of view (see also Figure IV.6 and Figure IV.8) but falls outside of the scope of the study reported in this manuscript.

In this chapter, we showed the impact of the seeds' chosen parameters on incoherent nonlinear processes and demonstrated that carefully optimizing these parameters allows for interesting insights into the MI phenomena unfolding during nonlinear guided propagation. Our

exploration revealed that the evolution of these parameters during optimization is not straightforward but was however empirically successful.

As we look ahead, the path to deeper understanding and control of noise-driven MI dynamics becomes even more intriguing. The application of machine learning allowed for a fine-tuning optical seed parameters in real-time, enabling us to significantly reduce the time and effort required for manual adjustment while simultaneously improving the precision of our results in realistic experimental environments. Next, an important aspect of MI control will arise from using quasi-coherent signal for optimization in experimental frameworks more adapted to a large variety of experimental conditions for numerous applications involving optical seeding (e.g. study the impact of seed coherence in the overall MI processes, but also leverage spontaneous MI to assess and measure signal coherence via nonlinear amplification).

Similarly, an in-depth study of the phase-dependent incoherent process and their impact in cascaded and complex FWM dynamics will be particularly interesting, especially for regimes at the boundary between nonlinear and quantum signal processing (see also Chapter III).

Another avenue of exploration lies in the use of deep learning and neural networks for the study of incoherent MI process, along with their prediction and advanced control beyond simple iterative optimization algorithms (an approach currently implemented and undergoing development in our lab in the framework of MI processes). These powerful computational tools have the potential to predict the optimal input parameters to achieve a desired output, whether in numerical simulations or experimental studies, paving the way for more efficient and impactful investigations in various research domains [148], [267], [268]. Finally, we note that these studies, although oriented on nonlinear dynamics, possess applications that extend far beyond the realm of MI control. The ability to finely tailor fluctuating nonlinear dynamics has profound implications for fields such as imaging and nonlinear microscopy/spectroscopy techniques (see e.g. Appendix 1).

Conclusion

The main objectives of this thesis were to develop fundamentally novel approaches for tailoring the spectral and temporal properties of ultrafast optical laser pulses. Leveraging machine learning, we have demonstrated the ability to adapt the pulse's characteristics and optimize multidimensional nonlinear propagation in selected optical waveguides. The fast and practical adjustment of output wave packets paves the way towards various applications, notably for adaptable multiphoton microscopy techniques with enhanced computational imaging capabilities.

Chapters I and II were dedicated to reviewing nonlinear effects in optical fibers and presenting the various numerical and experimental methodologies employed throughout this manuscript, ranging from optical pulse processing and characterization techniques to optimization approaches using machine learning strategies.

The key results of this work (Chapter III) were centered on the development of a novel dispersive Fourier-transform-based characterization technique (DFT), using multiple single-photon detectors (SPD). This innovative approach enabled us to analyze spectral instabilities with high resolution, sensitivity, and an enhanced dynamic range. By studying the dynamics of modulation instability (MI) within a highly nonlinear fiber, we have experimentally demonstrated, using this quantum-inspired method, the capability to perform spectral correlation measurements across broadband (40 nm bandwidth) fluctuating MI spectra by means of coincident photo-events acquired by the single-photon detectors. By employing statistical mutual information analysis (MIA) and computing the spectral correlation maps corresponding to these measurements, we conducted a thorough comparison with the "standard" DFT technique. Remarkably, we showed that the low temporal jitter provided by these detectors (25 ps) and their exceptional quantum efficiency (exceeding 90%) allowed our DFT approach to offer significantly superior performances in terms of signal sensitivity (detection below the femtowatt level) and spectral resolution (reaching approximately 53 pm), which proved helpful in measuring high dynamic range (over 80 dB) and detecting very low-intensity signals that can merely be resolved by commercial instruments such as optical spectral analyzers, and out of the reach of standard real-time characterization techniques. We anticipate that this SPD-DFT technique will hold a strong potential for various applications. This includes, among other, the fields of imaging and multiphoton spectroscopy/microscopy, where high sensitivity and advanced spectral detection are essential for non-repetitive multidimensional signal analysis. This also covers diverse aspects of optical metrology (e.g. frequency comb stability monitoring) and quantum photonics (e.g. quantum state manipulation, squeezing and phase-sensitive amplification, to only name a few examples).

In Chapter IV, building on the experimental observations of Chapter III, we conducted an in-depth exploration of the significance of introducing optical seeding into an initial pulse to spectrally shape the input signal and study its impact on incoherent nonlinear dynamics. In this case, we specifically focused our work in the context of modulation instability occurring during optical fiber propagation. We first performed a numerical study using GNLS simulations to investigate MI instabilities within a regime situated between spontaneous and induced MI. Our results were obtained for two distinct scenarios, which we examined through statistical Pearson's correlation analysis. In the first scenario, we combined the initial pump with coherent optical seeds, carefully considering various parameters such as the seeds' frequency detuning

and phase, and we demonstrated the influence of the initial conditions on the resulting output spectrum. In the second scenario, we introduced quasi-coherent seeds to an amplified pump, leading to a competition between induced modulation and noise-driven dynamics during nonlinear propagation, which also impacted MI dynamics, thus affecting the correlation features between the spectral components. We noticed that in both cases, the addition of extremely weak optical seeds can drastically modify even highly incoherent fiber propagation regimes, including noise-driven and cascaded FWM processes excited by MI. Our investigation extended to an experimental setup involving coherent optical seeds, where we tried to optimize the correlation between two frequency targets selected from the output MI spectrum (after nonlinear propagation). Leveraging evolutionary algorithms, we adjusted the seeds' parameters to optimize the correlation coefficient between selected target wavelengths. Among others, genetic algorithm optimization demonstrated excellent results to effectively maximize or minimize the correlation between different pairs of frequency targets. This approach allowed for analyzing the statistical relationships and correlations among particular spectral components. For instance, we successfully characterized noise-driven MI dynamics and their incoherent cascaded four-wave mixing processes. Clear changes in the correlation maps within the output spectrum were identified when slightly adjusting the initial conditions. Interestingly, we were able to illustrate the relationship between the chosen seeds and the target wavelengths via simple FWM processes. These results, although promising, now require further analysis in a more fundamental framework and to address in more details the impact of the phase and coherence of the seeds in the adjustment of complex incoherent MI dynamics.

It is worth mentioning that the points addressed over this thesis within this research subject paves the way towards deeper studies of MI dynamics, investigating e.g. different regimes with a larger set of seed parameters using other evolutionary algorithms, or artificial neural network strategies. In particular, the use of neural networks is expected to allow for a predictive behavior of incoherent nonlinear processes, which could prove significant for e.g. forecasting extreme event formation [269], [270]. More importantly, such ANN approaches are expected to learn and predict optimal seed or input conditions from experimental output spectra and correlation maps (when trained in an inverse problem configuration). This ANN prospect should enable gaining further insights in the underlying physical process and complexity of the system, which is an approach currently being studied in our team from both a numerical and experimental viewpoint [271].

In this thesis, we mainly presented results leveraging spectral control of ultrafast optical laser pulses for tailoring nonlinear propagation dynamics. As described in Chapter II, my research work also involved significant contributions in temporal pulse shaping, and the preparation of the numerical and experimental framework for coherent pulse preparation with an integrated photonics system (IPPP). While these studies are not explicitly presented in the core of this manuscript, I also included numerical results and preliminary experiments involving IPPP processing for which I contributed in the Appendices section.

Based on this work, the exploration can now continue towards harnessing control of signal temporal processing within the IPPP and characterize tailored nonlinear dynamics with newly developed characterization tools (i.e. the DFT techniques [272], [222] presented in Chapter II and III, but also the home-made FROG system described in Chapter II and characterized in the Appendix 2, as well as an asynchronous X-FROG system recently developed in the lab for fast and iterative spectro-temporal characterization of broadband optical signals [273]).

Extending the control of nonlinear dynamics towards the generation of supercontinuum, we were for instance able to demonstrate, in a numerical study, the ability to manipulate broadband optical sources with important implications for shaping the signal for selective multi-photon imaging applications [274] (see Appendix 1). Exploiting the concepts of selective dual pumping at different wavelengths, with direct synchronization from tailored supercontinuum, we expect to reach selective two-photon excitations and generate CARS signals with spectrally and temporally selective responses. Importantly, with the appropriate multidimensional (spectro-temporal) signal enhancement and filtering, a completely new, autonomous, versatile, and self-optimized fibered architecture suitable for advanced multimodal imaging capabilities may be envisioned in the future.

In this framework, we also plan to manipulate the above-studied nonlinear effects in the context of multidimensional interactions within a multimode fiber. Exploiting the complex system inherent to variable dispersion and nonlinearity between modes, we aim at strategically adjusting the initial conditions of each spatial mode to control 3+1D nonlinear propagation and shape the output wavepacket effectively. Multiple spatial modes can be coherently (or incoherently) seeded using a fibered spatial mode multiplexer (SMUX) to ideally create specific interference patterns at the fiber output after suitable adjustment of the initial conditions. The work reported in this thesis thus constitutes a strong basis for such spatial, temporal, and spectral wavepacket control that should provide optimal point spread functions, limited beam diffraction, adjustable nonlinear focusing, and controlled polarization/OAM states. Such innovations can open exciting possibilities in imaging, spectroscopy, and tailored light generation, offering numerous and promising avenues for future research and development.

Appendices

Appendix 1. Numerical study: Supercontinuum optimization towards multiphoton microscopy.....	146
Appendix 2. Characterization of ultrashort pulse patterns generated by an integrated photonic chip: Experimental implementation of advanced FROG system.....	152
Appendix 3. Acronym list.....	155
Appendix 4. Publication list.....	157
Appendix 4.1. Peer-reviewed articles.....	157
Appendix 4.2. Articles in preparation.....	157
Appendix 4.3. International conferences (<i>with proceedings</i>).....	157
Appendix 4.4. National conferences (<i>with proceedings</i>).....	158
Appendix 4.5. Other symposiums and workshops.....	158

Appendix 1. Numerical study: Supercontinuum optimization towards multiphoton microscopy

As we already mentioned in Chapter II.2, several tools can be applied to adjust the spectral, but also the temporal properties of an input pulse. In this context, we performed extensive numerical studies on the potential of using the IPPP chip (described in Chapter II.2.2) in order to control and optimize the spectro-temporal content of supercontinuum generation, for multiphoton microscopy purposes [275], specifically multi-photon excitation (MPE) microscopy.

MPE is a fundamental aspect of multi-photon microscopy, crucial for various imaging modalities, allowing for selective imaging and examination of biological living tissues in four dimensions (x-y-z-t) [276]. It provides excellent sectioning effects, ensuring sufficient spatial resolution. In addition, due to its large wavelength range of potential excitations (visible and near-IR) [277], [278], this technique possesses the ability to mitigate both scattering loss and photodamage of the tissue sample, typically enabling imaging with further penetration depth [279], [280]. However, MPE faces limitations associated to conventional laser sources arising from factors such as the narrow bandwidth of typical laser gain media and the constraints of wavelength conversion techniques for selective and efficient MPE. As an alternative solution, this study explores the concept of supercontinuum generation for reconfigurable and selective MPE microscopy.

Broad supercontinuum spectra encompass numerous absorption peaks of different fluorophores, making it suitable for various imaging techniques and potential multiplexed spectroscopy [281]. In this study, we employ machine learning techniques such as GA and PSO to enhance the spectro-temporal properties of supercontinuum generation. This optimization process aims to selectively enhance multi-photon absorption (MPA) signals compatible with various fluorophores or imaging modalities. The numerical modeling is based on a realistic experimental setup shown in Figure A.1 and uses the split-step Fourier method to solve the GNLSE in an on-chip programmable delay line (PDL), with adjustable splitting ratio (see Figure II.6), before propagation in HNLF [282].

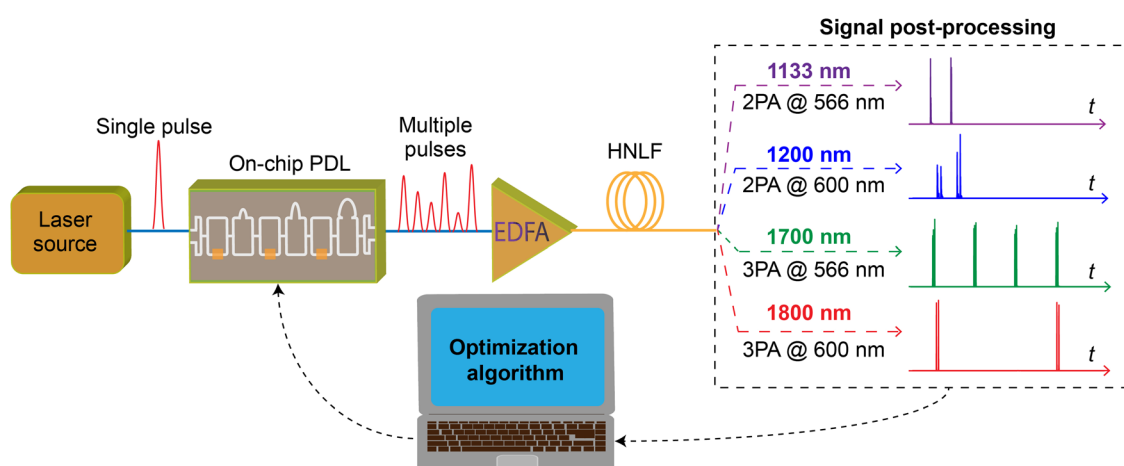


Figure A.1 Schematic representation of the proposed system, showing how reconfigurable temporal pulse patterns, generated by the PDL, drive nonlinear propagation in a HNLF, thus resulting in reconfigurable spectral broadening. The PDL's interferometer settings can be optimized using machine learning methods to selectively enhance MPA signals at wavelengths of interest (see right panel).

The PDL (also termed IPPP for its processing capabilities beyond simple delay adjustment) is constituted from 5 cm waveguide structures with a high nonlinear parameter $\gamma = 233 \text{ W}^{-1} \cdot \text{km}^{-1}$, a GVD parameter $\beta_2 = -2.87 \text{ ps}^2 \cdot \text{km}^{-1}$, and a TOD parameter $\beta_3 = -0.0224 \text{ ps}^3 \cdot \text{km}^{-1}$, with relatively low losses (0.06 dB/cm), as described in section II.2.2 of the main manuscript and in [282], [283], [275]. The HNLF is a 10 m-long Ge-doped homemade fiber, and its characteristic are: $\gamma = 3.5 \text{ W}^{-1} \cdot \text{km}^{-1}$, $\beta_2 = -2.15 \text{ ps}^2 \cdot \text{km}^{-1}$, and $\beta_3 = 0.0693 \text{ ps}^3 \cdot \text{km}^{-1}$.

A Gaussian laser pulse with adjustable power, temporal width, and chirp, centered at 1560 nm travels within the PDL to generate a single pulse seed (when the splitting ratios on all the MZI are equal to zero), or reconfigurable pulse patterns (when the splitting ratios are adjusted).

The obtained signal is then amplified by an EDFA before entering the HNLF. We then consider two spectral regions with wavelengths suitable for MPA excitation, specifically two-photon absorption (2PA) excitation such as $\lambda_1=1133 \text{ nm}$ (2PA centered at 566 nm) and $\lambda_2=1200 \text{ nm}$ (2PA at 600 nm), or three-photon absorption (3PA) excitation such as $\lambda_3=1700 \text{ nm}$ (with a 3PA at 566 nm) and $\lambda_4=1800 \text{ nm}$ (3PA at 600 nm).

We illustrate the temporal and spectral evolution (Figure A.2.a–b) of a 100 fs Gaussian input pulse (with a peak power of 12 kW and a negative chirp $C = -5$) during HNLF propagation, and we highlight the four chosen wavelengths at the output (Figure A.2.c) in the spectral and temporal domains.

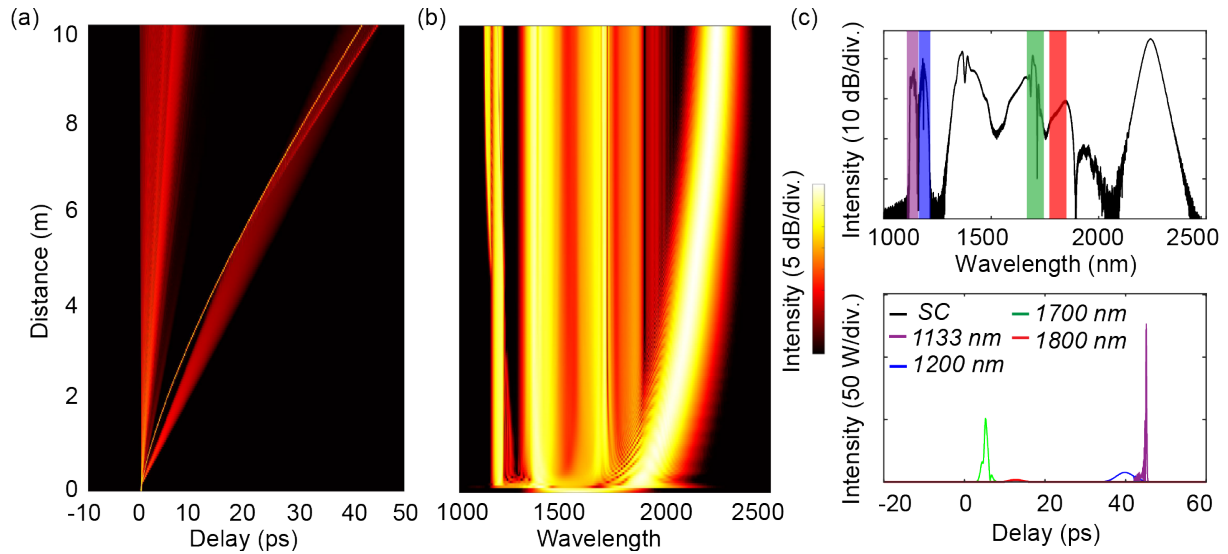


Figure A.2 Temporal (a) and spectral (b) evolution of a SC generation in a 10 m-long HNLF, obtained from numerical simulations using a single pulse with a peak power $P_0= 12 \text{ kW}$ and 100 fs temporal width, with a negative chirp $C = -5$. (c) The corresponding output spectrum (top panel) and temporal waveforms (bottom panel) filtered at selected wavelengths.

For the optimization, we try to maximize, using evolutionary algorithms (specifically GA and PSO), the corresponding 2PA and 3PA intensities:

$$I_{2PA,\lambda_{1,2}} = \int (I_{\lambda_{1,2}})^2 dt \quad \text{and} \quad I_{3PA,\lambda_{3,4}} = \int (I_{\lambda_{3,4}})^3 dt$$

The first results are shown in Figure A.3, obtained by varying the input parameters of a single input pulse: the peak power from 5 to 20 kW, the temporal width between 50-200 fs, and the chirp parameter between -10 and +10. The GA optimization is compared with random Monte-Carlo (MC) simulations using 10^5 sets of different initial parameters. As we can see for the four

wavelengths of interests, the GA optimization yields higher MPE signals than random probing of the parameter space, with a number of simulations required typically one order of magnitude lower than the MC approaches.

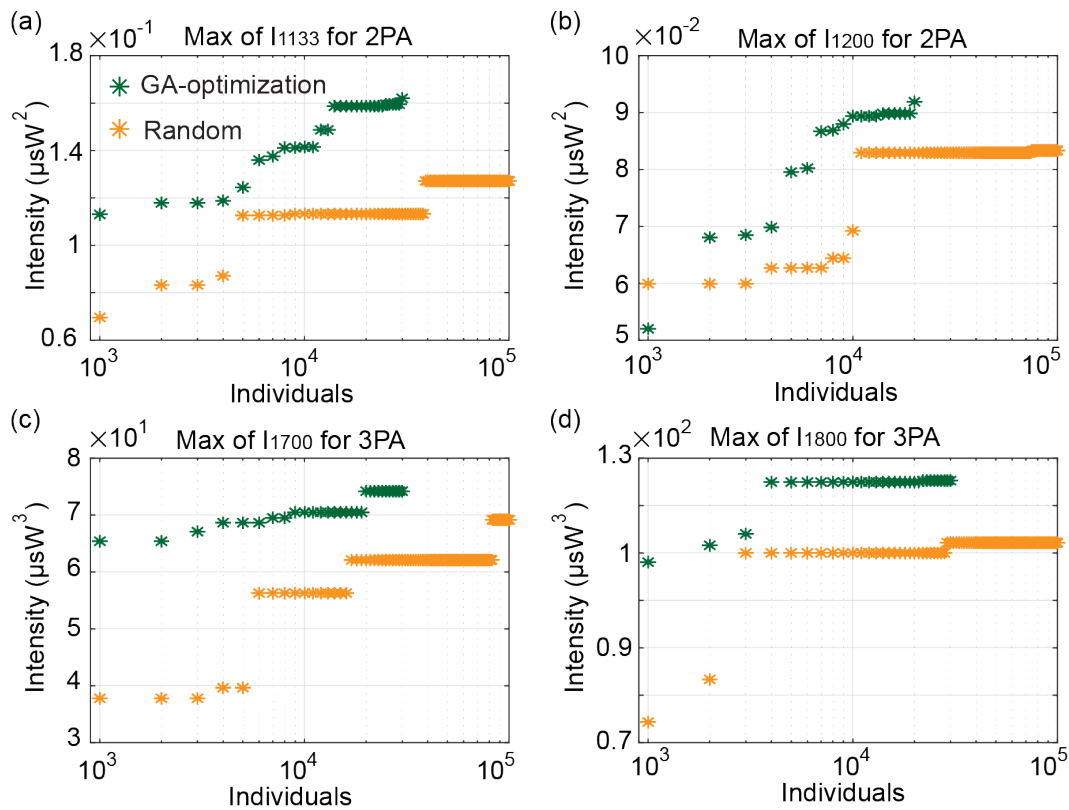


Figure A.3 Comparison between GA and random Monte Carlo method, for MPA signals optimization for the four wavelengths of interest, using a single input pulse seed with tunable parameters.

These results, providing up to a 3-fold MPA signal enhancement, may be put in perspective with the use of multiple input pulse generated from the PDL system. For the case of reconfigurable pulse patterns, we define a constant peak power $P_0 = 1$ kW for the input pulse, with a temporal width of 100 fs, and consider optical processing with the PDL using adjustable splitting ratios to generate reconfigurable pulse patterns.

For example, in Figure A.4.a–b we show the propagation in HNLF of an input pulse pattern obtained via PDL processing, and suitable to excite conjoint 3PA signals at the wavelengths of 1700 nm and 1800 nm. The obtained temporal and spectral signals are shown in Figure A.4.c.

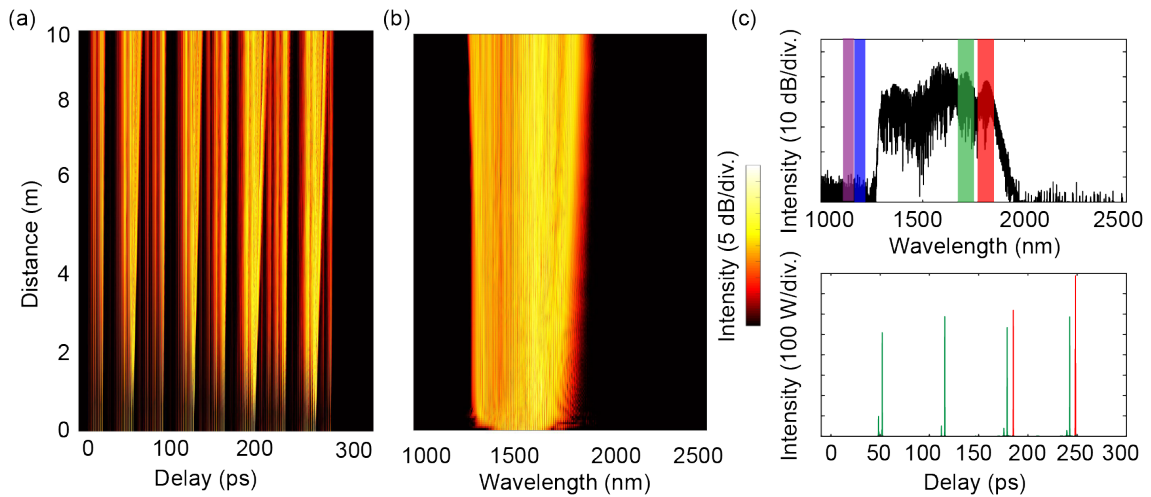


Figure A.4 Temporal (a) and spectral (b) evolution of a SC generation in a 10 m-long HNLF, obtained from numerical simulations using an adaptable input pulse pattern employed to excite conjoint 3PA processes of various fluorophores at wavelengths of 1700 nm and 1800 nm. (c) The corresponding output spectrum (top panel) and temporal waveforms (bottom panel) filtered at selected wavelengths.

In Figure A.5, we show different examples of reconfigurable pulse patterns obtained from random MC simulations. In Figure A.5.a–c we can see that for different wavelength, we can obtain with the single-pulse, a single-pulse like output pattern, or a more complex pattern.

In addition, for an improved control and characterization of various MPA processes and fluorophore combinations, we can also enhance conjoint MPA processes as seen in Figure A.5.d–e. Different temporal waveforms can be obtained by adjusting the input signal parameters, allowing to obtain different temporal delays between the filtered signals (Figure A.5.d(1-3) – e(1-3)), but also temporally-interleaved MPA signals (Figure A.5.d(4-6) – e(4-6)).

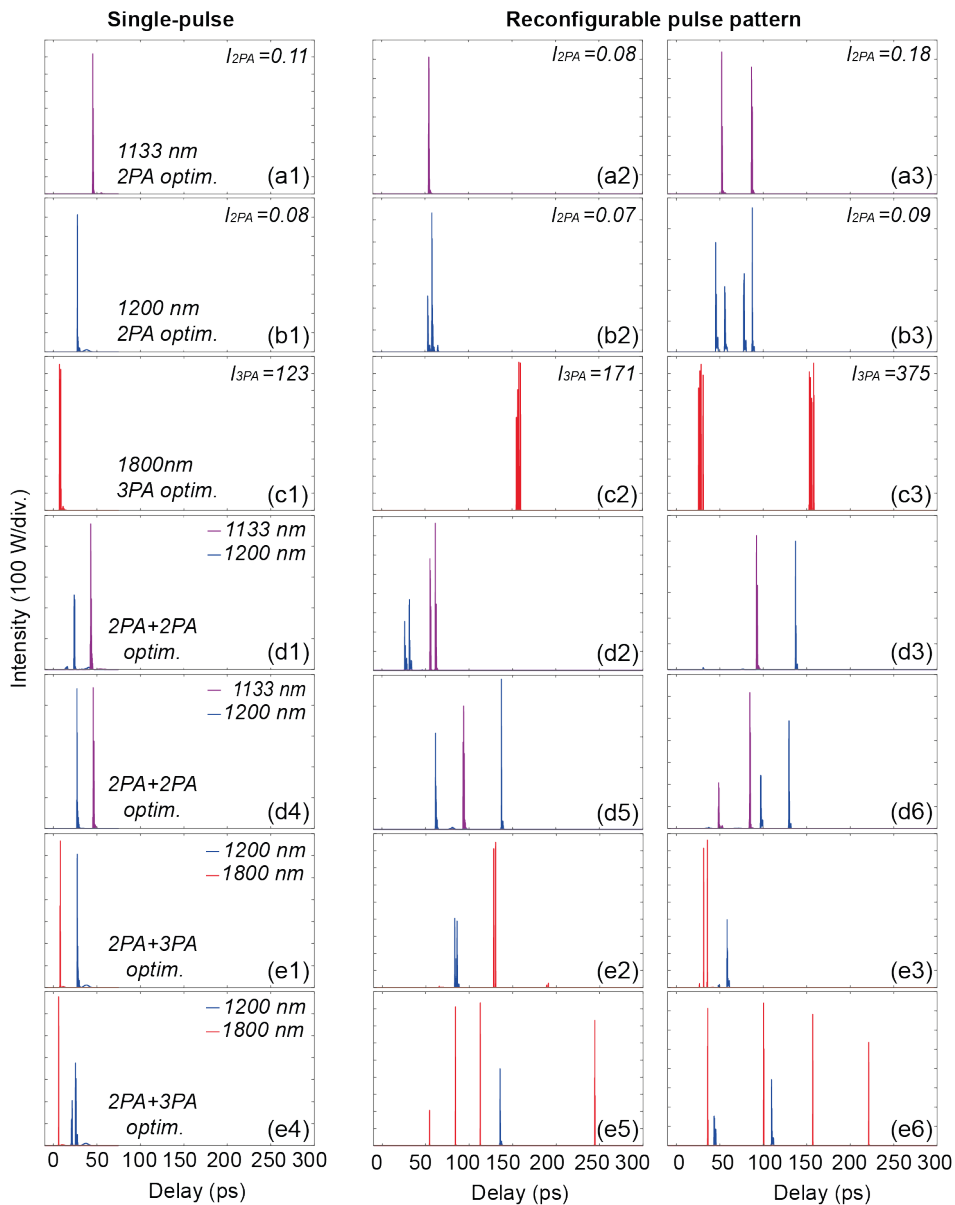


Figure A.5 Examples of filtered output waveforms generated from single pulses and reconfigurable pulse patterns when filtered at (a1-a3) 1133 nm, (b1-b3) 1200 nm, and (c1-c3) 1800 nm, and for conjoint (d1-d6) 2PA-2PA with 1133 nm -1200 nm, and (e1-e6) 2PA-3PA with 1200 nm -1800 nm.

By changing the splitting ratios in the PDL, we can therefore tailor the intensity and delay of the individual pulses depending on the desired properties of the excitation pulse used for MPE microscopy. The intensities of such excitation pulses can be maximized using optimization algorithms such as GA and PSO, yielding over 5-fold MPE signal enhancement as displayed in Figure A.6.

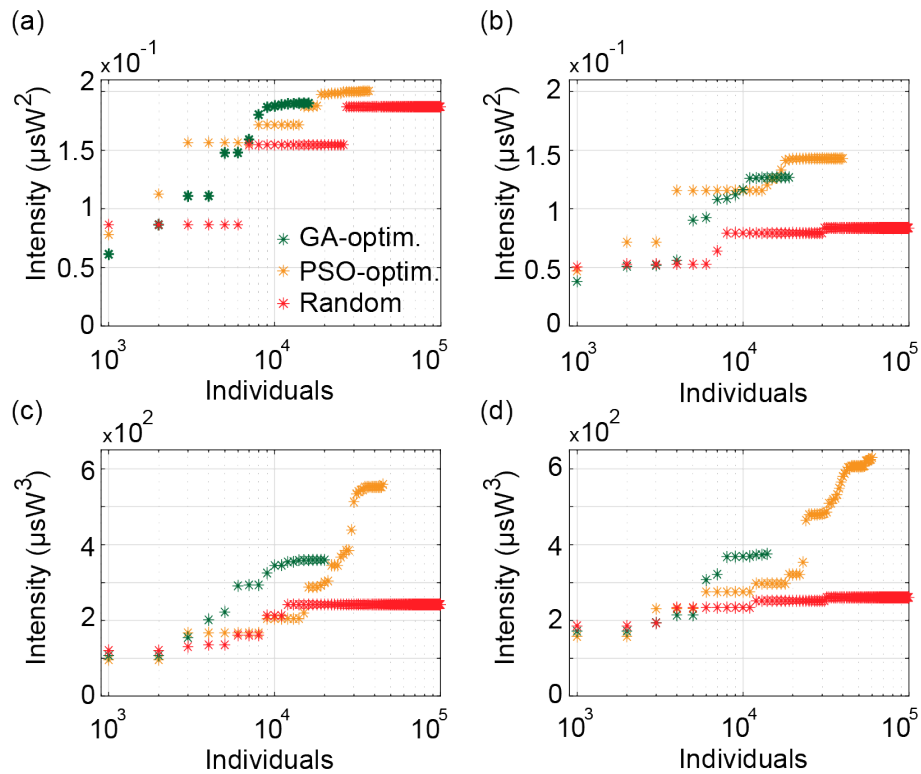


Figure A.6 Comparison between GA, PSO and random Monte Carlo method, for MPA signals optimization for the four wavelengths of interest, using reconfigurable input pulse patterns as processed by the PDL system.

The results of the study demonstrate a promising and practical approach for controlling the spectro-temporal properties of excitation lasers for multiphoton microscopy. Our approach leverages the temporal dimension as an extended degree of freedom, enabling the optimization of multiphoton excitations at specific wavelengths, but also introduces a versatile and adaptable method for imaging applications.

We anticipate that our results will pave the way for real-time supercontinuum shaping, promising significant improvements in multi-photon microscopy. These advancements could for instance lead to enhanced spatial 3D resolution, reduced optical toxicity, and improved wavelength selectivity.

Appendix 2. Characterization of ultrashort pulse patterns generated by an integrated photonic chip: Experimental implementation of advanced FROG system

In this section we show a study that was conducted with the aim of experimentally validating the numerical results presented in Appendix 1. A single input pulse signal is directed into the PDL, which can be reshaped into various pulse pattern configurations. To characterize the patterns obtained, we have developed a custom FROG technique as described in Chapter II.4.1.

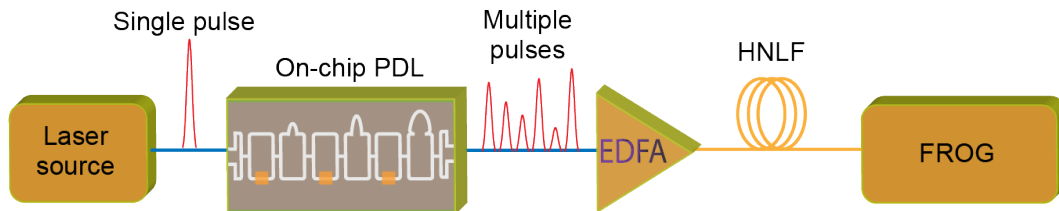


Figure A.7 Experimental setup: A femtosecond laser pulse is transformed into an adjustable train of pulses within the PDL, before being amplified with an EDFA and characterized by the home-made FROG.

For this study we used an 80 fs laser (Menlo, C-fiber) entering the PDL with an average power $P_{avg} = 4.5$ mW. The PDL consisting of 8 MZI interferometers enabling to split a single pulse into 256 pulses (2^8 pulses) with a minimum of 1 ps separation between each two adjacent pulses, encounters a loss of approximately -7 dB. For power recovery and amplification, we use an EDFA and enter the FROG setup with an average power of 18.3 mW (see Figure A.7). In the PDL, we can adjust the splitting ratio between each interferometer arms between 0 and 1, where 0 indicates that the light is following the “short arm” of the MZI, and 1 indicates the light is following the “long arm” of the MZI, thus a 0.5 ratio infers a 50% split-and-delay operation of each individual pulse(s), separated by the delay related to the long arm subsequent to the MZI interferometer [275], [282].

For example, in Figure A.8, we show the FROG traces experimentally recorded of the generated pulse patterns obtained by adjusting the splitting ratio of the PDL: Here, we show the cases where (i) the pulse passes by one interferometer into 2 pulses, (ii) by two interferometers into $2^2 = 4$ pulses, or (iii) by three interferometers into $2^3 = 8$ pulses.

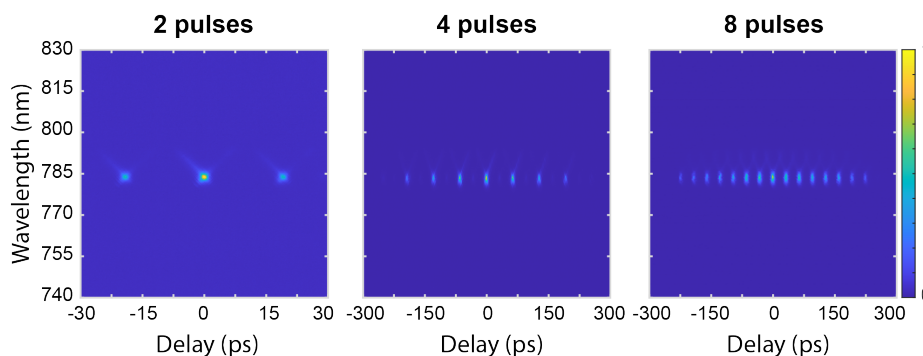


Figure A.8 Examples of FROG traces obtained experimentally by different configurations of the MZI splitting ratios within the PDL to obtain 2,4 or 8 pulses equally spaced in time. Here we used picosecond pulse duration and separation for illustrative purposes.

This approach allows us to get reconfigurable pulse train with defined temporal separation between each pulse than can be easily adjusted. For example in Figure A.8, we show for the case of 2 pulses, a separation of 16 ps, but also 4 pulses with a 64 ps separation, and 8 pulses with 32 ps separation. These results clearly illustrate both the versatility of this approach for temporal pulse shaping, as well as the quality of the home-made FROG setup for measuring extremely long pulse patterns with good temporal resolution. The study can be further expanded up until generating 256 pulses with 1 ps separation.

In our setup, the FROG traces are measured using a spectrometer (see Chapter II.4.1), and the temporal resolution of the setup (down to 0.6 fs) depends on the number of steps chosen along the temporal scan with our translation stage. The autocorrelation signal, as well as spectral marginal can be extracted directly and showing the shape of the pulse patterns after propagation in the PDL.

In Figure A.9, we show the characterization of a signals constituted from $2^4=16$ pulses. The autocorrelation trace indicating a 16 ps temporal delay between each pulse (in accordance with the $256/2^4$ ps pulse delay imposed by the PDL). The FROG trace allows us to analyze the properties of the obtained signal, such as its temporal width (~ 240 ps pattern), its spectral bandwidth and the intensity of each generated pulse. The presence of an interferometric figure on the spectrogram, infers a mutual coherence between the subsequent pulses, a consequence of the phase information carried by the spectrogram, retrievable by an appropriate algorithm [180].

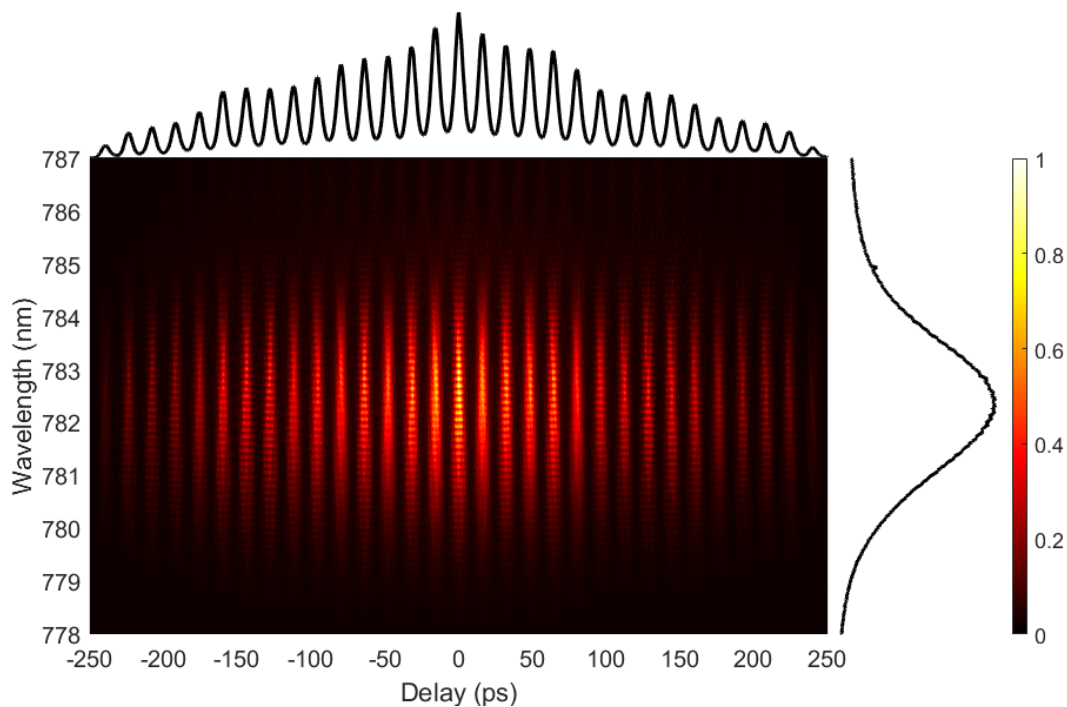


Figure A.9 FROG trace, obtained by sending an 80 fs laser into the PDL configured to generate 16 pulses with a separation of 16 ps. The signal is then amplified by an EDFA before FROG characterization.

Further investigation of such experiment will involve the propagation of the train pulse within a nonlinear waveguide to achieve reconfigurable spectral broadening. Such broadening may be obtained by coherent nonlinear effects to generate e.g. broadband supercontinuum or to study

fundamental effects associated with incoherent nonlinear dynamics (e.g. noise-driven MI, as discussed in Chapter IV).

Having access to a coherent and scalable pulse processing tool, as well as to the intensity and phase properties of the signal obtained from the PDL (that can be retrieved from FROG characterization) is of tremendous importance for the follow up of the studies reported in this thesis. It will allow for a finer adjustment of the pulse properties before propagation, enabling a smart tuning of different configurations in the PDL and an optimization towards different applications such as imaging techniques and multiphoton microscopy. This will also allow for gaining insight into the impact of the phase and coherence within complex and incoherent nonlinear dynamics found in many guided light propagation regimes.

Appendix 3. Acronym list

MI: Modulation Instability
EDFA: Erbium-Doped Fiber Amplifier
SMF: Single-Mode Fibers
MMF: Multi-Mode fibers
GRIN: Graded-index
HNLF: Highly Nonlinear Fiber
PCF: Photonic Crystal fibers
PM: Polarization Maintaining
PIC: Photonic Integrated Circuit
GVD: Group Velocity Dispersion
TOD: Third-Order Dispersion
ZDW: Zero Dispersion Wavelength
SVEA: Slowly Varying Envelop Approximation
SPM: Self-Phase Modulation
XPM: Cross Phase Modulation
SC: Supercontinuum
SCG: Supercontinuum Generation
NLSE: Nonlinear Schrödinger Equation
GNLSE: Generalized Nonlinear Schrödinger Equation
FWHM: Full Width at Half Maximum
TBP: Time-Bandwidth Product
FWM: Four-Wave Mixing
TWM: Three-Wave Mixing
AB: Akhmediev Breathers
CW: Continuous Wave
DW: Dispersive Wave
FROG: Frequency-Resolved Optical Gating
DFT: Dispersive-Fourier Transform
FT: Fourier Transform
ASE: Amplification Spontaneous Emission
WS: Waveshaper
IPPP: Integrated Photonic Pulse Processor

MZI: Mach-Zehnder Interferometer
AOM: Acousto-Optic Modulator
EOM: Electro-Optic Modulator
NN: Neural Network
GA: Genetic Algorithm
PSO: Particle Swarm Optimization
OSA: Optical Spectrum Analyzer
PUT: Pulse Under Test
SHG: Second Harmonic Generation
XFROG: Cross-Correlation Frequency-Resolved Optical Gating
DCF: Dispersion Compensating Fiber
SPD: Single-Photon Detector
STEAM: Serial Time-Encoded Amplification Microscopy
JSI: Joint Spectral Intensity
SNSPD: Superconducting Nanowire Single-Photon Detector
HBT: Hanbury-Brown and Twiss
MIA: Mutual Information Analysis
PD: Photodiode
SNR: Signal-to-Noise Ratio
MC: Monte Carlo
PDL: Programmable Delay Line

Appendix 4. Publication list

Appendix 4.1. Peer-reviewed articles

- 1- **L. Sader**, S. Bose, A. Khodadad Kashi, Y. Boussafa, R. Dauliat, P. Roy, M. Fabert, A. Tonello, V. Couderc, M. Kues, B. Wetzel, “Single-photon level dispersive Fourier-transform: Ultra-sensitive characterization of noise-driven nonlinear dynamics,” *ACS Photonics*, Vol. 10, pp. 3915–3928 (2023), <https://doi.org/10.1021/acsp Photonics.3c00711>
- 2- V. T. Hoang, Y. Boussafa, **L. Sader**, S. Février, V. Couderc, B. Wetzel, “Optimizing supercontinuum spectro-temporal properties by leveraging machine learning towards multi-photon microscopy,” *Frontiers in Photonics*, Vol. 3, pp. 940902 (2022) – Invited contribution “Rising Stars in Europe”, <https://doi.org/10.3389/fphot.2022.940902>
- 3- T. Godin, **L. Sader**, A. Khodadad Kashi, P.H. Hanzard, A. Hideur, D.J. Moss, R. Morandotti, G. Genty, J.M. Dudley, A. Pasquazi, M. Kues, B. Wetzel, “Recent advances on time-stretch dispersive Fourier transform and its applications,” *Advances in Physics: X*, Vol. 7, Issue 1, pp. 2067487 (2022) – Invited contribution (Review), <https://doi.org/10.1080/23746149.2022.2067487>
- 4- A. Khodadad Kashi, **L. Sader**, R. Haldar, B. Wetzel, M. Kues, “Frequency-to-time mapping technique for direct spectral characterization of biphoton states from pulsed spontaneous parametric processes,” *Frontiers in Photonics*, Vol. 3, pp. 834065 (2022), <https://doi.org/10.3389/fphot.2022.834065>

Appendix 4.2. Articles in preparation

- 1- **L. Sader**, V. T. Hoang, Y. Boussafa, R. Haldar, V. Kermene, M. Kues, B. Wetzel, “Modulation Instability Control through Optical Seeding and Machine Learning optimization strategies,” – (In preparation)
- 2- Y. Boussafa, **L. Sader**, V.T. Hoang, B.P. Chaves, A. Tonello, B. Wetzel, “Numerical prediction of incoherent modulation instability dynamics through deep learning approaches,” – (In preparation)

Appendix 4.3. International conferences (*with proceedings*)

Note that the speakers are underlined, and Keynote presentations are explicitly mentioned.

- 1- V.T. Hoang, Y. Boussafa, B. P. Chaves, **L. Sader**, B. Fischer, M. Chemnitz, P. Roztock, B. MacLellan, C. Reimer, R. Helsten, S. Février, V. Couderc, M. Kues, A. Pasquazi, M. Peccianti, B. Little, S. T. Chu, D.J. Moss, J. Azaña, R. Morandotti, B. Wetzel, “On-chip temporal pulse pattern generation and fiber propagation: Multidimensional wave-packet control and characterization,” *IEEE Photonics Society Summer Topicals Meeting Series (SUM)*, Sicily, Italy (2023) – *Invited Presentation*.
- 2- V.T. Hoang, Y. Boussafa, B. P. Chaves, **L. Sader**, B. Fischer, M. Chemnitz, P. Roztock, B. MacLellan, C. Reimer, R. Helsten, S. Février, V. Couderc, M. Kues, A. Pasquazi, M. Peccianti, B. Little, S. T. Chu, D.J. Moss, J. Azaña, R. Morandotti, B. Wetzel, “Smart nonlinear photonics: From on-chip pulse processing to tailored nonlinear fiber propagation,” *CLEO: Fundamental Science*, San Jose, USA (2023) – *Invited Presentation*.
- 3- **L. Sader**, S. Bose, A. Khodadad Kashi, Y. Boussafa, R. Dauliat, P. Roy, M. Fabert, A. Tonello, V. Couderc, M. Kues, B. Wetzel, “Ultrasensitive dispersive Fourier transform

characterization of nonlinear instabilities,” CLEO Europe-EQEC, Munich, Germany (2023) – *Oral Presentation*.

- 4- V.T. Hoang, Y. Boussafa, **L. Sader**, S. Février, V. Couderc, **B. Wetzel**, “Smart control of supercontinuum generation by machine learning towards multiphoton microscopy applications,” CLEO Europe-EQEC, Munich, Germany (2023) – *Oral Presentation*.
- 5- **L. Sader**, Y. Boussafa, R. Haldar, V. Kermene, M. Kues, B. Wetzel, “Modulation instability control via optical seeding and machine learning optimization,” CLEO Europe-EQEC, Munich, Germany (2023) – *Oral Presentation*.
- 6- Y. Boussafa, **L. Sader**, V.T. Hoang, B.P. Chaves, A. Tonello, B. Wetzel, “Numerical prediction of incoherent modulation instability dynamics through deep learning approaches,” CLEO Europe-EQEC, Munich, Germany (2023) – *Poster*.
- 7- **L. Sader**, S. Bose, A. Khodadad Kashi, Y. Boussafa, R. Dauliat, P. Roy, M. Fabert, A. Tonello, V. Couderc, M. Kues, B. Wetzel, “Ultrasensitive dispersive Fourier transform technique for nonlinear instability characterization,” Frontiers in Optics + Laser Science 2022, Rochester, USA (2022) – *Oral Presentation*.
- 8- V.T. Hoang, Y. Boussafa, **L. Sader**, S. Février, V. Couderc, B. Wetzel, “Machine learning optimization of supercontinuum properties towards multiphoton microscopy,” Advanced Photonics Congress – Nonlinear Photonics (NP 2022), Maastricht, Netherlands (2022) – *Oral Presentation*.
- 9- **L. Sader**, S. Bose, A. Khodadad Kashi, R. Dauliat, P. Roy, M. Fabert, A. Tonello, V. Couderc, M. Kues, B. Wetzel, “Ultra-sensitive characterization of nonlinear instabilities via single photon dispersive Fourier-transform,” CLEO/QELS, San Jose, USA (2022) – *Poster*.

Appendix 4.4. National conferences (with proceedings)

- 1- **L. Sader**, V.T. Hoang, Y. Boussafa, B. P. Chaves, S. Bose, A. Khodadad Kashi, R. Haldar, S. Février, A. Tonello, V. Kermene, V. Couderc, B. Little, S. T. Chu, D.J. Moss, R. Morandotti, M. Kues, **B. Wetzel**, “Caractérisation et contrôle intelligent des effets non-linéaires en optique guidée,” Journées Nationales de l’Optique Guidée (JNOG), Lyon, France (2023) – *Invited presentation*.
- 2- **L. Sader**, S. Bose, A. Khodadad Kashi, R. Dauliat, P. Roy, M. Fabert, A. Tonello, V. Couderc, M. Kues, **B. Wetzel**, “Nouvelle technique ultra-sensible de caractérisation des instabilités non-linéaires par étirage temporel dispersif,” OPTIQUE Nice, Nice, France (2022) – *Oral Presentation*.
- 3- V.T. Hoang, Y. Boussafa, **L. Sader**, S. Février, V. Couderc, B. Wetzel, “Optimisation des propriétés d’un supercontinuum par apprentissage automatique pour la microscopie multiphotonique,” OPTIQUE Nice, Nice, France (2022) – *Oral Presentation*.
- 4- **L. Sader**, R. Haldar, V.T. Hoang, M. Kues, B. Wetzel, “Contrôle de l’instabilité de modulation par injection optique,” OPTIQUE Nice, Nice, France (2022) – *Poster*.

Appendix 4.5. Other symposiums and workshops

- 1- Y. Boussafa, B.P. Chaves, **L. Sader**, V.T. Hoang, **B. Wetzel**, “Caractérisation photonique avancée : Données multidimensionnelles et apprentissage automatique,” Journée thématique Fédération MIREs, Poitiers, France (2023) – *Oral Presentation*.

- 2- **L. Sader**, S. Bose, A. Khodadad Kashi, Y. Boussafa, R. Dauliat, P. Roy, M. Fabert, A. Tonello, V. Couderc, M. Kues, B. Wetzel, "Ultra-sensitive characterization of nonlinear instabilities via single photon dispersive Fourier Fourier-transform," Journées Fibres Optiques : Applications et dernières tendances (Alpha-RLH), Limoges, France (2022) – *Poster*.
- 3- V.T. Hoang, Y. Boussafa, **L. Sader**, S. Février, V. Couderc, B. Wetzel, "Machine learning optimization of supercontinuum properties towards multiphoton microscopy," Journées Fibres Optiques : Applications et dernières tendances (Alpha-RLH), Limoges, France (2022) – *Poster*.
- 4- **L. Sader**, S. Bose, A. Khodadad Kashi, Y. Boussafa, R. Dauliat, P. Roy, M. Fabert, A. Tonello, V. Couderc, M. Kues, B. Wetzel, "Ultra-sensitive dispersive Fourier-transform characterization technique," GDR ELIOS Annual Meeting, Marseille, France (2022) – *Oral Presentation*.
- 5- V.T. Hoang, Y. Boussafa, **L. Sader**, S. Février, V. Couderc, B. Wetzel "Machine learning optimization of supercontinuum properties towards multiphoton microscopy," GDR ELIOS Annual Meeting, Marseille, France (2022) – *Oral Presentation*.
- 6- **L. Sader**, S. Bose, A. Khodadad Kashi, R. Dauliat, P. Roy, M. Fabert, A. Tonello, V. Couderc, M. Kues, B. Wetzel, "Novel characterization technique based on dispersive Fourier transform and single photon detection," Humboldt meets Leibniz - Emerging Topics in Optics and Photonics, Hannover, Germany (2022) – *Oral Presentation*.
- 7- V.T. Hoang, **L. Sader**, B. Wetzel, "Tunable adjustment of supercontinuum spectro-temporal properties by leveraging on-chip coherent temporal synthesis," GDR ELIOS Annual Meeting, Lille, France (2021) – *Poster*.
- 8- **L. Sader**, V.T. Hoang, R. Haldar, M. Kues, B. Wetzel, "Modulation instability control via optical seeding," GDR ELIOS Annual Meeting, Lille, France (2021) – *Poster*.

Bibliography

1. T. H. Maiman, "Stimulated Optical Radiation in Ruby," *Nature* **187**, 493–494 (1960).
2. J. Hecht, "A short history of laser development," *Appl. Opt.* **49**, F99 (2010).
3. P. A. Franken, A. E. Hill, C. W. Peters, and G. Weinreich, "Generation of Optical Harmonics," *Phys. Rev. Lett.* **7**, 118–119 (1961).
4. K. C. Kao, "Dielectric-fibre surface waveguides for optical frequencies," **113**, (1966).
5. R. R. Alfano and S. L. Shapiro, "Direct Distortion of Electronic Clouds of Rare-Gas Atoms in Intense Electric Fields," *Phys. Rev. Lett.* **24**, 1217–1220 (1970).
6. C. Lin and R. H. Stolen, "New nanosecond continuum for excited-state spectroscopy," *Applied Physics Letters* **28**, 216–218 (2008).
7. D. B. Ostrowsky and R. Reinisch, eds., *Guided Wave Nonlinear Optics* (Springer Netherlands, 1992).
8. G. Genty, L. Salmela, J. M. Dudley, D. Brunner, A. Kokhanovskiy, S. Kobtsev, and S. K. Turitsyn, "Machine learning and applications in ultrafast photonics," *Nat. Photonics* **15**, 91–101 (2021).
9. J. Hecht, *City of Light: The Story of Fiber Optics* (Oxford University Press, 2004).
10. G. P. Agrawal, *Fiber-Optic Communication Systems* (John Wiley & Sons, 2012).
11. B. H. Lee, E. J. Min, and Y. H. Kim, "Fiber-based optical coherence tomography for biomedical imaging, sensing, and precision measurements," *Optical Fiber Technology* **19**, 729–740 (2013).
12. T. G. Giallorenzi, J. A. Bucaro, A. Dandridge, G. H. Sigel, J. H. Cole, S. C. Rashleigh, and R. G. Priest, "Optical Fiber Sensor Technology," *IEEE Transactions on Microwave Theory and Techniques* **30**, 472–511 (1982).
13. S. Rizzolo, C. Sabatier, A. Boukenter, E. Marin, Y. Ouerdane, M. Cannas, J. Périssé, J.-R. Macé, S. Bauer, and S. Girard, "Radiation Characterization of Optical Frequency Domain Reflectometry Fiber-Based Distributed Sensors," *IEEE Transactions on Nuclear Science* **63**, 1688–1693 (2016).
14. C. Buckley, M. Fabert, D. Kinet, V. Kucikas, and D. Pagnoux, "Design of an endomicroscope including a resonant fiber-based microprobe dedicated to endoscopic polarimetric imaging for medical diagnosis," *Biomed. Opt. Express*, **BOE 11**, 7032–7052 (2020).
15. C. J. Koester and E. Snitzer, "Amplification in a Fiber Laser," *Appl. Opt.*, **AO 3**, 1182–1186 (1964).
16. T. Udem, R. Holzwarth, and T. W. Hänsch, "Optical frequency metrology," *Nature* **416**, 233–237 (2002).
17. J. Zubia and J. Arrue, "Plastic Optical Fibers: An Introduction to Their Technological Processes and Applications," *Optical Fiber Technology* **7**, 101–140 (2001).
18. M. N. Zervas, R. I. Laming, and D. N. Payne, "Efficient erbium-doped fibre amplifier with an integral isolator," in *Optical Amplifiers and Their Applications (1992)*, Paper FB2 (Optica Publishing Group, 1992), p. FB2.
19. N. S. Kapany and R. J. Simms, "Recent developments in infrared fiber optics*," *Infrared Physics* **5**, 69–80 (1965).
20. D. Tran, G. Sigel, and B. Bendow, "Heavy metal fluoride glasses and fibers: A review," *Journal of Lightwave Technology* **2**, 566–586 (1984).

21. H. Kogelnik, "Theory of Optical Waveguides," in *Guided-Wave Optoelectronics*, T. Tamir, ed., Springer Series in Electronics and Photonics (Springer, 1988), pp. 7–88.
22. J. Arnaud, "Optical waveguide theory," *Opt Quant Electron* **12**, 187–191 (1980).
23. D. Marcuse, *Principles of Optical Fiber Measurements* (Elsevier, 2012).
24. G. P. Agrawal, *Nonlinear Fiber Optics*, 3rd ed. (Academic Press, 2001).
25. K. Schuster, S. Unger, C. Aichele, F. Lindner, S. Grimm, D. Litzkendorf, J. Kobelke, J. Bierlich, K. Wondraczek, and H. Bartelt, "Material and technology trends in fiber optics," *Advanced Optical Technologies* **3**, 447–468 (2014).
26. R. Gautam, A. Bezryadina, Y. Xiang, T. Hansson, Y. Liang, G. Liang, J. Lamstein, N. Perez, B. Wetzel, R. Morandotti, and Z. Chen, "Nonlinear optical response and self-trapping of light in biological suspensions," *Advances in Physics: X* **5**, 1778526 (2020).
27. R. Guan, F. Zhu, Z. Gan, D. Huang, and S. Liu, "Stress birefringence analysis of polarization maintaining optical fibers," *Optical Fiber Technology* **11**, 240–254 (2005).
28. S. Inao, T. Sato, S. Sentsui, T. Kuroha, and Y. Nishimura, "Multicore optical fiber," in *Optical Fiber Communication (1979), Paper WB1* (Optica Publishing Group, 1979), p. WB1.
29. K. Imamura, Y. Tsuchida, K. Mukasa, R. Sugizaki, K. Saitoh, and M. Koshiba, "Investigation on multi-core fibers with large Aeff and low micro bending loss," *Opt. Express*, OE **19**, 10595–10603 (2011).
30. J. C. Knight, T. A. Birks, D. M. Atkin, and P. S. J. Russell, "PURE SILICA SINGLE-MODE FIBRE WITH HEXAGONAL PHOTONIC CRYSTAL CLADDING," in *Optical Fiber Communication Conference (1996), Paper PD3* (Optica Publishing Group, 1996), p. PD3.
31. P. S. J. Russell, "Photonic-Crystal Fibers," *J. Lightwave Technol.*, JLT **24**, 4729–4749 (2006).
32. F. Benabid and P. J. Roberts, "Linear and nonlinear optical properties of hollow core photonic crystal fiber," *Journal of Modern Optics* **58**, 87–124 (2011).
33. C. Markos, J. C. Travers, A. Abdolvand, B. J. Eggleton, and O. Bang, "Hybrid photonic-crystal fiber," *Rev. Mod. Phys.* **89**, 045003 (2017).
34. V. T. Hoang, R. Kasztelan, A. Anuszkiewicz, G. Stepniewski, A. Filipkowski, S. Ertman, D. Pysz, T. Wolinski, K. D. Xuan, M. Klimczak, and R. Buczynski, "All-normal dispersion supercontinuum generation in photonic crystal fibers with large hollow cores infiltrated with toluene," *Opt. Mater. Express*, OME **8**, 3568–3582 (2018).
35. G. Fanjoux, S. Margueron, J.-C. Beugnot, and T. Sylvestre, "Supercontinuum generation by stimulated Raman–Kerr scattering in a liquid-core optical fiber," *J. Opt. Soc. Am. B*, JOSAB **34**, 1677–1683 (2017).
36. D. Moss, A. Pasquazi, M. Peccianti, L. Razzari, D. Duchesne, M. Ferrera, S. Chu, B. Little, and R. Morandotti, "Hydex waveguides for nonlinear optics," (2014).
37. T. A. Birks, W. J. Wadsworth, and P. S. J. Russell, "Supercontinuum generation in tapered fibers," *Opt. Lett.*, OL **25**, 1415–1417 (2000).
38. F. A. Kish, D. Welch, R. Nagarajan, J. L. Pleumeekers, V. Lal, M. Ziari, A. Nilsson, M. Kato, S. Murthy, P. Evans, S. W. Corzine, M. Mitchell, P. Samra, M. Missey, S. DeMars, R. P. Schneider, M. S. Reffle, T. Butrie, J. T. Rahn, M. Van Leeuwen, J. W. Stewart, D. J. H. Lambert, R. C. Muthiah, H.-S. Tsai, J. S. Bostak, A. Dentai, K.-T. Wu, H. Sun, D. J. Pavinski, J. Zhang, J. Tang, J. McNicol, M. Kuntz, V. Dominic, B. D. Taylor, R. A. Salvatore, M. Fisher, A. Spannagel, E. Strzelecka, P. Studenkov, M. Raburn, W. Williams, D. Christini, K. J. Thomson, S. S. Agashe, R. Malendevich, G. Goldfarb, S. Melle, C. Joyner,

- M. Kaufman, and S. G. Grubb, "Current Status of Large-Scale InP Photonic Integrated Circuits," *IEEE Journal of Selected Topics in Quantum Electronics* **17**, 1470–1489 (2011).
39. W. S. Zaoui, A. Kunze, W. Vogel, M. Berroth, J. Butschke, F. Letzkus, and J. Burghartz, "Bridging the gap between optical fibers and silicon photonic integrated circuits," *Opt. Express*, OE **22**, 1277–1286 (2014).
 40. K. Minoshima, A. M. Kowalevich, I. Hartl, E. P. Ippen, and J. G. Fujimoto, "Photonic device fabrication in glass by use of nonlinear materials processing with a femtosecond laser oscillator," *Opt. Lett.*, OL **26**, 1516–1518 (2001).
 41. C. Florea and K. A. Winick, "Fabrication and characterization of photonic devices directly written in glass using femtosecond laser pulses," *Journal of Lightwave Technology* **21**, 246–253 (2003).
 42. B. Fischer, M. Chemnitz, B. MacLellan, P. Roztock, R. Helsten, B. Wetzel, B. E. Little, S. T. Chu, D. J. Moss, J. Azaña, and R. Morandotti, "Autonomous on-chip interferometry for reconfigurable optical waveform generation," *Optica* **8**, 1268 (2021).
 43. B. Wetzel, M. Kues, P. Roztock, C. Reimer, P.-L. Godin, M. Rowley, B. E. Little, S. T. Chu, E. A. Viktorov, D. J. Moss, A. Pasquazi, M. Peccianti, and R. Morandotti, "Customizing supercontinuum generation via on-chip adaptive temporal pulse-splitting," *Nat Commun* **9**, 4884 (2018).
 44. V. T. Hoang, Y. Boussafa, L. Sader, S. Février, V. Couderc, and B. Wetzel, "Optimizing supercontinuum spectro-temporal properties by leveraging machine learning towards multi-photon microscopy," *Frontiers in Photonics* **3**, (2022).
 45. R. W. Boyd, *Nonlinear Optics* (Academic Press, 2013).
 46. V. Brückner, "To the use of Sellmeier formula," (2014).
 47. L. E. Sutton and O. N. Stavroudis, "Fitting Refractive Index Data by Least Squares," *J. Opt. Soc. Am.*, JOSA **51**, 901–905 (1961).
 48. I. H. Malitson, "Interspecimen Comparison of the Refractive Index of Fused Silica*,†," *J. Opt. Soc. Am.*, JOSA **55**, 1205–1209 (1965).
 49. A. Kobayakov, M. Sauer, and D. Chowdhury, "Stimulated Brillouin scattering in optical fibers," *Adv. Opt. Photon.*, AOP **2**, 1–59 (2010).
 50. M. Merklein, A. Casas-Bedoya, D. Marpaung, T. F. S. Büttner, M. Pagani, B. Morrison, I. V. Kabakova, and B. J. Eggleton, "Stimulated Brillouin Scattering in Photonic Integrated Circuits: Novel Applications and Devices," *IEEE Journal of Selected Topics in Quantum Electronics* **22**, 336–346 (2016).
 51. M. Zerbib, V. T. Hoang, J. C. Beugnot, K. P. Huy, B. Little, S. T. Chu, D. J. Moss, R. Morandotti, B. Wetzel, and T. Sylvestre, "Observation of Brillouin scattering in a high-index doped silica chip waveguide," *arXiv preprint arXiv:2305.11502* (2023).
 52. K. J. Blow and D. Wood, "Theoretical description of transient stimulated Raman scattering in optical fibers," *IEEE Journal of Quantum Electronics* **25**, 2665–2673 (1989).
 53. Q. Lin and G. P. Agrawal, "Raman response function for silica fibers," *Opt. Lett.*, OL **31**, 3086–3088 (2006).
 54. K. Okamoto and T. Okoshi, "Vectorial Wave Analysis of Inhomogeneous Optical Fibers Using Finite Element Method," *IEEE Transactions on Microwave Theory and Techniques* **26**, 109–114 (1978).
 55. R. A. Fisher and W. K. Bischel, "Numerical studies of the interplay between self-phase modulation and dispersion for intense plane-wave laser pulses," *Journal of Applied Physics* **46**, 4921–4934 (2008).

56. J. Hult, "A Fourth-Order Runge–Kutta in the Interaction Picture Method for Simulating Supercontinuum Generation in Optical Fibers," *Journal of Lightwave Technology* **25**, 3770–3775 (2007).
57. J. Nuño, C. Finot, G. Xu, G. Millot, M. Erkintalo, and J. Fatome, "Vectorial dispersive shock waves in optical fibers," *Commun Phys* **2**, 1–9 (2019).
58. L. F. Mollenauer, R. H. Stolen, and J. P. Gordon, "Experimental observation of picosecond pulse narrowing and solitons in optical fibers," in *Conference on Lasers and Electro-Optics (1981), Paper WF1* (Optica Publishing Group, 1981), p. WF1.
59. C. Chen, *Foundations for Guided-Wave Optics*, 1st ed. (Wiley, 2006).
60. J. P. Gordon, "Theory of the soliton self-frequency shift," *Opt. Lett.*, OL **11**, 662–664 (1986).
61. F. M. Mitschke and L. F. Mollenauer, "Discovery of the soliton self-frequency shift," *Opt. Lett.*, OL **11**, 659–661 (1986).
62. J. M. Dudley, G. Genty, and S. Coen, "Supercontinuum generation in photonic crystal fiber," *Rev. Mod. Phys.* **78**, 1135–1184 (2006).
63. G. Cappellini and S. Trillo, "Third-order three-wave mixing in single-mode fibers: exact solutions and spatial instability effects," *J. Opt. Soc. Am. B, JOSAB* **8**, 824–838 (1991).
64. G. Van Simaey, P. Emplit, and M. Haelterman, "Experimental study of the reversible behavior of modulational instability in optical fibers," *J. Opt. Soc. Am. B* **19**, 477 (2002).
65. D. M. Nguyen, T. Godin, S. Toenger, Y. Combes, B. Wetzel, T. Sylvestre, J.-M. Merolla, L. Larger, G. Genty, F. Dias, and J. M. Dudley, "Incoherent resonant seeding of modulation instability in optical fiber," *Opt. Lett.* **38**, 5338 (2013).
66. A. M. Perego, F. Bessin, and A. Mussot, "Complexity of modulation instability," *Phys. Rev. Research* **4**, L022057 (2022).
67. C. J. McKinstrie and M. G. Raymer, "Four-wave-mixing cascades near the zero-dispersion frequency," *Opt. Express*, OE **14**, 9600–9610 (2006).
68. J. M. Dudley, G. Genty, F. Dias, B. Kibler, and N. Akhmediev, "Modulation instability, Akhmediev Breathers and continuous wave supercontinuum generation," *Opt. Express* **17**, 21497 (2009).
69. T. B. Benjamin and J. E. Feir, "The disintegration of wave trains on deep water Part 1. Theory," *J. Fluid Mech.* **27**, 417–430 (1967).
70. S. G. Thornhill and D. ter Haar, "Langmuir turbulence and modulational instability," *Physics Reports* **43**, 43–99 (1978).
71. A. Sheveleva, U. Andral, B. Kibler, P. Colman, J. M. Dudley, and C. Finot, "Idealized four-wave mixing dynamics in a nonlinear Schrödinger equation fiber system," *Optica*, OPTICA **9**, 656–662 (2022).
72. A. Sheveleva, P. Colman, John. M. Dudley, and C. Finot, "Trajectory control in idealized four-wave mixing processes in optical fiber," *Optics Communications* **538**, 129472 (2023).
73. A. Bendahmane, A. Mussot, A. Kudlinski, P. Szriftgiser, M. Conforti, S. Wabnitz, and S. Trillo, "Optimal frequency conversion in the nonlinear stage of modulation instability," *Opt. Express*, OE **23**, 30861–30871 (2015).
74. S. Wabnitz and B. Wetzel, "Instability and noise-induced thermalization of Fermi–Pasta–Ulam recurrence in the nonlinear Schrödinger equation," *Physics Letters A* **378**, 2750–2756 (2014).
75. G. Van Simaey, Ph. Emplit, and M. Haelterman, "Experimental Demonstration of the Fermi-Pasta-Ulam Recurrence in a Modulationally Unstable Optical Wave," *Phys. Rev. Lett.* **87**, 033902 (2001).

76. J. M. Dudley, F. Dias, M. Erkintalo, and G. Genty, "Instabilities, breathers and rogue waves in optics," *Nature Photon* **8**, 755–764 (2014).
77. B. Frisquet, B. Kibler, and G. Millot, "Collision of Akhmediev Breathers in Nonlinear Fiber Optics," *Phys. Rev. X* **3**, 041032 (2013).
78. B. Kibler, J. Fatome, C. Finot, G. Millot, G. Genty, B. Wetzel, N. Akhmediev, F. Dias, and J. M. Dudley, "Observation of Kuznetsov-Ma soliton dynamics in optical fibre," *Scientific Reports* **2**, 463 (2012).
79. A. Mathis, L. Froehly, S. Toenger, F. Dias, G. Genty, and J. M. Dudley, "Caustics and Rogue Waves in an Optical Sea," *Sci Rep* **5**, 12822 (2015).
80. D. R. Solli, C. Ropers, P. Koonath, and B. Jalali, "Optical rogue waves," *Nature* **450**, 1054–1057 (2007).
81. N. Akhmediev, B. Kibler, F. Baronio, M. Belić, W.-P. Zhong, Y. Zhang, W. Chang, J. M. Soto-Crespo, P. Vouzas, P. Grelu, C. Lecaplain, K. Hammani, S. Rica, A. Picozzi, M. Tlidi, K. Panajotov, A. Mussot, A. Bendahmane, P. Szriftgiser, G. Genty, J. Dudley, A. Kudlinski, A. Demircan, U. Morgner, S. Amiranashvili, C. Bree, G. Steinmeyer, C. Masoller, N. G. R. Broderick, A. F. J. Runge, M. Erkintalo, S. Residori, U. Bortolozzo, F. T. Arecchi, S. Wabnitz, C. G. Tiofack, S. Coulibaly, and M. Taki, "Roadmap on optical rogue waves and extreme events," *J. Opt.* **18**, 063001 (2016).
82. J. M. Dudley, G. Genty, and B. J. Eggleton, "Harnessing and control of optical rogue waves in supercontinuum generation," *Opt. Express*, OE **16**, 3644–3651 (2008).
83. W. Yu, R. R. Alfano, C. L. Sam, and R. J. Seymour, "Spectral broadening of picosecond 1.06 μ pulse in KBr," *Optics Communications* **14**, 344–347 (1975).
84. W. Werncke, A. Lau, M. Pfeiffer, K. Lenz, H.-J. Weigmann, and C. D. Thuy, "An anomalous frequency broadening in water," *Optics Communications* **4**, 413–415 (1972).
85. A. Husakou and J. Herrmann, "Supercontinuum Generation of Higher-Order Solitons by Fission in Photonic Crystal Fibers," *Physical review letters* **87**, 203901 (2001).
86. J. Dudley, L. Provino, N. Grossard, H. Maillotte, R. Windeler, B. Eggleton, and S. Coen, "Supercontinuum generation in air-silica microstructured fibers with nanosecond and femtosecond pulse pumping," *Journal of The Optical Society of America B-optical Physics - J OPT SOC AM B-OPT PHYSICS* **19**, (2002).
87. P. A. Champert, V. Couderc, and A. Barthelemy, "1.5-2.0- μ m multiwatt continuum generation in dispersion-shifted fiber by use of high-power continuous-wave fiber source," *IEEE Photonics Technology Letters* **16**, 2445–2447 (2004).
88. M. González-Herráez, S. Martín-López, P. Corredera, M. L. Hernanz, and P. R. Horche, "Supercontinuum generation using a continuous-wave Raman fiber laser," *Optics Communications* **226**, 323–328 (2003).
89. G. Genty, M. Surakka, J. Turunen, and A. T. Friberg, "Complete characterization of supercontinuum coherence," *J. Opt. Soc. Am. B* **28**, 2301 (2011).
90. C. Finot, B. Kibler, L. Provost, and S. Wabnitz, "Beneficial impact of wave-breaking for coherent continuum formation in normally dispersive nonlinear fibers," *J. Opt. Soc. Am. B, JOSAB* **25**, 1938–1948 (2008).
91. A. M. Heidt, J. S. Feehan, J. H. V. Price, and T. Feurer, "Limits of coherent supercontinuum generation in normal dispersion fibers," *J. Opt. Soc. Am. B, JOSAB* **34**, 764–775 (2017).
92. R. N. Bracewell, "The Fourier Transform," *Scientific American* **260**, 86–95 (1989).
93. A. M. Weiner, "Ultrafast optical pulse shaping: A tutorial review," *Optics Communications* **284**, 3669–3692 (2011).

94. J. W. Goodman, *Introduction to Fourier Optics* (McGraw-Hill, 1968).
95. P. M. Duffieux, *The Fourier Transform and Its Applications to Optics* (Wiley, 1983).
96. B. Wetzel, D. Bongiovanni, M. Kues, Y. Hu, Z. Chen, S. Trillo, J. M. Dudley, S. Wabnitz, and R. Morandotti, "Experimental Generation of Riemann Waves in Optics: A Route to Shock Wave Control," *Phys. Rev. Lett.* **117**, 073902 (2016).
97. Y. Hu, Z. Li, B. Wetzel, R. Morandotti, Z. Chen, and J. Xu, "Cherenkov Radiation Control via Self-accelerating Wave-packets," *Sci Rep* **7**, 8695 (2017).
98. E. E. Morales-Delgado, S. Farahi, I. N. Papadopoulos, D. Psaltis, and C. Moser, "Delivery of focused short pulses through a multimode fiber," *Opt Express* **23**, 9109–9120 (2015).
99. L. Wright, D. Christodoulides, and F. Wise, "Controllable spatiotemporal nonlinear effects in multimode fibres," *Nature Photonics* **9**, (2015).
100. K. Krupa, C. Louot, V. Couderc, M. Fabert, R. Guenard, B. M. Shalaby, A. Tonello, D. Pagnoux, P. Leproux, A. Bendahmane, R. Dupiol, G. Millot, and S. Wabnitz, "Spatiotemporal characterization of supercontinuum extending from the visible to the mid-infrared in a multimode graded-index optical fiber," *Opt. Lett.*, OL **41**, 5785–5788 (2016).
101. U. Teğin, B. Rahmani, E. Kakkava, N. Borhani, C. Moser, and D. Psaltis, "Controlling spatiotemporal nonlinearities in multimode fibers with deep neural networks," *APL Photonics* **5**, 030804 (2020).
102. S. Boscolo and C. Finot, "Nonlinear Pulse Shaping in Fibres for Pulse Generation and Optical Processing," *International Journal of Optics* **2012**, e159057 (2012).
103. C. J. Bardeen, V. V. Yakovlev, J. A. Squier, K. R. Wilson, S. D. Carpenter, and P. M. Weber, "Effect of pulse shape on the efficiency of multiphoton process: implications for biological microscopy," *JBO* **4**, 362–367 (1999).
104. V. J. Yallapragada, H. Rigneault, and D. Oron, "Spectrally narrow features in a supercontinuum generated by shaped pulse trains," *Opt. Express* **26**, 5694 (2018).
105. N. Valero, D. Marion, J. Lhermite, J.-C. Delagnes, W. Renard, R. Royon, and E. Cormier, "High-power amplified spontaneous emission pulses with tunable coherence for efficient non-linear processes," *Sci Rep* **11**, 4844 (2021).
106. F. Parmigiani, P. Petropoulos, M. Ibsen, and D. J. Richardson, "All-optical pulse reshaping and retiming systems incorporating pulse shaping fiber Bragg grating," *J. Lightwave Technol.* **24**, 357–364 (2006).
107. P. Petruzzi, C. Lowry, and S. Ponniah, "Dispersion compensation using only fiber Bragg gratings," *Selected Topics in Quantum Electronics, IEEE Journal of* **5**, 1339–1344 (1999).
108. P. Petropoulos, M. Ibsen, M. N. Zervas, and D. J. Richardson, "Generation of a 40-GHz pulse stream by pulse multiplication with a sampled fiber Bragg grating," *Opt. Lett.*, OL **25**, 521–523 (2000).
109. G. Curatu, S. LaRochelle, C. Pare, and P.-A. Belanger, "Pulse shaping with a phase-shifted fiber Bragg grating for antisymmetric pulse generation," in *Optical Pulse and Beam Propagation III* (SPIE, 2001), Vol. 4271, pp. 213–221.
110. W. E. Martin, "Pulse stretching and spectroscopy of subnanosecond optical pulses using a Fabry-Perot interferometer," *Optics Communications* **21**, 8–12 (1977).
111. Y. Zhao, X. Wang, D. Gao, J. Dong, and X. Zhang, "On-chip programmable pulse processor employing cascaded MZI-MRR structure," *Front. Optoelectron.* **12**, 148–156 (2019).

112. M. Plewicky, F. Weise, S. M. Weber, and A. Lindinger, "Phase, amplitude, and polarization shaping with a pulse shaper in a Mach-Zehnder interferometer," *Appl. Opt.*, **AO 45**, 8354–8359 (2006).
113. J. Beeckman, "Liquid-crystal photonic applications," *Opt. Eng* **50**, 081202 (2011).
114. S. Ertman, K. Rutkowska, and T. R. Wolinski, "Recent Progress in Liquid-Crystal Optical Fibers and Their Applications in Photonics," *J. Lightwave Technol.* **37**, 2516–2526 (2019).
115. M. Pessot, P. Maine, and G. Mourou, "1000 times expansion/compression of optical pulses for chirped pulse amplification," *Optics Communications* **62**, 419–421 (1987).
116. D. Vettese, "Liquid crystal on silicon," *Nature Photon* **4**, 752–754 (2010).
117. G. Baxter, S. Frisken, D. Abakoumov, H. Zhou, I. Clarke, A. Bartos, and S. Poole, "Highly programmable wavelength selective switch based on liquid crystal on silicon switching elements," in *2006 Optical Fiber Communication Conference and the National Fiber Optic Engineers Conference* (2006), p. 3 pp.-.
118. "WaveShaper® 1000A Programmable Optical Filter | Coherent Corp.," (n.d.).
119. M. R. Fetterman, D. Goswami, D. Keusters, W. Yang, J.-K. Rhee, and W. S. Warren, "Ultrafast pulse shaping: amplification and characterization," *Opt. Express* **3**, 366 (1998).
120. M. Roth, M. Mehendale, A. Bartelt, and H. Rabitz, "Acousto-optical shaping of ultraviolet femtosecond pulses," *Appl. Phys. B* **80**, 441–444 (2005).
121. K. Ohno, T. Tanabe, and F. Kannari, "Adaptive pulse shaping of phase and amplitude of an amplified femtosecond pulse laser by direct reference to frequency-resolved optical gating traces," *J. Opt. Soc. Am. B, JOSAB* **19**, 2781–2790 (2002).
122. S. Jafari, D. Fathi, and H. Taleb, "Optimal Pulse-Shaping in Actively Q-Switched Ytterbium-Doped Fiber Lasers," *IEEE Access* **8**, 77716–77724 (2020).
123. P. Imany, O. D. Odele, J. A. Jaramillo-Villegas, D. E. Leaird, and A. M. Weiner, "Characterization of coherent quantum frequency combs using electro-optic phase modulation," *Phys. Rev. A* **97**, 013813 (2018).
124. S. Thomas, A. Malacarne, F. Fresi, L. Poti, and J. Azana, "Fiber-Based Programmable Picosecond Optical Pulse Shaper," *Journal of Lightwave Technology* **28**, 1832–1843 (2010).
125. A. Malinowski, K. T. Vu, K. K. Chen, J. Nilsson, Y. Jeong, S. Alam, D. Lin, and D. J. Richardson, "High power pulsed fiber MOPA system incorporating electro-optic modulator based adaptive pulse shaping," *Opt. Express* **17**, 20927 (2009).
126. A. Parriaux, K. Hammani, and G. Millot, "Electro-optic frequency combs," *Adv. Opt. Photon.*, **AOP 12**, 223–287 (2020).
127. R. Amin, R. Maiti, C. Carfano, Z. Ma, M. H. Tahersima, Y. Lilach, D. Ratnayake, H. Dalir, and V. J. Sorger, "0.52 V mm ITO-based Mach-Zehnder modulator in silicon photonics," *APL Photonics* **3**, 126104 (2018).
128. L. Franks, "Carrier and Bit Synchronization in Data Communication - A Tutorial Review," *IEEE Transactions on Communications* **28**, 1107–1121 (1980).
129. K. Zhong, X. Zhou, J. Huo, C. Yu, C. Lu, and A. P. T. Lau, "Digital Signal Processing for Short-Reach Optical Communications: A Review of Current Technologies and Future Trends," *Journal of Lightwave Technology* **36**, 377–400 (2018).
130. B. Fischer, M. Chemnitz, B. MacLellan, P. Roztocky, R. Helsten, B. Wetzel, B. E. Little, S. T. Chu, D. J. Moss, J. Azaña, and R. Morandotti, "Autonomous on-chip interferometry for reconfigurable optical waveform generation," *Optica*, **OPTICA 8**, 1268–1276 (2021).

131. M. I. Jordan and T. M. Mitchell, "Machine learning: Trends, perspectives, and prospects," *Science* **349**, 255–260 (2015).
132. D. Piccinotti, K. F. MacDonald, S. A. Gregory, I. Youngs, and N. I. Zheludev, "Artificial intelligence for photonics and photonic materials," *Rep. Prog. Phys.* **84**, 012401 (2020).
133. J. Zhou, B. Huang, Z. Yan, and J.-C. G. Bünzli, "Emerging role of machine learning in light-matter interaction," *Light Sci Appl* **8**, 84 (2019).
134. Y. Rivenson, Z. Göröcs, H. Günaydin, Y. Zhang, H. Wang, and A. Ozcan, "Deep learning microscopy," *Optica*, *OPTICA* **4**, 1437–1443 (2017).
135. H. S. Stein, D. Guevarra, P. F. Newhouse, E. Soedarmadji, and J. M. Gregoire, "Machine learning of optical properties of materials – predicting spectra from images and images from spectra," *Chemical Science* **10**, 47–55 (2019).
136. E. Kakkava, B. Rahmani, N. Borhani, U. Teğın, D. Loterie, G. Konstantinou, C. Moser, and D. Psaltis, "Imaging through multimode fibers using deep learning: The effects of intensity versus holographic recording of the speckle pattern," *Optical Fiber Technology* **52**, 101985 (2019).
137. D. Wang and M. Zhang, "Artificial Intelligence in Optical Communications: From Machine Learning to Deep Learning," *Frontiers in Communications and Networks* **2**, (2021).
138. D. Zibar, L. H. H. de Carvalho, M. Piels, A. Doberstein, J. Diniz, B. Nebendahl, C. Franciscangelis, J. Estaran, H. Haisch, N. G. Gonzalez, J. C. R. F. de Oliveira, and I. T. Monroy, "Application of Machine Learning Techniques for Amplitude and Phase Noise Characterization," *Journal of Lightwave Technology* **33**, 1333–1343 (2015).
139. J. Thrane, J. Wass, M. Piels, J. C. M. Diniz, R. Jones, and D. Zibar, "Machine Learning Techniques for Optical Performance Monitoring From Directly Detected PDM-QAM Signals," *Journal of Lightwave Technology* **35**, 868–875 (2017).
140. A. Herrero-Bermello, J. Li, M. Khazaei, Y. Grinberg, A. V. Velasco, M. Vachon, P. Cheben, L. Stankovic, V. Stankovic, D.-X. Xu, J. H. Schmid, and C. Alonso-Ramos, "On-chip Fourier-transform spectrometers and machine learning: a new route to smart photonic sensors," *Opt. Lett.*, *OL* **44**, 5840–5843 (2019).
141. C. Zuo, J. Qian, S. Feng, W. Yin, Y. Li, P. Fan, J. Han, K. Qian, and Q. Chen, "Deep learning in optical metrology: a review," *Light Sci Appl* **11**, 39 (2022).
142. W. Ma, Z. Liu, Z. A. Kudyshev, A. Boltasseva, W. Cai, and Y. Liu, "Deep learning for the design of photonic structures," *Nat. Photonics* **15**, 77–90 (2021).
143. R. S. Hegde, "Deep learning: a new tool for photonic nanostructure design," *Nanoscale Adv.* **2**, 1007–1023 (2020).
144. Y. Shen, N. C. Harris, S. Skirlo, M. Prabhu, T. Baehr-Jones, M. Hochberg, X. Sun, S. Zhao, H. Larochelle, D. Englund, and M. Soljačić, "Deep learning with coherent nanophotonic circuits," *Nature Photon* **11**, 441–446 (2017).
145. G. Genty, L. Salmela, J. Dudley, D. Brunner, A. Kokhanovskiy, S. Kobtsev, and S. k Turitsyn, "Machine learning and applications in ultrafast photonics," *Nature Photonics* **15**, 1–11 (2020).
146. S. Boscolo and C. Finot, "Artificial neural networks for nonlinear pulse shaping in optical fibers," *Optics & Laser Technology* **131**, 106439 (2020).
147. M. Närhi, L. Salmela, J. Toivonen, C. Billel, J. M. Dudley, and G. Genty, "Machine learning analysis of extreme events in optical fibre modulation instability," *Nat Commun* **9**, 4923 (2018).

148. L. Salmela, M. Hary, M. Mabed, A. Foi, J. M. Dudley, and G. Genty, "Feed-forward neural network as nonlinear dynamics integrator for supercontinuum generation," *Opt. Lett.*, OL **47**, 802–805 (2022).
149. L. Salmela, C. Lapre, J. M. Dudley, and G. Genty, "Machine learning analysis of rogue solitons in supercontinuum generation," *Sci Rep* **10**, 9596 (2020).
150. M. Mabed, L. Salmela, A. Ermolaev, C. Finot, G. Genty, and J. M. Dudley, "Neural network analysis of unstable temporal intensity peaks in continuous wave modulation instability," *Optics Communications* **541**, 129570 (2023).
151. S. Kleinert, A. Tajalli, T. Nagy, and U. Morgner, "Rapid phase retrieval of ultrashort pulses from dispersion scan traces using deep neural networks," *Opt. Lett.* **44**, 979 (2019).
152. C. Wu, H. Yu, S. Lee, R. Peng, I. Takeuchi, and M. Li, "Programmable phase-change metasurfaces on waveguides for multimode photonic convolutional neural network," *Nat Commun* **12**, 96 (2021).
153. R. A. Herrera, "Evaluating a neural network and a convolutional neural network for predicting soliton properties in a quantum noise environment," *J. Opt. Soc. Am. B, JOSAB* **37**, 3094–3098 (2020).
154. L. Salmela, N. Tspinakis, A. Foi, C. Billet, J. M. Dudley, and G. Genty, "Predicting ultrafast nonlinear dynamics in fibre optics with a recurrent neural network," (2020).
155. U. Teğın, N. U. Dinç, C. Moser, and D. Psaltis, "Reusability report: Predicting spatiotemporal nonlinear dynamics in multimode fibre optics with a recurrent neural network," *Nat Mach Intell* **3**, 387–391 (2021).
156. A. Diamond, M. Schmuker, and T. Nowotny, "An unsupervised neuromorphic clustering algorithm," *Biol Cybern* **113**, 423–437 (2019).
157. C. M. Valensise, A. Giuseppi, G. Cerullo, and D. Polli, "Deep reinforcement learning control of white-light continuum generation," *Optica, OPTICA* **8**, 239–242 (2021).
158. C. Sun, E. Kaiser, S. L. Brunton, and J. N. Kutz, "Deep reinforcement learning for optical systems: A case study of mode-locked lasers," *Mach. Learn.: Sci. Technol.* **1**, 045013 (2020).
159. J. Bueno, S. Maktoobi, L. Froehly, I. Fischer, M. Jacquot, L. Larger, and D. Brunner, "Reinforcement learning in a large-scale photonic recurrent neural network," *Optica* **5**, 756 (2018).
160. J. N. Kutz and S. L. Brunton, "Intelligent Systems for Stabilizing Mode-Locked Lasers and Frequency Combs: Machine Learning and Equation-Free Control Paradigms for Self-Tuning Optics," *Nanophotonics* **4**, 459–471 (2015).
161. S. F. Shu, "Evolving ultrafast laser information by a learning genetic algorithm combined with a knowledge base," *IEEE Photonics Technology Letters* **18**, 379–381 (2006).
162. G. Pu, L. Yi, L. Zhang, and W. Hu, "Intelligent programmable mode-locked fiber laser with a human-like algorithm," *Optica, OPTICA* **6**, 362–369 (2019).
163. G. Pu, L. Yi, L. Zhang, C. Luo, Z. Li, and W. Hu, "Intelligent control of mode-locked femtosecond pulses by time-stretch-assisted real-time spectral analysis," *Light Sci Appl* **9**, 13 (2020).
164. F. Meng and J. M. Dudley, "Toward a self-driving ultrafast fiber laser," *Light: Science & Applications* **9**, 26 (2020).
165. R. I. Woodward and E. J. R. Kelleher, "Towards 'smart lasers': self-optimisation of an ultrafast pulse source using a genetic algorithm," *Sci Rep* **6**, 37616 (2016).

166. U. Andral, R. S. Fodil, F. Amrani, F. Billard, E. Hertz, and P. Grelu, "Fiber laser mode locked through an evolutionary algorithm," *Optica*, OPTICA **2**, 275–278 (2015).
167. R. I. Woodward and E. J. R. Kelleher, "Genetic algorithm-based control of birefringent filtering for self-tuning, self-pulsing fiber lasers," *Opt. Lett.*, OL **42**, 2952–2955 (2017).
168. X. Fu, S. L. Brunton, and J. Nathan Kutz, "Classification of birefringence in mode-locked fiber lasers using machine learning and sparse representation," *Opt. Express* **22**, 8585 (2014).
169. W. Q. Zhang, S. A. V, and T. M. Monroe, "A genetic algorithm based approach to fiber design for high coherence and large bandwidth supercontinuum generation," *Opt. Express*, OE **17**, 19311–19327 (2009).
170. F. R. Arteaga-Sierra, C. Milián, I. Torres-Gómez, M. Torres-Cisneros, G. Moltó, and A. Ferrando, "Supercontinuum optimization for dual-soliton based light sources using genetic algorithms in a grid platform," *Opt. Express*, OE **22**, 23686–23693 (2014).
171. A. Kokhanovskiy, E. Kuprikov, A. Bednyakova, I. Popkov, S. Smirnov, and S. Turitsyn, "Inverse design of mode-locked fiber laser by particle swarm optimization algorithm," *Sci Rep* **11**, 13555 (2021).
172. S. phase-sensitive optical pulse characterization on a chip Pu, L. Yi, L. Zhang, and W. Hu, "Genetic Algorithm-Based Fast Real-Time Automatic Mode-Locked Fiber Laser," *IEEE Photonics Technology Letters* **32**, 7–10 (2020).
173. A. E. Eiben and J. E. Smith, *Introduction to Evolutionary Computing*, Natural Computing Series (Springer, 2015).
174. C. Audet and W. Hare, "Genetic Algorithms," in *Derivative-Free and Blackbox Optimization*, C. Audet and W. Hare, eds., Springer Series in Operations Research and Financial Engineering (Springer International Publishing, 2017), pp. 57–73.
175. J. H. Holland, *Adaptation in Natural and Artificial Systems: An Introductory Analysis with Applications to Biology, Control, and Artificial Intelligence* (MIT Press, 1992).
176. S. Katoch, S. S. Chauhan, and V. Kumar, "A review on genetic algorithm: past, present, and future," *Multimed Tools Appl* **80**, 8091–8126 (2021).
177. X.-S. Yang, *Nature-Inspired Optimization Algorithms* (Academic Press, 2020).
178. M. Jaberipour, E. Khorram, and B. Karimi, "Particle swarm algorithm for solving systems of nonlinear equations," *Computers & Mathematics with Applications* **62**, 566–576 (2011).
179. R. C. Eberhart and Y. Shi, "Comparison between genetic algorithms and particle swarm optimization," in *Evolutionary Programming VII*, V. W. Porto, N. Saravanan, D. Waagen, and A. E. Eiben, eds., Lecture Notes in Computer Science (Springer, 1998), pp. 611–616.
180. R. Trebino, *Frequency-Resolved Optical Gating: The Measurement of Ultrashort Laser Pulses* (Springer US, 2000).
181. L. Taylor, "The phase retrieval problem," *IEEE Transactions on Antennas and Propagation* **29**, 386–391 (1981).
182. L. Cohen, "The generalization of the Wiener-Khinchin theorem," in *Proceedings of the 1998 IEEE International Conference on Acoustics, Speech and Signal Processing, ICASSP '98 (Cat. No.98CH36181)* (1998), Vol. 3, pp. 1577–1580 vol.3.
183. J.-C. M. Diels, J. J. Fontaine, I. C. McMichael, and F. Simoni, "Control and measurement of ultrashort pulse shapes (in amplitude and phase) with femtosecond accuracy," *Appl. Opt.*, AO **24**, 1270–1282 (1985).

184. K. W. DeLong, R. Trebino, J. Hunter, and W. E. White, "Frequency-resolved optical gating with the use of second-harmonic generation," *J. Opt. Soc. Am. B, JOSAB* **11**, 2206–2215 (1994).
185. J. Paye, M. Ramaswamy, J. G. Fujimoto, and E. P. Ippen, "Measurement of the amplitude and phase of ultrashort light pulses from spectrally resolved autocorrelation," *Opt. Lett.*, **OL 18**, 1946–1948 (1993).
186. R. Trebino and D. J. Kane, "Using phase retrieval to measure the intensity and phase of ultrashort pulses: frequency-resolved optical gating," *J. Opt. Soc. Am. A, JOSAA* **10**, 1101–1111 (1993).
187. D. J. Kane, J. Weston, and K.-C. J. Chu, "Real-time inversion of polarization gate frequency-resolved optical gating spectrograms," *Appl. Opt.*, **AO 42**, 1140–1144 (2003).
188. K. DeLong, "FROG (Frequency-Resolved Optical Gating) Software," (2023).
189. P. O'Shea, S. Akturk, M. Kimmel, and R. Trebino, "Practical issues in ultra-short-pulse measurements with 'GRENOUILLE,'" *Appl. Phys. B* **79**, 683–691 (2004).
190. C. Iaconis and I. A. Walmsley, "Spectral phase interferometry for direct electric-field reconstruction of ultrashort optical pulses," *Opt. Lett.*, **OL 23**, 792–794 (1998).
191. A. Pasquazi, M. Peccianti, Y. Park, B. E. Little, S. T. Chu, R. Morandotti, J. Azafía, and D. J. Moss, "Sub-picosecond phase-sensitive optical pulse characterization on a chip," *Nature Photonics* **5**, 618–623 (2011).
192. V. Messenger, F. Louradour, C. Froehly, and A. Barthelemy, "Coherent measurement of short laser pulses based on spectral interferometry resolved in time," *Opt. Lett.* **28**, 743 (2003).
193. J. M. Dudley, L. P. Barry, J. D. Harvey, M. D. Thomson, B. C. Thomsen, P. G. Bollond, and R. Leonhardt, "Complete characterization of ultrashort pulse sources at 1550 nm," *IEEE J. Quantum Electron.* **35**, 441–450 (1999).
194. J. M. Dudley, L. P. Barry, P. G. Bollond, J. D. Harvey, and R. Leonhardt, "Characterizing Pulse Propagation in Optical Fibers around 1550 nm Using Frequency-Resolved Optical Gating," *Optical Fiber Technology* **4**, 237–265 (1998).
195. X. Gu, L. Xu, M. Kimmel, E. Zeek, P. O'Shea, A. P. Shreenath, R. Trebino, and R. S. Windeler, "Frequency-resolved optical gating and single-shot spectral measurements reveal fine structure in microstructure-fiber continuum," *Opt Lett* **27**, 1174–1176 (2002).
196. L. P. Barry, S. Del burgo, B. Thomsen, R. T. Watts, D. A. Reid, and J. Harvey, "Optimization of optical data transmitters for 40-Gb/s lightwave systems using frequency resolved optical gating," *IEEE Photonics Technology Letters* **14**, 971–973 (2002).
197. A. Mahjoubfar, D. V. Churkin, S. Barland, N. Broderick, S. K. Turitsyn, and B. Jalali, "Time stretch and its applications," *Nature Photon* **11**, 341–351 (2017).
198. A. S. Bhushan, F. Coppinger, and B. Jalali, "Time-stretched analogue-to-digital conversion," *Electronics Letters* **34**, 839–841 (1998).
199. T. Godin, L. Sader, A. Khodadad Kashi, P.-H. Hanzard, A. Hideur, D. J. Moss, R. Morandotti, G. Genty, J. M. Dudley, A. Pasquazi, M. Kues, and B. Wetzal, "Recent advances on time-stretch dispersive Fourier transform and its applications," *Advances in Physics: X* **7**, 2067487 (2022).
200. M. Närhi, B. Wetzal, C. Billet, S. Toenger, T. Sylvestre, J.-M. Merolla, R. Morandotti, F. Dias, G. Genty, and J. M. Dudley, "Real-time measurements of spontaneous breathers and rogue wave events in optical fibre modulation instability," *Nat Commun* **7**, 13675 (2016).

201. R. Salem, M. A. Foster, A. C. Turner, D. F. Geraghty, M. Lipson, and A. L. Gaeta, "Optical time lens based on four-wave mixing on a silicon chip," *Opt. Lett.*, OL **33**, 1047–1049 (2008).
202. M. A. Foster, R. Salem, D. F. Geraghty, A. C. Turner-Foster, M. Lipson, and A. L. Gaeta, "Silicon-chip-based ultrafast optical oscilloscope," *Nature* **456**, 81–84 (2008).
203. K. Goda, D. R. Solli, K. K. Tsia, and B. Jalali, "Theory of amplified dispersive Fourier transformation," *Phys. Rev. A* **80**, 043821 (2009).
204. B. H. Kolner, "Space-time duality and the theory of temporal imaging," *IEEE Journal of Quantum Electronics* **30**, 1951–1963 (1994).
205. B. Wetzel, A. Stefani, L. Larger, P. A. Lacourt, J. M. Merolla, T. Sylvestre, A. Kudlinski, A. Mussot, G. Genty, F. Dias, and J. M. Dudley, "Real-time full bandwidth measurement of spectral noise in supercontinuum generation," *Scientific Reports* **2**, 882 (2012).
206. G. V. Grigoryan, J. I. T. Lima, T. Yu, V. S. Grigoryan, and C. R. Menyuk, "Using Color to Understand Light Transmission," *Optics & Photonics News*, OPN **11**, 44–50 (2000).
207. D. R. Solli, G. Herink, B. Jalali, and C. Ropers, "Fluctuations and correlations in modulation instability," *Nature Photon* **6**, 463–468 (2012).
208. T. Godin, B. Wetzel, T. Sylvestre, L. Larger, A. Kudlinski, A. Mussot, A. B. Salem, M. Zghal, G. Genty, F. Dias, and J. M. Dudley, "Real time noise and wavelength correlations in octave-spanning supercontinuum generation," *Opt. Express*, OE **21**, 18452–18460 (2013).
209. P. Robert, C. Fourcade-Dutin, C. Fourcade-Dutin, R. Dauliat, R. Jamier, H. Muñoz-Marco, P. Pérez-Millán, J. M. Dudley, P. Roy, H. Maillotte, D. Bigourd, and D. Bigourd, "Spectral correlation of four-wave mixing generated in a photonic crystal fiber pumped by a chirped pulse," *Opt. Lett.*, OL **45**, 4148–4151 (2020).
210. X. Wang, D. Bigourd, A. Kudlinski, K. K. Y. Wong, M. Douay, L. Bigot, A. Lerouge, Y. Quiquempois, and A. Mussot, "Correlation between multiple modulation instability side lobes in dispersion oscillating fiber," *Opt. Lett.*, OL **39**, 1881–1884 (2014).
211. J. M. Dudley, G. Genty, and S. Coen, "Supercontinuum generation in photonic crystal fiber," *Rev. Mod. Phys.* **78**, 1135–1184 (2006).
212. J. M. Dudley, F. Dias, M. Erkintalo, and G. Genty, "Instabilities, breathers and rogue waves in optics," *Nature Photon* **8**, 755–764 (2014).
213. C. Lapre, C. Billet, F. Meng, P. Ryczkowski, T. Sylvestre, C. Finot, G. Genty, and J. M. Dudley, "Real-time characterization of spectral instabilities in a mode-locked fibre laser exhibiting soliton-similariton dynamics," *Sci Rep* **9**, 13950 (2019).
214. G. Herink, B. Jalali, C. Ropers, and D. R. Solli, "Resolving the build-up of femtosecond mode-locking with single-shot spectroscopy at 90 MHz frame rate," *Nature Photon* **10**, 321–326 (2016).
215. K. Krupa, K. Nithyanandan, U. Andral, P. Tchofo-Dinda, and P. Grelu, "Real-Time Observation of Internal Motion within Ultrafast Dissipative Optical Soliton Molecules," *Phys. Rev. Lett.* **118**, 243901 (2017).
216. A. F. J. Runge, C. Aguergaray, N. G. R. Broderick, and M. Erkintalo, "Coherence and shot-to-shot spectral fluctuations in noise-like ultrafast fiber lasers," *Opt. Lett.*, OL **38**, 4327–4330 (2013).
217. K. Goda and B. Jalali, "Dispersive Fourier transformation for fast continuous single-shot measurements," *Nature Photon* **7**, 102–112 (2013).
218. J. Chou, D. R. Solli, and B. Jalali, "Real-time spectroscopy with subgigahertz resolution using amplified dispersive Fourier transformation," *Appl. Phys. Lett.* **92**, 111102 (2008).

219. Y. Sych, R. Engelbrecht, B. Schmauss, D. Kozlov, T. Seeger, and A. Leipertz, "Broadband time-domain absorption spectroscopy with a ns-pulse supercontinuum source," *Opt. Express*, OE **18**, 22762–22771 (2010).
220. K. Goda, K. K. Tsia, and B. Jalali, "Serial time-encoded amplified imaging for real-time observation of fast dynamic phenomena," *Nature* **458**, 1145–1149 (2009).
221. S. H. Kim, K. Goda, A. Fard, and B. Jalali, "Optical time-domain analog pattern correlator for high-speed real-time image recognition," *Opt. Lett.*, OL **36**, 220–222 (2011).
222. L. Sader, S. Bose, A. K. Kashi, Y. Boussafa, R. Haldar, R. Dauliat, P. Roy, M. Fabert, A. Tonello, V. Couderc, M. Kues, and B. Wetzel, "Single-Photon Level Dispersive Fourier Transform: Ultrasensitive Characterization of Noise-Driven Nonlinear Dynamics," *ACS Photonics* **10**, 3915–3928 (2023).
223. T. Godin, B. Wetzel, J. M. Dudley, G. Herink, F. Dias, G. Genty, B. Jalali, C. Ropers, and D. R. Solli, "Ultrafast Single-Shot Measurements in Modulation Instability and Supercontinuum," *Optics & Photonics News* **24**, 55 (2013).
224. M. Touil, R. Becheker, T. Godin, and A. Hideur, "Spectral correlations in a fiber-optical parametric oscillator," *Phys. Rev. A* **103**, 043503 (2021).
225. D. M. Nguyen, T. Godin, S. Toenger, Y. Combes, B. Wetzel, T. Sylvestre, J.-M. Merolla, L. Larger, G. Genty, F. Dias, and J. M. Dudley, "Incoherent resonant seeding of modulation instability in optical fiber," *Opt. Lett.* **38**, 5338 (2013).
226. J. M. Dudley, G. Genty, F. Dias, B. Kibler, and N. Akhmediev, "Modulation instability, Akhmediev Breathers and continuous wave supercontinuum generation," *Opt. Express* **17**, 21497 (2009).
227. A. Bendahmane, J. Fatome, C. Finot, G. Millot, and B. Kibler, "Coherent and incoherent seeding of dissipative modulation instability in a nonlinear fiber ring cavity," *Opt. Lett.*, OL **42**, 251–254 (2017).
228. S. Sugavanam, M. K. Kopae, J. Peng, J. E. Prilepsky, and S. K. Turitsyn, "Analysis of laser radiation using the Nonlinear Fourier transform," *Nat Commun* **10**, 5663 (2019).
229. K. Goda, D. R. Solli, K. K. Tsia, and B. Jalali, "Theory of amplified dispersive Fourier transformation," *Phys. Rev. A* **80**, 043821 (2009).
230. C. Lei, Y. Wu, A. C. Sankaranarayanan, S.-M. Chang, B. Guo, N. Sasaki, H. Kobayashi, C.-W. Sun, Y. Ozeki, and K. Goda, "GHz Optical Time-Stretch Microscopy by Compressive Sensing," *IEEE Photonics Journal* **9**, 1–8 (2017).
231. A. Pasquazi, M. Peccianti, L. Razzari, D. J. Moss, S. Coen, M. Erkintalo, Y. K. Chembo, T. Hansson, S. Wabnitz, P. Del'Haye, X. Xue, A. M. Weiner, and R. Morandotti, "Microcombs: A novel generation of optical sources," *Physics Reports* **729**, 1–81 (2018).
232. A. Cutrona, V. Cecconi, P. H. Hanzard, M. Rowley, D. Das, A. Cooper, L. Peters, L. Olivieri, B. Wetzel, R. Morandotti, S. T. Chu, B. E. Little, D. J. Moss, J. S. Toterogongora, M. Peccianti, and A. Pasquazi, "Nonlocal bonding of a soliton and a blue-detuned state in a microcomb laser," *Commun Phys* **6**, 1–10 (2023).
233. M. Nie, B. Li, K. Jia, Y. Xie, J. Yan, S. Zhu, Z. Xie, and S.-W. Huang, "Dissipative soliton generation and real-time dynamics in microresonator-filtered fiber lasers," *Light Sci Appl* **11**, 296 (2022).
234. X. Wei, Y. Shen, J. C. Jing, A. S. Hemphill, C. Yang, S. Xu, Z. Yang, and L. V. Wang, "Real-time frequency-encoded spatiotemporal focusing through scattering media using a programmable 2D ultrafine optical frequency comb," *Sci Adv* **6**, eaay1192 (2020).
235. X. Liu, X. Yao, and Y. Cui, "Real-Time Observation of the Buildup of Soliton Molecules," *Phys. Rev. Lett.* **121**, 023905 (2018).

236. M. Chernysheva, S. Sugavanam, and S. Turitsyn, "Real-time observation of the optical Sagnac effect in ultrafast bidirectional fibre lasers," *APL Photonics* **5**, 016104 (2020).
237. S. Tiedeck, M. B. Heindl, P. Kramlinger, J. Naas, F. Brütting, N. Kirkwood, P. Mulvaney, and G. Herink, "Single-Pixel Fluorescence Spectroscopy Using Near-Field Dispersion for Single-Photon Counting and Single-Shot Acquisition," *ACS Photonics* **9**, 2931–2937 (2022).
238. S. M. Kolenderska, S. M. Kolenderska, F. Vanholsbeeck, F. Vanholsbeeck, and P. Kolenderski, "Quantum-inspired detection for spectral domain optical coherence tomography," *Opt. Lett.*, OL **45**, 3443–3446 (2020).
239. P.-H. Hanzard, T. Godin, S. Idlahcen, C. Rozé, and A. Hideur, "Real-time tracking of single shockwaves via amplified time-stretch imaging," *Applied Physics Letters* **112**, 161106 (2018).
240. M. Avenhaus, A. Eckstein, P. J. Mosley, and C. Silberhorn, "Fiber-assisted single-photon spectrograph," *Opt. Lett.* **34**, 2873 (2009).
241. A. Eckstein, G. Boucher, A. Lemaître, P. Filloux, I. Favero, G. Leo, J. E. Sipe, M. Liscidini, and S. Ducci, "High-resolution spectral characterization of two photon states via classical measurements," *Laser & Photonics Reviews* **8**, L76–L80 (2014).
242. K. Zielnicki, K. Garay-Palmett, D. Cruz-Delgado, H. Cruz-Ramirez, M. F. O'Boyle, B. Fang, V. O. Lorenz, A. B. U'Ren, and P. G. Kwiat, "Joint Spectral Characterization of Photon-Pair Sources," *Journal of Modern Optics* **65**, 1141–1160 (2018).
243. T. Gerrits, F. Marsili, V. B. Verma, L. K. Shalm, M. Shaw, R. P. Mirin, and S. W. Nam, "Spectral correlation measurements at the Hong-Ou-Mandel interference dip," *Phys. Rev. A* **91**, 013830 (2015).
244. T. Gerrits, M. J. Stevens, B. Baek, B. Calkins, A. Lita, S. Glancy, E. Knill, S. W. Nam, R. P. Mirin, R. H. Hadfield, R. S. Bennink, W. P. Grice, S. Dorenbos, T. Zijlstra, T. Klapwijk, and V. Zwiller, "Generation of degenerate, factorizable, pulsed squeezed light at telecom wavelengths," *Opt. Express* **19**, 24434 (2011).
245. M. Karpiński, M. Jachura, L. J. Wright, and B. J. Smith, "Bandwidth manipulation of quantum light by an electro-optic time lens," *Nature Photon* **11**, 53–57 (2017).
246. A. Khodadad Kashi, L. Sader, R. Haldar, B. Wetzal, and M. Kues, "Frequency-to-Time Mapping Technique for Direct Spectral Characterization of Biphoton States From Pulsed Spontaneous Parametric Processes," *Front. Photon.* **3**, 834065 (2022).
247. R. Hanbury Brown and R. Q. Twiss, "A Test of a New Type of Stellar Interferometer on Sirius," *Nature* **178**, 1046–1048 (1956).
248. B. Silva, C. Sánchez Muñoz, D. Ballarini, A. González-Tudela, M. de Giorgi, G. Gigli, K. West, L. Pfeiffer, E. del Valle, D. Sanvitto, and F. P. Laussy, "The colored Hanbury Brown–Twiss effect," *Sci Rep* **6**, 37980 (2016).
249. J. M. Dudley and J. R. Taylor, *Supercontinuum Generation in Optical Fibers* (Cambridge University Press, 2010).
250. X. Wang, D. Bigourd, A. Kudlinski, K. K. Y. Wong, M. Douay, L. Bigot, A. Lerouge, Y. Quiquempois, and A. Mussot, "Correlation between multiple modulation instability side lobes in dispersion oscillating fiber," *Opt. Lett.* **39**, 1881 (2014).
251. G. Grynberg, A. Aspect, C. Fabre, and C. Cohen-Tannoudji, *Introduction to Quantum Optics: From the Semi-classical Approach to Quantized Light* (Cambridge University Press, 2010).

252. B. Wetzel, K. J. Blow, S. K. Turitsyn, G. Millot, L. Larger, and J. M. Dudley, "Random walks and random numbers from supercontinuum generation," *Opt. Express* **20**, 11143 (2012).
253. A. Bendahmane, J. Fatome, C. Finot, G. Millot, and B. Kibler, "Coherent and incoherent seeding of dissipative modulation instability in a nonlinear fiber ring cavity," *Opt. Lett.* **42**, 251 (2017).
254. D. R. Solli, C. Ropers, and B. Jalali, "Active Control of Rogue Waves for Stimulated Supercontinuum Generation," *Phys. Rev. Lett.* **101**, 233902 (2008).
255. B. Wetzel, M. Kues, P. Roztocky, C. Reimer, P.-L. Godin, M. Rowley, B. E. Little, S. T. Chu, E. A. Viktorov, D. J. Moss, A. Pasquazi, M. Peccianti, and R. Morandotti, "Customizing supercontinuum generation via on-chip adaptive temporal pulse-splitting," *Nat Commun* **9**, 4884 (2018).
256. A. De la Cadena, C. M. Valensise, M. Marangoni, G. Cerullo, and D. Polli, "Broadband stimulated Raman scattering microscopy with wavelength-scanning detection," *Journal of Raman Spectroscopy* **51**, 1951–1959 (2020).
257. A. Mussot, M. Conforti, S. Trillo, F. Copie, and A. Kudlinski, "Modulation instability in dispersion oscillating fibers," *Adv. Opt. Photon., AOP* **10**, 1–42 (2018).
258. A. Demircan and U. Bandelow, "Supercontinuum generation by the modulation instability," *Optics Communications* **244**, 181–185 (2005).
259. J. Zhao, L.-K. Chen, C.-K. Chan, and C. Lin, "Analysis of performance optimization in supercontinuum sources," *Opt. Lett., OL* **29**, 489–491 (2004).
260. A. Mussot, C. Naveau, M. Conforti, A. Kudlinski, F. Copie, P. Szriftgiser, and S. Trillo, "Fibre multi-wave mixing combs reveal the broken symmetry of Fermi–Pasta–Ulam recurrence," *Nature Photon* **12**, 303–308 (2018).
261. A. Mussot, A. Kudlinski, M. Droques, P. Szriftgiser, and N. Akhmediev, "Fermi-Pasta-Ulam Recurrence in Nonlinear Fiber Optics: The Role of Reversible and Irreversible Losses," *Phys. Rev. X* **4**, 011054 (2014).
262. M. Droques, A. Kudlinski, G. Bouwmans, G. Martinelli, and A. Mussot, "Experimental demonstration of modulation instability in an optical fiber with a periodic dispersion landscape," *Opt. Lett., OL* **37**, 4832–4834 (2012).
263. A. Kudlinski, B. Barviau, A. Leray, C. Spriet, L. Hélot, and A. Mussot, "Control of pulse-to-pulse fluctuations in visible supercontinuum," *Opt. Express, OE* **18**, 27445–27454 (2010).
264. K. Hammani, B. Wetzel, B. Kibler, J. Fatome, C. Finot, G. Millot, N. Akhmediev, and J. M. Dudley, "Spectral dynamics of modulation instability described using Akhmediev breather theory," *Opt. Lett., OL* **36**, 2140–2142 (2011).
265. G. E. Van Simaey, Ph. Emplit, and M. Haelterman, "Observation of modulational instability recurrence in optical fibers," in *Nonlinear Guided Waves and Their Applications* (OSA, 2001), p. WB5.
266. C. Finot and S. Wabnitz, "Influence of the pump shape on the modulation instability process induced in a dispersion-oscillating fiber," *J. Opt. Soc. Am. B* **32**, 892 (2015).
267. A. Sheveleva, P. Colman, J. M. Dudley, and C. Finot, "Phase space topology of four-wave mixing reconstructed by a neural network," *Opt. Lett., OL* **47**, 6317–6320 (2022).
268. H. Sui, H. Zhu, L. Cheng, B. Luo, S. Taccheo, X. Zou, and L. Yan, "Deep learning based pulse prediction of nonlinear dynamics in fiber optics," *Opt. Express, OE* **29**, 44080–44092 (2021).

269. G. Genty, L. Salmela, J. M. Dudley, D. Brunner, A. Kokhanovskiy, S. Kobtsev, and S. K. Turitsyn, "Machine learning and applications in ultrafast photonics," *Nat. Photonics* **15**, 91–101 (2021).
270. S. Coulibaly, F. Bessin, M. G. Clerc, and A. Mussot, "Precursors-driven machine learning prediction of chaotic extreme pulses in Kerr resonators," *Chaos, Solitons & Fractals* **160**, 112199 (2022).
271. Y. Boussafa, L. Sader, V. T. Hoang, B. P. Chaves, A. Tonello, and B. Wetzel, "Numerical Prediction of Incoherent Modulation Instability Dynamics through Deep Learning Approaches," in *Conference on Lasers and Electro-Optics/Europe (CLEO/Europe 2023) and European Quantum Electronics Conference (EQEC 2023) (2023), Paper Ef_p_10* (Optica Publishing Group, 2023), p. ef_p_10.
272. T. Godin, L. Sader, A. Khodadad Kashi, P.-H. Hanzard, A. Hideur, D. J. Moss, R. Morandotti, G. Genty, J. M. Dudley, A. Pasquazi, M. Kues, and B. Wetzel, "Recent advances on time-stretch dispersive Fourier transform and its applications," *Advances in Physics: X* **7**, 2067487 (2022).
273. B. P. Chaves, V. T. Hoang, V. Couderc, B. E. Little, S. T. Chu, D. J. Moss, R. Morandotti, and B. Wetzel, "Spectro-temporal Characterization of Tunable Supercontinuum using X-FROG Measurements," in *Conference on Lasers and Electro-Optics/Europe (CLEO/Europe 2023) and European Quantum Electronics Conference (EQEC 2023) (2023), Paper Ee_5_3* (Optica Publishing Group, 2023), p. ee_5_3.
274. V. T. Hoang, Y. Boussafa, L. Sader, S. Février, V. Couderc, and B. Wetzel, "Optimizing supercontinuum spectro-temporal properties by leveraging machine learning towards multi-photon microscopy," *Frontiers in Photonics* **3**, (2022).
275. V. T. Hoang, Y. Boussafa, L. Sader, S. Février, V. Couderc, and B. Wetzel, "Optimizing supercontinuum spectro-temporal properties by leveraging machine learning towards multi-photon microscopy," *Frontiers in Photonics* **3**, (2022).
276. W. R. Zipfel, R. M. Williams, and W. W. Webb, "Nonlinear magic: multiphoton microscopy in the biosciences," *Nat Biotechnol* **21**, 1369–1377 (2003).
277. J. Cheng, A. Volkmer, L. D. Book, and X. S. Xie, "Multiplex Coherent Anti-Stokes Raman Scattering Microspectroscopy and Study of Lipid Vesicles," *J. Phys. Chem. B* **106**, 8493–8498 (2002).
278. L. G. Rodriguez, S. J. Lockett, and G. R. Holtom, "Coherent anti-stokes Raman scattering microscopy: A biological review," *Cytometry Part A* **69A**, 779–791 (2006).
279. F. Helmchen and W. Denk, "Deep tissue two-photon microscopy," *Nat Methods* **2**, 932–940 (2005).
280. A. M. Larson, "Multiphoton microscopy," *Nature Photon* **5**, 1–1 (2011).
281. C. Poudel and C. F. Kaminski, "Supercontinuum radiation in fluorescence microscopy and biomedical imaging applications," *J. Opt. Soc. Am. B, JOSAB* **36**, A139–A153 (2019).
282. B. Wetzel, M. Kues, P. Roztock, C. Reimer, P.-L. Godin, M. Rowley, B. E. Little, S. T. Chu, E. A. Viktorov, D. J. Moss, A. Pasquazi, M. Peccianti, and R. Morandotti, "Customizing supercontinuum generation via on-chip adaptive temporal pulse-splitting," *Nat Commun* **9**, 4884 (2018).
283. B. Fischer, M. Chemnitz, B. MacLellan, P. Roztock, R. Helsten, B. Wetzel, B. E. Little, S. T. Chu, D. J. Moss, J. Azaña, and R. Morandotti, "Autonomous on-chip interferometry for reconfigurable optical waveform generation," *Optica, OPTICA* **8**, 1268–1276 (2021).

Résumé

Les effets non linéaires ont pris de l'importance dans la photonique moderne en offrant de nouveaux moyens de générer de la lumière avec des propriétés accordables. Au fil des années, des travaux importants ont été consacrés à la compréhension et à la manipulation de ces phénomènes non linéaires, avec un regain d'intérêt récent dans le domaine avec l'essor de l'intelligence artificielle. Cette thèse vise à développer de nouvelles approches pour contrôler les impulsions ultracourtes et optimiser leurs dynamiques de propagation non linéaire dans les fibres optiques. Dans ces travaux, nous concentrons nos études sur le processus d'instabilité de modulation, que nous considérons comme un cas particulier d'élargissement spectral non linéaire incohérent, un phénomène induit par le bruit qui se traduit par des caractéristiques spectrales fluctuantes. Nous abordons ici la mesure et l'analyse statistique de ces fluctuations par le biais de techniques de caractérisation en temps réel. Nous présentons le développement d'une approche de caractérisation ultrasensible permettant de détecter, de caractériser et d'étudier ces instabilités non linéaires avec des performances améliorées. Nous examinons également comment ces dynamiques de propagation incohérente peuvent être contrôlées par des techniques d'optimisation et d'apprentissage automatique. Ce travail couvre à la fois des études numériques et expérimentales examinant l'impact d'un contrôle optique sur la formation de l'instabilité de modulation et l'optimisation de ses propriétés à l'aide d'algorithmes évolutionnaires. Enfin, nous discutons brièvement des perspectives du contrôle temporel avancé de l'élargissement non linéaire fibré via des systèmes photoniques intégrés programmables. Dans l'ensemble, ces études ouvrent la voie au développement de sources photoniques intelligentes pour des applications couvrant la microscopie avancée, de nouvelles techniques d'imagerie et la métrologie, avec un potentiel dans divers domaines scientifiques.

Mots-clés : Optique non linéaire, photonique ultra-rapide, fibre optique, instabilité de modulation, techniques de caractérisation optique, apprentissage automatique

Abstract

Nonlinear effects have gained importance in modern photonics as they provide new means for the generation of light with tunable properties. Over the years, important work has been dedicated to understanding and manipulating these nonlinear phenomena, with a recently renewed interest in the field with the rise of artificial intelligence. This thesis aims at the development of novel approaches for controlling ultrashort pulses and optimizing their propagation dynamics in nonlinear fiber optics. In this work, we focus our studies on the process of modulation instability, which we consider a case study of incoherent nonlinear spectral broadening, a noise-driven phenomenon resulting in fluctuating output spectral characteristics. Here, we discuss the measurement and statistical analysis of these fluctuations via real-time characterization techniques. We report on the development of an ultra-sensitive characterization approach allowing to detect, characterize and study these nonlinear instabilities with improved performances. We further examine how such incoherent propagation dynamics can be controlled via optimization and machine learning techniques. This work covers both numerical and experimental studies investigating the impact of optical seeding on the formation of modulation instability and the optimization of its properties using evolutionary algorithms. Finally, we briefly discuss perspectives towards advanced temporal control of nonlinear fiber broadening via programmable integrated photonics systems. Overall, these studies pave the way towards the development of smart photonic sources for applications spanning advanced microscopy, novel imaging techniques, and metrology, with a strong potential across various scientific domains.

Keywords: Nonlinear optics, ultrafast photonics, fiber optics, modulation instability, optical characterization techniques, machine learning

